

**WASHINGTON UNIVERSITY  
THE HENRY EDWIN SEVER GRADUATE SCHOOL  
DEPARTMENT OF CHEMICAL ENGINEERING**

---

**Analyzing and Modeling of Airlift Photobioreactors  
for Microalgal and Cyanobacteria Cultures**

**by**

**Hu-Ping Luo**

**Prepared under the direction of Prof. M. H. Al-Dahhan**

---

**A dissertation presented to the Henry Edwin Sever Graduate School of  
Washington University in partial fulfillment of the  
requirements of the degree of  
DOCTOR OF SCIENCE  
August 2005  
Saint Louis, Missouri**

WASHINGTON UNIVERSITY  
THE HENRY EDWIN SEVER GRADUATE SCHOOL  
DEPARTMENT OF CHEMICAL ENGINEERING

---

ABSTRACT

---

**Analyzing and Modeling of Airlift Photobioreactors  
for Microalgal and Cyanobacteria Cultures**

by

**Hu-Ping Luo**

**ADVISOR: Professor M. H. Al-Dahhan**

---

**August 2005  
St. Louis, Missouri**

---

Microalgae and cyanobacteria cultures are attracting great attentions in many industrial applications. However, their mass production in enclosed photobioreactors faces prohibitively high production costs with special difficulty in reactor design and scale-up. The major problem for the PBR design and scale-up is light: its availability and utilization efficiency. It has been found that hydrodynamics and mixing can greatly enhance the biomass productivity by improving the light use efficiency. However, the local flow characteristics remain unclear, and the mechanism of how hydrodynamics interacts with photosynthesis is not fully understood yet.

The overall objective of this study is to advance the understanding of hydrodynamics' role in the photosynthesis and thus the photobioreactor performance, and to develop a fundamentally based modeling approach for photobioreactor performance evaluation. Two experimental techniques (i.e., Computer Automated Radioactive Particle Tracking - CARPT and Computer Tomography - CT) and the Computational Fluid Dynamics (CFD) technique were applied to study the local flow dynamics in a draft tube airlift column photobioreactor.

Based on the findings of the flow dynamic study, how hydrodynamics interact with photosynthesis was carefully analyzed. The time series of irradiance transferred to the microorganisms were computed, and parameters to quantitatively characterize the irradiance patterns were also proposed. Moreover, a fundamentally based dynamic modeling approach is developed for photobioreactor performance evaluation, which integrates the knowledge of photosynthesis, hydrodynamics, and irradiance.

Finally, *Porphyridium* sp. was grown in three types of airlift column reactors. The biomass concentrations, multiphase flow dynamics, physical properties, and irradiance distribution of the culturing systems were monitored. Nice agreements between the predictions by the developed dynamic model and the experimental data were achieved, indicating the applicability of the dynamic model in industrial interested condition.

To Xiangyu, Mindy, and the family

# Contents

<b>List of Figures.....</b>	<b>viii</b>
<b>List of Tables.....</b>	<b>xviii</b>
<b>Nomenclatures.....</b>	<b>xix</b>
<b>Acknowledgements.....</b>	<b>xxvi</b>
<b>Chapter 1 Introduction.....</b>	<b>1</b>
1.1 Problem Identification .....	2
1.2 Motivation.....	6
1.3 Research Objectives.....	10
1.4 Structure of Dissertation .....	13
<b>Chapter 2 Background.....</b>	<b>14</b>
2.1 Scope.....	14
2.2 An overview of photosynthesis.....	15
2.3 Flashing Light Effects.....	18
2.3.1 How Flashing Lights Work.....	18
2.3.2 Characterization of Flashing Light .....	21
2.4 Modeling Approaches for Photobioreactors .....	22
2.4.1 Modeling Approaches Based on the Static Photosynthetic Rate Model.....	23
2.4.2 Modeling Approaches Based on the Dynamic Photosynthetic Rate Model.....	26
2.5 Enclosed Photobioreactors.....	30
2.6 Investigations of Hydrodynamics for Airlift Column Reactor .....	32
2.6.1 Experimental measurements .....	32
2.6.2 CFD Modeling of Airlift Columns .....	36
2.7 Summary .....	40

<b>Chapter 3 Feasibility of Using CARPT Technique for Photobioreactor Analysis...</b>	<b>41</b>
3.1 Scope.....	41
3.2 CARPT Technique.....	42
3.2.1 CARPT Setup.....	42
3.2.2. CARPT Data Processing Procedure.....	44
3.3 CARPT Experiments .....	45
3.4 Results and Discussion .....	48
3.4.1 Liquid Flow Field .....	48
3.4.2 Cell Movements .....	49
3.4.3 Temporal Light Patterns .....	53
3.5 Summary .....	56
<b>Chapter 4 Integrating Reactor Hydrodynamics with Photosynthesis to Characterize     Flashing light Effects and to Evaluate PBR Performance .....</b>	<b>58</b>
4.1 Scope.....	58
4.2 Temporal irradiance pattern.....	60
4.3 Interactions between Hydrodynamics and Photosynthesis.....	62
4.4 Characterization of Photobioreactors in Terms of Light Fluctuations.....	63
4.4.1 Average Irradiance.....	66
4.4.2 Irradiance fluctuations .....	68
4.5 Dynamic Modeling Approach for Reactor Performance Evaluation.....	71
4.5.1 The governing equations for the model .....	72
4.5.2 Numerical solution.....	72
4.5.3 Reactor performance simulation .....	75
4.6 Effects of reactor geometry and superficial gas velocity .....	76
4.7 Summaries.....	77
<b>Chapter 5 Local Characteristics of Hydrodynamics in an Draft Tube Airlift Column     Photobioreactor:Experimental Analysis .....</b>	<b>79</b>
5.1 Scope.....	79
5.2 Introduction.....	81
5.3 Reactor Configurations and Experimental Conditions .....	83

5.4 CARPT Experiments .....	86
5.4.1 Details of the CARPT Setup .....	86
5.4.2 Calibration.....	89
5.4.3 Measurement Errors of the CARPT Experiments .....	90
5.5 CT Experiments .....	92
5.6 Multiphase Flow Dynamics in the Airlift Column Reactor.....	95
5.6.1 Lagrangian Particle Trajectories .....	95
5.6.2 Overall Liquid Macro-Mixing .....	98
5.6.3 Liquid Mixing in Individual Regions .....	103
5.6.4 Liquid Flow Field .....	108
5.6.5 Turbulent Kinetic Energy .....	112
5.6.6 Shear Stress.....	116
5.6.7 Turbulent Eddy Diffusivity.....	120
5.6.8 Gas holdup.....	122
5.7 Photobioreactor Analysis .....	127
5.7.1 Characterization of Flashing Lights.....	127
5.7.2 Reactor Performance Evaluation .....	131
5.8 Summary and Conclusions .....	133
<b>Chapter 6 CFD Simulations for Local Flow Dynamics, Particle Tracking, and PBR Analysis in a Draft Tube Airlift Column Reactor .....</b>	<b>135</b>
6.1 Scope.....	135
6.2 Theory .....	137
6.2.1 Mathematic Modeling of the Two-Fluid Model .....	137
6.2.2 Multiphase Turbulent equations .....	139
6.2.3 Interfacial Momentum Forces.....	140
6.2.4 Particle (Cell) Tracking.....	143
6.2.5 Mathematical Solution.....	145
6.3 CFD Simulations.....	146
6.3.1 2D Simulations.....	146
6.3.2 3D simulations .....	147

6.4 Closure Evaluations .....	149
6.4.1 Effects of Types of Simulations and Griding Size.....	150
6.4.2 Turbulent Models.....	152
6.4.3 Effects of Turbulent Dispersion Coefficient, $C_{\mu}$ .....	154
6.4.4 Drag Correlations.....	155
6.4.5 Effects of Turbulent Dispersion Force.....	157
6.4.6 Effects of Saffman Force .....	158
6.5 Simulations for Different Superficial Gas Velocities .....	160
6.6 Particle (Cell) Trajectory Verification .....	161
6.7 Photobioreactor Performance Prediction Using CFD Results .....	164
6.7 Summary .....	166
<b>Chapter 7 Culturing <i>Porphyridium sp.</i> in Airlift Column Photobioreactors.....</b>	<b>168</b>
7.1 Scope.....	168
7.2 Introduction.....	170
7.3 Experiments .....	171
7.3.1 Algae Culture Preparation.....	171
7.3.2 Airlift Column Photobioreactors.....	172
7.3.3 Liquid Phase Physical Properties.....	175
7.3.4 Hydrodynamic Characterization under Real Culture Conditions .....	175
7.3.5 Light intensity measurements .....	176
7.3.6 Biomass Concentration measurements .....	177
7.4 Results and Discussions.....	181
7.4.1 Physical Properties of the Culture Medium .....	181
7.4.2 Fluid Dynamics of the Draft Tube Photobioreactor .....	182
7.4.3 Irradiance Distribution inside the reactor .....	186
7.4.4 Photobioreactor Performance of the Draft Tube Column.....	190
7.4.5 Effects of reactor Geometry on the Performance .....	194
7.5 Simulations of the Dynamic Growth Rate Model.....	197

7.5.1 Simulation for the Reactor Performance of Merchuk et al. (2000).....	197
7.5.2 Simulation for the Reactor Performance of this Work .....	198
7.6 Summary .....	199
<b>Chapter 8 Conclusions and Recommendations.....</b>	<b>202</b>
8.1 Summaries and Conclusions.....	202
8.1.1 Using the CARPT Technique for PBR Analysis .....	202
8.1.2 Using CARPT, CT, and CFD to Obtain Flow Dynamic Information .....	204
8.1.3 Verifying the Dynamic Growth Rate Model .....	205
8.2 Recommendations.....	207
<b>Appendix A Automatic Calibration Device for CARPT Experiments.....</b>	<b>210</b>
A.1 Structure of the calibration device .....	211
A.2 Operation of the Calibration Device .....	216
A.3 Summary .....	216
<b>Appendix B Measurement Errors of the CARPT Experiments.....</b>	<b>217</b>
<b>Appendix C Flowchart of the Algorithm for the Dynamic Growth Rate Model....</b>	<b>222</b>
<b>Appendix D Irradiance Distribution inside Photobioreactors.....</b>	<b>223</b>
<b>Reference .....</b>	<b>226</b>
<b>Vita .....</b>	<b>244</b>



# List of Figures

<b>1-1.</b> Schematic illustration of the flashing light effect (a time series of irradiance a cell could experience in a draft tube airlift column reactor is shown on the right) .....	4
<b>2-1.</b> Conceptual schematic diagram of photosynthesis and cell growth processes (ATP: Adenosine TriPhosphate).....	15
<b>2-2.</b> A typical photosynthesis-Irradiance (P-I) curve (modified from Vonshak, 1992)....	17
<b>2-3.</b> Illustration of the well-defined light/dark cycles.....	22
<b>2-4.</b> (a) Schematic representation of the interaction of photosynthetic kinetics and the fluid dynamics in the photobioreactor (from Wu and Merchuk, 2001). The reactor is divided into a dark and an illuminated region. Photons are captured by the cells in the illuminated region, where photosynthetic factory (PSF) deactivation takes place. The cells are cyclically transported to the dark zone, where PSF recovery takes place. (b) Structure of the three states model proposed by Eilers and Peeters (1988) (duplicated from Wu and Merchuk, 2001). Photons are captured by a PSF in state $x_1$ which passes at a rate that is proportional to $I$ . The PSF in state $x_2$ can either return to state $x_1$ at a constant rate, $\gamma$ , or capture another photon and pass to the inhibited state $x_3$ . The PSF at state $x_3$ returns to state $x_1$ at a constant rate, $\delta$ . The chain of dark reactions is started by the direct passage of $x_2 \Rightarrow x_1$ .....	28
<b>3-1.</b> Schematic Diagram of the CARPT Facility at the Chemical Reaction Engineering Laboratory (CREL)-Washington University (WU) .....	43
<b>3-2</b> Configuration of draft tube and split airlift bioreactor .....	46
<b>3-3.</b> Visualization of the liquid flow field for draft tube column and split column at $U_g = 5$ cm/s. The time-averaged velocity vectors have been further axially averaged according to the developed flow zone and shown in the cross-sectional plane for both reactors, while only for the draft tube column, the velocity vectors have been	

azimuthally averaged and shown in the r-z plane. Please see the text for details. Also note the arrows present the liquid flow directions, and the blue lines represent the walls and internals (i.e. the draft tube or split wall).....	49
<b>3-4.</b> Typical particle trajectories in the draft tube and the split columns. Only one recirculation is shown for each reactor, while both the front and the top view of the trajectories are shown respectively in the r-z plane and the cross-sectional plane. Please note the blue lines represent the walls and internals, i.e. draft tube and split wall. $U_g=1\text{cm/s}$ . .....	50
<b>3-5.</b> Circulation time distribution and single trajectory length distribution at superficial gas velocity of 5 cm/s. ....	52
<b>3-6.</b> Typical temporal irradiance pattern for the three PBRs at different biomass concentrations at different superficial gas velocities. Calculated by combing CARPT-obtained trajectories and the irradiance distribution model proposed by Acien, et al., 1997. $K_a = 0.05\text{ m}^2/\text{g}$ .....	54
<b>4-1.</b> Time series of irradiance a cell experienced in the bioreactors. Calculated by Equation (1). External irradiance: $2000\text{ }\mu\text{E m}^{-2}\text{s}^{-1}$ , Cell concentration: $80\times 10^6\text{ cells/ml}$ . .....	61
<b>4-2.</b> Illustration of the parameters to characterize the dynamic feature of irradiance fluctuation. A: well-defined light/dark cycle; B: over-/under- charged cycle in real reactors.....	64
<b>4-3.</b> Typical photosynthesis-Irradiance (P-I) curve (modified from Vonshak, 1992) .....	65
<b>4-4.</b> Probability density functions of the over-/under- charged cycle frequencies. External irradiance: $2000\mu\text{E m}^{-2}\text{s}^{-1}$ , Cell concentration: $80\times 10^6\text{ cells/ml}$ . A: Superficial gas velocity of 1 cm/s; B: Superficial gas velocity of 5 cm/s. ....	69
<b>4-5.</b> PDF of the dimensionless relaxation time presented by plotting $-\ln(1/\varphi - 1)$ vs. the number of occurrence per hour, which in fact shows the PDF of the over-/under-charged time ratio ( $t_{over}/t_{under}$ ) in a logarithmic axis coordinate. External irradiance: $2000\text{ }\mu\text{E m}^{-2}\text{s}^{-1}$ , Cell concentration: $80\times 10^6\text{ cells/ml}$ . A: Superficial gas velocity of 1 cm/s; B: Superficial gas velocity of 5 cm/s.. .....	70

<b>4-6.</b> Computed Photosynthesis-Irradiance (P-I) curve together with profiles of PSF states by the dynamic photosynthesis rate model proposed by Eilers and Peeters (1988) for <i>Porphyridium, sp.</i> See text for details.....	73
<b>4-7.</b> Simulation results by the dynamic model for the draft tube column (on the right) at $U_g$ of 1 cm/s. The experimental data (Merchuk, et al., 2000) and simulation results of Wu and Merchuk (2001) are also presented, which are based on the draft tube column on the left at the superficial gas velocity of 0.29 cm/s.....	75
<b>4-8.</b> Numerical simulated cell's concentration profiles for different type of reactors and superficial gas velocities. Simulation condition: External Irradiance: $2000 \mu\text{E m}^{-2} \text{s}^{-1}$ ; Initial Cells concentration: $8 \times 10^6 \text{ cells/ml}$ (BC: Bubble column; SC: Split column; DC: draft tube column.) .....	76
<b>5-1.</b> Configuration of the studied airlift column reactor .....	84
<b>5-2.</b> Illustration of the individual regions of the draft tube column reactor.....	85
<b>5-3.</b> (a) Top view of the CARPT setup for the draft tube column. Each aluminum support has four detectors mounted on different axial levels. The front view of the detectors mounted on supports A and B is further illustrated in Figure 5-3(b).....	87
<b>5-4.</b> Configuration of the tracer particle used for the CARPT experiments .....	88
<b>5-5.</b> Configurations of the calibration positions on a cross-sectional plane. The thick lines represent the column walls.....	90
<b>5-6.</b> Illustration of the different reconstruction errors when the radioactive particle is in different reactor regions.....	91
<b>5-7.</b> Schematic diagram of the $\gamma$ -ray beam attenuation.....	92
<b>5-8.</b> (a). Schematic diagram of the CT setup (Adopted From Aravind, 2002). .....	94
<b>5-8.</b> (b). Schematic diagram of the CT setup (Adopted From Aravind, 2002). The axial levels scanned in this study are also show .....	94
<b>5-9.</b> Visualization of typical trajectories of the tracer particle in the studied airlift draft tube column at $U_g$ of 1 cm/s, bottom clearance of 5 cm, and top clearance of 3 cm: (a) 3D visualization; (b) projected on the r-z plane; and (c) on the cross-sectional	

plan. Different colors are used to present each circulation of the particle around the draft tube. ....	96
<b>5-10.</b> Particle occurrence density distribution (unit: number of occurrence per milliliter) in the reactor at $U_g$ of 1cm/s, Bottom clearance of 5cm, and top clearance of 3 cm. (a). Occurrence density distribution on the r-z plane after being azimuthally averaged; (b). Radial profiles of the occurrence density distribution according to the fully developed flow zone (i.e., $Z = 30\sim 80\text{cm}$ ). ....	97
<b>5-11.</b> Typical single trajectories with their residence time in individual regions of the draft tube column reactor. ....	100
<b>5-12.</b> PDF of circulation time for single trajectories together with the mean, the dimensionless variance (STD), and the Peclet number. (operating condition: $U_g$ of 1cm, bottom clearance of 5cm, and top clearance of 3cm) ....	101
<b>5-13.</b> Effects of superficial gas velocity on the overall liquid macro-mixing: the circulation time (a) and the dimensionless variance (b). (operating condition: $U_g$ of 1cm, bottom clearance of 5cm, and top clearance of 3cm) ....	102
<b>5-14.</b> Effects of Top and Bottom clearances on the overall liquid macro-mixing: the circulation time and the dimensionless variance at superficial gas velocity of 1cm/s. (TC: top clearance; BC: bottom clearance) ....	103
<b>5-15.</b> PDF of residence time in individual regions in the reactor together with the mean, the dimensionless variance (STD), and the Peclet number (operating condition: $U_g$ of 1 cm/s, Bottom clearance of 5 cm, and Top clearance of 3 cm). ....	104
<b>5-16.</b> Effects of superficial gas velocity on the liquid macro-mixing in individual regions: (a) on the circulation time in the Riser and the Downcomer; (b) on the dimensionless variance in the Riser and the Downcomer; (c) on the circulation time in the Top and Bottom; (d) on the dimensionless variance in the Top and Bottom. ....	106
<b>5-17.</b> Effects of top and bottom clearance on the liquid macro-mixing in individual regions at superficial gas velocity of 1cm/s: (a) on the circulation time in the Riser and the Downcomer; (b) on the circulation time in the Top and Bottom; (c) on the dimensionless variance in the Riser and the Downcomer; (d) on the dimensionless variance in the Top and Bottom. ....	107

<b>5-18.</b> Visualization of liquid velocity vectors on r-z and cross-sectional planes (the solid blue area shows the draft tube). Operating conditions: $U_g = 1$ cm/s, bottom clearance = 5 cm, top clearance = 3 cm. Please note the different scales used to present the velocities in the radial and axial directions for better visualization on the r-z plane. ....	109
<b>5-19.</b> Effects of superficial gas velocity on the liquid flow velocities: (a) Effects on the axial liquid velocity profiles; (b) Effects on the liquid circulation velocity (normalized by the Riser cross-sectional area). ....	110
<b>5-20.</b> Effects of Top and Bottom clearances on the axial liquid velocity profiles.....	111
<b>5-21.</b> Visualization of time- and azimuthally-averaged turbulent kinetic energy in r-z plane (unit: $\text{cm}^2/\text{s}^2$ ) at 1cm/s $U_g$ , 5 cm bottom clearance, and 3 cm top clearance. ....	113
<b>5-22.</b> Radial profile of the time- and azimuthally-averaged turbulence kinetic energy, $k$ , in the fully developed flow zone ( $H = 30\sim 80$ cm) at different superficial gas velocities with 5 cm bottom clearance and 3 cm top clearance. ....	114
<b>5-23.</b> Effects of the top and bottom clearances on the radial profiles of time- and azimuthally-averaged turbulent kinetic energy at superficial gas velocity of 1 cm/s: (a) in the fully developed flow zone; (b) in the Top and the Bottom regions (axially averaged to cover the whole Top or Bottom regions). A schematic diagram of the draft tube column is also shown.....	115
<b>5-24.</b> Visualization of time- and azimuthally-averaged shear stress ( $\tau_{rz}$ ) in r-z plane at 1 cm/s superficial gas velocity, 5 cm bottom clearance, and 3 cm top clearance.....	117
<b>5-25.</b> Radial profile of the time- and azimuthally-averaged shear stress ( $\tau_{rz}$ ) in the fully developed flow zone ( $H = 30\sim 80$ cm) at 5 cm bottom clearance and 3 cm top clearance. ....	118
<b>5-26.</b> Effects of Top and Bottom clearances on the radial profiles of time- and azimuthally-averaged shear stress ( $\tau_{rz}$ ) at superficial gas velocity of 1 cm/s: (a) in the fully developed flow zone; (b) in the Top and the Bottom regions (axially averaged to cover the whole Top or Bottom regions). A schematic diagram of the draft tube column is also shown. ....	119

<b>5-27.</b> Radial profiles of the eddy diffusivities at different superficial gas velocities with 5 cm bottom clearance and 3 cm top clearance: (a) axial eddy diffusivity; (b) radial eddy diffusivity. ....	121
<b>5-28.</b> Effects of top and bottom clearances on the radial profiles at 1 cm/s superficial gas velocities: (a) axial eddy diffusivity (Please note the circled point is viewed as a runaway point, however, the reason is not clear); (b) radial eddy diffusivity. ....	122
<b>5-29.</b> Visualization of time-averaged local gas holdup in different axial levels of the column at 1 cm/s superficial gas velocities, 5 cm bottom clearance, and 3 cm top clearance. Scanned axial levels are: Top (H= 110cm), HM (higher middle, H= 97.7cm), Middle (H= 67.7cm), LM (lower middle H=34.2cm), and Bottom (H= 4.2 cm) .....	123
<b>5-30.</b> Axial evolution of the radial profiles of time- and azimuthally-averaged gas holdup at 1cm/s superficial gas velocities, 5 cm bottom clearance, and 3 cm top clearance. ....	124
<b>5-31.</b> Effects of superficial gas velocities on the time- and azimuthally-averaged local gas holdup profiles in the middle of the column (H = 67.7 cm) at operating condition of 5 cm bottom and 3 cm top clearances. ....	125
<b>5-32.</b> Effects of superficial gas velocities on the overall gas holdup at operating condition of 5 cm bottom and 3 cm top clearances.....	125
<b>5-33.</b> Effects of top and bottom clearances on the time- and azimuthally-averaged local gas holdup profiles in the middle of the column (H = 67.7 cm) at operating condition of 1 cm/s superficial gas velocity.....	126
<b>5-34.</b> Temporal irradiance pattern calculated by Equation (4-1) using CARPT measured particle trajectories obtained at operating conditions of 1cm/s superficial gas velocity, 5 cm bottom clearance and 3 cm top clearance. Calculation conditions: External Irradiance= $2000\mu E m^{-2} s^{-1}$ ; Cell concentration= $80\times 10^6$ cells/ml .....	128
<b>5-35.</b> Characteristics of the light fluctuations delivered to the cells at the operating conditions of 1 cm/s superficial gas velocity, 5 cm bottom clearance and 3 cm top clearance. (a). PDFs of the frequency for the over-/under- charged cycles; (b). PDFs of the dimensionless relaxation time, $\varphi$ , for the over-/under- charged cycles.....	129

<b>5-36.</b> Photobioreactor performance predictions at different superficial gas velocities compared with the experimental data measured by Merchuk et al. (2000).....	132
<b>6-1.</b> Geometry and gridding for the 2D steady state simulations .....	147
<b>6-2.</b> Configurations of the computational domain in 3D simulations. (a) Overview of the computational geometry for a 3D steady state simulation with height of 1.16m (the whole column with height of 1.5m is modeled in a 3D transient simulation); (b) Sparger configuration; (c) Mesh on the cross-sectional plane for the fine gridding; (d) Mesh in the axial direction for the fine gridding. ....	148
<b>6-3.</b> Effects of gridding on the CFD simulations. (a) Effects on the axial liquid velocity profile; (b) Effects on the gas holdup profile; (c) Effects on the turbulent kinetic energy profile. ....	151
<b>6-4.</b> CFD simulation results by different turbulent models. (a) Results of the axial liquid velocity profile; (b) Results of the gas holdup profile; (c) Results of the turbulent kinetic energy profile. ....	153
<b>6-5.</b> CFD simulation results using different magnitude of turbulent dispersion coefficient, $C_{\mu}$ . (a) Results of the axial liquid velocity profile; (b) Results of the gas holdup profile; (c) Results of the turbulent kinetic energy profile. ....	154
<b>6-6.</b> Effects of drag correlations on the CFD simulations. (a) Effects on the axial liquid velocity profile; (b) Effects on the gas holdup profile; (c) Effects on the turbulent kinetic energy profile. ....	156
<b>6-7.</b> Effects of the turbulent dispersion force on the CFD simulations. (a) Effects on the axial liquid velocity profile; (b) Effects on the gas holdup profile; (c) Effects on the turbulent kinetic energy profile.....	157
<b>6-8.</b> Effects of the Saffman lift force on the CFD simulations. (a) Effects on the axial liquid velocity profile; (b) Effects on the gas holdup profile; (c) Effects on the turbulent kinetic energy profile.....	159
<b>6-9.</b> CFD simulations for different superficial gas velocities. (a) Results of the axial liquid velocity profile; (b) Results of the gas holdup profile; (c) Results of the turbulent kinetic energy profile.....	160

<b>6-10.</b> PDFs of the trajectory length and the circulation time distributions based on single trajectory analysis. (a). CFD simulation results; (b) CARPT results. Operating conditions: $U_g$ of 0.82cm/s, top clearance of 3cm, and bottom clearance of 5cm.	163
<b>6-11.</b> Radial profile of the normalized occurrence probability for the tracer particle in the airlift column reactor (normalized by the total number of occurrences) at superficial gas velocity of 0.82 cm/s. ....	164
<b>6-12.</b> Predicted photobioreactor performance using CFD simulated trajectories together with the experimental data measured by Merchuk et al. (2000) and prediction using CARPT data. Simulation conditions: External irradiance: $250 \mu E m^{-2} s^{-1}$ , Superficial gas velocity: 0.82 cm/s.....	165
<b>7-1.</b> Configuration of three types of airlift column photobioreactors (same procedure has been applied to these reactors).....	173
<b>7-2.</b> Configuration of the lamps to illuminate the reactor. (a) Schematic diagram of the configuration; (b) photo taken during the real experiments.....	174
<b>7-3.</b> Quantum scalar irradiance sensor (placed in the reactor center to monitor the biomass concentration) .....	177
<b>7-4.</b> Calibration curve of optical density versus dry biomass concentration .....	178
<b>7-5.</b> Calibration curve of cell numbers versus the optical density.....	179
<b>7-6.</b> Profiles of apparent viscosity versus shear stress at different biomass concentrations. ....	182
<b>7-7.</b> Comparison of the local hydrodynamic characteristics in the draft tube column between the real alga culture system obtained in this Chapter and the air-water system obtained in Chapter 5. (a) Radial profile of the occurrence density normalized by the total number of occurrences; (b) axial liquid velocity profiles; (c) turbulent kinetic energy profiles; (d) profiles of the Reynolds shear stress, $\tau_z$ ; (e) gas holdup profiles at the middle level ( $H = 67$ cm). Operating conditions: bottom clearance = 5cm and top clearance = 3 cm (for $U_g = 0.076$ cm/s in the air-water system, the top clearance is 0 cm) .....	185



<b>7-8.</b> Irradiance measurements in the draft tube column reactor. (a) Under low PFD and biomass concentration (optical density of 0.006 with four lamps on). (b) Under high PFD and biomass concentration (optical density of 0.99 with all lamps on).. .....	187
<b>7-9.</b> Azimuthally averaged irradiance versus distance from the sensor to the outer illuminated wall .....	188
<b>7-10.</b> Relationship between the optical density and the light intensity in the bubble column photobioreactor center. ....	189
<b>7-11.</b> Biomass concentration evolutions in the draft tube airlift column photobioreactors for <i>Porphyridium</i> sp. culturing. (a) Evolution of the culture medium's optical density; (b) Evolution of the dry biomass concentration; (c) Evolution of the normalized chlorophyll (a) concentration by the dry biomass concentration; (d) Evolution of irradiance in the reactor center.....	191
<b>7-12.</b> Comparison of the reactor performance data measured in this study and the ones measured by Merchuk et al. (2000) at superficial gas velocity: 0.3 cm/s. please see the text for the details of the operating conditions. Only data obtain at low PFD stage in this work were shown for better comparison.....	193
<b>7-13.</b> Biomass concentration evolutions in three airlift column photobioreactors for <i>Porphyridium</i> sp. culturing. (a) Evolution of the culture media's optical density; (b) Evolution of the dry biomass concentration; (c) Evolution of chlorophyll (a) concentration normalized by the dry biomass concentration. Please note that the culture in the bubble column failed due to overheating after the high light intensity lamps were switched on (halogen lamps was used in the first trial). The experiment with high PFD in the bubble column therefore was repeated using fluorescent lamps as described in the experimental section.....	195
<b>7-14.</b> Evolution of the optical density in the studied PBRs for <i>Porphyridium</i> sp. culturing at the active growth stage.....	196
<b>7-15.</b> Dynamic simulation of the reactor performance measured by Merchuk et al. (2000) using CARPT data obtained from <i>Porphyridium</i> sp. culturing system. The prediction made in Chapter 5 based on CARPT data obtained from an air-water system is also shown. The time-averaged light intensities were calculated by Equation (4-1) for	

Case I (i.e., External Irradiance= $250\mu\text{E m}^{-2} \text{ s}^{-1}$ ; Cell concentration= $8\times 10^6$ cells/ml). Model parameters listed in Table 4-2 were used for all simulations. ....	198
<b>7-16.</b> Dynamic simulation of the reactor performance measured in this study using the CARPT data obtained in <i>Porphyridium</i> sp. culturing system. Model parameters: equation (7-9) was used for the light intensity distribution and parameters listed in Table 4-2 were used for photosynthetic growth rates with justified $k$ and $M_e$ .....	199
<b>A-1.</b> Schematic diagram of the calibration device (Please note the drawing is not in scale) .....	211
<b>A-2.</b> Picture of the automatic calibration device .....	212
<b>A-3.</b> Major dimensions of the base and the rotate plates for the calibration .....	214
<b>A-4.</b> Dimension of the rational plate for the calibration device .....	215
<b>A-5.</b> Schematic diagram of the unislide systems for the calibration device.....	215
<b>B-1.</b> Comparisons of the real particle positions and the reconstructed positions in a calibration. (a) Particle positions on the x-z plane; (b) Particle positions on the cross-sectional plane. Please note the dots with light color are the real particle positions while the dots with dark color are the reconstructed ones.....	218
<b>B-2.</b> Reconstruction errors for a fixed radioactive particle on the reactor wall. (a) before the wavelet filtering; (b) after the wavelet filtering. Please note that, since the tracer particle was fixed on the wall at position of ( $x=2.83\text{cm}$ , $y=3.65\text{cm}$ , and $z=80.44\text{cm}$ ), all reconstructed position of the tracer ideally should be identical. However, due to the white noise, the reconstructed tracer positions were actually scattered around the mean. Wavelet filtering technique significantly reduced the scattering as shown above.....	221
<b>C-1.</b> Flowchart of the numerical simulation algorithm for the overall growth rate based on CARPT measured trajectories.....	222
<b>D-1.</b> Schematic Diagram of one-half of a cross-section through a cylinder PBR. $ab$ is light path, $r$ is cylinder radius, $s$ is distance to the reactor surface, and $\theta$ is angle between light path and the straight line through the column center (Ever, 1990)..	224

# List of Tables

<b>2-1.</b> Typical static growth rate models in literature .....	23
<b>2-2.</b> Typical hydrodynamic measurements for airlift column reactors.....	33
<b>4-1.</b> Average irradiance and variance for the photobioreactors. Unit: $\mu E m^{-2} s^{-1}$ .....	67
<b>4-2.</b> Parameters of the dynamic photosynthesis rate model for <i>Porphyridium</i> , sp. (Wu and Merchuk, 2002).....	73
<b>5-1.</b> Operating conditions.....	85
<b>5-2.</b> Characteristics of the light availability and fluctuation for the studied draft tube column reactor in an air-water system .....	130
<b>B-1.</b> Estimated reconstruction error for a typical measurement .....	218

# Nomenclature

## *In Chapter 1-2*

$d$	Radial distance from the cells to the illuminated surface, $m$
$f$	Frequency of the light intensity fluctuations, $s^{-1}$
$I$	Instantaneous Incident light intensity on the cells, $\mu Em^{-2} s^{-1}$
$I_E$	External irradiance exposed to the photobioreactor surface, $\mu Em^{-2} s^{-1}$
$I_{av}^t$	Time-averaged light intensity, $\mu Em^{-2} s^{-1}$
$I_{av}^V$	Volume-averaged light intensity, $\mu Em^{-2} s^{-1}$
$I_k$	Half-saturation irradiance, $\mu Em^{-2} s^{-1}$
$I_{Pi}$	Local irradiance value at the finite control volume $dV$ , $\mu Em^{-2} s^{-1}$
$I_{sat}$	Saturation light intensity, $\mu Em^{-2} s^{-1}$
$j$	Index of the sampling points
$k$	Yield of photosynthesis production to the transition of $x_2$ to $x_1$ , dimensionless
$k_m$	Extinction coefficient of shear stress in Equation (2-12), $Pa^{-1}$
$k_w$	Extinction constant for water in Equation (2-2), $m^{-1}$
$k_x$	Extinction constant for biomass in Equation (2-2), $ml/(m \cdot 10^6 \text{ cells})$
$Me$	Maintenance in Equation (2-12), $s^{-1}$
$\overline{Me}$	Maintenance without shear stress effects in Equation (2-12), $s^{-1}$
$n_{PSF}$	Number of the photosynthesis factories per mg-chlorophyll, $mol O_2 (mg chl a)^{-1}$
$N$	Total number of sampling points
$r$	Oxygen evolution rate, $mol O_2 (mg chl a)^{-1} s^{-1}$
$t_d$	Time when light is on in a Light/Dark cycle, $s$
$t_l$	Time when light is off in a Light/Dark cycle, $s$

$t_{over}$	Overcharged time in an over-/under- charged cycle, $s$
$t_{under}$	Undercharged time in an over-/under- charged cycle, $s$
$T$	Total sampling time, $s$
$U_g$	Superficial gas velocity, $cm/s$
$V$	Total volume of the bioreactor, $m^3$
$x$	Biomass concentration, $10^6 \text{ cells/ml}$
$x_1$	Fraction of PSF in open state
$x_2$	Fraction of PSF in closed state
$x_3$	Fraction of PSF in inhibited state

### **Greece**

$\mu$	Specific growth rate, $s^{-1}$
$\mu_{max}$	maximal specific growth rate, $s^{-1}$
$\sigma_{PSF}$	Functional absorption cross-section area of a PSF, $m^2 (\text{mol } O_2)^{-1}$
$\tau$	Shear stress, $Pa$
$\tau_c$	Critical shear stress in Equation (2-12), $Pa$
$\alpha$	Rate constant of photon utilization to transfer $x_1$ to $x_2$ , $(\mu E m^{-2})^{-1}$
$\gamma$	Rate constant of transfer $x_2$ to $x_1$ , $(\mu E m^{-2})^{-1}$
$\delta$	Rate constant of transfer $x_3$ to $x_1$ , $(\mu E m^{-2})^{-1}$
$\beta$	Rate constant of photon utilization to transfer $x_2$ to $x_3$ , $(\mu E m^{-2})^{-1}$
$\phi$	Quantum yield of the oxygen evolution, $\text{mol } O_2 (\mu E)^{-1}$
$\varphi$	Dimensionless relaxation time

### ***In Chapter 3***

$C_b$	Biomass concentration, $g m^{-3}$
$I$	Light intensity, $\mu E m^{-2} s^{-1}$
$I_0$	External irradiance, $\mu E m^{-2} s^{-1}$
$K_a$	extinction coefficient, $m^2/g$

$\langle l \rangle$	Average single trajectory length, $m$
$L$	Path length of the circulation in the reactor, $m$
$M$	Micromixing indexes, dimensionless
$U_g$	Superficial gas velocity, $cm/s$

**Greek symbol**

$\sigma$	Dimensionless variance of PDFs
----------	--------------------------------

***In Chapter 4***

$d$	Radial distance from the cells to the illuminated surface, $m$
$f$	Frequency of the light intensity fluctuations, $s^{-1}$
$I$	Instantaneous Incident light intensity on the cells, $\mu Em^{-2} s^{-1}$
$I_E$	External irradiance exposed to the photobioreactor surface, $\mu Em^{-2} s^{-1}$
$I'_{av}$	Time-averaged light intensity, $\mu Em^{-2} s^{-1}$
$I^V_{av}$	Volume-averaged light intensity, $\mu Em^{-2} s^{-1}$
$I_{Pi}$	Local irradiance value at the finite control volume $dV$ , $\mu Em^{-2} s^{-1}$
$I_{sat}$	Saturation light intensity, $\mu Em^{-2} s^{-1}$
$j$	Index of the sampling points
$k$	Yield of photosynthesis production to the transition of $x_2$ to $x_1$ , dimensionless
$k_m$	Extinction coefficient of shear stress, $Pa^{-1}$
$k_w$	Extinction constant for water in, $m^{-1}$
$k_x$	Extinction constant for biomass, $ml/(m \cdot 10^6 \text{ cells})$
$Me$	Maintenance constant, $s^{-1}$
$\overline{Me}$	Maintenance without shear stress effects, $s^{-1}$
$N$	Total number of sampling points
$t_d$	Time when light is on in a Light/Dark cycle, $s$
$t_l$	Time when light is off in a Light/Dark cycle, $s$
$t_{over}$	Overcharged time in an over-/under- charged cycle, $s$

$t_{under}$	Undercharged time in an over-/under- charged cycle, $s$
$T$	Total sampling time, $s$
$U_g$	Superficial gas velocity, $cm/s$
$V$	Total volume of the bioreactor, $m^3$
$x$	Biomass concentration, $10^6 \text{ cells/ml}$
$x_1$	Fraction of PSF in open state
$x_2$	Fraction of PSF in closed state
$x_3$	Fraction of PSF in inhibited state

### **Greece**

$\mu$	Specific growth rate, $s^{-1}$
$\tau$	Shear stress, $Pa$
$\tau_c$	Critical shear stress, $Pa$
$\alpha$	Rate constant of photon utilization to transfer $x_1$ to $x_2$ , $(\mu Em^{-2})^{-1}$
$\gamma$	Rate constant of transfer $x_2$ to $x_1$ , $(\mu Em^{-2})^{-1}$
$\delta$	Rate constant of transfer $x_3$ to $x_1$ , $(\mu Em^{-2})^{-1}$
$\beta$	Rate constant of photon utilization to transfer $x_2$ to $x_3$ , $(\mu Em^{-2})^{-1}$
$\varphi$	Dimensionless relaxation time

### ***In Chapter 5***

$BC$	Bottom Clearance, $cm$
$Bo$	Bodenstein number
$e_d$	CARPT reconstruction error from source I in 3-D domain, $mm$
$e_r$	CARPT reconstruction error from source I in radial direction, $mm$
$E_z$	Dispersion coefficient
$H$	Axial level of the column, $cm$
$k$	Turbulent kinetic energy estimated from Equation 3, $cm^2/s^2$

$Pe$	Peclet number
$r/R$	Radial position normalized by the column radius
$t_c$	Overall circulation time in the column, $s$
$TC$	Top clearance, $cm$
$t_r$	Residence time in individual regions of the column, $s$
$U_g$	Superficial gas velocity, $cm/s$
$U_L$	Liquid circulation velocity normalized by the Riser cross-sectional area, $cm/s$
$u_r'$	The radial component of the fluctuation liquid velocity, $cm/s$
$u_z'$	The axial component of the fluctuation liquid velocity, $cm/s$
$u_\theta'$	The tangential component of the fluctuation liquid velocity, $cm/s$

### **Greek Symbol**

$\sigma_d$	Dimensionless deviations for RTD analyses
$\tau$	Reynolds shear stress, $cm^2/s^2$

### ***In Chapter 6***

$\vec{g}$	Gravity vector, $m/s^2$
$\vec{M}_\alpha$	Interfacial momentum transfer acted on phase $\alpha$
$\vec{M}_{\alpha\beta}$	Interfacial momentum transfer between phase $\alpha$ and $\beta$
$\vec{U}$	Velocity vector, $m/s$
$C_{\epsilon 1}, C_{\epsilon 2}, C_\mu$	Constants in k- $\epsilon$ model, dimensionless
$C_D$	Drag coefficient, dimensionless
$C_L$	Saffman lift force coefficient
$C_{TD}$	Coefficient of the turbulent dispersion force
$d_b$	Bubble diameter, $cm$
$Eo$	Evoter number
$k$	Turbulence kinetic energy



$p$	Pressure, $Pa$
$P$	Production of turbulence kinetic energy
$Pr$	Prantl constant
$r$	Volume fraction of phase $\alpha$ , dimensionless
$Re$	Reynolds number, dimensionless
$t$	Time, s
$v_p$	Tracer particle velocity vector, cm/s

### **Greek letters**

$\alpha$	Volume fraction (holdup) of phases
$\rho$	Density of phase, $kg/m^3$
$\mu_{\alpha,eff}$	Effective dynamic viscosity of phase $\alpha$ , $kg/m^{-1} s^{-1}$
$\mu_{\alpha}$	Molecular viscosity of phase $\alpha$ , $kg/m^{-1} s^{-1}$
$\mu_{\alpha}^T$	Dynamic viscosity of phase $\alpha$ due to turbulence, $kg/m^{-1} s^{-1}$
$\tau$	Stress tensor, $N/m^2$
$\Gamma$	Random number in Equation (23)
$\varepsilon$	Turbulent dissipation rate, $m^2/s^3$
$\sigma_k$	Constants in $k$ - $\varepsilon$ model for phase $k$
$\sigma$	Surface tension of the gas phase

### **Superscripts and subscripts**

$b$	Bubble
$c$	Continuous phase, liquid phase in this work
$d$	Dispersed phase, gas phase in this work
$f$	Fluid elements in Equation (22)
$p$	Particles in Equation (22)
$T$	Turbulence
$\alpha, \beta$	Phase index

## *In Chapter 7*

$Ca$	Concentrations of chlorophyll a, $g/ml$
$\bar{d}$	Average distance of any points on the spherical sensor to the illuminated wall in Equation (7-6), $m$
$d$	Distance from the sensor center to the wall, $m$
$I$	Instantaneous Incident light intensity on the cells, $\mu E m^{-2} s^{-1}$
$I_w$	light intensity on the illuminated wall, $\mu E m^{-2} s^{-1}$
$k_x$	Extinction coefficient due to cellular absorption, $m^{-1}$
$OD$	Optical densities, dimensionless
$r$	Radial position of a interested points within the column in Equation (7-6), $m$
$R$	Radius of the airlift column, $m$
$x$	Biomass concentration, i.e., optical density in Chapter 7

# Acknowledgements

I would like to express my deep gratitude to my advisor, Professor Al-Dahhan, for his consistent support from the first day of my study at Washington University in St. Louis, and his guidance and freedom while working towards this thesis. His enthusiasm on exploring new area, his encouragements of independent thoughts, his hard-working, and the active discussions between us made this thesis work possible. I also owe him tremendously for his help on my career development and on my personal happy life in St. Louis.

I sincerely appreciate Professor Mike Dudukovic for his constant inspiration towards high standards of fundamental and creative work. He has been an important driving force behind me towards better work. I have also greatly benefited from the projects he had me involved, which significantly enriched my researching experience.

I would like to acknowledge all my other committee members: Professor Brain Wrenn, Professor Lars Angenent, Prof. E. Molina Grima (University of Almería, Spain), Prof. J.M. Fernandez Sevilla (University of Almería, Spain), and Dr. Miguel Olaizola (Mera Pharmaceuticals Inc., Hawaii). I owe special thanks to Professor Fernandez Sevilla who started this photobioreactor project at CREL and is a continuous source of knowledge about microalgae cultures to me.

I want to thank Dr. Xiaoxi Wu for providing me invaluable information and instructions on the photosynthetic growth rate model; Dr. Abdenour Kemoun for teaching me CARPT and CT techniques, for kindly providing me available CARPT data, and for his help on my career development; Dr. Karim, a great friend, for all his helps on my biological

experiments; Dr. Ales Alajbegovic for his instructions and encouragements on my CFD simulations by AVL code during the first but the most stressful semester; and Dr. Rama for providing us free CFX code. I would also express my sincerely appreciations to Mr. Steve Picker for his help on all my experiment setups, to Professor James Ballard and Sue Rode-Perkins for their help on technique writing.

CREL has been such a great place for me that I won't be able to over-stress my pleasure for working here for the last four and a half years. CREL provides wonderful opportunities to work with industrial people that I have greatly benefited, and provides a great cooperative environment among all my colleagues. I like to all my CREL colleagues: Professor Ramachandran for his constant caring, Dr. Novica Rados and Dr. Booncheng Ong for their teaching me CARPT technique, Mr. Satish Bhusarapu, Mr. R.C. Ramaswamy, Dr. Aravind Rammohan, Mr. Shaibal Roy, Dr. Peng Chen, Dr. Junli Xue, Dr. Jing Guo, Mr. Ashfaq Shaikh, Mr. Rajneesh Varma, Mr. Mehul Vesvikar, Mr. Chengyu Mao, Mr. Lu Han, Mr. Chentian Wu, Ms. Rebecca Hoffmann, etc.

Last but not the least, I owe tremendously to all my family members: my parents, my sisters and brothers, my mother-in-law, my daughter, and of course my wife. Without their constant support, I would not have had a chance to be here and without their patience, I would not have been able to finish this thesis.

Hu-Ping Luo  
Washington University in Saint Louis  
Saint Louis, Missouri  
August 2005

# Chapter 1

## Introduction

Solar energy, harvested by photosynthetic organisms, is by far the primary form of energy supporting the lives on earth. By consuming light energy, the green house gas CO<sub>2</sub>, and other simple inorganic compounds (e.g., minerals, nitrogen, and phosphorus sources), these organisms produce complex organic molecules, oxygen, and storable energy sources. Among these organisms, microalgae and cyanobacteria are widely recognized as the most efficient solar energy harvesters (Becker, 1994). The obvious advantages of the microalgae/ cyanobacteria cultures are twofold: abating environmental pollution (e.g., wastewater treatment, CO<sub>2</sub> fixation) and producing useful biomass, e.g., aquaculture biomass feed, food additives (alginates, xantangum), and single cell proteins (SCP) for feeding livestock and human nutrition. As crude oil and natural gas will be depleted in the foreseeable future and their prices are increasing sharply nowadays, potential applications of microalgae/cyanobacteria cultures in producing clean bio-fuels for their high lipid contents are attracting great attention.

Moreover, these biomasses are a source of many high-value products, such as:

- polyunsaturated fatty acids (PUFAs);
- antiviral agents – red antiviral polysaccharides (RMP) and anti-herpes;

- natural, environmentally-friendly compounds for combating plant pathogens, e.g., antifungal agents (Kulick, 1995);
- pigments (natural food colorants and fluorescence indicators for use in clinical and research immunoassays).

These products all have high commercial value. For example, the price of highly purified microalgal eicosapentaenoic acid (EPA, a free fatty acid) was reported to be \$150,000 per kg (Ibáñez González et al., 1998), with increasing worldwide demand.

Generally, there are two types of systems for mass photosynthetic microorganism production, either open or enclosed. The open systems, i.e., raceway ponds and lakes, are usually illuminated naturally (outdoors) and open to the environment. They are cost-effective but intrinsically hard to control. Hence, they are usually used to grow resistant strains, such as *Spirulina platensis* and *Dunaliella salina*. Those strains can stand extreme environmental conditions (such as high pH for *Spirulina* and high salinity for *Dunaliella*) that prevent contaminations by other strains.

The enclosed systems, usually called photobioreactors (PBR) (e.g., tubular, panel, airlift bubble column reactors), can be either illuminated naturally or artificially (indoors) and allow axenic cultures under full control. These enclosed systems, thus, are suitable for growing strains for high value products, as these strains usually require protection from the exterior environment and must be maintained at appropriate temperature, pH value, salinity, etc. However, PBRs are complex systems due to the integrated effects of photosynthesis, hydrodynamics, and irradiance distribution. Proper understanding of the interactions among these elements is crucial for photobioreactor design, scale-up, operation, and process intensification.

## 1.1 Problem Identification

Numerous versions of enclosed PBR design have been tried in the last few decades, resulting in the great diversity of reactor types summarized by Lee (1986) and Pulz and

Scheibenbogen (1998). However, although many types of the PBRs (e.g., tubular reactors, thin panel reactors, fiber optic reactors, etc.) work fine on a laboratory scale, few industrial efforts for mass production of microalgae/cyanobacteria have been made, and moreover, most of them have failed (Olaizola, 2000; Tredici, 2004). These PBRs encounter a major problem in scaling up: the areal or volume productivity drops dramatically while the investment and operational costs increase greatly (Pulz and Scheibenbogen, 1998). Indeed, the levels of cost and difficulty are proportional to the size of the PBR and to the tolerance of the growth conditions (Olaizola, 2000).

The major problem is light: its availability and its utilization efficiency. Light is usually supplied to reactor surfaces, and its intensity decreases exponentially from the illuminated surface to the reactor center. Governed by radiative transfer theory (Vincenti and Kruger, 1965; Cassano et al., 1995), the irradiance distribution inside the PBRs is a complex function of incident irradiance, biomass concentration and composition, flow dynamics, and reactor geometry. The light intensity usually decreases sharply due to the extensive cellular absorption, scattering, and reflection among the microorganism cells and the liquid elements.

Those attenuating phenomena are more prominent in industrial cases. In large scale mass production systems, both the reactor volume and the biomass concentration (usually on the order of grams dry weight biomass per liter) have to be large enough to maximize the productivity and to cut costs for economic considerations. Under such conditions, light penetration depth (i.e., the maximal distance a photon can penetrate into the medium) is usually only a few millimeters to a few centimeters (Figure 1-1). Therefore, a large dark zone in the reactor center and a small high light intensity zone near the illuminated surface coexist in PBRs. Both zones are not conducive for the cell's growth, as high irradiance may cause photoinhibition, while low irradiance can not support the needed growth (photolimitation). Although the overall effect is photolimitation, photoinhibition is also significant along the illuminated reactor surface where light energy is abundant. As a result, the light use efficiency is usually very low (Pulz and Schebenbogen, 1998).

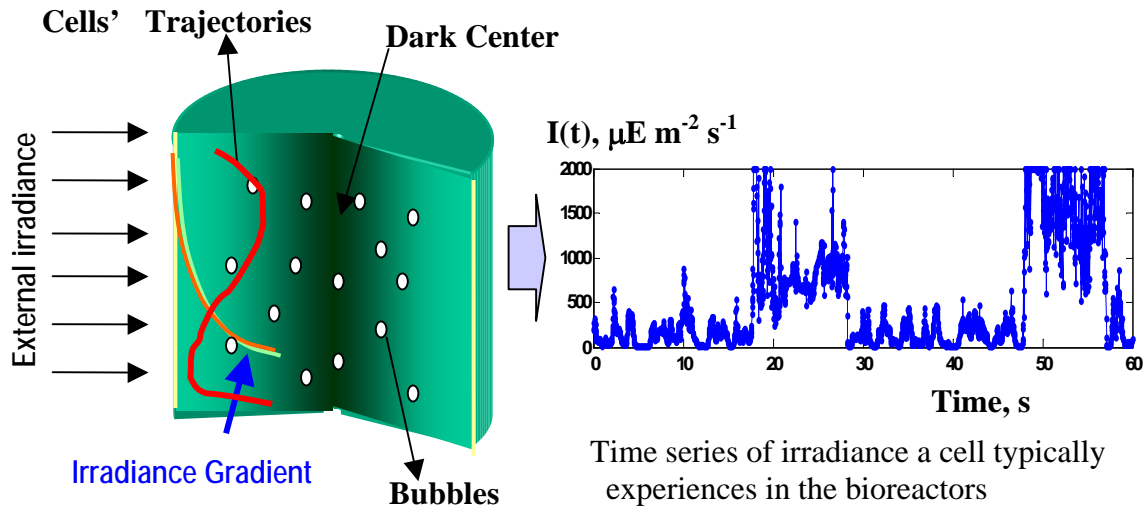


**Figure 1-1.** Schematic illustration of the flashing light effect (a time series of irradiance a cell could experience in a draft tube airlift column reactor is shown on the right)

Different approaches (Lee, 1986; Pulz and Scheibenbogen, 1998; Robinson et al., 1986) have been attempted to enhance the PBR performance. These approaches usually target light availability and its usage efficiency problems, such as by increasing reactor surface area/volume ratio (Hu et al., 1998), by introducing light distributing glass fiber into the medium (Janssen et al., 2003). Among them, one of the most promising approaches is increasing the turbulent mixing in the reactor.

It has been found that turbulent mixing can greatly enhance productivity for a wide range of operating conditions by improving the light usage efficiency (Winokur, 1948; Markl, 1980; Laws et al., 1983; Terry, 1986; Merchuk, et al., 1998a; Molina Grima et al., 1999). For example, in an experiment conducted in a race pond with algal cells exposed to ambient light, Law et al. (1983) used a simple device to generate rotational flows that enhanced the turbulence within the culture. They found that the productivity of algae *Phaeodactylum* more than doubled compared to conditions without the rotational flow. Bosca et al. (1991) also reported cases with 2.5 times enhancement of productivity when mixing was improved in a  $25\text{m}^3$  pond with 0.5m depth.



Many researchers (Grobbelaar, 1994; Lee and Pirt, 1981; Terry, 1986) attribute such productivity improvement to the so-called flashing light effect, an effect stemming from the cells' movements in the bioreactor, as illustrated in Figure 1-1. Due to the size of the microorganism cells (in micrometers) and their density (close to that of the culture medium), their movements in the reactor are fully determined by the chaotic local flow phenomena. Therefore, the cells travel randomly between the illuminated surface and the dark region in the center, experiencing a random time series of light intensities or flashing lights, as shown in Figure 1-1. Such flashing lights delivered to the cells, as suggested by many researchers, may enhance the photosynthetic efficiency and help the cells avoid photoinhibition. As a result, the overall reactor performance significantly relies on the interactions between the reactor flow dynamics and the photosynthesis. Hence, by affecting the light fluctuations, flow dynamics plays an important role in photobioreactor performance.

Moreover, hydrodynamics also affect the mass and heat transfer rates, and the shear stresses. Usually, in a fully controllable enclosed photobioreactor, sufficient nutrients are needed to maximize the growth rate, and the operating conditions (e.g., temperature and pH value) have to be maintained at appropriate levels for the best performance. Failure to achieve such conditions usually will cause severe operational problems. For example, a pilot plant constructed in Spain (Sanchez Miron et al., 1999) was abandoned soon after its start-up because the extremely high O<sub>2</sub> concentration accumulated in its long tubular reactors greatly inhibited the cells' growth and eventually killed most of the cells.

In addition, intense flow shear stress can disintegrate even the most robust microorganisms (Chisti and Moo Young, 1986). When a cell breaks, cytoplasm (cell contents) spills into the culture medium, nourishing bacteria that are usually much smaller than the cells, while cell walls remain in the medium or stick on the reactor surface, deteriorating transparency. Cell walls and other components can even end up clogging spargers and other components, such as oxygen and pH probes. In the end, high stress compromises long-term operation. Therefore, hydrodynamic effects on

photobioreactor operation are one of the major problems that an engineer has to consider for reactor design and scale-up. Indeed, selecting a reactor type with appropriate turbulent intensity and manipulating the mixing inside the PBR are two of the most important issues (Huntley, et al., 1996).

Among all types of photobioreactors studied, both as mentioned above and discussed in detail in Chapter 2, airlift column reactors have emerged as one of the most promising photobioreactors for their excellent mixing intensity (Merchuk et al., 2000; Sanchez Miron et al., 1999; Garcia Camacho, 1999; Chini Zetteli et al., 2003). These reactors have been widely used in the chemical, biochemical fermentation and biological wastewater treatment industries, where high mass transfer and good mixing are required. They possess many advantages that are especially suitable for mass microalgae/cyanobacteria cultures, such as simple construction, long liquid phase residence time, and low shear stress while maintaining high turbulence intensity (Sanchez Miron et al., 1999). Therefore, exploring the possibility of applying airlift column reactors in mass autotrophic microorganism production and advancing the understanding of their design, scale-up and process intensification are very important. This undertaking requires in-depth knowledge of their local multiphase flow characteristics.

## 1.2 Motivation

Substantial work on photobioreactor modeling, design, and scale-up for phototrophic cultures exists in the literature. However, hydrodynamics, especially its local characteristics that determine the cells' movement in the photobioreactors, is not fully understood yet. Three reasons contribute to such poor understanding.

- 1) Photobioreactors are opaque systems involving complex multiphase flow. In PBRs, multiphase flow is involved since  $\text{CO}_2$  has to be supplied as major carbon source and  $\text{O}_2$  has to be removed from the liquid phase. Moreover, due to the targeted high cell concentration in mass production, extensive cellular absorption of light photons and

- self-shading effects among the cells are present in PBRs. Therefore, they are essentially opaque systems.
- 2) Most traditional experimental techniques (e.g., manometer, Pitot tube, laser doppler anemometry, particle image velocimetry) are not feasible as they either cannot provide in-depth hydrodynamic knowledge or cannot be applied in the opaque systems.
  - 3) The physical properties of the culture media are not constants. In fact, many microorganisms excrete secondary metabolic products which can change the physical properties of the liquid phase, and thus the flow dynamics in the reactor system. For example, *Porphyridium sp.*, a red marine alga, is encapsulated within sulphated cell-wall polysaccharides (Eteshola et al., 1996; Gu and Liu, 2001). These polysaccharides, accumulating in the culture medium especially at the stationary growth stage, can considerably affect the viscosity of the culture medium (Eteshola et al., 1996, 1998; Geresh et al., 2002).

As a consequence, the exact mechanism of how light flashes interact with photosynthesis is still under debate, with controversial findings. Moreover, most current studies analyze photobioreactor performance based on static photosynthetic rate models with limited flow dynamic information, as will be summarized in section 2.3. These studies, applying empirical or semi-empirical correlations, usually ignore the flashing light effects. Only a few of them consider photoinhibition effects, which are very important when strong external irradiance is used. Therefore, these studies can be applied only to specific conditions (Aiba, 1982; Jassby and Platt, 1976; Rorrer and Mullikin, 1999).

Recently, Wu and Merchuk (2001, 2002) developed a dynamic growth rate model for reactor performance evaluations. This modeling approach uses the physiologically based three-state photosynthetic rate model proposed by Eilers and Peeters (1988), and requires the time series of incident irradiance as input. Such time series could be estimated from the cells' movement data and an appropriate irradiance distribution model. However, because Wu and Merchuk (2001, 2002) were not able to experimentally obtain the cells'

movement data, they used a non-physical multi-circulation model developed by Joshi and Sharma (1979) to estimate the cells' trajectories in the reactors. With this approach, Wu and Merchuk (2001, 2002) simulated the growth rate of *Porphyridium sp.* in a bubble column and a draft tube column reactor, using the photosynthetic kinetic parameters they measured for *Porphyridium sp.* in a small tubular reactor. Although their simulation results matched their experimental data reasonably, such an approach lacks generality. The multi-circulation model they used to predict the cells' trajectories does not represent the flow pattern in bubble or airlift columns (Degaleesen, 1997) as discussed in Chapter 3. Moreover, many parameters for this model were either hard to estimate or were purely fitted parameters.

Given the limitations of the current modeling approaches mentioned above, the design and scale-up of photobioreactors for the growth of phototrophic culture requires extensive, costly, and labor-intensive empirical developmental efforts. These cause a substantial increase in the production costs and in the prices of the downstream products. For example, potential worldwide demands for EPA are larger than 125 tons per year (e.g., current market demand for EPA in Japan alone is about 125 tons, Molina Grima et al., 1996b), and the demands are still increasing due to the clinical success of EPA based drugs for a number of ailments. Fish oil derived EPA is cheap (about \$650 kg<sup>-1</sup>), but is unlikely to be sufficient to supply the EPA market in the long run. Thus microalgae EPA is attracting more and more attention. To compete with fish oil derived EPA, however, the price for microalgal should be less than \$5 kg<sup>-1</sup>, which is two orders of magnitude lower than the current technique can provide (Harel et al., 2002; El-Hassan et al., 2000; Molina Grima et al., 1996b).

Accordingly, a thorough study of the local flow dynamics in photobioreactors and a fundamentally based modeling approach are required to better understand how flashing lights interact with photosynthesis and to advance in general the design, scale-up, and operation of PBRs. Such an approach should integrate the first principles of hydrodynamics, photosynthesis, and irradiance to enhance biomass productivity by

maximizing growth rate and light use efficiency. In-depth knowledge of the flow dynamics in the bioreactors is the key for the development of such an approach.

In the Chemical Reaction Engineering Laboratory (CREL) at Washington University in Saint Louis, two advanced non-invasive hydrodynamic measurement techniques, namely Computer Automated Radioactive Particle Tracking (CARPT) and Computed Tomography (CT), have been used extensively and successively in characterizing the flow field in multiphase and opaque reactors (Roy, et al., 2002; Kumar and Dudukovic, 1997; Luo et al., 2003). CARPT has been used to measure particle trajectories and their residence distributions, liquid velocities, turbulence parameters, etc., while CT has been used to measure the local phase distributions. Combined, these two techniques provide unique and in-depth knowledge of local characteristics of hydrodynamics.

In addition, Computational Fluid Dynamics (CFD) modeling is a powerful tool in obtaining rich information of flow dynamics. Considering the fact that CARPT and CT techniques are not generally accessible, CFD technique is more favorable in obtaining the needed flow dynamic information for PBR analysis. However, at current stage, the CFD model and the various closures still need to be verified against experimental data before they can be used for design and scale-up of selected PBRs.

Hence, CARPT, CT, and CFD modeling are proposed to study the details of the hydrodynamics in photobioreactors, focusing on a draft tube column PBR in this work. Such a PBR is proposed for the following reasons:

- in a similar photobioreactor with same dimensions, Merchuk et al. (2000) and Wu and Merchuk (2001, 2002) extensively investigated the reactor performance of *Porphyridium sp.*, and they also studied the kinetics parameters of photosynthesis for *Porphyridium sp.*;
- the reactor has been considered as one of the most promising PBRs as will be summarized in section 2.1;
- the reactor is widely used in bioengineering processes.

Based on the obtained in-depth knowledge of hydrodynamics, a careful analysis of flashing light effects on photobioreactor performance will be conducted in this study. A fundamentally based modeling approach will also be developed to predict the reactor performance by integrating the knowledge of hydrodynamics, photosynthesis, and irradiance distribution.

Successful execution of this fundamental study will considerably enhance the understanding of hydrodynamic effects on photosynthesis and PBR performance. Moreover, although this study focuses on airlift column reactors, it will advance the operation, design, and scale-up of any other types of PBRs for industrial interests. It is noteworthy that the obtained hydrodynamic information will also significantly enrich the knowledge base for airlift column reactors and thus benefit the design and scale-up of such reactors in many other applications.

### **1.3 Research Objectives**

The overall objectives of the proposed research are to advance the understanding of the role of hydrodynamics in the photobioreactor performance and to develop a fundamental modeling approach for cell growth prediction that integrates the hydrodynamics, photosynthesis, and irradiance distribution.

Specifically, the goals are to:

1. Use advanced measurement techniques (CARPT and CT) to investigate the hydrodynamics in a draft tube airlift column reactor. The reactor will be similar to the one used by Merchuk et al. (2000) for microalgae/cynobacteria culturing studies. An air-water system will be used due to its simplicity. A new calibration device with high accuracy and full automation will be developed to perform CARPT measurements properly in the proposed reactor. The effects of selected geometrical and operating parameters on the hydrodynamics of the airlift column reactor will be investigated.

These experiments are a starting point to understand the complex multiphase flow dynamics in the airlift column reactors. They will provide two types of essential information for further analysis. The first is the cells' movements, which will be further processed to estimate the time series of irradiance needed for reactor performance evaluation. The second is the flow dynamic information, such as the liquid velocity profiles, gas holdup profiles, distributions of shear stresses and other turbulent parameters, and cells' local residence time distributions, etc. Such information forms the knowledge base for advancing photobioreactor design and scale-up, and also provides a benchmark database for CFD modeling validations.

2. Study the flashing light effects due to the hydrodynamics on photosynthesis. This investigation consists of the following three sub-objectives:
  - estimate the temporal irradiance pattern (i.e., the time series of irradiance experienced by the cells in the reactors). A full spectrum of the time series of irradiance will be computed using a selected irradiance distribution model, and the cells' trajectories which will be obtained by CARPT measurements or CFD simulations;
  - study the interactions between photosynthesis and hydrodynamics. A mechanism for such interactions will be suggested based on the obtained temporal irradiance pattern;
  - characterize the random series of the temporal irradiance pattern. Based on the suggested mechanism of the interaction between hydrodynamics and photosynthesis, parameters will be identified to quantitatively characterize the estimated random time series of irradiance.
  
3. Develop a novel fundamental modeling approach that integrates the first principles of photosynthesis, hydrodynamics, and irradiance distributions in the reactor to evaluate the reactor performance. The cells' specific growth rates and population concentrations will be evaluated. This modeling approach will not only shed light on

understanding how microorganisms acclimate to the random time series of irradiance, but also benefit photobioreactor design and scale-up for industrial interests.

To verify this model, *Porphyridium sp.*, the same red marine alga used by Merchuk et al. (2000), will be grown in three types of airlift column reactors at two irradiance regimes and two flow conditions. The biomass concentration, multiphase flow dynamics, physical properties, and irradiance distribution of the culturing systems will be monitored. The experimental results will be compared with the predictions by the developed dynamic model.

4. Use CFD models to obtain the local characteristics of hydrodynamics in the studied airlift column reactor. First, the experimental data obtained from CARPT and CT measurements will be used to validate the CFD modeling and its closures. Then, the validated CFD models will be used to predict the hydrodynamics in the airlift column reactors and to obtain the cells' trajectories in the reactor. Finally, the obtained cells' movement data will be used as an input to the developed dynamic modeling approach for reactor performance evaluation.

Therefore, the validated CFD modeling will provide not only detailed understanding of the local flow dynamic characters in the reactors, but also an alternative method to obtain essential information for the photobioreactor performance evaluation other than CARPT and CT measurements with much lower cost. Hence, the integration of the CFD modeling with a photosynthetic model will form a general approach for the photobioreactor design, scale-up, operation, and process intensification.

From this study, we will considerably enhance the understanding of the hydrodynamics' role in the photobioreactor's performance. The developed general modeling approach can also advance the reactor design, scale-up, and operation by improving the light use



efficiency, maximizing the biomass productivity, and cutting production costs for potential industrial applications.

## **1.4 Structure of Dissertation**

This dissertation is structured as follows.

A literature review is provided in Chapter 2, summarizing the available knowledge of photosynthesis, flashing light effects, photosynthesis modeling, photobioreactor design, and hydrodynamics studies for airlift column reactors. Chapter 3 discusses the feasibility of employing CARPT for photobioreactor analysis using available CARPT data in our laboratory. Based on the improved understanding, methods to characterize the flashing lights and a dynamic growth rate model for photobioreactor performance evaluation are developed in Chapter 4. This model directly integrates CARPT data with knowledge of photosynthetic kinetics and irradiance model.

To further explore the capability of airlift columns in microalgae culturing, the multiphase flow dynamics in a draft tube airlift column reactor are studied in detail using both CARPT and CT techniques. Chapter 5 presents these results, which have been further utilized in Chapter 6 to guide the development of a CFD simulation model with proper closures. Further verification of the developed dynamic growth rate model against experimentally measured real culturing data collected in this project is discussed in Chapter 7. Finally, Chapter 8 summarizes the conclusions reached in this study and make recommendations for future study.

## **Chapter 2**

### **Background**

#### **2.1 Scope**

Microalgae and Cyanobacteria cultures in photobioreactors are complex systems involving interactions among photosynthesis, hydrodynamics, and irradiance distribution. Extensive research has been done on modeling, design, and scale-up of photobioreactors based on static photosynthetic rate models and on hydrodynamics investigations in terms of global parameters (such as the bulk liquid circulation velocity and overall gas holdup). However, little work has been done to study the local characteristics of hydrodynamics (such as cell trajectories and stress distributions) and to combine fundamentals of photosynthesis and hydrodynamics. This section will briefly introduce the photosynthesis process, and then review current studies in terms of the following aspects: photosynthesis, PBR modeling approaches, enclosed PBR design, and hydrodynamics investigations in airlift column reactors.

## 2.2 An overview of photosynthesis

Microalgae and cyanobacteria use light and cheap inorganic compounds (e.g., water, CO<sub>2</sub>, some sources of nitrogen and phosphorus, mineral, etc.) to produce complex organic molecules through photosynthesis. Photosynthesis is a complex biological process converting light energy into chemical bond energy occurring in the photosynthetic apparatus of the microorganism cells.

The photosynthetic reactions start with the absorption of photons by the antenna complex in the cell's thylakoids in a time scale of picoseconds as shown in the conceptual schematic diagram in Figure 2-1. The resulting excitation energy can be reradiated into fluorescence, dissipated as heat, or transferred to other pigment molecules and ultimately to the reaction centers (Falkowski and Raven, 1997). How the energy distributes between these processes depends on the fraction of reaction centers in the oxidized state, the state that is able to accept excitons.

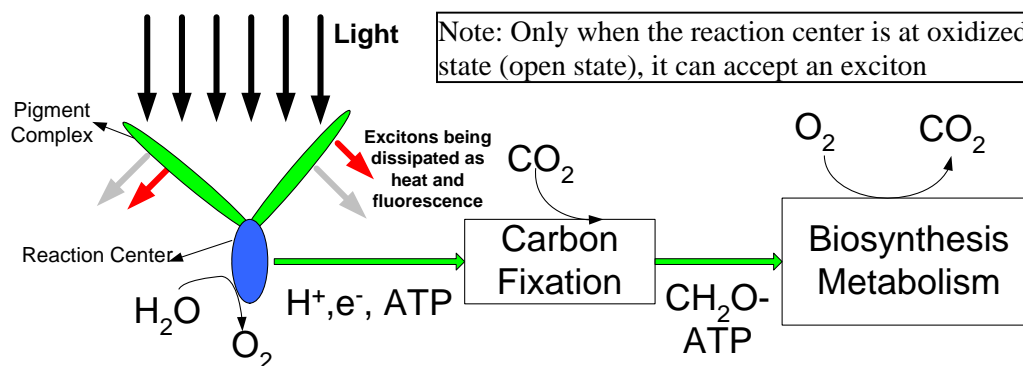


**Figure 2-1.** Conceptual schematic diagram of photosynthesis and cell growth processes (ATP: Adenosine TriPhosphate)

In the reaction centers, the excitation energy is utilized to split water molecules, evolve oxygen, and produce chemical reductants and chemical energy (e.g., ATP) through a complex electron transport chain (e.g., the famous Z-scheme) in a time scale of 10 milliseconds (Falkowski and Raven, 1997). These chemical reductants and energies, then, are transferred into the surrounding aqueous phase, the *stroma*, and are used to assimilate inorganic carbon into organics through the Calvin-Benson cycle in a time scale of 10 milliseconds. In fact, the turnover time of the overall electron transfer chain (i.e., the minimal time required for an electron to be transferred from water to inorganic carbon) is within the range of 1ms to 50ms (Falkowski and Raven, 1997), and usually is assumed to be a constant under steady state. Finally, the produced organics, e.g., glucose, are further used for cell metabolism and duplication.

If the microorganisms are exposed under constant irradiance, their growth will reach the so-called “balanced” status, a term referring to a status when the reaction rates for all steps of the cell’s growth are equal to each other (Falkowski and Raven, 1997). In such cases, the overall photosynthetic rate can be represented in general by the oxygen evolution rate, according to Han (2001) as:

$$r = I \times \sigma_{PSF} \times n_{PSF} \times \phi \quad (2-1)$$

where  $I$  is the incident irradiance to the cells;  $\sigma_{PSF}$  is the functional absorption cross-sectional area of the photosynthesis factory (PSF), a conception referred to as an ensemble of chlorophyll molecules involved in the evolution of one molecule of oxygen or carbon dioxide, i.e., Photosystem I, Photosystem II, and electron transport chains (Han, 2001);  $n_{PSF}$  is the number of the PSFs per mg-chlorophyll; and  $\phi$  is the overall quantum yield of the oxygen evolution.

The influence of irradiance on photosynthesis is usually represented by the well-known Photosynthesis-Irradiance (P-I) curve as shown in Figure 2-2, where the photosynthetic rate (e.g., oxygen evolution rate, CO<sub>2</sub> assimilation rate, or any other biomass concentration measures) is plotted against the irradiance intensity. At low incident irradiance, the light absorption is the limiting step. A large fraction of the reaction centers

are at the oxidative state that is ready to accept excitons, and the electron transfer rate is high enough to promptly convert the excitation energy into chemical energy. Hence, the overall quantum yield,  $\phi$ , is high (in fact,  $\phi$  approaches unity when the irradiance is very low, Falkowski and Raven, 1997). The photosynthetic rate is approximately a linear function of irradiance, with ratio of  $\alpha$  as shown in Figure 2-2.

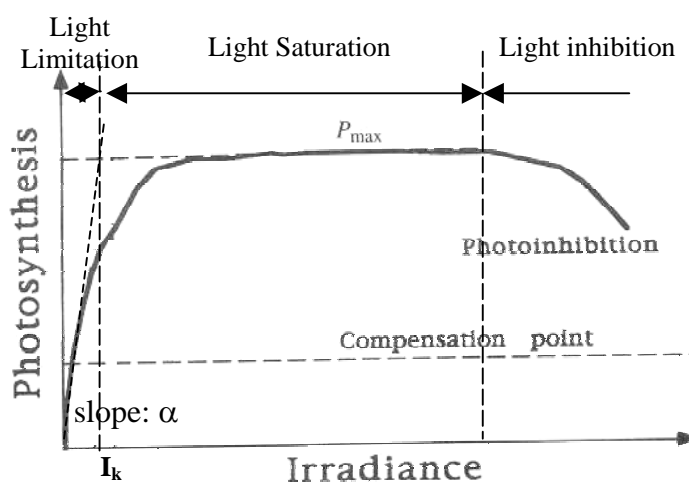


**Figure 2-2.** A typical photosynthesis-Irradiance (P-I) curve (modified from Vonshak, 1992)

On the other hand, at high incident irradiance, the electron transfer rate is the limiting step, resulting in a large fraction of reduced reaction centers. The overall quantum yield is low as many excitation energies are dissipated into heat or radiated into fluorescence. Hence, the photosynthetic rate mainly depends on the electron transfer rate, or the turnover time, which usually is a constant. At certain irradiance levels, the photosynthetic rate reaches a plateau, namely the light-saturated or the maximal rate,  $P_{max}$ . The irradiance at which the photosynthesis rate reaches  $P_{max}$  is called the half-saturation irradiance,  $I_k$ , which represents the optimum irradiance (Falkowski and Raven, 1997).

As the incident light increases further, some of the proteins in the electron transfer chain may be damaged and need a long time to recover. Hence, the photosynthetic rate drops dramatically. This is called the photoinhibition effect (Barber and Andersson, 1992).

In a photobioreactor, due to the unevenly distributed light intensity inside the reactor, the irradiance experienced by a cell is a random time series or flashing lights. The balanced status cannot be reached, and the P-I curve is theoretically not applicable. Therefore, proper understanding of how a cell responds to the flashing light is important for photobioreactor design.

## **2.3 Flashing Light Effects**

The flashing light effects stem from the random movements of cells in the reactor following the liquid eddies. The cells thus experience a random time series of light intensity which is fully determined by the local flow phenomena in the reactor. Two questions need to be answered in studying the flashing light effects: how the flashing lights interact with photosynthesis (Pulz and Scheibenbogen, 1998), and how to characterize the flashing lights in a real PBR.

### **2.3.1 How Flashing Lights Work**

Although all researchers unanimously agree that biomass productivity improves with increasing turbulent mixing, some (Schadlich, 1993; Sager and Giger, 1980; Rabinowitch, 1956) suggested it could be a result of the enhanced mass transfer rate rather than the flashing light effects. They argue that, based on the electron transport mechanism theory of photosynthesis, the limiting step is the enzyme reactions rather than the productivity rate of the light-collecting pigments. The quantum utilization at intermittent light will thus not be improved. Therefore, the flashing lights do not have direct effects on the photosynthesis.

However, more researchers believe flashing lights do interact with photosynthesis directly and can greatly enhance the photosynthetic efficiency (Nedbal et al., 1996; Lee and Pirt, 1981; Terry, 1986). Weller and Franck (1941) proposed that, at high flash frequencies, the photosynthetic rate is determined by the average irradiance received by the cells (full irradiance integration); while at low frequencies the cells respond to the instantaneous irradiance (no irradiance integration). Pirt (1986) further suggested that some microalgae could keep the maximal growth rate in the dark for almost 10 seconds by using the light energy they stored during the light period.

Carried out in a very small chamber (volume of 1 ml), Terry's experiments (1986) supported Weller and Franker's hypothesis. His experimental results showed that the full irradiance integration can occur at frequencies of 8 Hz in terms of the oxygen evolution rates. Moreover, he found that the full irradiance integration is a hyperbolic function of the flashing light frequency.

Nedbal et al. (1996) conducted a more comprehensive experiment using a 30ml bubble column bioreactor. In their experiment, they found 10~20% improvement in the overall photosynthetic rate (in terms of dry biomass weight) when the flashing light's frequency is in the range of 10~1000Hz. They also found that the photoinhibition level is reduced under flashing light conditions. Therefore, they proposed that the dark intervals during the intermittent lights help to re-oxidize the plastoquinone pool in the reaction centers, and enhance the overall photosynthetic rates.

However, in larger scale photobioreactors, inconsistent experimental results have been reported. Merchuk et al. (1998a) studied the reactor performance of a 15L draft tube column reactor culturing *Porphyridium* sp., a red marine alga. In favor of Pirt's hypothesis (1986), they suggested that *Porphyridium* sp. could sustain maximal growth rate in darkness for 6 s during a Light/Dark cycle of 27 s.

Janssen et al. (1999, 2000a, 2000b, 2001, 2002) challenged these suggestions after conducted a series of experiments. Using the same strains Pirt (1986) used but in a smaller reactor (liquid volume of 0.6 L), Janssen and his colleagues failed to observe any photosynthetic efficiency enhancement under flashing light with frequencies in the order of 0.1Hz (i.e., Light/Dark cycle of 13~87 s). And they only observed such enhancement under flashing light with frequency in the order of 10Hz (i.e., Light/Dark cycle of 0.188 s) by using some other strains.

However, it is noteworthy that such controversial can be resolved if the effects of local flow dynamics are taken into consideration. The time scale of the Light/Dark cycle cited in Merchuk et al. (1998) is actually the time scale for the bulk liquid circulation between the riser (i.e., the dark center) and the downcomer (the illuminated zone). But in a draft tube column reactor with volume of 15L and running at the bubbly flow regime as in their experiments, the time scales for the Light/Dark cycles could be much lower.

Based on theory of turbulence, turbulent flows contain a spectrum of turbulent eddies with different time and length scales. In the downcomer of the reactor used by Merchuk et al. (1998), the Kolmogoroff's time scale of the smallest turbulent eddies is in milliseconds. The frequency of the flashing lights a cell experienced in such reactors thus could be close to or even larger than 100Hz, rather than close to the time scales of the bulk liquid circulations. These time scales overlap the typical range of time scales of photosynthesis, e.g., photon absorption reactions in  $10^{-8}$ s (Junge, 1977),  $\text{CO}_2$  fixation in  $10^{-2}$ s or even longer (Falkowski and Raven, 1997). Therefore, interactions between mixing and photosynthesis must have a significant potential to influence the performance of photobioreactors.

On the other hand, in the experiments carried out by Janssen et al. (1999), either fairly low cell concentration (e.g., optical density of 0.2) or short light path (e.g., 1.45cm) was used to guarantee low mutual shading among the microorganisms. Therefore, the Light/Dark cycles experienced by the cells are purely come from the intermittent lights



imposed by the illumination lamps. With low Light/Dark frequency imposed by the lamps, the productivity will not be improved as proved by Nedbal et al. (1996). This explains why Janssen and his coworkers failed to observe the productivity improvements.

Based on these reported experimental results, it can be concluded that only flashing lights with higher enough frequency (i.e., in the order of 10 Hz) can interact with photosynthesis to enhance the photosynthetic efficiency. Under such conditions, the time scales of the flashing lights and photosynthesis are overlapping.

### 2.3.2 Characterization of Flashing Light

To study the flashing light effects, square wave signals of incident irradiance, i.e., well defined Light/Dark (L/D) cycles as shown in Figure 2-3, have been widely used as the light sources to dilute microalgae culturing mediums (Phillips and Myers, 1954; Terry, 1986; Nedbal et al., 1996; Janssen, 2002). Terry (1986) tried to establish the quantitative relationship between the photosynthetic efficiency enhancement and the parameters characterizing the Light/Dark cycle, i.e., incident irradiance ( $I_E$ ), frequency ( $f$ ), and fraction of the light time in a cycle (namely dimensionless relaxation time,  $\varphi$ ):

$$f = 1/(t_d + t_l); \quad \varphi = t_l / (t_l + t_d) \quad (2-2)$$

where  $t_l$  is the time when the light is on, and  $t_d$  is the time when the light is off in one cycle. He found that the photosynthetic efficiency enhancement is a hyperbolic function of both frequency and the dimensionless relaxation time when flashing light frequency is higher than 1 Hz.

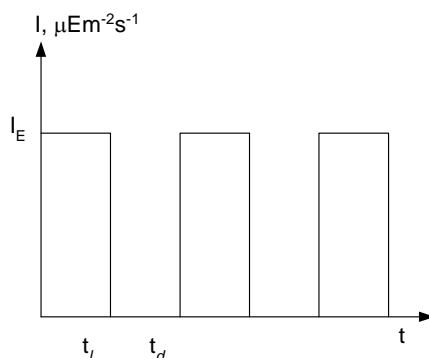


**Figure 2-3.** Illustration of the well-defined light/dark cycles

Such well defined Light/Dark cycle, however, could never be experienced by the cells in a real culturing system. Instead, they would experience a random time series of irradiance with a cascade of fluctuation frequency due to the chaotic nature of flow dynamics, which determines the cells' movement in the reactors. Indeed, considering the well-known fact that the Komogoroff time scales in many medium size reactors are in the range of micron to milliseconds as mentioned above, the local characters of the hydrodynamics, such as turbulence, should have significant effects on photosynthesis.

As a result, two questions exist in studying the flashing light effects due to hydrodynamics on the photobioreactor performance in a real culturing system:

- How the random time series of the irradiance should be characterized;
- How the microorganisms would acclimate to such random incident irradiances.

To answer these questions and to evaluate the photobioreactor performance, fundamental knowledge of hydrodynamics and photosynthesis is required.

## 2.4 Modeling Approaches for Photobioreactors

Modeling the influence of light intensity on the photosynthesis rate has been the subject of extensive research (Phillips and Myers, 1954; Crill, 1977; Eilers and Peeters, 1988,

1993; Pahl-Wostl and Imboden, 1990). In the literature, two types of models, namely static and dynamic, exist that relate the photosynthetic rate with the irradiance received. The static models simply try to fit the parabolic P-I curve (as shown in Figure 2.2) with empirical parameters while the dynamic models try to establish the photosynthetic growth rate based on the first principles of photosynthesis.

### 2.4.1 Modeling Approaches Based on the Static Photosynthetic Rate Model

Typically, static photosynthetic growth rate models use modified Monod type functions as (Molina Grima, et al., 1994):

$$\mu = \frac{\mu_m \cdot I^n}{I_k^n + I^n} \quad (2-3)$$

or use the Poisson function (MacIntyre et al., 2002)

$$\mu = \mu_m (1 - \exp(-I / I_k)) \quad (2-4)$$

to fit the P-I curve as summarized in Table 2-1. In these equations,  $I$  is the incident irradiance (a detailed definition of irradiance and its calculation are presented in Appendix D), and  $\mu$  is the specific growth rate, defined by:

**Table 2-1.** Typical static growth rate models in literature

1. $\mu = \frac{\mu_{\max} I_{av}}{\mu_{\max} + I_{av}}$ (Tamiya et al., 1953)	4. $\mu = \mu_{\max} (1 - \text{Exp}(-\frac{I_{av}}{I_{\max}}))$ (Van Oorschot, 1955)
2. $\mu = \frac{\mu_{\max} I_{av}}{(K_i^m + I_{av}^m)^{1/m}}$ (Bannister, 1979)	5. $\mu = \mu_{\max} \frac{I_{av}}{I_{\max}} \text{Exp}(1 - \frac{I_{av}}{I_{\max}})$ (Steele, 1977)
3. $\mu = \frac{\mu_{\max} I_{av}}{K_s + I_{av} + \frac{I_{av}^2}{K_i}}$ (Aiba, 1982)	6. $\mu = \frac{\mu_{\max} I_{av}^n}{I_k^n + I_{av}^n}$ (Molina Grima et al., 1994)
7. $\mu = \frac{\mu_{\max} I_{av}^n}{I_k^n + I_{av}^n} - m \begin{cases} n = n_2 + n_3 / I_0 \\ I_k = I_k' + (\frac{I_0}{K_I})^{n_1} \end{cases}$ (Molina Grima et al., 1996a)	
8. $\mu = \frac{2\mu_s (I_s - I_e)(I - I_e)}{(I_s - I_e)^2 + (I - I_e)^2}$ ( $I_e$ is the compensation light energy) (Muller-Euga, 1998)	

$$\mu = \frac{1}{x} \frac{dx}{dt} \quad (2-5)$$

where  $x$  is any measure of biomass abundance, such as the cell population or oxygen evolution rate.

Both functions have the same mathematical origin, which can be characterized by two basic parameters: maximal specific growth rate ( $\mu_m$ ) and half-saturation irradiance ( $I_k$ ) (Jassby and Platt, 1976; Iwakuma and Yasuno, 1983). On a P-I curve, the maximal specific growth rate corresponds to the maximum plateau, where the growth rate is controlled by the turn over time of the electron transfer chain. And the half-saturation irradiance corresponds to the light intensity where a straight line drawn from the origin with the same slope as the P-I curve crosses the maximum plateau as shown in Figure 2-2. From these two parameters, we can calculate the initial slope of the P-I curve,  $\alpha$ , which is a measure of the maximum of the photon yield. It is believed that these parameters reflect the strategies the microorganism adopted for photoacclimation (Falkowski and Raven, 1997; MacIntyre et al., 2002).

Due to the simplicity, many researchers developed modeling approaches for reactor design and scale-up based on the static growth rate models. For example, Molina Grima et al. (2001) used Equation (2-3) as a principle to scale-up airlift driven tubular photobioreactors. To consider the hydrodynamic effects which are not included in Equation (2-3), they conducted a rough scale analysis of the flow and suggested flow conditions having similar Light/Dark cycles imposed to the cells in the reactors during the scale-up.

With limited hydrodynamic information provided, these approaches assume the cells use the light energy with same efficiency no matter how the light energy is delivered, i.e., ignoring the flashing light effects and the flow dynamics. Hence, the reactor performance prediction is essentially determined by the way of how to calculate the average

irradiance. The overall reactor performance is usually written in terms of the overall growth rate as suggested by Cornet and Albiol (2000):

$$\mu_r = \frac{1}{V} \iiint_V \mu dV = \frac{1}{V} \iiint_V \mu_m \frac{I_p}{I_p + I_k} dV \quad (2-6)$$

where  $V$  is the total volume of the reactor and  $I_p$  is the irradiance of the local  $dV$  volume.  $I_p$  is usually calculated from an appropriate irradiance distribution model (Cassano et al., 1995), which is discussed in detail in Appendix D. To calculate the integral term, some researchers (Molina Grima et al., 1997; Rorrer and Mullikin, 1999) simply assume the growth in an ideal mixed reactor corresponds to an average irradiance, which is the volume-averaged irradiance defined as (Molina Grima et al., 1997; Cassano et al., 1995):

$$I_{av} = \frac{1}{V} \iiint_V I_p dV \approx \frac{\sum_{i=1}^n V_i I_{p_i}}{V} \quad (2-5)$$

Thus, the overall growth rate is:

$$\mu_r = \mu_m \frac{I_{av}}{I_{av} + I_k} \quad (2-6)$$

Some other researchers divide the reactor into different metabolic zones and estimate the growth rate separately in each zone. For example, Cornet and Albiol (2000) divided the reactor into an illuminated zone and two dark zones with or without metabolic activity. This approach takes into account the fact that the kinetic parameters,  $\mu_m$  and  $I_k$ , are defined only in those parts of the reactor where metabolic activity occurs with a limited range of light intensity.

Pruvost et al. (2002) developed a Lagrangian approach to calculate the overall growth rate from the static models. They used PIV technique to study the liquid flow filed in a tubular photobioreactor and calculated the fluid trajectories which mimic the cells movement in the reactor. Then they were capable to integrate a static growth rate model, i.e., the Muller-Euga model (1998) shown in Table 2-1 (Equation 8), along the fluid trajectories with the help of an irradiance distribution model (i.e., Lambert-Beer Law). Using an appropriate time step and keep updating the biomass concentration and the

irradiance delivered to the cells after each time step, they obtained the overall performance of a tubular reactor. However, as no comparison between the experimentally measured and predicted data was reported, the reliability of this approach is unknown.

It is fair to say, although most of these approaches fit reasonably with observations, they lack generality. Theoretically, since the P-I curve is determined after the “balanced” growth condition is achieved for the studied irradiance (thus the cell is photo-acclimated to the new irradiance), these static models cannot be used to predict the photosynthetic growth rate of a cell when the incident irradiance keeps changing. Hence, the flashing light effects on the reactor performance are omitted. Moreover, since the Poisson function does not fit the supra-irradiance region in the P-I curve (Figure 1.2), usually the static models do not consider the photoinhibition effects (recently, the model developed by Molina Grima et al. (1996a) considered the photoinhibition effects with a revised Poisson function and extra fitting parameters). As a result, these models can only be applied to specific applications, and fail the industrial interests of operational conditions where dense cell population and strong external irradiance are widely used and light fluctuation effects are prominent.

#### **2.4.2 Modeling Approaches Based on the Dynamic Photosynthetic Rate Model**

Dynamic models have been developed to establish physiological relationship between photosynthetic rates and irradiance (Megard et al., 1984; Eilers and Peeters, 1988, 1993; Pahl-Wostl and Imboden, 1990; Zonneveld, 1998; Han et al., 2000; Han, 2001, 2002; Camacho Rubio, et al., 2003). In these models, concept of the photosynthetic factory (PSF) is widely used. Typically these models assume that a PSF has three states: reactive, activated, and inhibited (or inactivated), or two states when the inhibition effect is ignored. The interchange between these states represents different enzyme reactions, e.g., the light, the dark and the inhibition reactions. The advantage of these models with three states is their ability to represent photoacclimation strategies from the kinetic parameters,

and to take account of photoinhibition at supra-irradiance. The differential equations thus generated can be readily handled.

For example, the model proposed by Eilers and Peeters (1988), which has been further advanced by Wu and Merchuk (2001), assumes PSF has three states: the resting state,  $x_1$ , the activated state,  $x_2$ , and the inhibited state,  $x_3$  as shown in Figure 2-4. The probabilities of the state transitions following a photon capture are supposed to be proportional to the light intensity. In other words, these reactions are assumed to be first order reactions with reaction constants of  $\alpha I$  for  $x_1 \Rightarrow x_2$  and  $\beta I$  for  $x_2 \Rightarrow x_3$ . Since the rest state transitions can be happened in the dark, the reaction constants for these reactions are assumed to be constant, i.e.  $\gamma$  for  $x_2 \Rightarrow x_1$ , and  $\delta$  for  $x_3 \Rightarrow x_1$ . Thus, the following differential equations are proposed in the model:

$$\frac{dx_1}{dt} = -\alpha \cdot I \cdot x_1 + \gamma \cdot x_2 + \delta \cdot x_3 \quad (2-7)$$

$$\frac{dx_2}{dt} = \alpha \cdot I \cdot x_1 - \gamma \cdot x_2 - \beta \cdot I \cdot x_2 \quad (2-8)$$

$$\frac{dx_3}{dt} = \beta \cdot I \cdot x_2 - \delta \cdot x_3 \quad (2-9)$$

$$x_1 + x_2 + x_3 = 1 \quad (2-10)$$

where  $x_1$ ,  $x_2$ ,  $x_3$  are the fractions of the PSFs in the resting, activated, and inhibited state, respectively;  $I$  is the instant light intensity experienced by the cells; and  $\alpha$ ,  $\beta$ ,  $\delta$ ,  $\gamma$  are the reaction constants. The specific photosynthetic rate ( $\mu$ ) is proportional to the number of the state transitions from  $x_2$  to  $x_1$ , namely the dark reaction:

$$\frac{1}{x} \frac{dx}{dt} = \mu = k \cdot \gamma \cdot x_2 - Me \quad (2-11)$$

where  $x$  is the total number of PSFs or any other measure of biomass concentration, and  $k$  is the yield of the photosynthesis reaction.  $Me$  is a maintenance constant introduced by Wu and Merchuk (2002) to account for cellular damage due to adverse environments, e.g., high shear stress:

$$Me = \overline{Me} \cdot e^{k_m(\tau - \tau_c)} \quad (2-12)$$

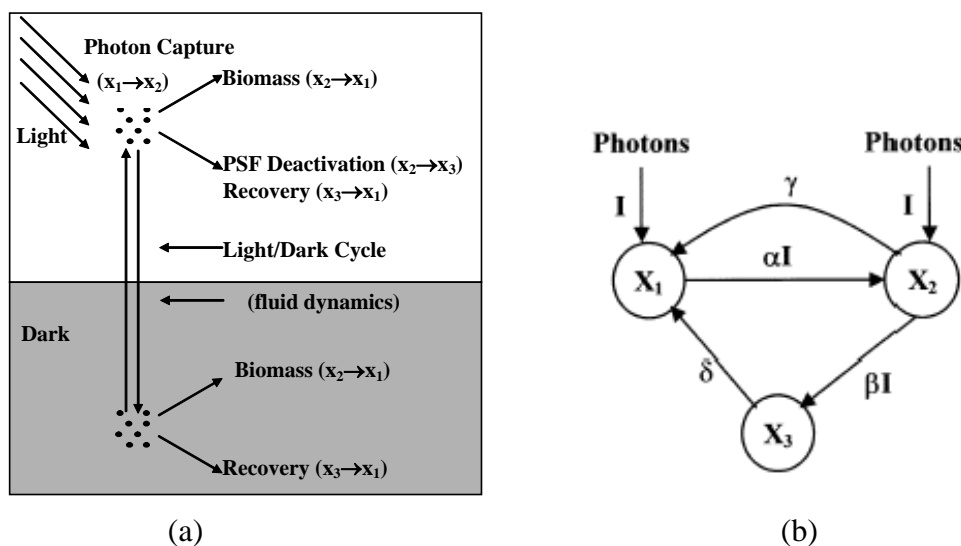


**Figure 2-4.** (a) Schematic representation of the interaction of photosynthetic kinetics and the fluid dynamics in the photobioreactor (from Wu and Merchuk, 2001). The reactor is divided into a dark and an illuminated region. Photons are captured by the cells in the illuminated region, where photosynthetic factory (PSF) deactivation takes place. The cells are cyclically transported to the dark zone, where PSF recovery takes place. (b) Structure of the three states model proposed by Eilers and Peeters (1988) (duplicated from Wu and Merchuk, 2001). Photons are captured by a PSF in state  $x_1$  which passes at a rate that is proportional to  $I$ . The PSF in state  $x_2$  can either return to state  $x_1$  at a constant rate,  $\gamma$ , or capture another photon and pass to the inhibited state  $x_3$ . The PSF at state  $x_3$  returns to state  $x_1$  at a constant rate,  $\delta$ . The chain of dark reactions is started by the direct passage of  $x_2 \Rightarrow x_1$ .

where  $\overline{Me}$  is the maintenance without shear stress effects,  $k_m$  is the extinction coefficient for shear stress,  $\tau$  is shear stress, and  $\tau_c$  is a constant that represents the critical level of shear stress below where no effect of shear stress on the growth is observed.

Due to the simplification of these models, however, not all of the physiology of photosynthesis has been accounted for. Recently, Han (2001, 2002) reviewed such models and incorporated more physiology to generate a four-parameter model. Camacho Rubio, et al. (2003) also proposed a mechanistic model by breaking down the photosynthesis process into two steps: a photochemical energy capturing step and a metabolic consumption step. This model takes account of the photoadaptive responses,



photoinhibition, and the flashing light effect, which, inevitably, generated a few rather mathematically complex equations.

Unfortunately, although many models have been developed, further verification and estimation of model parameters are very scarce in the literature. Moreover, the information of cells' movement, or the time series of light transferred to the cells, is required to implement such dynamic models to evaluate the reactor performance, which cannot be provided by many experimental measurements. Hence, few researchers used the dynamic models to analyze the photobioreactor performance and reactor design and scale-up (Wu and Merchuk, 2001; Pruvost et al., 2002).

Merchuk et al. (1998a, 2000), Wu and Merchuk (2001, 2002) experimentally investigated the effects of well-defined light/dark cycles with different periods and light/dark ratios on the photosynthetic rate of a red marine microalga, *Porphyridium sp* in a tubular loop reactor of diameter 7 mm. Using the obtained kinetic data, they estimated the model parameters of the dynamic model proposed by Eilers and Peeters (1988) and further advanced by introducing the maintenance constant as shown in Equation 2-12. Moreover, they experimentally studied the reactor performance of *Porphyridium sp*. in a bubble column and in a draft tube airlift column at different superficial gas velocities. Based on this dynamic model, Wu and Merchuk (2002) simulated the overall reactor performance in a draft tube column reactor. Apparently, due to the lack of cells' movement measurement data, they used the multi-circulation model developed by Joshi and Sharma (1979) to estimate the cells' trajectories in the reactors. Although the developed heuristic model successfully fitted the overall growth rate in the studied reactors, the model lacks generality. Many parameters for the multi-circulation model they used to predict the unrealistic cells' trajectories (Roy et al., 2002; Luo et al., 2003) were either hard to estimate or were purely fitted parameters.

In summary, it's clear that only model approaches based on dynamic photosynthetic rate model can represent the microorganism growth in PBRs and, thus, it is required for PBR

performance evaluation and design. These approaches consider the flashing light effects which are very important under industrial productions, and integrate fundamentals of hydrodynamics, photosynthesis, and irradiance distribution.

## **2.5 Enclosed Photobioreactors**

Numerous attempts on photobioreactor design have been made in the last decades, resulting in a wide variety of reactor types as summarized by Lee (1986) and Pulz and Scheibebogen (1998). This section focuses on those reactor types which have been tested extensively for photoautotrophic cultures, such as the tubular reactors (Chaumont et al., 1988; Tredici and Zitelli, 1998; Fernandez et al., 1998), the thin panel type reactors (Hu and Richmond, 1996), and the airlift bubble column reactors (Merchuk et al., 1998a; Janssen, 2002). The others, such as the fiber optic reactors (Javanmardian and Palsson, 1991), immobilized cell system (Robinson et al., 1986), and polyethylene bag (Becker, 1994), etc. will not be included in this review due to their apparent drawbacks or prohibitive manufacturing costs.

Generally, two approaches have been adopted for enclosed photobioreactor designs. Since the light availability is one of the controlling factors for the PBR performance, a straightforward approach for this problem is to increase the area/volume ratio. That is to decrease the reactor diameter, e.g., use tubular reactors with small diameter, or to use reactors with high area/volume ratio, e.g., thin panel reactors. Conventionally, tubular reactors and thin panel reactors are installed horizontally or almost horizontally inclining to sunlight. The biomass productivity based volume in these reactors is high as proven by many experimental works (Chini Zettelli et al., 2000; Zou et al., 2000).

However, these reactors possess some disadvantages. These reactors are likely to suffer severe photoinhibition effects when they are directly exposed to sunlight due to their short light-path (usually within 1~5 cm) and low turbulence intensity (Fernandez et al.,

1998; Janssen et al., 2002). They are usually difficult in temperature control due to the low mass and heat transfer rates, demand of frequent recarbonation due to long tubular length (for tubular reactor), and growth inhibition by accumulated oxygen, foaming, and fouling, etc. (Garcia Camacho, et al., 1999). Moreover, they are difficult to scale-up (Sanchez Miron et al., 1999; Janssen, 2002; Borowitzka, 1996)

The other approach is to improve light use efficiency by using reactors with better mixing, such as the vertically installed cylindrical airlift and bubble column reactors. Usually, these reactors have a smaller area/volume ratio than the short light path reactors do. But airlift and bubble column reactors possess some advantages over those light path reactors: they are pneumatic reactors without moving parts, have high mass and heat transfer rates, and provide homogeneous shear stress and rapid mixing. They are also easy to control and have great operational flexibility (Sanchez Miron et al., 1999). The homogeneity inside the reactor can further provide a consistent metabolic state to the cells and the light usage efficiency is high. Moreover, the scalability of the airlift reactors is better than the other types of reactor mentioned above (Janssen, 2002).

In fact, a combination of these two approaches is possible. Hu et al. (1998) developed a vertically installed thin panel photobioreactor, which actually works as a rectangular airlift column reactor. By applying high turbulence, they achieved very high cell population (26.6 g/L) and productivity under short light path (7.5mm) and ultrahigh irradiance (e.g.,  $8000 \mu\text{mol}/\text{m}^2 \text{s}^{-1}$ ). However, the scalability of such a reactor is doubtful as shown by Hu et al. (1998): when the light path (distance between the panels) increases from 7.5mm to 200mm, the volume productivity drops from  $621 \text{ mg l}^{-1} \text{h}^{-1}$  to  $12 \text{ mg l}^{-1} \text{h}^{-1}$ , almost two times faster than the increase of the light path. Moreover, the investment and the energy consumption could be very costly (Janssen, 2002).

It's fair to say that currently there is no reactor type that is superior to the others, which can satisfy all the requirements for industrial mass microalgal production. Since the investment and the operational costs are almost proportional to the size of reactor

(Olazola, 2001), scalability of the reactor is considered one of the major problems for meaningful reactor design for industrial interests. Based on this point, and the other advantages of the airlift column reactors as mentioned above, many researchers (Merchuk et al., 2000; Sanchez Miron et al., 1999; Garcia Camacho, 1999; Chini Zettelli et al., 2003) suggested the airlift column reactor as the reactor type for mass production.

## **2.6 Investigations of Hydrodynamics for Airlift Column Reactor**

In an airlift column reactor, air (or any other gas) is sparged into the column from the riser resulting in a continuous cyclical recirculation of liquid and solid (if any, e.g., cells) phases in the reactor. The advantages of the airlift reactor are: no moving parts; low power consumption; high mass and heat transfer characteristics; good solid suspending; homogeneous shear; and above all, rapid mixing (Petersen and Margaritis, 2001; Chisti, 1998). The airlift column reactor is widely used in biotechnological processing, such as fermentation (Pollard et al., 1998), wastewater treatment (Heijnen et al., 1990), cell production including animal, plant and microorganism cells (Chen et al., 1987), etc. The following sections outline the measurement techniques and modeling efforts reported for airlift bioreactors hydrodynamics investigations.

### **2.5.1 Experimental measurements**

Airlift bubble columns have been studied extensively over the last decades (Chisti and Moo-Yong, 1988; Joshi et al., 1990; Chisti, 1998; Petersen and Margaritis, 2001). However, most of the studies focused on the global hydrodynamics parameters (e.g., bulk liquid circulation velocities and overall gas holdups) by using traditional hydrodynamic measurement techniques as shown in Table 2-2. Only a few of the studies tried to investigate the local characteristics of hydrodynamics in the airlift column reactors using recently improved measurement techniques like Laser Doppler and optical fibre probe techniques (Vial et al., 2002).

**Table 2-2.** Typical hydrodynamic measurements for airlift column reactors

<b>Reference</b>	<b>Reactor type and dimensions</b>	<b>Variables measured</b>	<b>Techniques used for measurements</b>
Merchuk and Stein (1981)	External loop column	Gas holdup Liquid circulation velocity	Differential pressure Magnetic flow meter
Weiland and Onken (1981)	External loop column	Gas holdup Liquid circulation velocity Mixing time Dispersion coefficient	Differential pressure Magnetic flow Conductivity method Pulse tracer technique
Bello et al., 1984, 1985	External loop column Internal loop column	Liquid circulation velocity Gas holdup	Tracer technique Differential pressure
Chisti and Moo Young (1988)	Internal loop column Split cylinder	Liquid Circulation velocity	Tracer technique
Young et al., 1991	External loop column	Local liquid velocity Local gas velocity Local gas holdup	Hot-film anemometry Resistivity probe Gamma densitometry
Merchuk et al., 1998b	Internal loop column	Overall gas holdup Liquid circulation velocity	Differential pressure Pulse injection-response
Vial et al., 2002	External loop column	Liquid circulation velocity Overall gas holdup Local liquid velocity rms velocity Local gas velocity Local gas holdup	Pulse injection-response Differential pressure Laser Doppler Anemometer Aerometric Ultra-sound Doppler Optical fibre probe
Zhang et al. (2002)	Internal loop column	Gas holdup (overall, riser, and downcomer) Liquid circulation velocity	Volume expansion and Differential pressure Pulse injection-response

Table 2-2 Continue

Baten et al. (2003)	Internal loop column	Gas holdup Liquid circulation velocity	Differential pressure Pulse injection-response
Klein et al. (2003)	Internal loop column	Gas holdup (riser and downcomer) Liquid circulation velocity	Differential pressure Magnetic tracer method
Nakao et al. (2003)	External loop column	Liquid circulation velocity	Pitot tube
Lo and Hwang, 2003	Internal loop column	Bubble dynamics (gas holdup, gas velocity, bubble size distribution)	Dual electrical resistivity probes
Wu and Merchuk, 2003	Internal loop column	Liquid circulation velocity	PIV technique

Conventionally, bulk liquid circulation velocity (Bello et al., 1984, 1985; Chisti and Moo Young, 1988; Merchuk et al., 1998b; Baten et al., 2003; Zhang et al., 2002) was measured using the typical tracer technique, in which a salt solution (or an acid solution) is introduced from the bottom of the column while conductivity probes (or pH probes for acid tracer) are mounted on the top. Thus, the bulk circulation velocity can be calculated from the peak pulses detected by the probe and the distance between the conductivity probes and the injection locations of the tracer solution. However, while Pitot tube measurements (Soderberg, 1980; Nakao et al., 2003) could disturb the flow considerably, the magnetic tracer method (Weiland and Onken, 1981; Klein et al., 2003) could not detect the turbulence flow because of the size of the tracer particles used (the particle used by Klein et al., 2003 is 11 mm in diameter).

The gas holdup measurements were conducted using the differential pressure technique for the gas holdup in the downcomer and the riser region, and the volume expansion method for the overall gas holdup. For the Reynolds shear stress, only a few studies (Contreras et al., 1999; Vial et al., 2002) tried to estimate it from purely dimensional considerations based on energy input and the total area of bubbles or the mixing length scale.

Young et al. (1991) is among the first investigators to study the local two-phase hydrodynamics in an external loop airlift column reactor. They measured the local liquid velocity by the hot-film technique (the liquid turbulence intensity thus calculated), local gas velocity by resistivity probe technique, and overall and radial gas holdup by gamma densitometry techniques. Thus the slip velocity between gas and liquid phases can be calculated.

Vial et al. (2002) investigated the global and local hydrodynamics in the riser of an external airlift column. They measured the overall gas holdup and bulk liquid circulation by conventional techniques, the bubble size distribution by photograph techniques, the local gas holdup by the optical fibre probes technique, the local gas velocity by the

ultrasound Doppler technique, and the local liquid velocity and thus rms velocities by the Laser Doppler Anemometer Aerometrics.

Lo and Hwang (2003) further investigated the bubble dynamics in an internal loop airlift column, i.e., local and overall gas holdups, local gas velocity, bubble size distribution, by using the dual electrical resistivity probe technique.

Wu and Merchuk (2003) used the PIV technique to measure the liquid flow map in the wall vicinity of the downcomer in an internal loop reactor.

Since the photobioreactor is an opaque system involved multiphase flow, most of the techniques mentioned above cannot be applied to measure the local characteristics in PBRs because of their inability to be either used in the opaque system or for multiphase flows. Therefore, due to the limited hydrodynamic information provided by traditional measurement techniques, the knowledge base for reactor design and operation of the bioreactors is insufficient, leaves much unknown and uncertainties (Chisti, 1998). Additionally, the local characteristics of the flow, e.g. the velocity profiles, the gas holdup profiles, and the radial and axial profiles of Reynolds stress, remain unclear.

## **2.6.2 CFD Modeling of Airlift Columns**

Photobioreactors (e.g., airlift reactors) are operated in the homogeneous flow regime (bubbly flow regime) where a more or less uniform bubble size and distribution are obtained (Krishna et al., 1999; Clift et al., 1978; Devanathan et al., 1995). In these reactors, the bubble-driven flow is a typical two-phase (gas and liquid) system in which the flow is driven by buoyancy. Two-phase bubbly flow is usually defined as a flow pattern in which the gas phase is distributed within a liquid continuum in discrete bubbles (dispersed phase) much smaller than the characteristic dimensions of the reactor (Pan et al., 1999, 2000; Sanyal et al., 1999; Krishna et al., 1999).



Due to the limited hydrodynamic knowledge, purely empirical and semi-empirical correlations are widely used in the literature to relate the operational and the geometrical parameters with the liquid circulation velocity, gas holdup, mass transfer rate, etc. as summarized by Chisti (1998), and Petersen and Margaritis (2001). Additionally, a large number of phenomenological models were also developed. However, no matter how their forms change, these models (Hsu and Dudukovic, 1980; Chisti et al., 1988; Merchuk et al., 1994; Merchuk and Berzin, 1995) are usually based on bulk energy balance and momentum balance equations, in which only one dimension is considered. These models usually require gas holdup correlations and empirical coefficients of the hydraulic friction losses for closure purpose and can only be used to estimate the bulk liquid circulation velocity.

Recently, Computational Fluid Dynamics (CFD) simulations have been employed to study the local characteristics (e.g., liquid velocity profiles, gas holdup profiles, shear stress profiles) of the flow in airlift reactors (Mudde and Van Den Akker, 2001). CFD becomes one of the most important techniques to study the multiphase flow dynamics in general. Based on the Navier-Stokes equations, CFD has been used to study both the mean flows, such as local gas and liquid velocities, local gas holdups (Mudde and Van Den Akker, 2001), and the dynamic features of the multiphase flow, such as Reynolds stresses, time dependent flow evolution (Pan and Dudukovic, 1999). Numerous efforts have also been attempted to track solid or gas particles within the multiphase flow domains (Anderson and Jackson, 1967; Delnoij et al., 1997a, b, c, 1999; Lain et al., 1999; Pflieger et al., 1999; Sokolichen, 2004).

Two basic approaches exist in modeling the bubble-driven flows in airlift bubble columns. Based on the volume-averaged Navier-Stokes equations, the Eulerian-Eulerian approach treats both the dispersed and the continuous phases as interpenetrating continuum and describes the motion for each of the two phases in Eulerian frame of references (Pan et al., 1999, 2000; Sokolichin and Eigenberger, 1994, 2004; Becker et al., 1994).

On the other hand, the Eulerian-Lagrangian approach treats these two phases differently. Although the continuous phase is still treated in the same way as in the Eulerian-Eulerian approach, the dispersed phase (i.e., discrete bubbles) is tracked by solving the motion equations taking into account a balance of all relevant forces as pressure, gravity, drag, lift, and added mass (Becker et al., 1994; Delnoij et al., 1997a, b, c, 1999; Lain et al., 1999; Pflieger et al., 1999; Thakre and Joshi, 1999; Jakobsen et al., 1997; Sankaranarayanan, 2000). Since a very large number of discrete bubbles have to be tracked even in the bubbly flow regime, the computational cost is usually very expensive in the Eulerian-Lagrangian approach. Moreover, it is not suitable to model churn-turbulent flows as the volume fraction of the dispersed phase is usually very high.

Therefore, the two-fluid model based on the Eulerian-Eulerian approach is more widely used in the literature to study the multiphase flow dynamics in airlift column at bubbly flow regime. However, although the Eulerian-Eulerian approach is relatively simple, further simplifying the complete set of the Navier-Stokes equations is still inevitable for practical cases due to the complexity of the multiphase flow. In these simplifications, the modeling of the multiphase turbulence and the interfacial momentum transfer are most commonly used. While these simplifications greatly reduced the computational costs, they introduced uncertainty and inaccuracy (Sokolichin et al., 2004).

For example, the standard  $k-\varepsilon$  turbulence model, the most often used and extensively studied turbulence model in the literature, is well-known to over-estimate the eddy viscosities that damps out small scale turbulence (Borchers et al., 1999). Although modifications of the  $k-\varepsilon$  model (e.g., RNG model) and alternative turbulence models (e.g., the Reynolds shear stress model, large eddy simulations) have been reported in the literature, their applications have been limited in specific cases.

Similarly, most correlations proposed in the literature to model the interfacial momentum forces (i.e., drag force, lift force, turbulent dispersion force, added mass force, etc.) can

only be applied in certain conditions. For instance, the widely used Schiller-Naumann correlation (1935) for the drag force between the gas and the liquid phases was developed from single bubble circumstance, thus, theoretically cannot be applied to high bubble density flow fields. On the other hand, model parameters for most correlations vary case by case. Jacobsen (1997) pointed out cases with either positive or negative values and cases with order of magnitude difference for the Saffman lift force coefficient. Therefore, systematical verification of these models and closures against experimental measurements, especially against rich information obtained from newly developed measurement techniques, is vital for the application of CFD in reactor design and scale-ups.

Moreover, a balance between the computational cost and the simulation accuracy is also required for any practical applications of the CFD simulation. Such balance is especially important in particle trajectory predictions, which is required for photobioreactor analysis as mentioned earlier. Due to the chaotic nature of the flow dynamics, a 3D transient simulation using Euler-Lagrangian approach is required to track a particle's movement in a multiphase flow field (Delnoij et al., 1997a, b, c, 1999; Lain et al., 1999; Pflieger et al., 1999). However, this approach could be extremely time-consuming even for engineering accuracy predictions (Sokolichin et al., 1994).

To cut the computational cost, Rammohan (2002) adopted an Euler/Pseudo-Lagrangian approach to track a neutrally buoyancy particle in a stirred tank. Based on a commercial CFD code, Fluent, he first used a Euler/Euler approach to generate the Euler flow field, and then introduced a single particle into the simulated flow field by which the particle motion (trajectory) within the domain is numerically simulated. Good agreements between the simulation and CARPT measured particle trajectories have been found. However, more verification is needed since his simulations are based on 2-D cases.

In summary, it can be concluded that further validation of the CFD modeling and identification of appropriate closures guided by experimental data obtained from the

advanced hydrodynamic measurement techniques, such as CARPT and CT, are required to apply CFD simulation in any meaningful flow dynamic studies. Combined, the advanced measurement and computational techniques could provide intrinsic information for photobioreactor analysis and form the knowledge base for reactor design and scale-up for any other applications of airlift column reactors at much lower costs.

## **2.7 Summary**

In this Chapter, the background knowledge of photosynthesis has been introduced and literature reviews have been carried out focusing on the flashing light effects, modeling work on photosynthesis, enclosed photobioreactor design, and hydrodynamic investigations for airlift column reactors. It is clear from the reviews that in-depth knowledge of hydrodynamics is required to study the flashing light effects in a real PBR, to develop reliable models for PBR performance evaluation using the dynamic photosynthetic rate model, and to design and scale-up large scale PBRs. Such in-depth knowledge has to be obtained from advanced hydrodynamic measurement techniques or from state-of-the-art computational techniques after having been verified against experimental data. The feasibility of applying the CARPT technique on PBR analysis will be discussed in the next Chapter.

## **Chapter 3**

# **Feasibility of Using CARPT Technique for Photobioreactor Analysis**

### **3.1 Scope**

Understanding the local flow dynamics is a prerequisite for photobioreactor analysis. However, since photobioreactors are opaque systems involving multiphase flows, most conventional hydrodynamic measurement techniques cannot be applied in PBR analysis. We thus proposed to use an advanced non-invasive hydrodynamic measurement technique which can be applied to opaque systems, i.e., Computer Automated Radioactive Particle Tracking (CARPT). In this Chapter, its feasibility to characterize photobioreactors is evaluated utilizing available CARPT data for three types of airlift column reactors. Liquid velocity profiles, cells' movement, and the temporal irradiance patterns (i.e., the time series of irradiance that the cells may experienced) are determined. The effects of the biomass concentration, reactor geometry, and the aeration rate on the irradiance patterns are discussed. The results demonstrate that the CARPT technique is promising for PBR analysis. It provides fundamental information needed to advance the cells' growth prediction and modeling, and the design, scale-up and operation of PBRs.

## 3.2 CARPT Technique

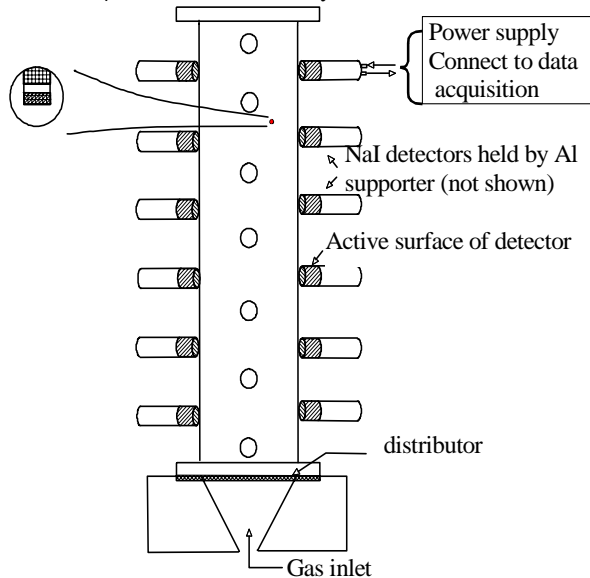
In principle, CARPT technique measures the flow field by tracking a small radioactive particle that is made specifically to follow the interested phase in the reactors. The thus yielded 3D Lagrangian particle trajectories provide intrinsic methods for classical residence time distribution analyses, and rich information about the time averaged velocity flow fields, the fluctuating velocities, mixing intensities, turbulence, etc. Since CARPT technique has been well documented and reported in literature (Kumar et al., 1994; Roy et al, 2002), a short introduction is presented here and some more details of the setup is discussed in Chapter 5.

### 3.2.1 CARPT Setup

CARPT setup consists of a radioactive tracer particle, a number of radiation detectors, a data acquisition system, and a calibration device as shown in Figure 3-1. Usually, the radioactive particle is a composite made by inserting a certain mass of SC-46 (which emits  $\gamma$ -rays with an activity of 50-500  $\mu\text{Ci}$ ) into a hollow polypropylene particle of diameter 0.8 mm to 2.3mm. In order to have the particle precisely follow the motion of the liquid phase or a liquid element in the reactor, it was treated by hydrophilic paint to have a fully wetted surface, and its density was adjusted to be neutrally buoyant, i.e., its density is as close as possible to the density of the liquid phase. Such adjustment is done by introducing additional non-radioactive material into the internal void of the hollow polypropylene particle (more details of making the particle is presented in Chapter 5). In addition, when mapping solid flow characteristics in systems such as gas-liquid-solid, liquid-solid, and gas-solid systems is required, a radioactive particle of the same density, size (the diameter can be as low as 100~150  $\mu\text{m}$ ), and shape as the solids phase can also be used.

**Radioactive Scandium**

- (Sc 46, 250 $\mu$ Ci, emitting  $\gamma$  rays)
- embedded in 0.8~2.3 mm polypropylene particle (neutrally buoyant with liquid)
  - 100~150 $\mu$ m for solids in a slurry bubble column



**Bubble column, slurry bubble column, etc.**

**Data Processing of Radiation Intensity Received by N Detectors from a Single Radioactive Sc-46 Particle**

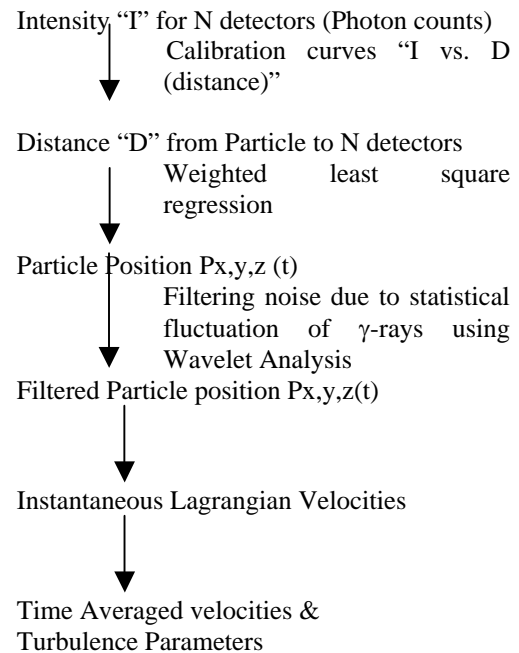


**Figure 3-1.** Schematic Diagram of the CARPT Facility at the Chemical Reaction Engineering Laboratory (CREL)-Washington University (WU)

The  $\gamma$ -ray radiation intensity emitted by the tracer particle is recorded by a set (16-32) of sodium iodide (NaI) detectors strategically mounted around the reactor as shown in Figure 3-1. These detectors register the radiation intensity at a sampling frequency up to 500 Hz, and transfer the signals to a data acquisition system. The data acquisition system, then, amplifies the signals and transfers them to a PC, where the signals are converted to digital information and stored for particle position reconstructions.

In order to properly reconstruct the particle's positions from recorded radiation intensities, calibration needs to be performed prior to the real particle tracking experiment. During calibrations, a calibration device is used to place the radioactive particle at many known locations (~500-3000 known positions depending on the reactor size) in the reactor for a

certain time (e.g., few seconds), while the reactor is operated at the same conditions that need to be studied. The distance from a detector to the radioactive particle thus can be calculated under such circumstance, and be directly related to the radiation intensities recorded by the detectors. Plotting the time-averaged (thus free of white noise) radiation intensities versus the distances forms the so-called calibration curve for each detector, which provides the basis to reconstruct the tracer particle's instantaneous positions.

### **3.2.2. CARPT Data Processing Procedure**

The data processing procedure is also shown in Figure 3-1. In a real particle tracking experiment, the radioactive particle is introduced into the reactor to freely follow the interested phase with the radiation intensity recorded by the detectors. Generally, during the particle position reconstructions, the distances of the tracer particle to all detectors are calculated from the recorded radiation intensity based on the calibration curve. The exact particle position at a given sampling instant thus can be evaluated by weighted regressions since all detectors' locations are known. Thereby, a sequence of instantaneous position data is obtained that yields the position of the particle at successive sampling instants (i.e., its trajectory). Due to the white noises introduced by the quantized nature of  $\gamma$ -ray and from the electronic transmission processes, such raw instantaneous position data needs to be filtered using a wavelet filtering method to get rid of these noises (Degaleesan et al., 2002).

The filtered Lagrangian particle trajectory is a nature source for a true Residence Time Distribution (RTD) analysis, and will be further processed to obtain the local liquid flow characteristics. To capture the local flow structures, the reactor is first divided into many compartments in a 3-D domain. Then, time differentiation the particle trajectory data (i.e., assuming the particle trajectory is a straight line between two successive particle locations in the interval of the sampling time) yields the particle instantaneous velocities, which are assigned to the compartments the particle traveled through between two successive locations. Next, ensemble averaging of the velocities for each compartment yields the time averaged velocities, by which the spatial liquid flow field for the whole column is



achieved. Further subtraction the instantaneous velocities from the time-averaged velocities yields the fluctuating velocities for each compartment. The cross correlations of the fluctuating velocities thus are calculated representing various turbulent parameters (turbulent kinetic energies, Reynolds stresses, etc.). Finally, the turbulent eddy diffusivities in the fully developed flow region are calculated through a procedure proposed by Degaleesan (1997). The hardware and software developed for the CARPT technique and its data processing are described elsewhere (Degaleesan, 1997; Roy, et al., 2002).

The accuracy of determining the fluid element velocity using the particle tracking technique depends in part on the ability of the tracer particle to follow the liquid element. Close matching of the density of the particle with that of the liquid ensures that the particle is neutrally buoyant. However, the finite size of the particle makes it differ from a liquid element and unable to sample small scale eddies. Degaleesan (1997) showed that for a particle of size 2.36 mm, and a difference of  $0.01 \text{ gm/cm}^3$  in density between the particle and the liquid, the maximum difference in the velocity (between particle and liquid) is 1 cm/s. Degaleesan (1997) estimated that the frequency at which the measured velocity of a 2.36 mm particle is follow up to 99% of the liquid velocity is 30 Hz and hence she suggested that 50 Hz sampling frequency is sufficient for bubble columns. She also showed that for frequency lower than 30 Hz, which represent the large scale eddies, the particle will be able to closely follow the liquid phase, and the measured particle fluctuating velocities can be considered to be those of the liquid phase. Small scale eddies cannot be followed by such particle. However, smaller radioactive particle ( $<2.36 \text{ mm}$ ) enhances the accuracy of its ability to follow fluid elements and eddies with 50 Hz or higher frequencies.

### **3.3 CARPT Experiments**

Available CARPT experiment results in our laboratory were used to test the feasibility of utilizing CARPT technique for photobioreactor analysis (a more comprehensive study

using both CARPT and CT techniques is presented in Chapter 5). These CARPT experiments were carried out in two airlift photobioreactors, a draft tube and a split column with outer cylinder diameter of 20 cm, to characterize their liquid flow pattern, the cells' movements, and the irradiance pattern. The configurations of the draft tube and the split columns, with their dimensions, are shown in Figure 3-2. In the draft tube bioreactor, an internal column was mounted coaxial to the primary cylinder, with bottom clearance of 1 cm. In the split column, a plate was inserted in the center of the column, separating the column into identical cross-sectional areas: a riser zone and a downcomer zone with bottom clearance of 2.3 cm, designed to match the bottom clearance area of the draft tube bioreactor (i.e., the flow area between the riser and the downcomer).

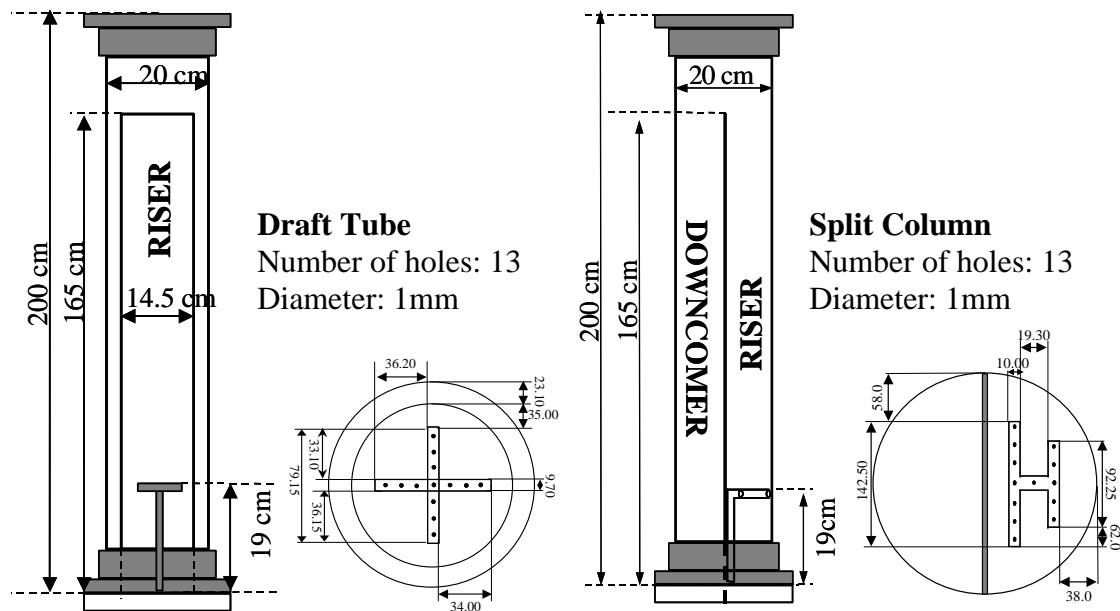


**Figure 3-2.** Configuration of draft tube and split airlift bioreactor

Different type of spargers, as shown in Figure 3-2, were used to generate rather uniform gas holdup in the aeration zone: a cross sparger was used in the draft tube column, while an 'H' type of sparger was used in the split column. Both spargers have 13 upward facing

holes of 1 mm diameter, and they were installed 19 cm above the base in the center of the corresponding aeration zone. In the CARPT experiments, air was bubbled through the sparger into a batch of tap water at ambient conditions at superficial gas velocities ( $U_g$ ) of 1 cm/s and 5 cm/s to mimic the typical conditions for microalgae and cyanobacteria cultivation processes. The static liquid level in the draft tube and split columns is 165 cm, corresponding to the top of the baffle in both bioreactors.

A neutrally buoyant radioactive particle with a diameter of 2.3 mm and a sampling frequency of 50 Hz were used to study the liquid flow fields in the airlift column reactors (the CARPT experiments presented in Chapter 5 use a 0.8mm particle and a 100 Hz sampling frequency). Since the microalgae cells are very small and their density is close to water, the cells can be assumed to closely follow the liquid flow. Hence, the tracer particle can also be assumed to mimic the cells' movements. Calibration was performed a priori for 672 known locations, which were selected to represent all the regions in the whole column. Each experiment was run for 24 hours to assure that the number of the tracer particle visits (occurrences) to each reactor compartment was statistically sufficient to confirm that the time averaged liquid velocity had reached plateau. It was found that 50 visits should be enough; however, in these experiments, the number of the particle visits (occurrences) in most compartments was more than 150.

In addition to the above mentioned CARPT experiments, CARPT results for a bubble column of diameter 20 cm based on the same setup and a similar tracer particle are also available in our laboratory. The operating conditions for these results are: superficial gas velocity of 5 cm/s, static liquid level of 115 cm, and a perforated plate sparger with open area of 0.1% and hole diameter of 0.33 mm. This particular set of CARPT data has also been processed to compare the evaluated irradiance patterns in airlift reactors with those obtained in bubble columns without internals at the same operating conditions.

## 3.4 Results and Discussion

### 3.4.1 Liquid Flow Field

Instantaneous velocity of the tracer particle is calculated by time-differentiating the successive particle location data obtained from CARPT experiments. To show the overview of the time averaged flow field, the liquid velocities were time- and ensemble-averaged. The resulting velocity vectors for the draft tube and the split column at  $U_g = 5$  cm/s are visualized in Figure 3-3. For the draft tube column, the time-averaged velocity vectors either were azimuthally averaged and shown in the r-z plane, or were axially averaged according to the developed flow zone and shown in the cross-sectional plane. For the split column, due to the asymmetric nature of the geometry and the fluid pattern, two planes in r-z plane were selected to show the velocity vectors in different flow zones: a plane ‘along’ the split plate (there is small angle between them) and a plane ‘perpendicular’ to the split plate as illustrated in Figure 3-3. In the cross-sectional plane, the velocity vectors were axially averaged corresponding to the developed zone as treated in the draft tube column.

The visualization of the flow field clearly shows how liquid circulates between the riser and the downcomer, and how liquid elements move in the radial direction. As can be seen, in the cross-sectional plane of the split column, four small eddy vortices are present in the riser and in the downcomer, indicating a possible spiral movement of the liquid elements, which is not observed in the draft tube column. Such flow patterns will certainly affect the growth of the cell as the cells circulate from the illuminated surface to the dark center, and experiencing the so-called light/dark cycle. The time scale for this fluctuation, called type II, is observed to be in order of 1 second. The length scale for the spiral movement in the radial direction is 10 cm (half of the column diameter). It is noteworthy here that, since the vortices are observed in the time-averaged vector plot, the liquid elements may not always follow the spiral movement.

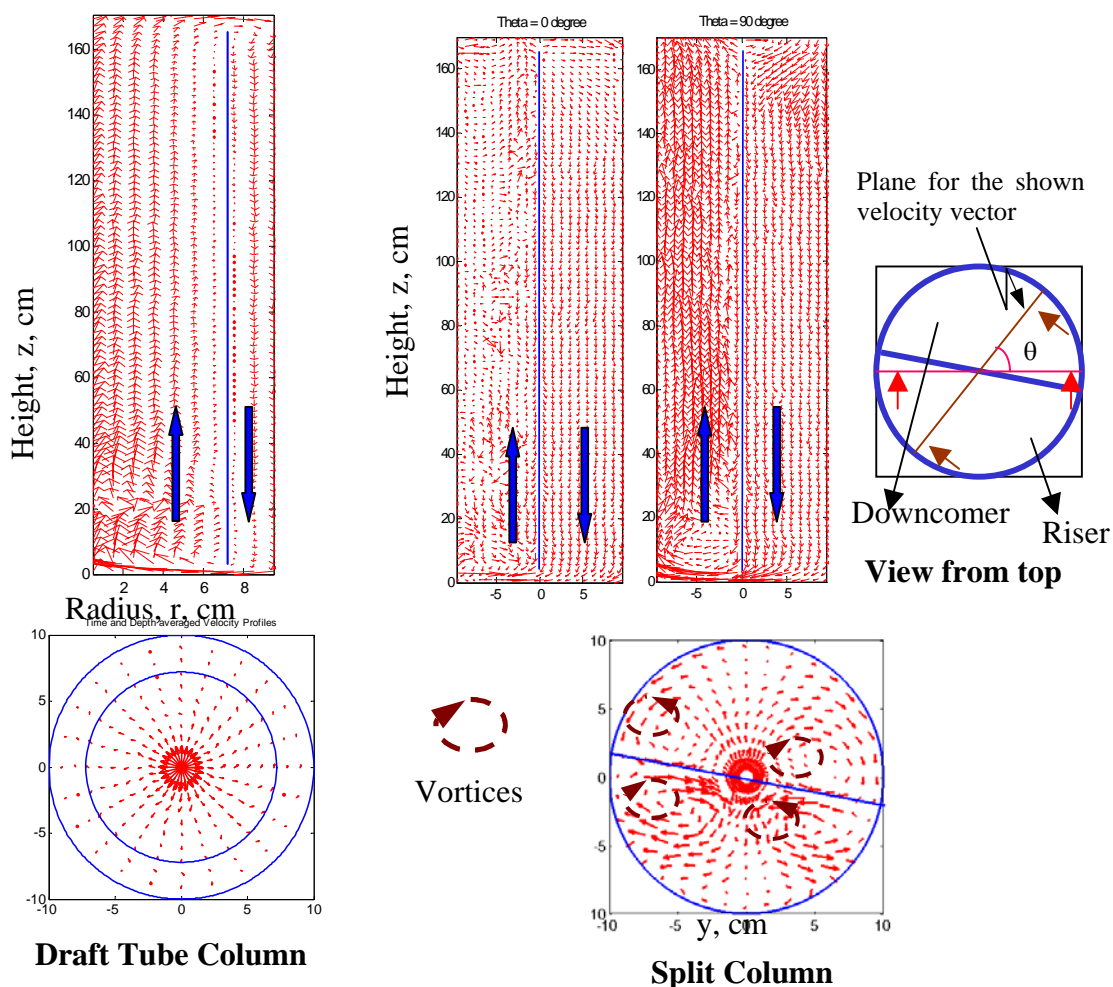


**Figure 3-3.** Visualization of the liquid flow field for draft tube column and split column at  $U_g = 5$  cm/s. The time-averaged velocity vectors have been further axially averaged according to the developed flow zone and shown in the cross-sectional plane for both reactors, while only for the draft tube column, the velocity vectors have been azimuthally averaged and shown in the  $r$ - $z$  plane. Please see the text for details. Also note the arrows present the liquid flow directions, and the blue lines represent the walls and internals (i.e. the draft tube or split wall).

### 3.4.2 Cell Movements

Figure 3-4 shows typical Lagrangian trajectories that represent the particle's movement for a single circulation in the reactor obtained from the CARPT experiments at a superficial gas velocity of 1 cm/s in both the draft tube and the split columns. As mentioned above, the

particle trajectories approximate the cells' movement. Since the particle movement has been measured for a long time (24 hours) that the particle visits any part of the reactor for many times, it is reasonable to assume that the obtained particle trajectories represent the movement of all the cells in the reactor. These are the basic information for further analysis of the flow pattern and hydrodynamics parameters.

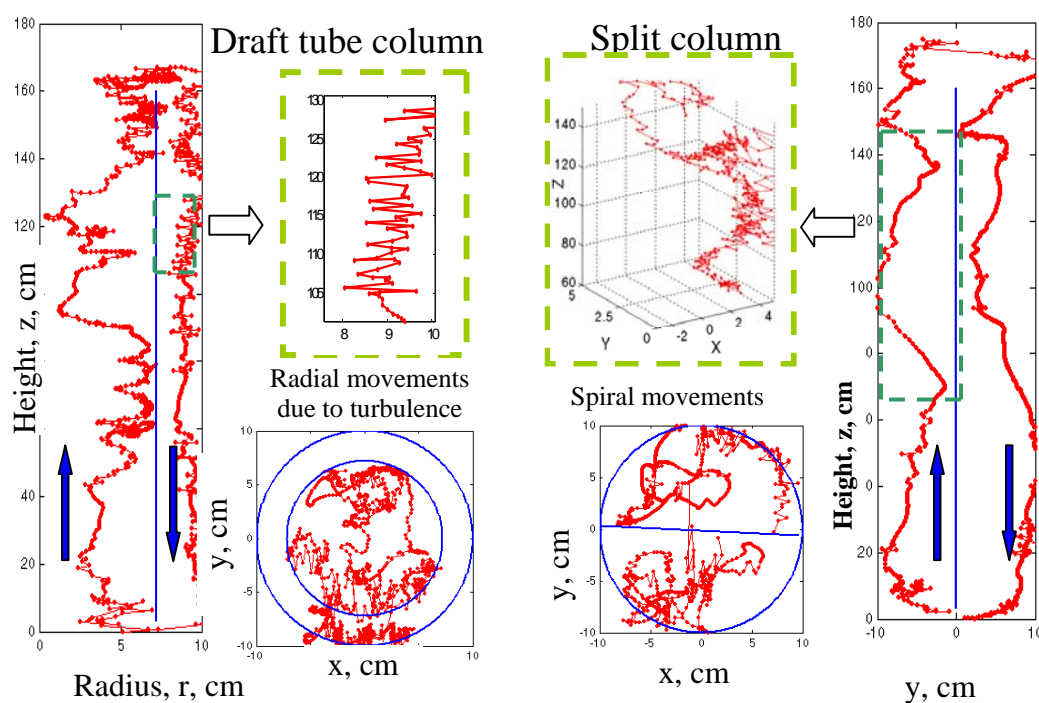


**Figure 3-4.** Typical particle trajectories in the draft tube and the split columns. Only one recirculation is shown for each reactor, while both the front and the top view of the trajectories are shown respectively in the  $r$ - $z$  plane and the cross-sectional plane. Please note the blue lines represent the walls and internals, i.e. draft tube and split wall.  $U_g=1\text{cm/s}$ .

As expected, the trajectories demonstrate the circulation of the cells between the riser and the downcomer over a time scale of 20 seconds and length scale of 20 cm (diameter of the reactor). In the draft tube column, where the riser is dark but the downcomer is illuminated,

this circulation again causes light fluctuation, called type I. Moreover, the trajectories also demonstrate a turbulence-induced radial fluctuation whose time scale is about 0.1 seconds (or even less, please note the sampling frequency is 50Hz) and length scale is 1cm as shown in Figure 3-4 (a more detailed analysis about the time scales for the radial fluctuations is presented in Chapter 4). In the dark center where the light intensity is very low and the gradient is also flat, this radial movement does not cause much light fluctuation experienced by a cell as it follows the trajectory. However, in the illuminated zone where the light intensity gradient is steep, the radial movements do introduce high light fluctuation experienced by the cells, called type III. As can be seen from Figure 3-4, more radial fluctuations are present in the draft tube column than in the split column. These results clearly demonstrate that the light fluctuations that a cell may experience consist of a spectrum of fluctuations with different time scales.

Using the ordered circulation between the riser and the downcomer in the airlift columns as basic units, the simulated cells' movement can be further analyzed statistically and quantitatively. A single trajectory is defined as one such circulation of the particle in the reactor, i.e. it starts from a given plane in the lower part of the draft tube and returns to this plane after it has traveled through the riser and the downcomer. For each CARPT experiment, more than 2000 trajectories were identified. The circulation time distribution and the trajectory length distribution for the two airlift columns at  $U_g = 5$  cm/s, as well as the average quantity and the dimensionless variance ( $\sigma$ ), are shown in Figure 3-5. As can be seen, the split column has a faster circulation and narrower distributions than the draft tube column, indicating that its flow characteristic is closer to plug flow (i.e., less macro-mixing).

This behavior can be further proved by Trajectory Length Distribution (TLD) analysis, proposed by Villermaux (1996). The macromixing index,  $M$ , to characterize the liquid mixing and the fluctuation, is defined as (Villermaux, 1996):

$$M = \frac{\langle l \rangle}{L} \quad (3-1)$$

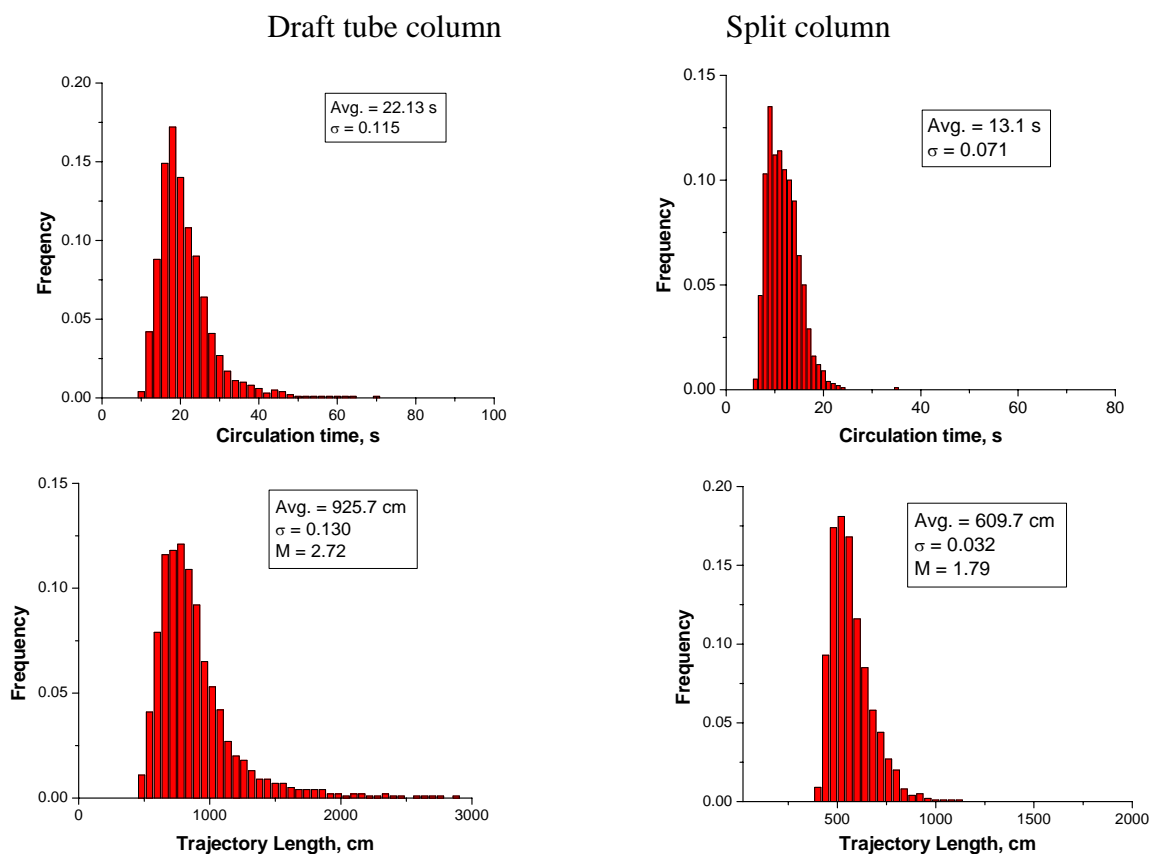


**Figure 3-5.** Circulation time distribution and single trajectory length distribution at superficial gas velocity of 5 cm/s.

where  $\langle l \rangle$  is the average single trajectory length and  $L$  is the characteristic length of the reactor (here it is two times the reactor height, due to the recirculation). A large  $M$  corresponds to very efficient macromixing, as fluid elements cover long distances with respect to the vessel size, indicating more radial variance or faster light fluctuation in PBRs. For example, in the case of perfect mixing,  $M \rightarrow \infty$ , while in the case of plug flow there is no macromixing at all and thus  $M = 1$ .

The calculated  $M$  for the two airlift columns at  $U_g$  of 5 cm/s is also shown in Figure 3-5. Again, a smaller  $M$  for the split column than for the draft tube column confirmed that its



flow characteristic is closer to plug flow with less radial fluctuation, which meets the observation from the particle trajectories in Figure 3-4. It is noteworthy that, although the statistical analysis is based on the cells' movement, it can be easily extended to analyze other variables. For example, when applied to the temporal light pattern, it can characterize the quantity and the quality of the light exposed to the cells.

### 3.4.3 Temporal Light Patterns

One significant advantage of using CARPT for PBR analysis is the coupling of the CARPT-obtained trajectories, which represent the cells' movement,  $f(x,y,z,t)$ , with a suitable irradiance distribution model, which provides light intensity distribution in the reactors,  $I(x,y,z)$ . The yielded temporal irradiance pattern,  $I(t)$ , represents the history of the light intensity experienced by a cell following the tracer particle trajectory. This coupling allows us to evaluate, for the first time, both the quantity and the quality of the light delivered to the cells grown in PBRs. We can analyze the total photon flux, the magnitude of the changes in irradiance, the frequencies and duration of dark periods, and the influences of reactor geometry and the operating conditions. Such information is critical for successful performance prediction and modeling, design, scale-up and operation of PBRs.

To calculate irradiance field,  $I(x,y,z)$ , Molina Grima et al. (1997) proposed a model which allows the calculation under much more complicated and realistic conditions. However, this model is quite complicated and computationally expensive. Therefore, Fernandez Sevilla (Luo et al., 2003) used the irradiance distribution model proposed by Acien, et al. (1997) to calculate the temporal irradiance pattern. For the sake of simplicity, the external irradiance ( $I_0$ ) was assumed to be  $1000 \mu\text{Em}^{-2}\text{s}^{-1}$  evenly distributed along the illuminated reactor outer surface, which gives radial symmetry. A constant extinction coefficient,  $K_a$  of  $0.05 \text{ m}^2/\text{g}$ , was also assumed. Figure 3-6 shows the calculated temporal irradiance patterns for a period of about 80 seconds for all the three studied PBRs at different biomass concentrations.

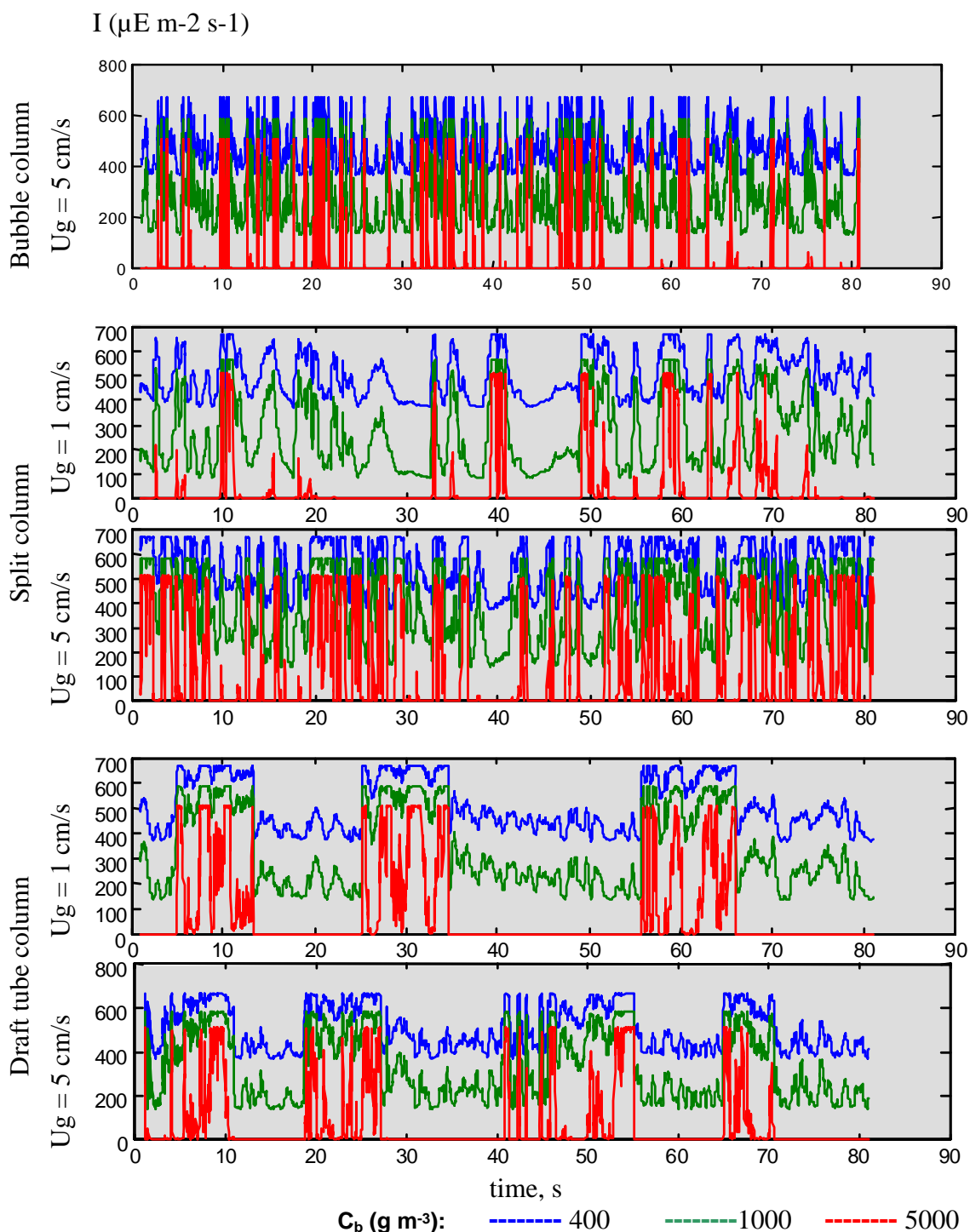


**Figure 3-6.** Typical temporal irradiance pattern for the three PBRs at different biomass concentrations at different superficial gas velocities. Calculated by combing CARPT-obtained trajectories and the irradiance distribution model proposed by Acien, et al., 1997.  $Ka = 0.05 \text{ m}^2/\text{g}$  (Luo et al., 2003)

As mentioned above, the cells experience three types of light fluctuations in the PBRs at different time scales. Type I is in the order of 10 seconds due to the circulation between the riser and the downcomer. Type II is in the order of 1 second due to the spiral movements. And type III is in the order of 0.1 second due to turbulence. In general, the temporal irradiance pattern is influenced by biomass concentration (or the resulting optical thickness), reactor geometry, and aeration rate. These variables either affect the total photon flux or affect any of the three types of light fluctuations.

The biomass concentration ( $C_b$ ) significantly affects the quantity of the photon flux and the magnitude of the fluctuations the cells experienced. For any type of reactor, it is clear from Figure 3-6 that the total photon flux decreases considerably as the biomass concentration increases, while the magnitude of the light fluctuation increases greatly. For example, whereas the calculated irradiance ( $I$ ) varies up to six times ( $100\sim 600 \mu\text{Em}^{-2}\text{s}^{-1}$ ) at  $C_b=1000 \text{ g m}^{-3}$ , the light exposure becomes an alternation of dark/light periods in the case of a more realistic biomass concentration,  $5000 \text{ g/m}^3$ .

The reactor geometry determines the flow field that in turn determines the cells' movement and hence the light fluctuations they experienced. Its influence on the irradiance pattern can be observed partly in Figure 3-6; however, further analysis to quantify such effects is needed. In Figure 3-6 for the bubble column, the fluctuation of type III is prominent, but the other two types of fluctuation are difficult or impossible to be observed. While rapid irradiance changes are an advantage, the drawback of the bubble column system is that it cannot guarantee that all the cells receive frequent exposure. Unlike airlift columns, there is a lack of ordered circulation.

In the split column, as mentioned above, the fluctuation of type II and III should present; however only type III is obvious from Figure 3-6. The fluctuation of type II is unobserved because the spiral movement, as shown in the time-averaged velocity vector plot in Figure 3-3, is rather a long time phenomenon that may not be obvious at each transient time window.

As for the draft tube column, both fluctuations of type III and I are obvious from Figure 3-6. It shows an ordered characteristic exposition pattern in which a fast alternation of light and darkness is followed by a long dark period. The long dark period may impair cell growth, but it is noteworthy that the time for this dark period can be adjusted by changing the relative area of the riser to the downcomer.

The time irradiance patterns in Figure 3-6 also show the effects of the aeration rate. Aeration is essential in pneumatic reactors as it provides metabolite removal (oxygen), CO<sub>2</sub> transport, and agitation, which is especially indispensable in optically dense cultures. It is clear from Figure 3-6 that, for any type of reactor, a higher aeration rate results in faster light fluctuation, indicating the promotion of mixing and turbulence. However, a higher aeration rate causes higher shear rates that could damage the cells.

From the above discussions, it is obvious that the irradiance pattern yield by combining the CARPT obtained Lagrangian trajectory with the irradiance model can be used to assess the effects of the operational conditions and reactor design parameters on the irradiance pattern of PBRs. However, to further analyze the effects of such irradiance patterns and their light fluctuation frequencies on bioreactor performance, one needs to quantify their effects on the mechanism of photoinhibition and photolimitation experienced in PBRs. Hence, further quantitative analysis that integrates irradiance pattern knowledge with proper photosynthesis models is needed to quantitatively characterize the cells' growth in PBRs.

### **3.5 Summary**

In this Chapter, the feasibility of utilizing CARPT technique for photobioreactor analysis is explored. The CARPT technique has been employed to determine the liquid flow field, liquid velocity profiles, cells' movements, and the temporal irradiance patterns, which was obtained by integrating the cells' trajectories and an irradiance distribution model. The

effects of biomass concentration, reactor geometry, and the aeration rate on the irradiance patterns are illustrated.

The results indicate that the CARPT technique is a very promising technique for the PBR analysis. It provides fundamental information needed to advance cells' growth rate predictions for PBR modeling, design, scale-up and operations. For the first time, CARPT results allow us to investigate the effect of the studied parameters on the irradiance patterns—the controlling step of biomass productivity—both quantitatively and qualitatively, which will be discussed in the next Chapter.

## **Chapter 4**

# **Integrating Reactor Hydrodynamics with Photosynthesis to Characterize Flashing light Effects and to Evaluate PBR Performance**

### **4.1 Scope**

As discussed earlier, one of the major effects of reactor hydrodynamics on a PBR's performance, especially on a nicely controlled enclosed PBR (e.g., free of nutrient shortage, optimized temperature and pH levels), is by affecting the light fluctuations delivered to the microorganism cells and thus the photosynthetic efficiency. Therefore, it is critical to understand how reactor hydrodynamics interact with photosynthesis, quantify the induced flashing light effects, and moreover, integrate the flow dynamics with photosynthesis for reactor performance evaluation, design and scale-up.

In this Chapter, based on the hydrodynamic findings from Chapter 3, a possible mechanism for the interaction between the mixing and the physiology of photosynthesis is presented.

The effects of reactor flow dynamics on light availability and light intensity fluctuations are discussed. Parameters are also suggested to quantitatively characterize the flashing light effects. Furthermore, a dynamic modeling approach is developed for photobioreactor performance evaluation, which integrates first principles of photosynthesis, hydrodynamics, and irradiance distribution within the reactor. The results demonstrate the reliability and the possible applicability of this approach to commercially interesting microalgae/cyanobacteria culture systems. Further verifications of this model are presented in the followed chapters.

## 4.2 Temporal irradiance pattern

The temporal irradiance patterns, representing the history of the light intensity experienced by a cell in the reactor, provide first hand data to understand the interactions between hydrodynamics and photosynthesis. In this Chapter, the temporal irradiance patterns are calculated by integrating the CARPT data used in Chapter 3 with an irradiance distribution model.

For simplicity and for demonstration purpose, the Lambert-Beer Law for a single light ray, which is suitable for a collimated irradiance model but is not for a diffuse or semi-diffuse model (Evers, 1991), is used to represent the light intensity distribution within the reactors (Wu and Merchuk, 2001):

$$I = I_E \cdot \exp[-(k_x \cdot x + k_w) \cdot d] \quad (4-1)$$

where  $I_E$  is the external irradiance on the illuminated photobioreactor surface;  $d$  is the radial distance from the cell to that surface;  $k_w$  and  $k_x$  are extinction coefficients taking into account of the reactor wall attenuation and the cellular absorptions, respectively; and  $x$  is any measure of the cells' concentration (e.g., the cell number, the optical density, dry biomass weight, etc.). This model assumes that the external light intensity is uniform along the illuminated reactor surface, and the photons travel towards the reactor center with high attenuation due to the cellular absorption. The light propagation is thus one-dimensional (Experimental verification of this model is presented in Chapter 7)

The calculated temporal irradiance patterns for the studied airlift bubble columns (i.e., the draft tube, the split, and the bubble columns) are shown in Figure 4-1. These patterns were calculated under conditions of  $2000 \mu E m^{-2} s^{-1}$  external irradiance and  $80 \times 10^6$  cells/ml cell concentration (typical industrial interested conditions with high biomass concentration and high external light intensity). All the characterizations and discussions presented later in this chapter are based on these calculated irradiance patterns.



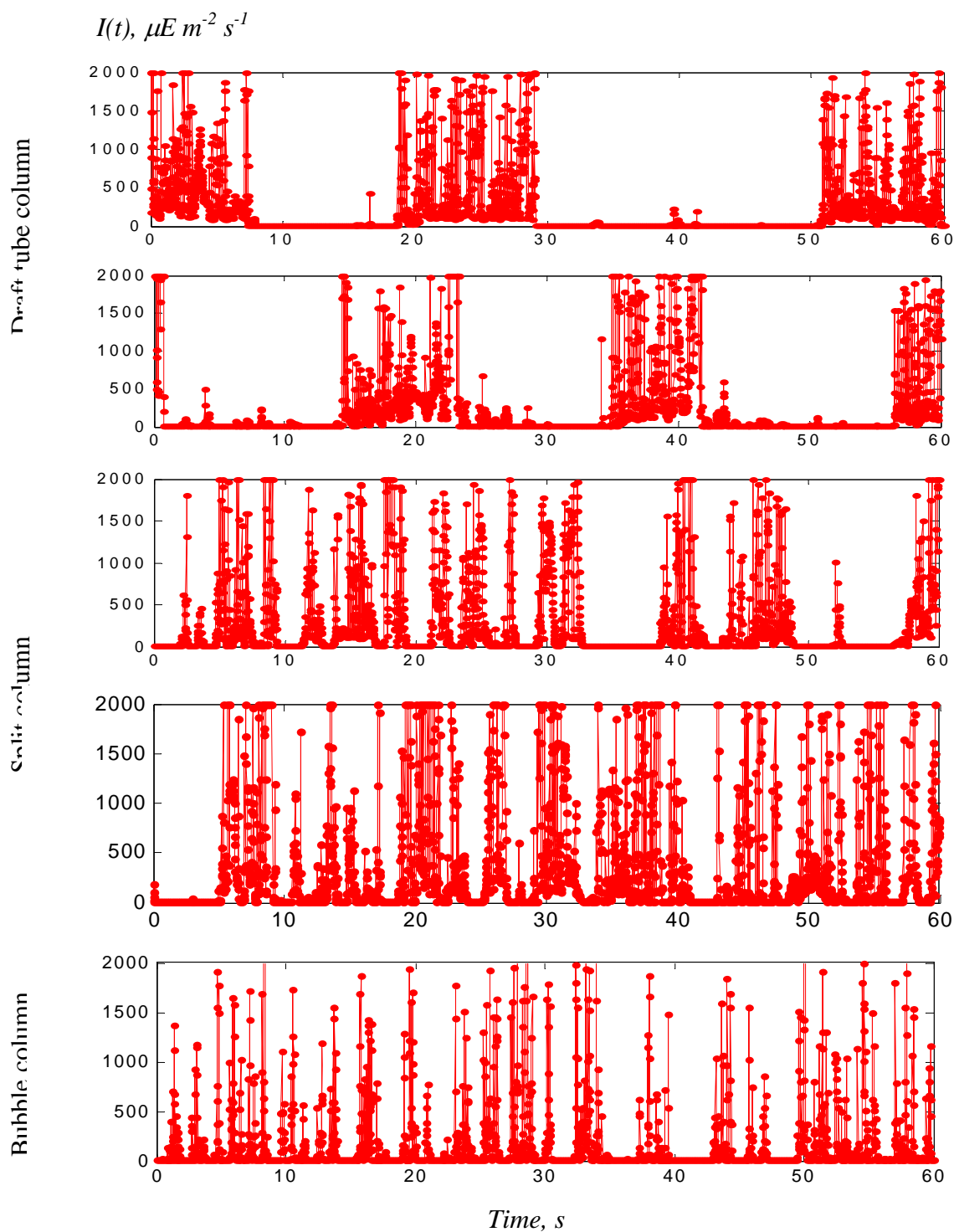


**Figure 4-1.** Time series of irradiance a cell experienced in the bioreactors. Calculated by Equation (4-1). External irradiance:  $2000 \mu E m^{-2} s^{-1}$ , Cell concentration:  $80 \times 10^6$  cells/ml.

### **4.3 Interactions between Hydrodynamics and Photosynthesis**

In Chapter 3, three types of liquid phase mixing mechanisms were found coexist in the studied airlift columns. They are: bulk circulation with time scale of 10 seconds, spiral movement with time scale of seconds, and radial fluctuation due to turbulence with time scale of 10 milliseconds (the sampling frequency of the CARPT data used is 50Hz or a time span of 20ms). Apparently, these types of mixings are the sources of the light fluctuations delivered to the cells as they travel inside the reactor following the liquid elements. Hence, the time scales associated with the induced light fluctuation experienced by the cells are not only in seconds, as reported by some researchers (Lee and Pirt, 1981), but also in 10 ms, which overlap with the range of time scales associated with the photosynthesis processes (Falkowski and Raven, 1997).

This is clearer from the temporal irradiance patterns shown in Figure 4-1. These patterns consisted of a cascade of light fluctuations with different frequencies due to the chaotic nature of flow dynamics. The patterns are dominated by the fast turbulence-induced fluctuations with a time scale of 10 ms. Since the time scale for the carbon fixation in photosynthesis is also 10 ms, a prompt relaxation of the reaction centers in the microorganisms from over-reduction is possible when a cell moves away from the highly illuminated surface. Such relaxation could considerably improve the photosynthesis efficiency.

In fact, for a cell shifting between the highly illuminated and the dark zones, the overall photosynthetic quantum yield and the photosynthesis rate depend on the residence times in each zone. If the cell can move to the dark center from the highly illuminated zone before all reaction centers are reduced, it is possible to keep the quantum yield and, therefore, the light energy efficiency remains at a high level. Moreover, this shifting can also greatly reduce the photoinhibition effect: the prompt “relaxation” prevents some proteins (responsible for the photoinhibition) from becoming over-oxidized. Such relaxation is very important for commercial mass microalgae cultures, where strong

external irradiance and high cell concentration are used. Based on such information, we can analyze the interaction between the mixing and the photosynthesis and characterize the light fluctuations experienced by the cells in the reactor.

## 4.4 Characterization of Photobioreactors in Terms of Light Fluctuations

To investigate the flashing light effects on microorganism cells' growth, many researchers have simply utilized a light on/off pattern, the so-called light/dark cycle as shown in Figure 4-2A. This pattern mimics the light fluctuation experienced by cells in photobioreactors as if the cells grow in a thin and sparse culturing system (Terry, 1986; Nedbal, et al., 1996; Jansson, et al., 2000, 2001; Wu and Merchuk, 2001).

Terry (1986) proposed three parameters to characterize this well-defined light/dark cycle: incident light intensity ( $I_E$ ), fluctuation frequency ( $f$ ), and fraction of the light time in a cycle (also called dimensionless relaxation time,  $\varphi$ ). The fluctuation frequency and the dimensionless relaxation time are defined as:

$$f = 1/(t_d + t_l); \quad \varphi = t_l / (t_l + t_d) \quad (4-2)$$

where  $t_l$  is the time when the light is on, and  $t_d$  is the time when the light is off in one cycle. Using these parameters, the square wave signals or the light intensity fluctuations on the cells are clearly and completely defined. In his experiments, Terry found that the photosynthetic rate is not just a function of the incident irradiance but also a function of the light fluctuations. Moreover, he found that the photosynthetic efficiency is a parabolic function of the flashing light frequency.

However, as shown in Figure 4-1, it's hard to find such well-defined light/dark cycles in the chaotic temporal irradiance patterns. Therefore, to characterize the irradiance pattern

in real reactors, the principles of how mixing affects the photosynthesis rate should be applied.

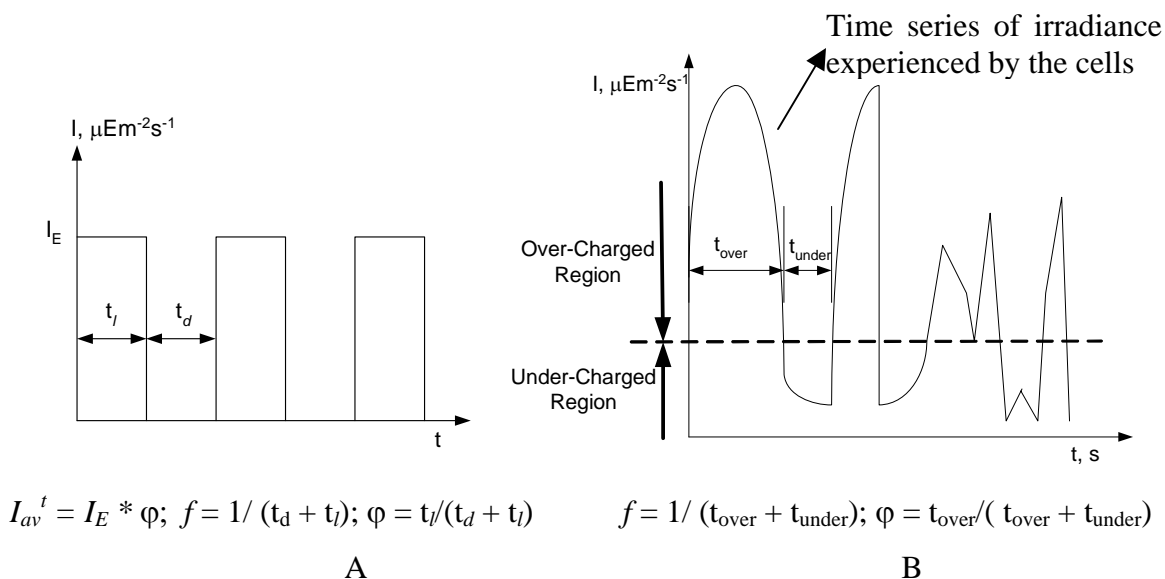


**Figure 4-2.** Illustration of the parameters to characterize the dynamic feature of irradiance fluctuation. A: well-defined light/dark cycle; B: over-/under- charged cycle in real reactors.

As mentioned above, the quantum yield can be kept at a high level because of the relaxation of the cells shifting between the illuminated zone and the dark zone. In fact, since the time scales of the micro-eddy mixing and the photosynthesis electron transfer are both in 10ms, a cell is likely to be “over-charged” whenever it enters the highly illuminated zone, where the light intensity is higher than the saturated light intensity. On the other hand, when a cell enters the dark zone, where its light intensity is lower than the saturated light intensity, the cell is likely to be “relaxed”.

This could be further explained by the classical Photosynthesis-Irradiance (P-I) curve as illustrated in Figure 4-3. When the incident light intensity is very low as in the case of “dark zone”, the overall quantum yield is high and the photosynthesis rate increases linearly as the light intensity increases. This can be called as the under-charged region in

the P-I curve. While when the incident light intensity exceeds the saturation light intensity as in the case of the “highly illuminated zone” in the reactor, the overall quantum yield could be very low and the photosynthesis rate reaches a plateau. This can be called as the over-charged region in the P-I curve. As the incident light increases further, some of the proteins in the electron transfer chain may be damaged and it requires a long time for recovery, resulting a rapid drop of the photosynthesis rate. This is called the supra-charged region in the P-I curve.

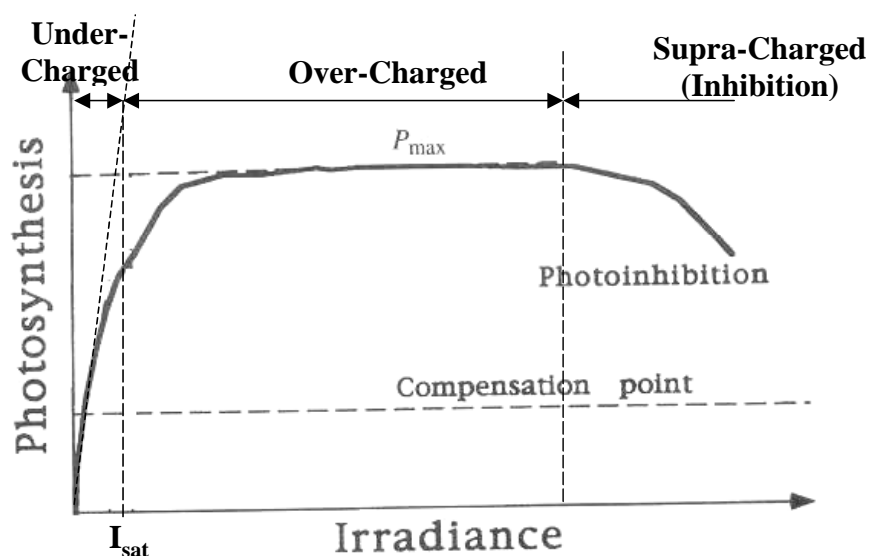


**Figure 4-3.** Typical photosynthesis-Irradiance (P-I) curve (modified from Vonshak, 1992)

Hence, separated by the saturation irradiance, the time series of irradiance could be roughly divided into two regions: overcharged and undercharged. The time series of the light intensity delivered to the cells can be decomposed into many such over-/under-charged cycles with different frequencies. These over-/under-charged cycles, following Terry’s analysis for the well-defined light/dark cycle, can be characterized by three parameters: time-averaged light intensity ( $I_{av}^t$ ) for the quantity of photons delivered to the cells, frequency ( $f$ ) for the light fluctuation, and the fraction of over-charged time

in a cycle ( $\varphi$ ) for the dimensionless relaxation time. Figure 4-2B is a schematic diagram that illustrates these proposed parameters to characterize the dynamic feature of the light fluctuations.

Once the over-/under- charged cycles are identified from the temporal irradiance patterns (typically around 4000 such over-/under- charged cycles per hour could be identified from the temporal irradiance patterns shown in Figure 4-1), the dynamic nature of the light fluctuation can be characterized by statistical methods, e.g., by the probability density function (PDF) of these three parameters mentioned above. Accordingly, the effects of the reactor geometry and the operational parameters on the irradiance pattern, and hence on the overall reactor performance, can possibly be further analyzed and used for reactor design and scale-up.

#### 4.4.1 Average Irradiance

The amount of the irradiance a cell experiences can be represented by the time-averaged irradiance:

$$I_{av}^t = \frac{1}{T} \int_0^T I(t) dt \quad (4-3)$$

where  $T$  is a very long time that covers all frequencies of irradiance fluctuations, and  $I(t)$  is the instant irradiance the cell experiences. It is noteworthy here that this definition is different from the one used by most authors in the literature, which is actually a volume-averaged irradiance (Molina Grima, 1997; Cassano et al., 1995):

$$I_{av}^V = \frac{1}{V} \int_0^V I_{P_i} dV \quad (4-4)$$

where  $V$  is the reactor volume and  $I_{P_i}$  is the local irradiance value at the finite control volume  $dV$ , which can be calculated by Equation (4-1). The time-averaged irradiance is a complex function of external irradiance, reactor geometry, flow dynamics, cell concentration and morphology, and even the absorption characteristics of the cellular

pigment. The volume-averaged irradiance is equivalent to the time-averaged value only when the cells are distributed homogeneously throughout the reactor (Molina Grima et al., 1999).

To show the differences between these two definitions, both of them have been used to estimate irradiance for the studied reactors. Two cases have been considered. Case I represents low external irradiance ( $250 \mu\text{E m}^{-2}\text{s}^{-1}$ ) plus low cell concentration ( $8 \times 10^6$  cells/ml) (the same as the experimental conditions used by Merchuk et al., 2000). Case II represents high external irradiance ( $2000 \mu\text{E m}^{-2}\text{s}^{-1}$ , typical light intensity at noon in the summer) plus high cell concentration ( $80 \times 10^6$  cells/ml, about the highest biomass concentration achieved in the experiments of Merchuk et al., 2000). The computed mean and variance of the averaged irradiances are shown in Table 4-1.

**Table 4-1.** Average irradiance and variance for the photobioreactors. Unit:  $\mu\text{E m}^{-2}\text{s}^{-1}$

Mean and Variance		Draft tube column		Split column		Bubble column
		1 cm/s	5cm/s	1cm/s	5 cm/s	5 cm/s
Case I	$I_{av}^t$	$135.0 \pm 65.7$	$140.0 \pm 63.7$	$141.5 \pm 63.3$	$152.7 \pm 62.2$	$123.3 \pm 60.1$
	$I_{av}^v$	$131.3 \pm 9.8$				
Case II	$I_{av}^t$	$90.2 \pm 297.2$	$93.8 \pm 306.2$	$126.9 \pm 389.9$	$174.9 \pm 444.5$	$46.3 \pm 231.3$
	$I_{av}^v$	$164.3 \pm 15.3$				

Case I: External Irradiance:  $250 \mu\text{E m}^{-2}\text{s}^{-1}$ ; Cell concentration:  $8 \times 10^6$  cells/ml

Case II: External Irradiance:  $2000 \mu\text{E m}^{-2}\text{s}^{-1}$ ; Cell concentration:  $80 \times 10^6$  cells/ml

As can be seen from Table 4-1, all calculated average light intensities are lower than the saturation light intensity, indicating the overall light limitation for these cultures. It is clear from the results that the reactor geometry and the superficial gas velocities do not affect the volume-averaged irradiance but do affect the time-averaged irradiance. Moreover, the

differences between the computed quantities are much larger in Case II than in Case I. These differences indicate that volume-averaged irradiance does not account for the effects of flow dynamics, which have significant influence in the case of dense culturing and strong external irradiance. Therefore, volume-averaged irradiance cannot represent the actual amount of irradiance the cells experience in the photobioreactor under these conditions.

The effects of reactor geometry and superficial gas velocity on the time-averaged irradiance can be discerned from the results in Table 4-1. As can be seen, the calculated quantities for the split column are larger than the quantities for the rest of reactors. This difference is because of the spiral movement observed in the split column (Luo et al., 2003), in which the cells may have more chances to visit the highly illuminated surface than to visit the dark center. By the contrast, in the draft tube and the bubble columns, the cells are more likely to visit the dark center, because liquid flows faster in the center region than in the near wall region. The draft tube column has a larger  $I'_{av}$  than the bubble column, since the liquid phase is forced to travel near the wall region (the downcomer), while it is not in the bubble column.

On the other hand, increasing the superficial gas velocity will increase the time-averaged irradiance. In fact, as the superficial gas velocity increases, the turbulence intensity increases and the thickness of the boundary layer near the wall tends to decrease. The cells thus can enter the wall's vicinity. Moreover, in the split column, when the superficial gas velocity increase, the spiral movement of the flow is more apparent (Luo et al., 2003), resulting in a larger diameter of circulation that increases the probability of the cells to visit the wall region as well.

#### **4.4.2 Irradiance fluctuations**

It is clear from Figure 4-1 that the temporal irradiance pattern consists of a cascade of light fluctuations with different frequencies. Thus, to better present the light fluctuations and the



dynamic nature of the system, statistical methods need to be used. In this work, the probability density functions (PDF) of the over-/under- charged cycle frequency and of the dimensionless relaxation time were estimated for the studied reactors under Case II. In Figure 4-4, the PDFs of the over-/under- charged cycle frequencies are shown by plotting the number of occurrences per hour vs. the frequencies ( $f$ ). In Figure 4-5, to better display the randomness of the system, the PDFs of the dimensionless relaxation time are presented by plotting the number of occurrences per hour vs.  $-\ln(1/\phi - 1)$ . This plot actually shows the PDFs of the over-/under- charged time ratio ( $t_{over}/t_{under}$ ) in a logarithmic axis coordinate.

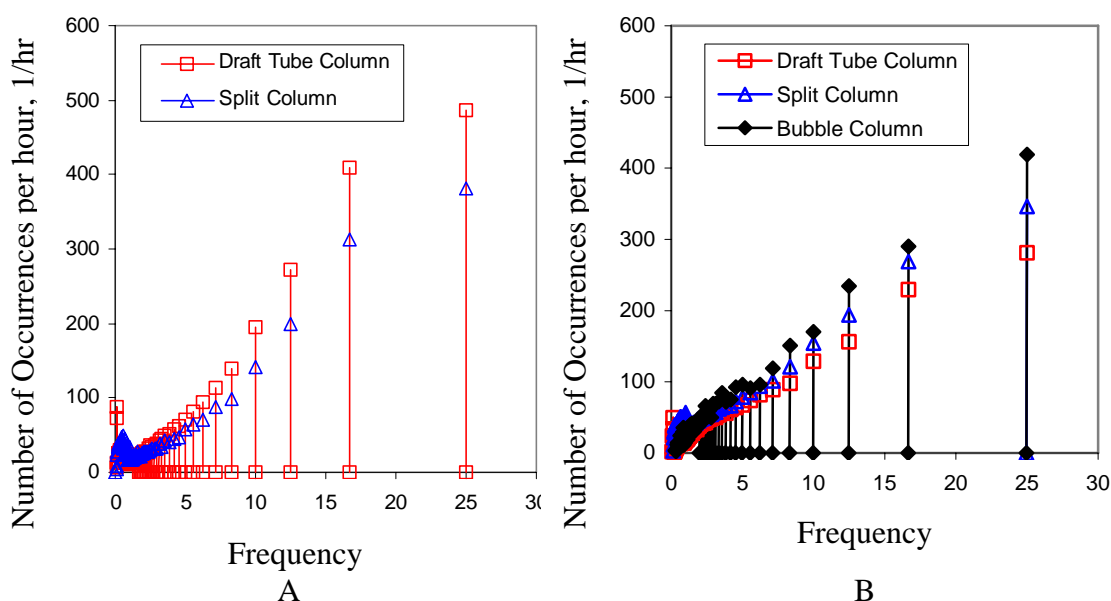


**Figure 4-4.** Probability density functions of the over-/under- charged cycle frequencies. External irradiance:  $2000\mu\text{E m}^{-2}\text{s}^{-1}$ , Cell concentration:  $80\times 10^6$  cells/ml. A: Superficial gas velocity of 1 cm/s; B: Superficial gas velocity of 5 cm/s.

Due to the limited sampling frequency used in the CARPT experiments (50Hz) as discussed in Chapter 3, the highest frequency observed is 25 Hz, and only discrete series

were obtained in the frequency field. As shown in Figure 4-4, the probability of the fluctuations increases almost linearly as its frequency increases. On the other hand, Figure 4-5 shows that the PDF of  $-\ln(1/\varphi - 1)$  is close to a Gaussian random distribution with a large peak in the center (i.e., overcharged time equals to undercharged time in a cycle). This Gaussian distribution indicates that the distribution of either the overcharged time or the undercharged time in a cycle is a random variable. In other words, around the saturation light intensity,  $I_{sat}$ , the cells have the same probability of entering the near wall region as of entering the center region. This is reasonable since the irradiance pattern is dominated by turbulence-induced fast fluctuations, and the turbulence under the studied conditions is often considered as isotropic.

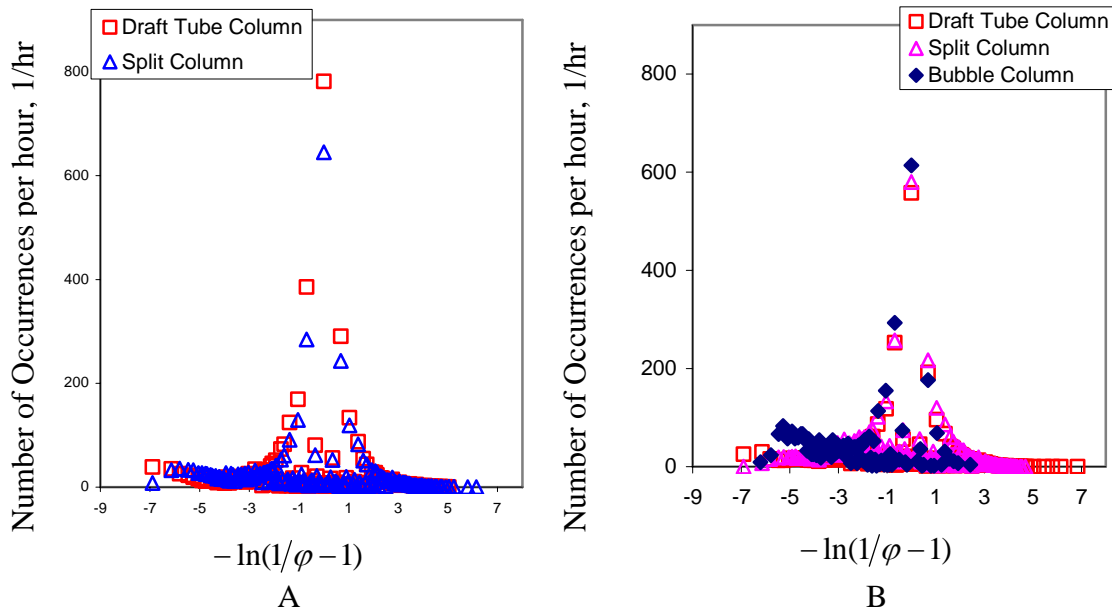


**Figure 4-5.** PDF of the dimensionless relaxation time presented by plotting  $-\ln(1/\varphi - 1)$  vs. the number of occurrence per hour, which in fact shows the PDF of the over-/under- charged time ratio ( $t_{over}/t_{under}$ ) in a logarithmic axis coordinate. External irradiance:  $2000 \mu\text{E m}^{-2}\text{s}^{-1}$ , Cell concentration:  $80 \times 10^6$  cells/ml. A: Superficial gas velocity of 1 cm/s; B: Superficial gas velocity of 5 cm/s..

Again, the effects of reactor geometry and superficial gas velocity on the fluctuations can be found from these results (Figure 4-4, 4-5). The draft tube column possesses more fast light intensity fluctuations than the other reactors because the axial liquid flow in the near wall region, the downcomer in the draft tube column, is faster than the axial velocity in the other reactors at the same superficial gas velocity, suggesting larger turbulence intensity. In the split column, although the turbulence intensity in the wall region is large in the riser, it is not in the downcomer, which offsets its overall effects on the light intensity fluctuations.

## **4.5 Dynamic Modeling Approach for Reactor Performance Evaluation**

A fundamentally based modeling approach will greatly benefit reactor design and scale-up to maximize biomass productivity. Such an approach should consider the physiology of photosynthesis and microorganism growth, the flow dynamics, and the irradiance distribution within the reactors. To begin, we need a dynamic photosynthesis rate model.

As mentioned in Chapter 2, although many models have been developed, further verification and model parameter estimation are very scarce in the literature. Merchuk et al. (1998a, 2000), Wu and Merchuk (2001, 2002) experimentally investigated the effects of well-defined light/dark cycles with different periods and light/dark ratios of the photosynthetic rate of a red marine microalgae, *Porphyridium sp.* Using the obtained experimental data, they estimated the model parameters of the dynamic model proposed by Eilers and Peeters (1988). And an additional maintenance term was introduced to account for the cellular damage under detrimental culturing conditions, e.g., in cases of high shear stress and very low light intensity when the photosynthesis rate can be negative. Hence, this model is used in this study and is further discussed in the following sections.

### 4.5.1 The governing equations for the model

As described in Chapter 2, the governing differential equations for the three-state growth rate model proposed by Eilers and Peeters (1988) and modified by Wu and Merchuk (2002) are:

$$\frac{dx_1}{dt} = -\alpha I(t) \cdot x_1 + \gamma \cdot x_2 + \delta \cdot x_3 \quad (2-7)$$

$$\frac{dx_2}{dt} = \alpha I(t) \cdot x_1 - \gamma \cdot x_2 - \beta I(t) \cdot x_2 \quad (2-8)$$

$$\frac{dx_3}{dt} = \beta I(t) \cdot x_2 - \delta \cdot x_3 \quad (2-9)$$

$$x_1 + x_2 + x_3 = 1 \quad (2-10)$$

$$\frac{1}{x} \frac{dx}{dt} = \mu = k \cdot \gamma \cdot x_2 - Me \quad (2-11)$$

$$Me = \overline{Me} \cdot e^{k_m(\tau - \tau_c)} \quad (2-12)$$

The model parameters estimated by Wu and Merchuk (2002) for a red marine algal, *Porphyridium sp.* are listed in Table 4-2. However, the instant light intensity,  $I(t)$ , and shear stress,  $\tau$ , experienced by a cell are time-dependent variables highly depend on the cell's position in the reactor, thus have to be supplied from the CARPT data.

### 4.5.2 Numerical solution

Generally, the differential equations (Eq.2.3 ~ Eq.2.5) for the photosynthetic rate are a linear initial value problem for given values of the model parameters. For a given light intensity, i.e.,  $I$  is constant, these equations can be solved explicitly by classical methods. Assuming the system reaches steady state, the analytical solution (Eilers and Peeters, 1988) of the system gives the photosynthetic rate for a given light intensity, which actually provides the photosynthesis-irradiance ( $P-I$ ) curve shown in Figure 4-6 (for *Porphyridium sp.*), where  $x_1$ ,  $x_2$ ,  $x_3$  profiles are shown as well. As can be seen, the specific growth rate reaches a maximum, or the saturation level, at  $250 \mu\text{Em}^{-2}\text{s}^{-1}$ .

**Table 4-2.** Parameters of the dynamic photosynthesis rate model for *Porphyridium, sp.* (Wu and Merchuk, 2002)

Parameter	Unit	Value
$k$	<i>Dimensionless</i>	$3.65 \times 10^{-4}$
$k_m$	$Pa^{-1}$	$1.6 \times 10^{-3}$
$k_w$	$m^{-1}$	0.2
$k_x$	$ml\ m^{-1}/10^6\ cell$	3.0
$\bar{M}e$	$s^{-1}$	$1.64 \times 10^{-5}$
$\alpha$	$(\mu E\ m^{-2})^{-1}$	$1.935 \times 10^{-3}$
$\beta$	$(\mu E\ m^{-2})^{-1}$	$5.7848 \times 10^{-7}$
$\delta$	$s^{-1}$	$4.796 \times 10^{-4}$
$\gamma$	$s^{-1}$	0.1460
$\tau_c$	$Pa$	2400

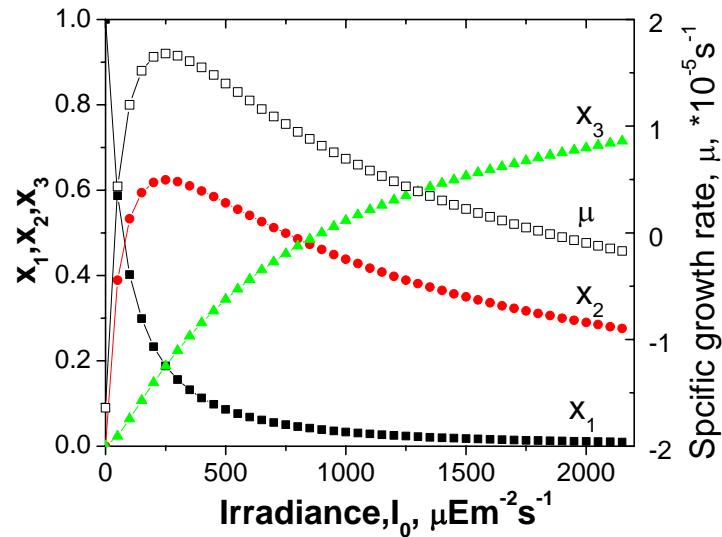


**Figure 4-6.** Computed Photosynthesis-Irradiance (P-I) curve together with profiles of PSF states by the dynamic photosynthesis rate model proposed by Eilers and Peeters (1988) for *Porphyridium, sp.* See text for details

For cells grow in a real photobioreactor, numerical methods are required to solve the differential equations due to the chaotic nature of the temporal irradiance patterns (i.e.  $I$  varies with time). The cells' trajectories measured by CARPT experiments consist of successive sampling points at frequency of 50 Hz. Between the short intervals of any two successive samples, the cells' concentration and the irradiance distribution inside the reactor can be assumed to be constant. Hence, the instant light intensity at any point between the two sampling points,  $I(t)$ , can be estimated by linear interpolation based on Equation (4-1) (Wu and Merchuk, 2002) for simplicity and demonstration purpose as mentioned above:

$$I(t) = I_E \cdot \exp\left\{-\left(k_x \cdot x^j + k_w\right) \cdot \left[d^j + \frac{t-t^j}{t^{j+1}-t^j} (d^{j+1} - d^j)\right]\right\} \quad t^j < t < t^{j+1}, j = 1, N-1 \quad (4-5)$$

where  $N$  is the total number of the trajectory points, and  $d$  is the distance to the illuminated surface. On the other hand, to account for the effects of shear stress, the time-averaged shear stress distribution obtained from CARPT experiments was used to calculate the maintenance constant,  $Me$ , by equation (2-12).

Therefore, the overall growth rate can be obtained by integrating the governing differential equations (Equation 2-7~2-12) along the whole cell's trajectory from point to point. The initial conditions we used in the simulation are:

$$x_1 = I, x_2 = x_3 = 0, \quad t = 0 \quad (4-6)$$

These conditions assume all cells are in the resting state as if they had been kept in dark for a long time.

5<sup>th</sup> order Ronge-Kuta algorithm (the subroutine available in MS Powerstation 4.0 was used here) was used to solve the above initial value problem. The flowchart of the algorithm is showed in Appendix C.

### 4.5.3 Reactor performance simulation

The dynamic model was implemented for the draft tube column at a superficial gas velocity of 1 cm/s. The simulation results were compared with the experimental data obtained by Merchuk et al. (2000), whose experiments were carried out in a different draft tube column, with a diameter of 0.13 m and a superficial gas velocity of 0.29 cm/s. Figure 4-7 shows both the experimental data and the simulation results in this work, together with the simulation results of Wu and Merchuk (2002), which were obtained by integrating the governing equations along imaginary trajectories predicted by the circulation cell model (Joshi and Sharma, 1979). For comparison of the experimental data over ten days, the numerical simulation was performed ten times based on the same 24 hours CARPT trajectory. This repetition is justified by the assumption of ergodicity of the tracking particle in CARPT experiments. As can be seen, without any fitted parameters, the simulation results of this work predict the experimental data reasonably well (this turns out to be a coincident as discussed in Chapter 5).

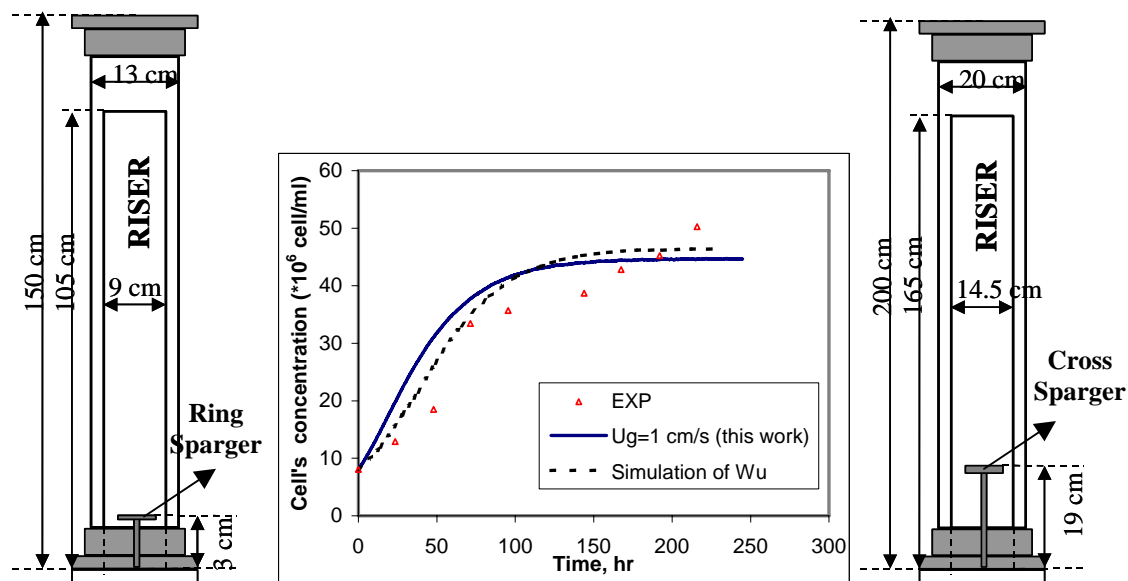


**Figure 4-7.** Simulation results by the dynamic model for the draft tube column (on the right) at  $U_g$  of 1 cm/s. The experimental data (Merchuk, et al., 2000) and simulation results of Wu and Merchuk (2001) are also presented, which are based on the draft tube column on the left at the superficial gas velocity of 0.29 cm/s.

## 4.6 Effects of reactor geometry and superficial gas velocity

Based on the dynamic model developed above, the overall growth rate of the cells in the three types of bioreactors were calculated and compared, as shown in Figure 4-8. Obviously, the overall performance of the split column excels that of the draft tube and the bubble columns, and the superficial gas velocities positively affect the performance. These results are consistent with the above analysis concerning the effects of the reactor geometry and the operational conditions on the parameters characterizing the temporal irradiance pattern. For example, since the overall control factor for the photobioreactor performance is the light limitation (e.g., the time-averaged irradiances for all cases in Table 4-1 are smaller than the saturation light intensity), the overall performance for the reactors is strongly affected by the average irradiance. Hence, as the cells in the split column are able to receive more light than the cells in the other types of reactors (due to the spiral liquid phase flow), the overall growth rate is higher in this type of reactor.

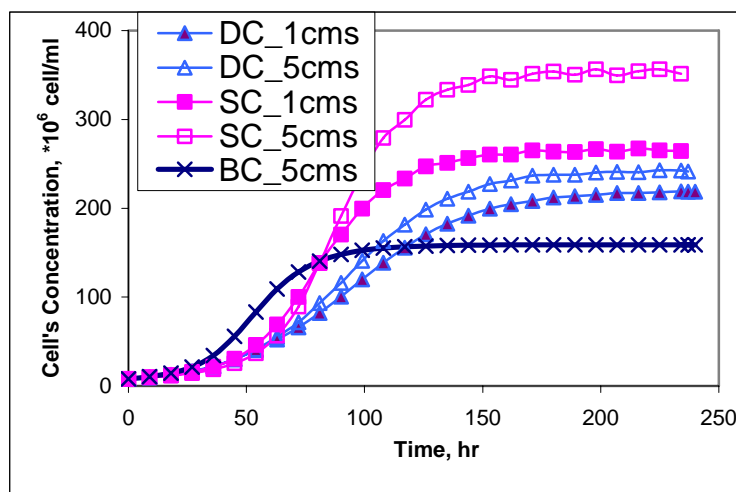


**Figure 4-8.** Numerical simulated cell's concentration profiles for different type of reactors and superficial gas velocities. Simulation condition: External Irradiance:  $2000 \mu\text{E m}^{-2} \text{s}^{-1}$ ; Initial Cells concentration:  $8 \times 10^6 \text{ cells/ml}$  (BC: Bubble column; SC: Split column; DC: draft tube column.)



The results also reveal the effects of the light intensity fluctuations. For example, although  $I_{av}^t$  for the split column at an Ug of 1cm/s is much larger than  $I_{av}^t$  for the draft tube column at the same superficial gas velocity, the overall performance for the split column is just slightly larger than that of the draft tube column. The irradiance patterns for the draft tube column consist of more fast fluctuations than the split column, indicating a better quantum yield. On the other hand, because of the chaotic nature of the fluctuations, the effect of the relaxation time is not clear in these cases. Actually, as shown in Figure 4-5, the profiles of the PDF for the relaxation time in all the cases almost collapse into one.

Accordingly, these proposed parameters, i.e., time-averaged irradiance ( $I_{av}^t$ ), over-/under-charged cycle frequencies ( $f$ ), and the dimensionless relaxation time ( $\varphi$ ), can be used to characterize the availability and the fluctuation of light transferred to the cells – the controlling factor of the photobioreactor performance. They integrate information of flow dynamics and irradiance transportation and are functions of reactor geometry, operational conditions and the optical properties of the culturing media. With the future availability of experimental data bank and validated Computational Fluid Dynamics (CFD) codes, it is possible to estimate these proposed parameters for different reactor geometry and operating variables, which will provide a mean to screen different reactor design and operating parameters for a desired photobioreactor performance.

## 4.7 Summaries

In this Chapter, efforts have been focused on analyzing the effects of mixing, or flow dynamics, on photobioreactor performance and on developing a dynamic growth rate model for photobioreactor performance evaluation. Based on the hydrodynamic findings obtained by CARPT technique, a possible mechanism of how flashing light interacts with photosynthesis is proposed. The effects of flow dynamics on light availability and light intensity fluctuations have also been analyzed and quantitatively characterized. Moreover, a dynamic modeling approach for photobioreactor performance evaluation has also been

developed and partly verified. This general modeling approach integrates first principles of photosynthesis, hydrodynamics, and irradiance distribution within the reactor.

It is also noteworthy that this general approach can be extended to include other physiologically based photosynthesis rate and irradiance distribution models, which will further improve the accuracy of and the reliability on the prediction of the cells growth and photobioreactor performance. Hence, this approach provides a direct and comprehensive tool for photobioreactor analysis, which should be essential for proper and efficient reactor design and scale-up for large-scale biomass production. However, it should also stress that the microalgae/cyanobacteria culturing system in a PBR is a very complex system. Its performance can be affected by many other factors except the light availability and usage efficiency, such as temperature, pH, salinity, medium composition, mass and heat transfer rate, etc. Therefore, accurate and reliable information for flow dynamics, irradiance distribution, and photosynthetic rates are critical to the prediction capability of this model.

Nevertheless, further verification of this model is required due to the fact that the reactor for the performance experiments (Merchuk et al., 2000) is not the same to the one where flow dynamic information was extracted as discussed in this Chapter. This calls for further comprehensive studies on both flow dynamics and real microalgae cultures implemented in the same reactors. On the other hand, this approach requires Lagrangian trajectory information of the cells' movement in the reactors and shear stress as inputs. In case of unavailability of CARPT technique particularly for large scale units, the needed information can be obtained by implementing CFD simulations provided that these codes are validated beforehand. Such validation, once again, calls for comprehensive studies on flow dynamics in the interested photobioreactors using both CT and CARPT techniques. Such studies are presented in Chapter 5 for an air-water system as a starting point to understand the complex fluid dynamics in airlift column reactors. Such studies are also presented in Chapter 7 for a real microalgae culture system to further verify the developed model from various aspects.

## **Chapter 5**

# **Local Characteristics of Hydrodynamics in an Draft Tube Airlift Column Photobioreactor: Experimental Analysis**

### **5.1 Scope**

Lagrangian information of the cells' movements inside the reactor is required to apply the methodology developed in Chapter 4 for the flashing light effect analyses and the dynamic model for PBR performance evaluation. Details of other flow dynamic information, such as mixing, mass and heat transfer rates, turbulence intensity, and shear stress, are also critical for proper design and scale-up of PBRs, as with any other types of bioreactor. Such in-depth hydrodynamic information can be obtained using CARPT and CT techniques.

Airlift column reactors have emerged as a promising reactor type for mass autotrophic cell cultures and for many other bioprocess applications. A comprehensive study of the

multiphase flow dynamics will deepen our understanding in the design, scale-up, and process intensification for such reactors.

In this chapter, local gas-liquid flow dynamics in an internal loop airlift column reactor are studied in detail using CARPT and CT techniques. Air-water system is used in this study due to its simplicity as a starting point to understand the complex multiphase flow dynamics in a real PBR system. With special measures to improve the measurement reliability, these CARPT and CT experiments focus on investigating macro- and micro-mixing and the liquid flow field in the fully developed flow region, as well as in the Top and the Bottom regions. The effects of selected geometrical and operating parameters (i.e., the superficial gas velocity and the sizes of the Top and Bottom regions) on the hydrodynamics of the airlift column reactor are also investigated. Moreover, the approaches developed in Chapter 4 are used to characterize the light availability and fluctuations delivered to the cells and to predict the photobioreactor's performance. The obtained information will form the knowledge base for the airlift photobioreactors' design and scale-up, and will also provide a database for CFD modeling validations discussed in Chapter 6.

## 5.2 Introduction

Airlift columns are pneumatically agitated reactors characterized by buoyancy driven flow. The gas phase, usually introduced from a sparger at the lower part of the column, moves upwards in the Riser and arrives at the Top, where it is separated from the liquid phase. Depending on the gas-liquid separation efficiency, the gas holdup in the Downcomer is generally much lower than in the Riser. The generated density or pressure difference between the Riser and the Downcomer drives the liquid phase circulating upwards in the Riser and downwards in the Downcomer.

Extensive studies on the hydrodynamics in airlift reactors have been seen in recent decades, as summarized in the review papers by Chisti and Moo-Yong (1988), Joshi et al. (1990), Chisti (1998), and Petersen and Margaritis (2001). Using conventional measurement techniques (e.g., pulse response technique, differential pressure drop, Pitot tube, etc.), most studies focus on studying the gas-liquid velocity fields in the fully developed flow region in the reactor. The global hydrodynamic parameters, such as cross-sectionally averaged liquid circulation velocity, overall gas holdup, overall mass transfer rate, etc., are widely used to represent the flow dynamics in the studied reactors. The applications of recently developed techniques for hydrodynamic measurements, however, are rare in the literature (Vial et al., 2002).

Although these studies have considerably enhanced our understanding of the gas-liquid flow dynamics in airlift column reactors, many unknowns, especially the local flow characteristics, remain unclear. For example, the macro-mixing, the turbulence intensity, and Reynolds shear stress fields in the liquid phases, all of which have significant effects on the flashing light effects and the PBR performance as discussed in Chapter 3, are not fully understood yet.

Moreover, the flow structures and degree of mixing in the Top and the Bottom regions in airlift reactors have rarely been studied. In these regions, the gas phase is separated from the liquid phase, and the liquid flow changes direction. Both phenomena have significant effects on the driving force and the hydraulic resistance to the liquid flow in the reactor. Thus, changing the size and shape of these two regions will alter the gas-liquid separation efficiency, the gas holdup in different regions, and the liquid flow velocities, and will further affect the flow structures in the whole column. Therefore, appropriate understanding of the flow phenomena in these regions is important for proper design and scale-up of airlift column reactors.

In this study, we used CARPT and CT techniques to investigate the details of the multiphase flow dynamics in an draft tube airlift column reactor for photobioreactor analysis. This study follows the work reported by Merchuk et al. (1998a), who investigated the reactor performance of *Porphyridium sp.* cultures in a similar reactor with the same dimensions. These experiments were conducted in an air-water system due to its simplicity (CARPT experiments for a real *Porphyridium sp.* culturing system will be discussed in Chapter 7). Special measures have also been taken to improve the measurement reliability over the CARPT experiments for the airlift column reactors of diameter 20cm discussed in Chapter 3.

These experiments will provide two types of essential information for further analysis. They first provide details of flow dynamic information, such as the liquid velocity profiles, degree of macro-mixing, gas holdup profiles, distributions of shear stresses, etc. Such information forms the knowledge base to advance reactor design and scale-up, and generates a benchmark database for CFD modeling validations discussed in Chapter 6. These experiments also provide the Lagrangian cell movement information which is further processed to estimate the time series of irradiance needed for reactor performance evaluation.

The following sections first describe the details of the experimental setup and the measurement techniques, then discuss the flow dynamic information obtained, and finally present the photobioreactor analyses, applying the methodology and the dynamic model developed in Chapter 4.

### **5.3 Reactor Configurations and Experimental Conditions**

As shown in Figure 5-1, a draft tube airlift column with a diameter of 0.13 m and a height of 1.5 m was used. This acrylic column had an inner draft tube with a diameter of 0.09 m and a height of 1.05 m. The draft tube was mounted co-axially to the outer cylinder and was supported by four tube supporters installed on the column base. These replaceable tube supporters, with various heights, can achieve different bottom clearances (i.e., the distance from the bottom of the draft tube to the reactor base as illustrated in Figure 5-2). Various top clearances (i.e., the distance from the top of the draft tube to the static liquid level, Figure 5-2) can also be obtained by adjusting the static liquid level or the total amount of liquid phase.

In all experiments, tap water was used as the liquid phase and run in a batch mode, while compressed air was used as the gas phase (CARPT experiments for a real microalgal culture system were also conducted and will be discussed in Chapter 7). Air was introduced into the reactor through a ring sparger with a diameter of 5 cm. This ring sparger was made from a 5mm diameter stainless tube, and has 15 evenly distributed up-facing holes with diameters of 1mm. Such a sparger provides rather uniform gas holdup in the Riser.

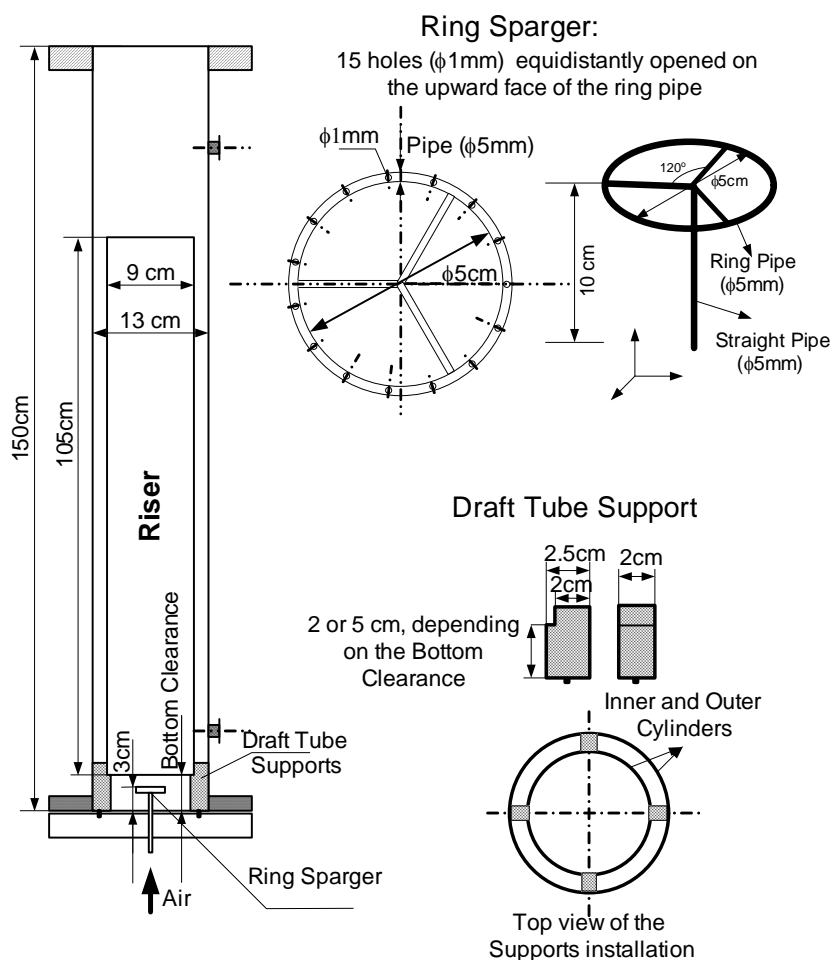


**Figure 5-1.** Configuration of the studied airlift column reactor

Table 5-1 lists the operating conditions applied in this study. The superficial gas velocities shown were calculated based on the whole column cross-section. To follow the work done by Merchuk et al. (1998a), three superficial gas velocities that they used (i.e.,  $U_g = 0.076$ ,  $0.29$ , and  $0.82$  cm/s) were selected, while another two were selected to cover the bubbly to transitional flow regimes (transition starts at  $U_g$  of  $2\text{cm/s}$  as discussed later). These superficial gas velocities represent the typical operating range for photobioreactors and other bioprocesses. Similarly, different bottom and top clearances were also selected to cover the typical operating range for photobioreactor and other bioprocess applications. The effects of these operating conditions and geometry parameters on the multiphase flow dynamics in the studied reactor thus can be investigated.



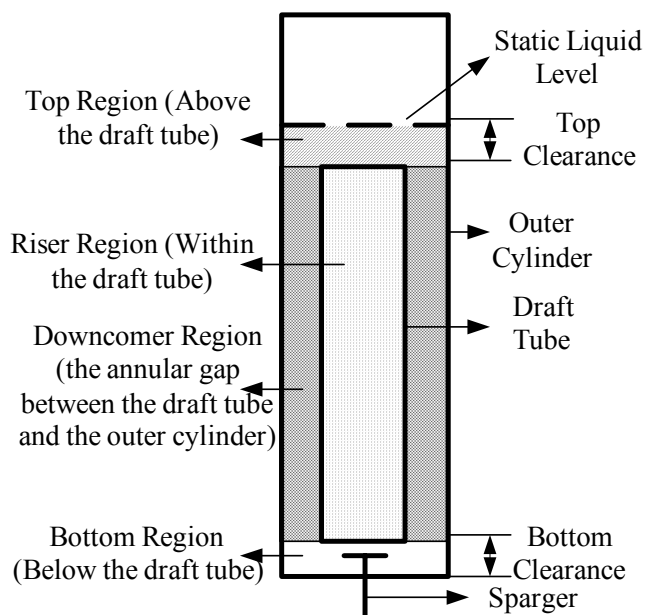


**Figure 5-2.** Illustration of the individual regions of the draft tube column reactor.

**Table 5-1.** Operating conditions

No. of run	Superficial gas velocity * (cm/s)	Bottom clearance (cm)	Top clearance (cm)
1	0.076	5	0
2	0.29	5	3
3	0.29	5	0
4	0.82	5	3
5	1.0	5	3
6	1.0	5	0
7	1.0	5	6
8	5.0	5	3
9	1.0	2	3

\* Superficial gas velocity is based on the whole cross-sectional area of the reactor

## 5.4 CARPT Experiments

The principles and data processing procedures of the CARPT technique were discussed in Chapter 3. This section discusses the details of the CARPT setup used to in this study.

### 5.4.1 Details of the CARPT Setup

As shown in Figure 5-3(a) and 5-3(b), the CARPT setup consisted of 24 NaI scintillation detectors with a diameter of 2 inches mounted on six aluminum supports. These aluminum supports were arranged evenly around the airlift column reactor at angles of  $60^\circ$  to each other. Each support had four detectors installed at different heights. To cover the whole liquid flow domain in the draft tube column, a total of eight equally spaced axial levels were selected to place these 24 detectors. Moreover, these detectors were arranged so that there were three detectors on each axial level. For example, as shown in Figure 5-3(a) and (b), detectors mounted on supports A, C, and E were placed at  $Z_1 = 5.26$  cm,  $Z_3 = 35.44$  cm,  $Z_5 = 65.80$  cm, and  $Z_7 = 96.32$  cm relative to the column base; while the detectors mounted on supports B, D, F were placed at  $Z_2 = 20.15$  cm,  $Z_4 = 50.44$  cm,  $Z_6 = 81.05$  cm, and  $Z_8 = 111.10$  cm. The gap between two axial levels was around 6 inches. With limited detectors, such an arrangement of the detectors presents the optimized measurement accuracy (Roy, 2002).

The tracer particle used to follow the liquid flow was a Sc-46 particle with a radiation intensity of around  $150 \mu Ci$ . This particle, with a diameter of around 0.8 mm, was prepared by the method discussed in Chapter 3, and is displayed in Figure 5-4. The radioactive Sc-46 metal with a diameter of  $150 \mu m$  was placed in the center hole of the polystyrene bead. A limited mass of non-radioactive glue was introduced into the hole to adjust the density of the tracer particle. To prevent the radioactive material from escaping the polystyrene bead, the tracer particle was covered by a thin film of hydrophilic paint, which bridged and sealed the opening of the hole. This treatment also provides a particle surface that could be fully wetted in water, allowing the particle to better follow the liquid flow in the reactor.

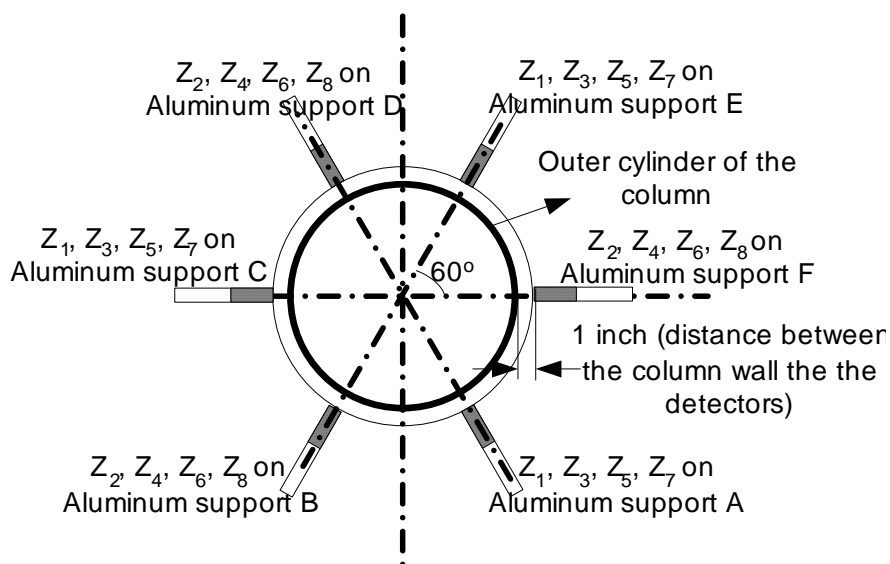


**Figure 5-3(a).** Top view of the CARPT setup for the draft tube column. Each aluminum support has four detectors mounted on different axial levels. The front view of the detectors mounted on supports A and B is further illustrated in Figure 5-3(b).

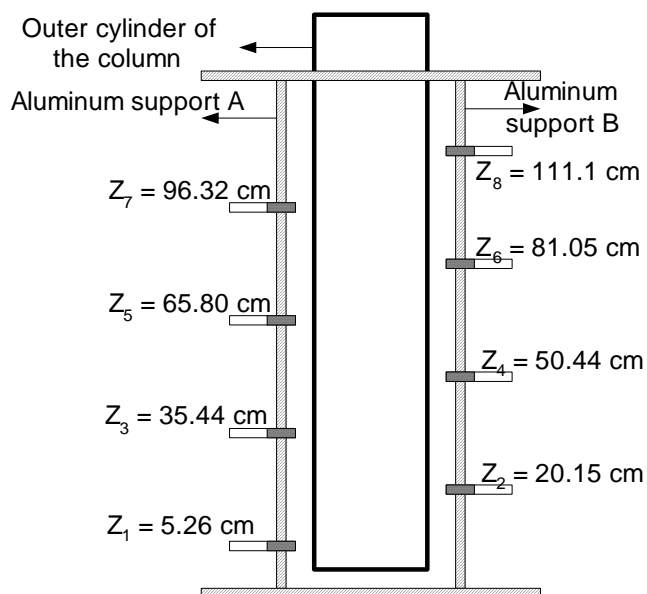


**Figure 5-3(b).** Front view of the CARPT setup for the draft tube column (only two aluminum supports are shown for illustration).

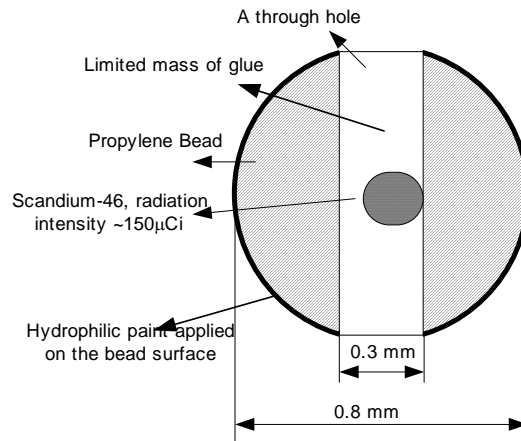


**Figure 5-4.** Configuration of the tracer particle used for the CARPT experiments (drawing not in scale).

The tracer particle's capability of closely following the liquid phase is one of the critical issues in the measurement errors associated with CARPT technique. It was found that a small particle and a close match of the densities between the tracer and the liquid phase are essential (Degaleesan, 1997; Devanathan, 1991). In this study, the tracer particle's density was adjusted to be very close to that of tap water, the liquid phase. Its terminal velocity measured in tap water was about 3mm/s, corresponding to a density of  $1.008 \text{ kg/m}^3$  calculated by Stokes law. Moreover, the particle diameter was around 0.8mm, which was much smaller than the 2.36 mm diameter particle used in the CARPT experiments discussed in Chapter 3. Therefore, this particle could better follow the liquid elements than the one used in the previous study discussed in Chapter 3.

Additionally, to better capture the dynamic features of the turbulent flow, a sampling frequency of 100 Hz was selected to record the  $\gamma$ -radiation emitted from the tracer particle. This is the highest sampling frequency that can be achieved, based on the particle's radiation intensity, without compromising the measurement error (the sampling frequency used in the CARPT experiments discussed in Chapter 3 is 50 Hz).

With these treatments, it can be anticipated that the CARPT experiments using the tracer particle prepared in this study and the 100 Hz sampling frequency can better capture the multiphase flow dynamics in the draft tube column reactor for PBR analysis than the experiments discussed in Chapter 3.

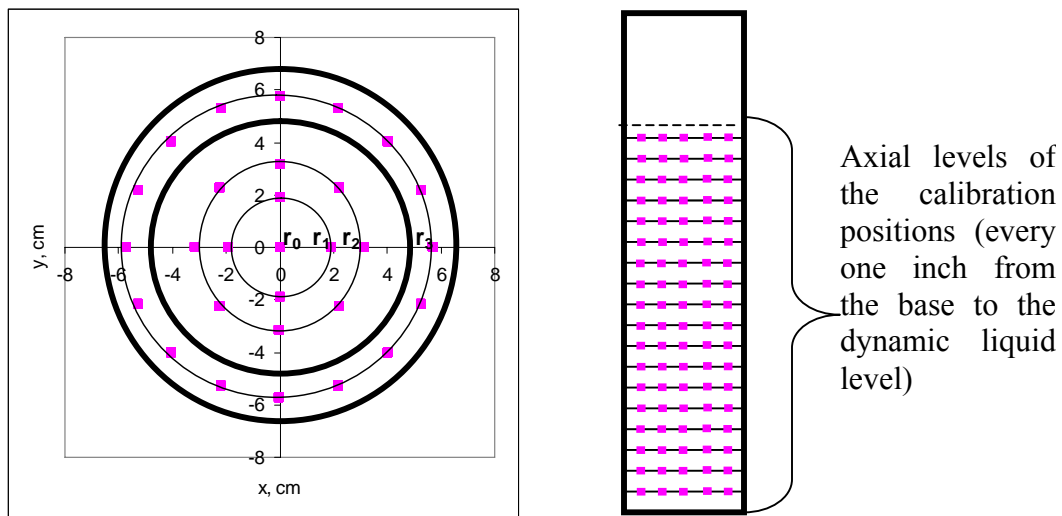
### **5.4.2 Calibration**

An automated calibration device was specifically developed in this study to facilitate the experimental work. This automated device is needed, even though a manual calibration device and another automated one are available in our laboratory. CARPT experiments using the manual calibration device are generally very time-consuming, unsafe to the experimentalists, and have low accuracy. Moreover, the available automated calibration device can be applied only to six-inch diameter columns, and can move radioactive particles only in axial and angular directions. Therefore, CARPT experiments using this calibration device are generally also time consuming and labor intensive.

The design and operation of the new calibration device developed in this study are described in detail in Appendix A. This novel calibration device allows full automation in moving the radioactive particle in radial, axial, and angular directions. It can also be applied to different sizes of columns (up to 18 inch) at atmospheric pressure. Moreover, it is more reliable and accurate than the available manual calibration device. And it is fast (around 5 hours to complete more than 1000 calibration positions). Therefore, this calibration device can be applied not only to this study but also to many other studies requiring CARPT experiments in our laboratory.

Using this novel automated calibration device, more than 1000 calibration positions were achieved for each operating condition listed in Table 5-1 (the number of calibration positions performed in the CARPT experiments discussed in Chapter 3 is 672 distributed on two radii). A schematic arrangement of these calibration positions on a cross-sectional plane is shown in Figure 5-5. Each cross-sectional plane has 29 calibration positions

arranged at four radial locations: one position at the column center ( $r_0$ ), four equally distanced positions at radii of 0.75 inch ( $r_1$ ), eight equally distanced positions at radii of 1.25 inch ( $r_2$ ), and sixteen equally distanced positions at radii of 2.25 inch ( $r_3$ ). In the axial direction, the levels of the calibration positions were arranged to cover the whole flow domain from the column base to the dynamic level. In this study, the distance between two calibration levels was one inch. Such an arrangement was attempted to achieve uniformly distributed calibration positions and to minimize the reconstruction error for the CARPT experiments.



$$r_0 = 0 \text{ inch}, r_1 = 0.75 \text{ inch}, r_2 = 1.25 \text{ inch}, r_3 = 2.25 \text{ inch}.$$

**Figure 5-5.** Configurations of the calibration positions on a cross-sectional plane. The thick lines represent the column walls.

### 5.4.3 Measurement Errors of the CARPT Experiments

Detailed discussion of the measurement errors associated with CARPT technique is presented in Appendix B. A summary of the major results follows.

Two major sources may introduce errors into the reconstructed tracer particle position in CARPT experiments as discussed by Romahhan et al. (2001) and Roy et al., (2002). The

first type of error is introduced by the imperfections of the reconstruction algorithm and errors in the calibration data. The second major source of reconstruction error stems from the quantized nature of the  $\gamma$ -ray. The emitted radiation intensity of the radioactive particle exhibits continuous fluctuations in time following a Poisson distribution. Therefore, the signals recorded by the detectors are contaminated by white noise.

Errors from the first source were found to be around 2~3 mm in the axial direction and 1~2mm in the radial direction for a total of 3~5mm. It was found that the reconstruction errors are larger when the tracer is in the downcomer region than when the tracer particle is in the riser region. The reason is illustrated in Figure 5-6. When the radioactive particle is in the Downcomer, the emitted  $\gamma$ -rays need to pass through the plastic outer cylinder once to reach the nearest detector (i.e., one wall thickness). But the  $\gamma$ -rays have to pass through three column walls to reach the detectors on the other side of the column. Such inequity does not happen when the particle is in the Riser, where the  $\gamma$ -rays always have to pass through two column walls to reach the detectors. Since the radiation attenuation coefficient for the plastic wall is different from that of water, the reconstructed particle positions are usually more erroneous when the particle is in the Downcomer region than in the Riser region.

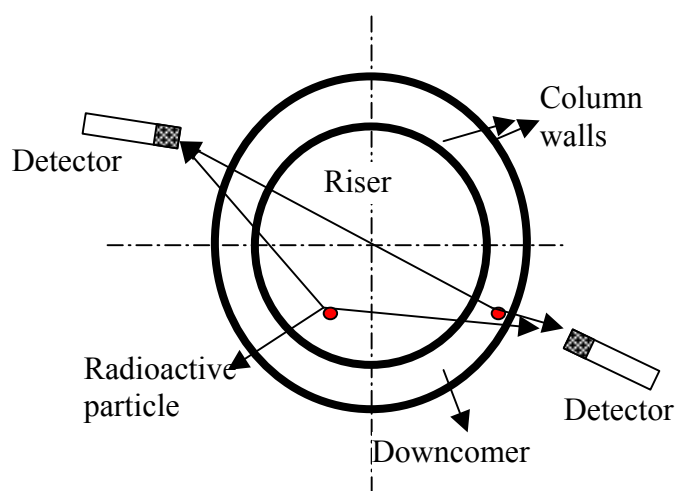


**Figure 5-6.** Illustration of the different reconstruction errors when the radioactive particle is in different reactor regions.

As for the second source of error, it was found that the wavelet filtering technique can significantly filter out the white noises introduced by the electronic system and the quantized nature of the  $\gamma$ -ray. After the filtering, these errors are around 1 mm.

## 5.5 CT Experiments

The local gas holdup in the reactor is measured by CT. The principle behind this technique is that when a beam of  $\gamma$ -ray passes through matter, the radiation intensity attenuates due to the absorption or scattering of photons by the intervening medium. The extent of such attenuation is a function of the medium's density and the distance the photon has traversed through the medium. The attenuation coefficient, a physical property of materials, is defined as the extent of attenuation after photons pass through a unit length of the material, and is usually expressed in  $cm^{-1}$ . Therefore, the total attenuation between a radioactive source and a detector is a function of the attenuation coefficients of all points along the beam of radiation, as illustrated in Figure 5-7. CT scans a material from many different angles (or projections). When the number of projections is greater than the number of points (or pixels) in the domain, the attenuation coefficient of each pixel in the domain can be calculated.

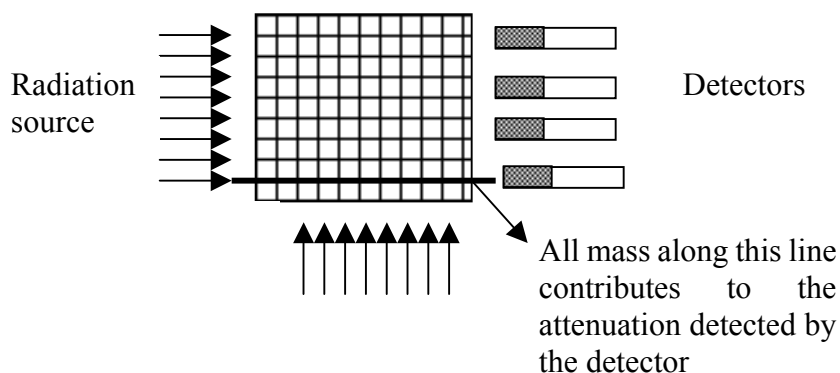


**Figure 5-7.** Schematic diagram of the  $\gamma$ -ray beam attenuation



In multiphase flow (e.g., in a gas-liquid system), the effective attenuation coefficient estimated for each pixel is the sum of the contributions from all phases present in that pixel as:

$$\langle \mu_{eff}(x, y) \rangle = \mu_l \langle \varepsilon_l(x, y) \rangle + \mu_g \langle \varepsilon_g(x, y) \rangle \quad (5-1)$$

where  $\mu_{eff}$ ,  $\mu_l$ , and  $\mu_g$  are, respectively, the effective attenuation coefficient and the attenuation coefficients for pure liquid and gas phases;  $\varepsilon_l$  and  $\varepsilon_g$  are volume fractions of liquid and gas phases, respectively. To obtain statistically meaningful results, these values are time-averaged quantities.

As shown in Figure 5-8, the CT setup available in our laboratory is a fan beam  $\gamma$ -ray scanner consisting of an array of 7 NaI detectors and a  $\gamma$ -ray source (i.e., encapsulated Cesium-137 with activity of about 100 *mCi*). The detectors and the source were mounted on a rotatable plate, which made it possible to get a 360° scan around the studied column. The plate could also be moved upwards or downwards to scan a column at different axial levels. For each selected cross-section along the reactor, the CT scan was performed for a total of 7×2475 projections, and it took about 5 hours to obtain good statistics for a time averaged phase distribution.

Reconstruction of the effective attenuation coefficient was performed with software based on the Estimation-Maximization (EM) algorithm (Kumar, 1994). In a gas-liquid system, the gas holdup distribution in the scanned cross-section thus can be calculated from the reconstructed attenuation coefficient by Equation (5-1). Further, azimuthally averaging the obtained gas holdup yielded the radial profile of the gas holdup. The details of the hardware and software have been described elsewhere (Kumar, 1994; Kumar et al., 1995).

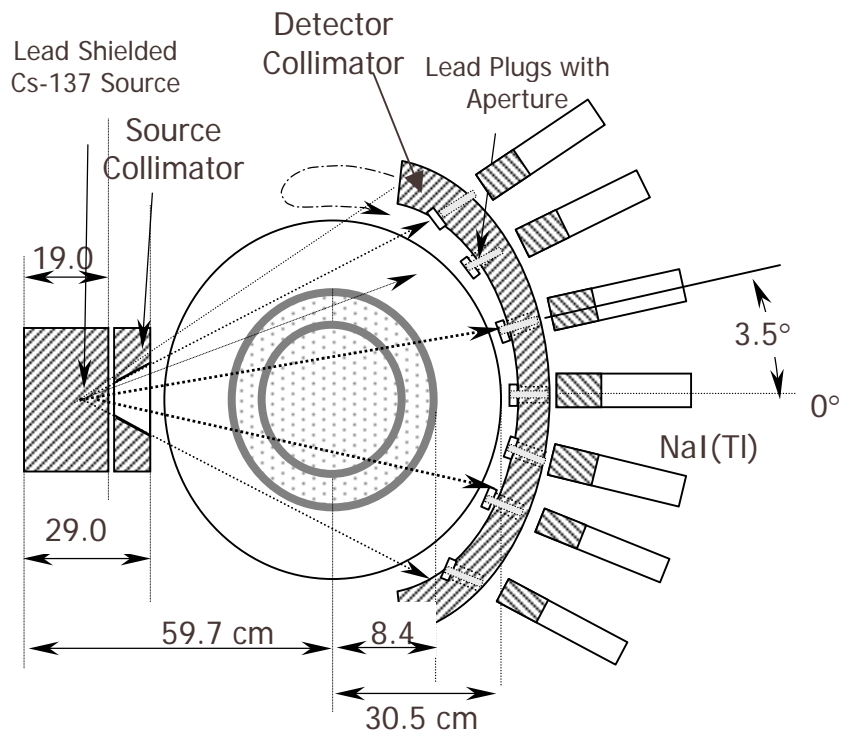


**Figure 5-8 (a).** Schematic diagram of the CT setup (Adopted From Aravind, 2002).

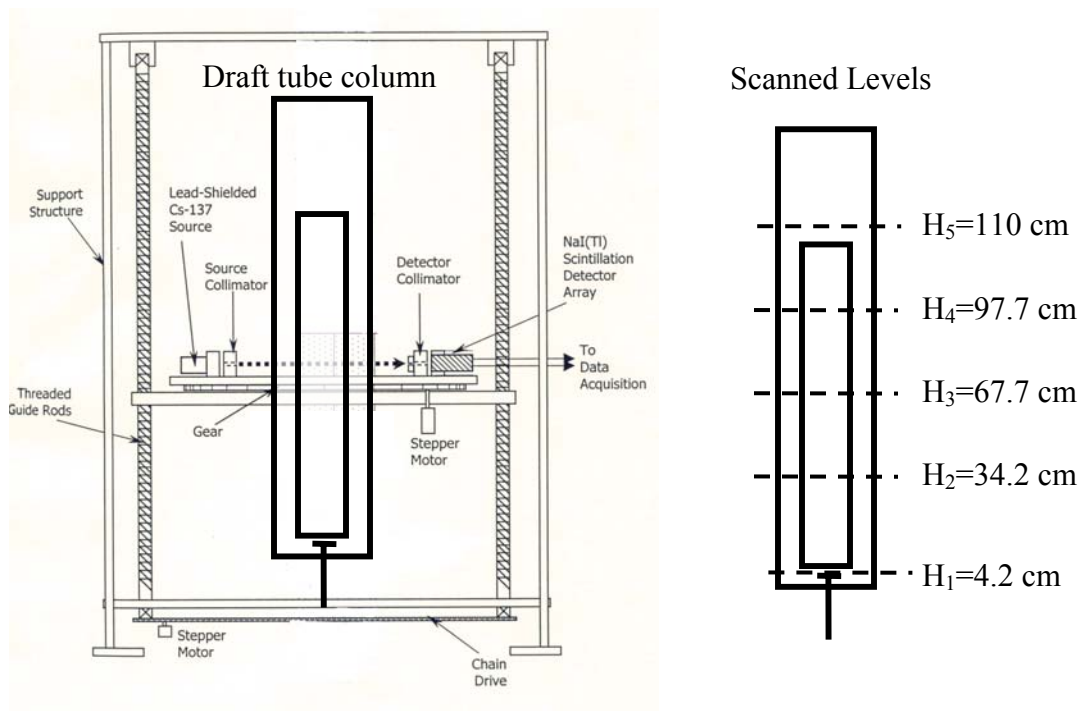


**Figure 5-8 (b).** Schematic diagram of the CT setup (Adopted From Aravind, 2002). The axial levels scanned in this study are also shown.

The cross-sectional planes scanned for the operating conditions listed in Table 5-1 are shown in Figure 5-8 (b). At least three cross-sections at different heights of the column were scanned for each condition, corresponding to the top ( $H_5=110\text{cm}$ ), the middle ( $H_3=67.7\text{cm}$ ), and the bottom regions ( $H_1=110\text{cm}$ ). To study the axial evolution of the local gas holdup at a superficial gas velocity of  $1\text{cm/s}$ , two more levels ( $H_2=34.2\text{cm}$  and  $H_4=97.7\text{cm}$ ) were also scanned at that operating condition.

## 5.6 Multiphase Flow Dynamics in the Airlift Column Reactor

Rich information about the global and the local characteristics of hydrodynamics can be obtained from CARPT and CT measurements (Devanathan, et al., 1990; Kumar et al., 1994; Luo et al., 2003). The following sections first discuss the results obtained by the CARPT experiments, such as the particle trajectories, macro-mixing, liquid flow field, turbulent parameters in the liquid phase, and then the CT results such as the local gas holdup profiles. Finally, an analysis of the draft tube airlift column photobioreactor is presented, using the obtained hydrodynamic information. The analysis used the methodology developed in Chapter 4 for the flashing light effect analyses and the dynamic model for the PBR performance evaluation. The experimental results obtained under operating condition of run #5 in Table 5-1, i.e.,  $U_g=1\text{cm/s}$ , a top clearance of  $3\text{cm}$ , and a bottom clearance of  $5\text{cm}$ , were used for the general discussions; while the others were used to discuss the effects of the superficial gas velocity and of the Top and Bottom clearances.

### 5.6.1 Lagrangian Particle Trajectories

Figure 5-9 shows typical CARPT measured particle trajectories in a 3-D plot as well as their projections on the r-z (i.e., radial vs. axial positions) and the cross-sectional planes obtained at operating conditions of  $1\text{ cm/s}$  superficial gas velocity,  $5\text{cm}$  bottom clearance, and  $3\text{ cm}$  top clearance. Clearly, the tracer particle, following the liquid flow, circulates

around the draft tube. Although a certain amount of radial fluctuations are present in all shown trajectories, back mixing in the axial direction is not common, especially in the Riser and the Downcomer regions.

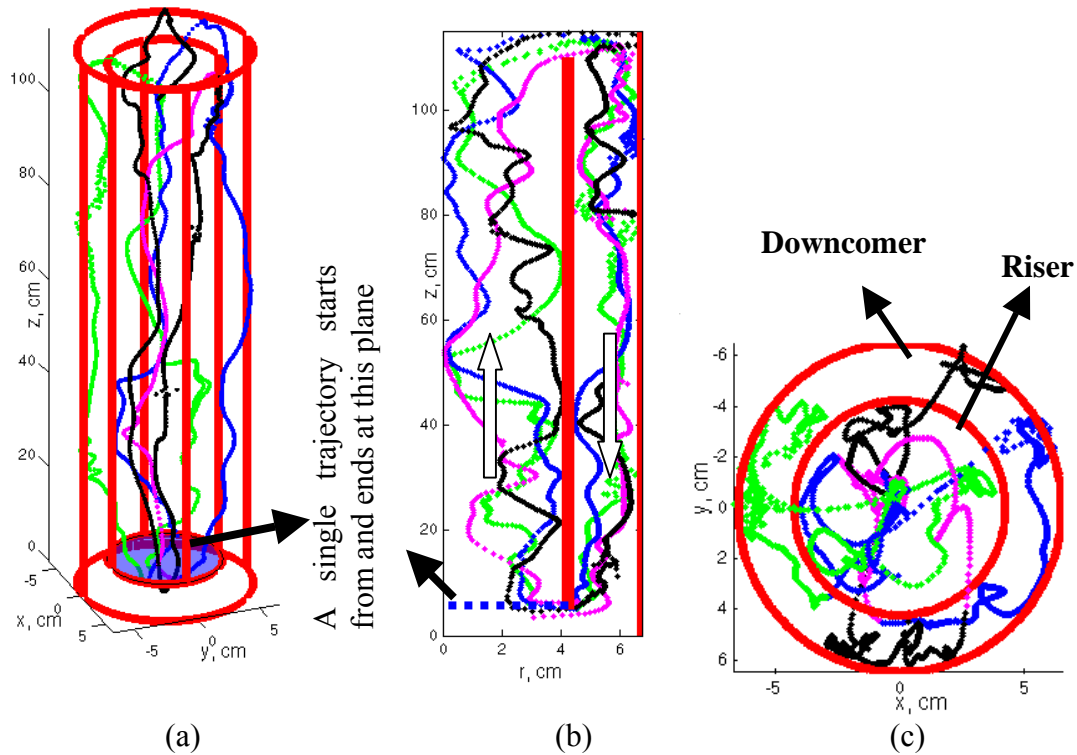


**Figure 5-9.** Visualization of typical trajectories of the tracer particle in the studied airlift draft tube column at  $U_g$  of 1 cm/s, bottom clearance of 5 cm, and top clearance of 3 cm: (a) 3D visualization; (b) projected on the r-z plane; and (c) on the cross-sectional plan. Different colors are used to present each circulation of the particle around the draft tube.

To statistically verify the assumption that the particle travels everywhere in the reactor for many times, the occurrence density (i.e., number of occurrences per milliliter) is shown in Figure 5-10. Figure 5-10 (a) shows the occurrence density distribution on the r-z plane after being azimuthally averaged, and Figure 5-7(b) shows the radial profile of the occurrence density distribution after being further axially averaged within the fully developed flow zone (i.e.,  $Z = 30\sim 80$ cm). With an averaged occurrence density around  $500\text{ ml}^{-1}$ , the

occurrence density distribution is quite uniform in the whole reactor, except at the wall regions, where the values are usually lower. However, a rather high occurrence density can be observed at the bottom (region A as indicated on figure 5-10(a)) and at the lower column corner (region B as indicated on figure 5-10(b)). Such behavior is reasonable considering the fact that the liquid flow changes direction at these regions. However, this may also suggest the existence of certain stagnancy or bypass zones in the bottom region, which becomes more obvious from a residence time distribution analysis, as follows.

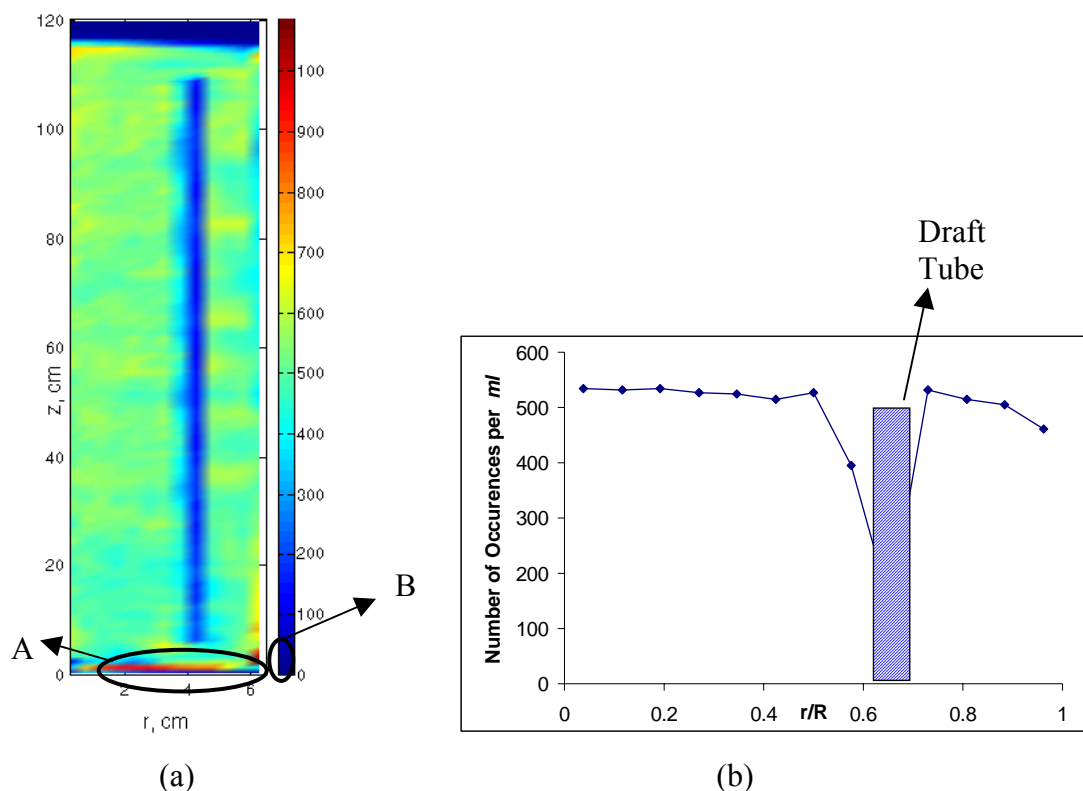


**Figure 5-10.** Particle occurrence density distribution (unit: number of occurrences per milliliter) in the reactor at  $U_g$  of 1cm/s, Bottom clearance of 5cm, and top clearance of 3 cm. (a). Occurrence density distribution on the  $r$ - $z$  plane after being azimuthally averaged; (b). Radial profiles of the occurrence density distribution within the fully developed flow zone (i.e.,  $Z = 30 \sim 80$ cm).

### 5.6.2 Overall Liquid Macro-Mixing

The degree of macro-mixing is an important parameter in photobioreactor design and scale-up, such as in determining the mass and heat transfer rates. Liquid mixing in airlift column reactors has been widely studied by pulse response techniques (Verlaan et al., 1989; Lu et al., 1994), and analyzed by the classical axial dispersion model (ADM) (Levenspiel, 1972; Chisti, 1998; Pertersen and Margaritis, 2001). Generally, to characterize the overall macro-mixing in the reactors, the Peclet number (Pe) (depending on the reactor type, sometimes the Bodenstein number, Bo, is used), the axial dispersion coefficient (Ez), and the mixing time (i.e., the time required for the tracer concentration distribution reach certain degree of macro-mixing, usually 95% of the equilibrium concentration) are estimated by fitting the pulse response curve based on ADM method. These parameters are usually defined as

$$Pe = \frac{uL}{Ez}; \quad Bo = \frac{ud_p}{D} \quad (5-2)$$

where  $u$  is a velocity scale,  $L$  is a reactor length scale,  $d_p$  is the reactor (usually a pipe) diameter, and  $D$  is the diffusivity coefficient.  $Ez$  is a parameter provided either by calculation from empirical correlations or estimation by fitting experimental data. This parameter can be related to the turbulent eddy diffusivity evaluated from CARPT data (Ong, 2002), which is discussed later.

Lu et al. (1994) even estimated these parameters for different regions in a draft tube reactor, such as the Riser, the Downcomer, the Top, and the Bottom regions as illustrated in Figure 5-2. A large Peclet number was obtained for the overall liquid mixing (50~70), the Riser (20~30), and the Downcomer (40~70) regions, while a small Peclet number (~10) was obtained for the top and bottom regions (Verlaan et al., 1989; Lu et al., 1994). Based on this understanding, many researchers modeled the Riser and the Downcomer as plug flows, and the Top and Bottom regions as a CSTR (Lu et al., 1994; Chisti, 1998; Pertersen and Margaritis, 2001).

Based on pulse response techniques and axial dispersion model, those studies provide important information to understand liquid mixing in airlift column reactors. However, they have limitations. Indeed, the pulse response technique cannot distinguish between mixing from convection and diffusion. The tracer's concentration usually reaches equilibrium in a short time after the tracer is injected. Only a few peak tracer concentrations can be detected by a probe installed in the reactor (detailed descriptions of this technique are given in Chapter 2). Therefore, with such limited liquid circulation information, this technique's accuracy is usually low and cannot be viewed as a true residence time distribution analysis.

Moreover, for systems with a Peclet number less than 20, the ADM is not valid. In fact, the ADM model is valid only for small diameter reactors with flows close to a plug flow. A small Peclet number indicates only that the system is not plug flow, not that it is close to CSTR. Therefore, a true residence time distribution (RTD) study is required to better understand the liquid mixing in airlift column reactors, especially in the Top and the Bottom regions, where mixing is significantly intense.

Such a true RTD analysis can be conducted based on CARPT measured particle trajectories. Following the particle trajectories, the residence time of the tracer particle in each section of a reactor can be calculated precisely. Since CARPT can run for a very long time, the information of such residence time has a natural statistical advantage. Therefore, a true RTD analysis based on CARPT measured particle trajectories can reveal the degree of overall macro-mixing in the studied reactor as well as in each section of the reactor.

For the draft tube column reactor, if we define one circulation of the tracer particle around the draft tube as a single trajectory (e.g., start from and end at the bottom of the Riser, as illustrated in Figure 5-11), the time of each circulation, or the circulation time ( $t_c$ ), is essentially the residence time of liquid phase in the loop of the draft tube column.

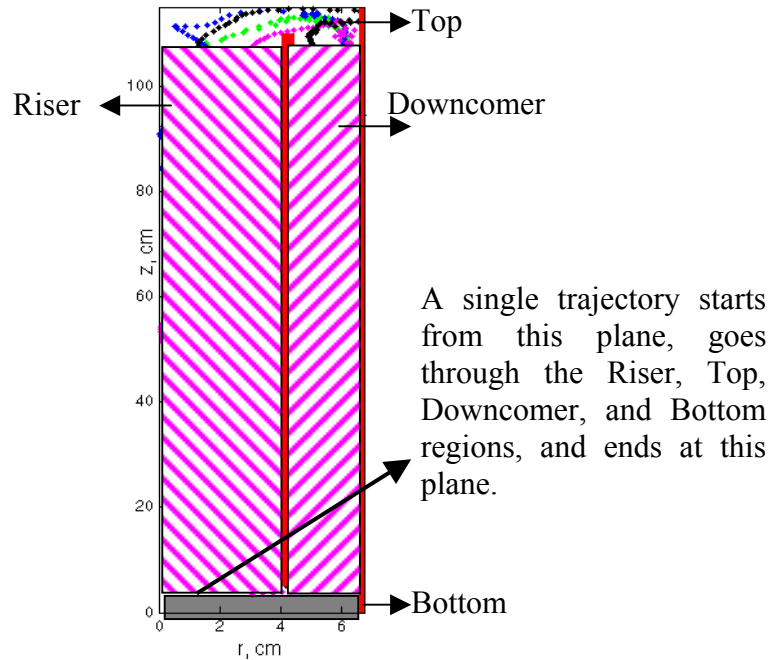


**Figure 5-11.** Typical single trajectories in the draft tube column reactor.

In this study, more than 3000 such single trajectories can be identified from the particle trajectories for most operating conditions listed in Table 5-1. The Probability Density Function (PDF) of the circulation time at  $U_g$  of  $1\text{ cm/s}$ , a bottom clearance of  $5\text{ cm}$ , and a top clearance of  $3\text{ cm}$  is shown in Figure 5-12, together with the dimensionless variance showing the broadness of the distribution. The Peclet number, also shown in Figure 5-11, is calculated from the dimensionless variance as (Levenspiel, 1972)

$$Pe = 2/\sigma_d^2; \quad \sigma_d = \frac{\sqrt{\sum_N (t_{ci} - \bar{t}_c)^2}}{\bar{t}_c}; \quad \bar{t}_c = \frac{\sum_N t_{ci}}{N} \quad (5-3)$$

where  $\sigma_d$  is the dimensionless variance,  $t_{ci}$  is the circulation time of  $i^{\text{th}}$  single trajectory, and  $N$  is the total number of single trajectories identified. The PDF of the circulation time is close to a normal distribution with a small dimensionless variance and a large Peclet number. All these suggest that the overall liquid flow is close to a plug flow.



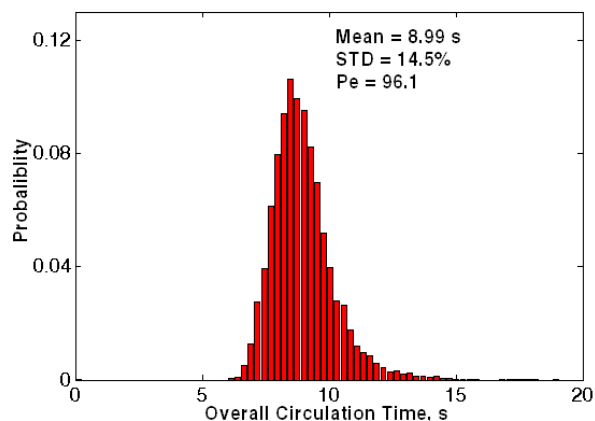


**Figure 5-12.** PDF of circulation time for single trajectories together with the mean, the dimensionless variance (STD), and the Peclet number. (operating condition:  $U_g$  of 1cm, bottom clearance of 5cm, and top clearance of 3cm)

**Effects of superficial gas velocity** The effects of superficial gas velocity on the overall liquid macro-mixing are displayed in Figure 5-13, where the mean overall circulation time and the dimensionless variance are plotted versus superficial gas velocity under two different top clearances. In Figure 5-13a, as the superficial gas velocity increases, the mean circulation time decreases for both top clearances, but at a faster rate for 0cm top clearance. Hence, the liquid flow velocities are always enhanced, more prominently for 0cm top clearance. This is because the size of the Top region increases relatively faster at 0cm top clearance as  $U_g$  increases, which further improves the gas-liquid separation and enhance the liquid velocities.

On the other hand, as shown in Figure 5-13b, the trends of  $\sigma_d$  with  $U_g$  strongly depend on the top clearance. As  $U_g$  increases,  $\sigma_d$  increases for 3cm top clearance but decreases for 0cm top clearance. Such behavior has never been reported in the literature. A possible reason for such behavior is that, at low top clearances, increasing  $U_g$  enlarges the Top region significantly, which provides a larger space for gas-liquid separation, facilitates the flow direction change of the liquid phase, and reduces the overall macro-mixing in the reactor. In contrast, at large top clearances, increasing the  $U_g$  only slightly enlarges the Top

region, minimally improves the gas-liquid separation, and do little to facilitate the reversal of the liquid flow. However, a larger gas input results in a larger gas holdup in the whole column and a faster liquid flow, and enhances the turbulence and the macro-mixing.

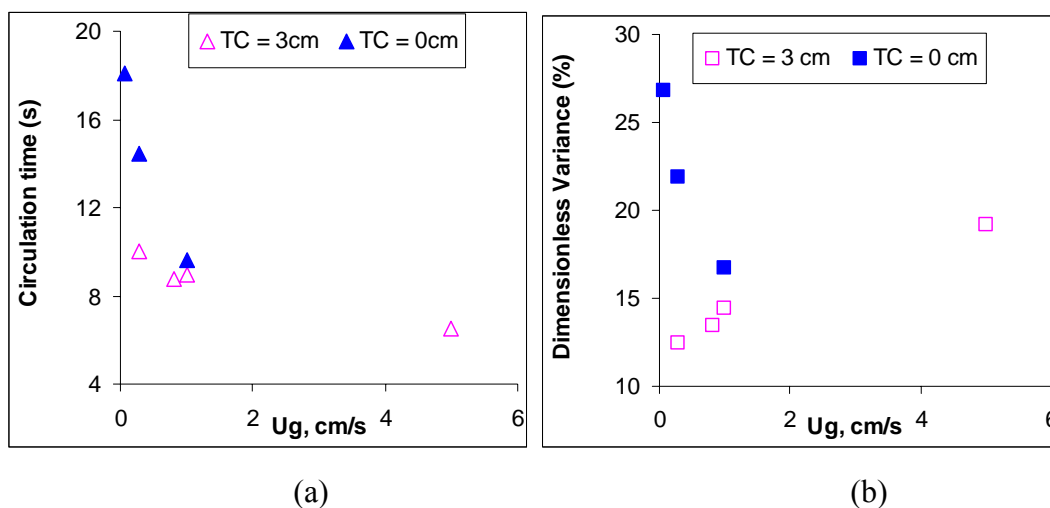


**Figure 5-13.** Effects of superficial gas velocity on the overall liquid macro-mixing: the circulation time (a) and the dimensionless variance (b). (operating condition:  $U_g$  of 1cm, bottom clearance of 5cm, and top clearance of 3cm)

**Effects of the top and bottom clearances** The effects of the top and bottom clearances on the overall liquid macro-mixing are displayed in Figure 5-14, where the overall circulation time and the dimensionless variance ( $\sigma_d$ ) are plotted versus the top and bottom clearances at a superficial gas velocity of 1cm/s. In Figure 5-14, as the top clearance increases, both the circulation time and  $\sigma_d$  decrease, indicating that a better gas-liquid separation in the top region could simultaneously enhance the liquid flow velocity and decrease the uncertainty of the overall liquid flow.

On the other hand, when the bottom clearance is decreased by more than half (from 5cm to 2cm), both  $t_c$  and  $\sigma_d$  change slightly as shown in Figure 5-14. Therefore, it can be

reasonably concluded that the hydraulic friction loss due to the reversal of the flow direction does not change much when the bottom clearance decreases under the studied conditions. However, a more thorough analysis of the macro-mixing requires more information of the flow structures and mixing status in individual regions.

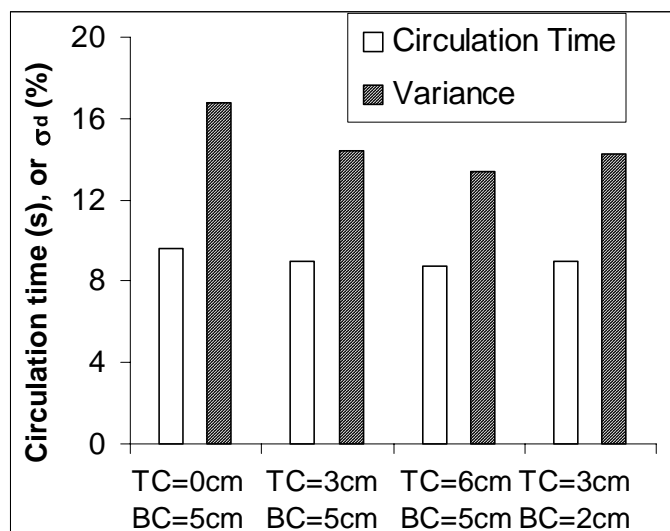


**Figure 5-14.** Effects of Top and Bottom clearances on the overall liquid macro-mixing: the circulation time and the dimensionless variance at superficial gas velocity of 1 cm/s. (TC: top clearance; BC: bottom clearance)

### 5.6.3 Liquid Mixing in Individual Regions

Further analysis of the single trajectories reveals the degree of macro-mixing in individual regions in the reactor. Based on the identified single trajectories, the residence time ( $t_r$ ) of the tracer particle in different regions can also be identified as illustrated in Figure 5-11. The results for the operating condition of 1 cm/s superficial gas velocity, 5 cm bottom clearance, and 3cm top clearance are demonstrated in Figure 5-15, where PDFs of the residence time in all individual regions are shown, together with the means and the dimensionless variance.

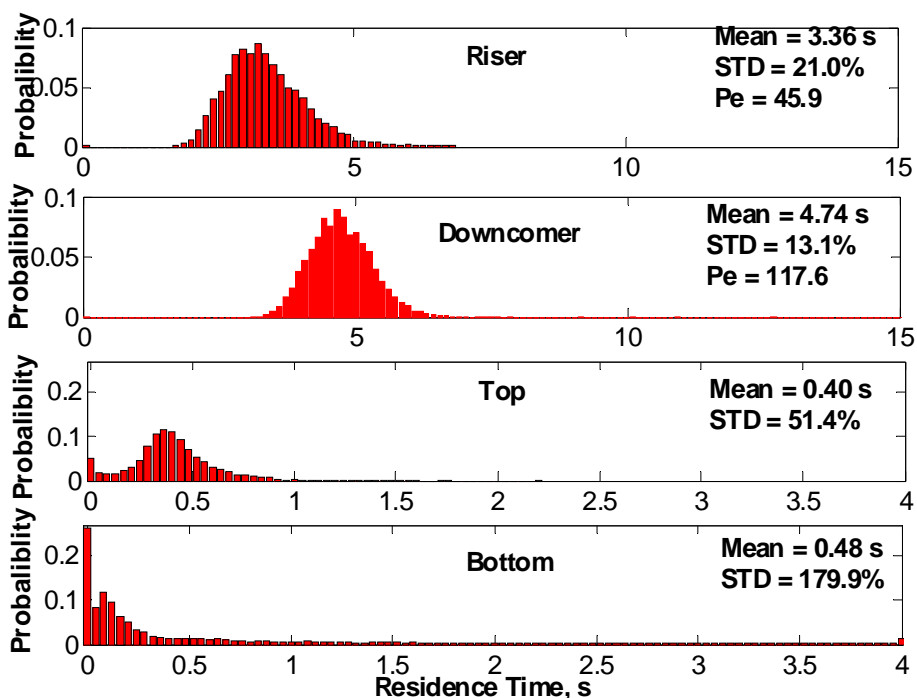


**Figure 5-15.** PDF of residence time in individual regions in the reactor together with the mean, the dimensionless variance (STD), and the Peclet number (operating condition:  $U_g$  of 1 cm/s, Bottom clearance of 5 cm, and Top clearance of 3 cm). Please note the scales are different for the shown figures.

The PDFs for the Riser and the Downcomer regions are similar to a normal distribution with small variance. The Peclet number, calculated by Equation (5-3), is around 100 for the Downcomer and 50 for the Riser, slightly larger than the values reported in the literature (Verlaan et al., 1989; Lu et al., 1994). Nevertheless, these results suggest that the flow in the Downcomer is more uniform and closer to the plug flow than the flow in the Riser.

On the other hand, the PDFs for the Top and Bottom regions both contain large peaks at low residence time, suggesting bypassing is important, and a long tail suggesting stagnancy may also exist. As a result, the dimensionless variances for these two regions, especially in the Bottom, are very large. These results partly confirm the widely accepted hypotheses that the riser and the downcomer can be modeled as plug flows. However, they

also suggest that simply modeling the Top and Bottom regions as CSTRs, as many researchers have done, can be misleading. Instead, a combination of CSTR and PFR behavior may be required to better model these two regions.

**Effects of superficial gas velocities** The effects of superficial gas velocities on the liquid macro-mixing in individual regions of the draft tube airlift column are revealed in Figure 5-16, where the residence time and the dimensionless variance in different regions under two top clearances are plotted versus the superficial gas velocities. It is clear from Figure 5-16a that the mean residence times in both the Riser and the Downcomer decrease as the superficial gas velocity increases, indicating once again the enhanced liquid flow velocity. However, the trends of the dimensionless variances for the Downcomer depend on the top clearance, while the dimensionless variances for the Riser hardly change. These results again suggest that a large top region improves gas-liquid separation, facilitates the reversal of the liquid flow, and enhances the uniformity of the liquid flow in the Downcomer. However, for the Riser, where strong gas-liquid interactions are dominant, increasing the gas input rate has only slight effects on the macro-mixing.

As shown in Figure 5-16c and 5-16d, in the Bottom region, as the superficial gas velocity increases, the mean residence time decreases while the dimensionless variances increases until the superficial gas velocity is high (5cm/s). In this case, the stagnancy zone in the Bottom shrinks and bypassing dominates under high  $U_g$ , resulting in a decreasing variance.

As for the Top region, the mean residence time in the Top can either increase or decrease with  $U_g$  increases, as shown in Figure 5-16c. This is apparently due to the contradictory effects of an enlarged Top region and an enhanced liquid flow velocity. Moreover, local minimum or maximum values of the dimensionless variance can be observed in Figure 5-16d, depending on the size of the top clearances. These trends, along with the results mentioned above, suggest that the macro-mixing status in the Top is a result of many contradictory factors such as the local gas holdup, gas-liquid separation efficiency, and the

liquid flow velocity. A better understanding of how superficial gas velocity affects these factors is thus required to understand the macro-mixing in the individual regions in the draft tube airlift column.

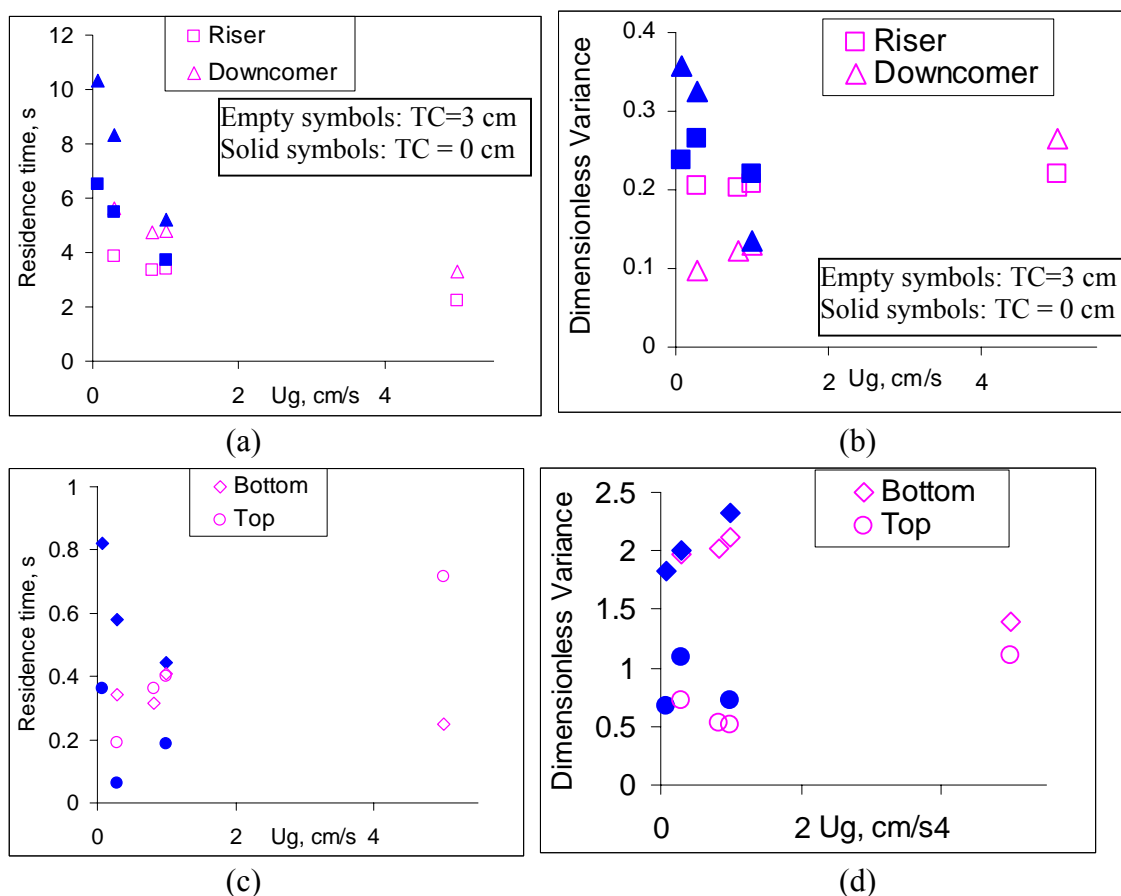


**Figure 5-16.** Effects of superficial gas velocity on the liquid macro-mixing in individual regions: (a) on the circulation time in the Riser and the Downcomer; (b) on the dimensionless variance in the Riser and the Downcomer; (c) on the circulation time in the Top and Bottom; (d) on the dimensionless variance in the Top and Bottom. Please note the y scales units differ in the figures.

**Effects of top and bottom clearances** The effects of top and bottom clearances on the liquid macro-mixing in individual regions are demonstrated in Figure 5-17, where the residence time and the dimensionless variance are plotted versus the top and bottom clearances under  $U_g$  of 1cm/s. As mentioned above, a large top clearance promotes

gas-liquid separation, directional change of the liquid flow, and the liquid flow rate; while a small bottom tends to reduce the stagnancy zone and increase the hydraulic resistance, thus slowing down the liquid flow velocity and entraining fewer bubbles in the Downcomer region.

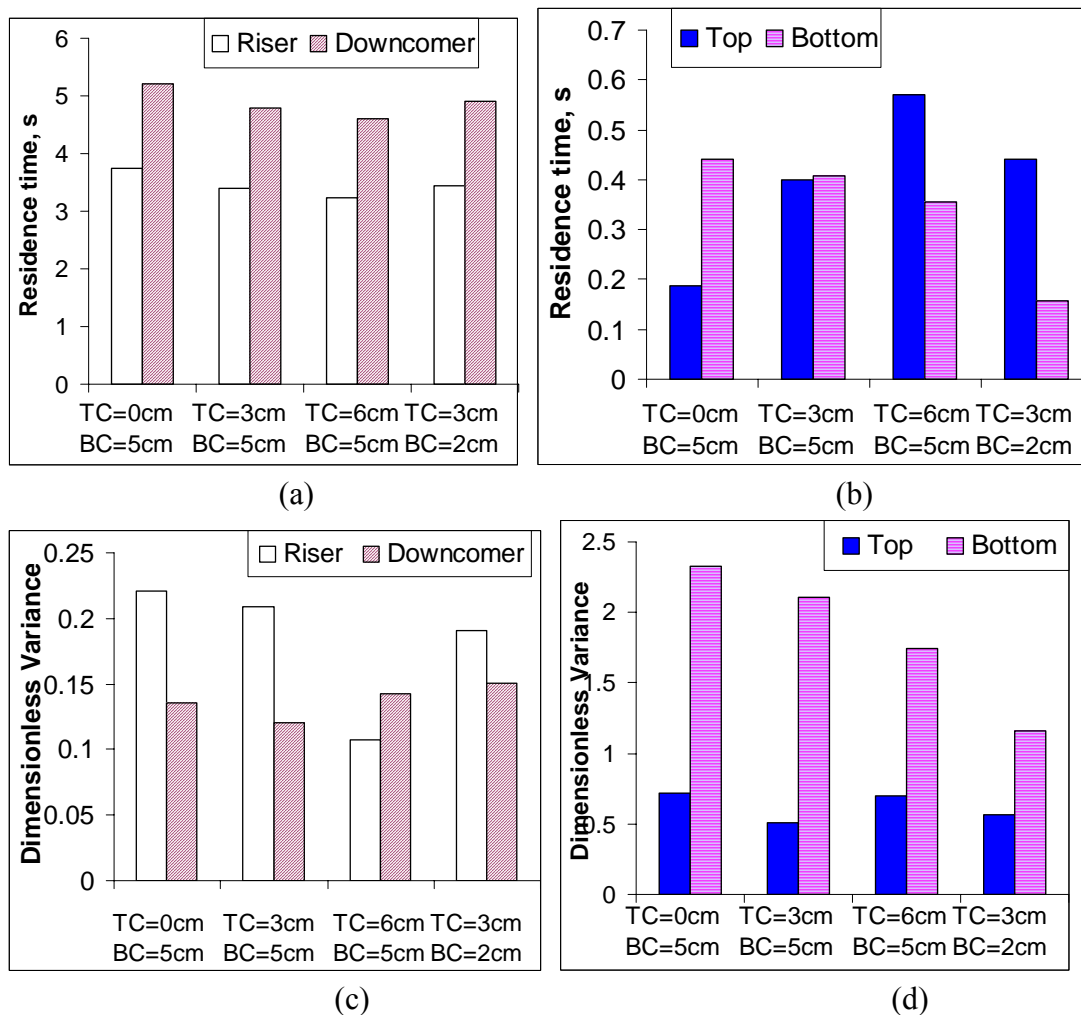


**Figure 5-17.** Effects of top and bottom clearance on the liquid macro-mixing in individual regions at superficial gas velocity of 1cm/s: (a) on the circulation time in the Riser and the Downcomer; (b) on the circulation time in the Top and Bottom; (c) on the dimensionless variance in the Riser and the Downcomer; (d) on the dimensionless variance in the Top and Bottom. Please note the y scales units differ in the figures.

Hence, as shown in Figure 5-17, increasing the top clearance will reduce the mean residence times in all but the Top regions (whose size increases as well), lower the dimensionless variances in the Riser and the Bottom, but have only minor effects on the variance in the Downcomer and the Top regions. On the other hand, decreasing the bottom clearance has minor effects on the mean residence time and the dimensionless variance, except in the Bottom region. These results further prove that the hydraulic resistance due to the reversal of the liquid flow changes slightly as the bottom clearance changes in the currently studied conditions. However, a better understanding of the macro-mixing in the individual regions requires more information about the local liquid flow structures and the phase distribution in the reactor.

#### **5.6.4 Liquid Flow Field**

The liquid flow maps in the studied draft tube column under different superficial gas velocities are shown in Figure 5-18, where the time and ensemble averaged liquid velocity vectors are projected on the r-z and the cross-sectional planes. The vectors plotted on the r-z plane were further tangentially averaged; while the vectors on the cross-sectional plane were further averaged in the axial direction within the fully developed flow zone ( $H=30\sim 80\text{cm}$ ).

As can be seen, the vectors on the r-z plane demonstrate a strong circulation cell, with the liquid phase flowing upwards in the Riser and downwards in the Downcomer. However, the vectors on the cross-sectional plane, with much smaller magnitudes than in the r-z plane, are quite uniform in the Downcomer region, and show a slight rotational flow pattern in the Riser. Such rotational flow pattern is much stronger under high superficial gas velocity. These flow phenomena represent two types of macro-mixing mechanisms, namely bulk circulation and spiral movement. Their time and length scales can be estimated from the reactor dimensions and the circulation or the residence time distributions analysis as discussed in Chapter 3.



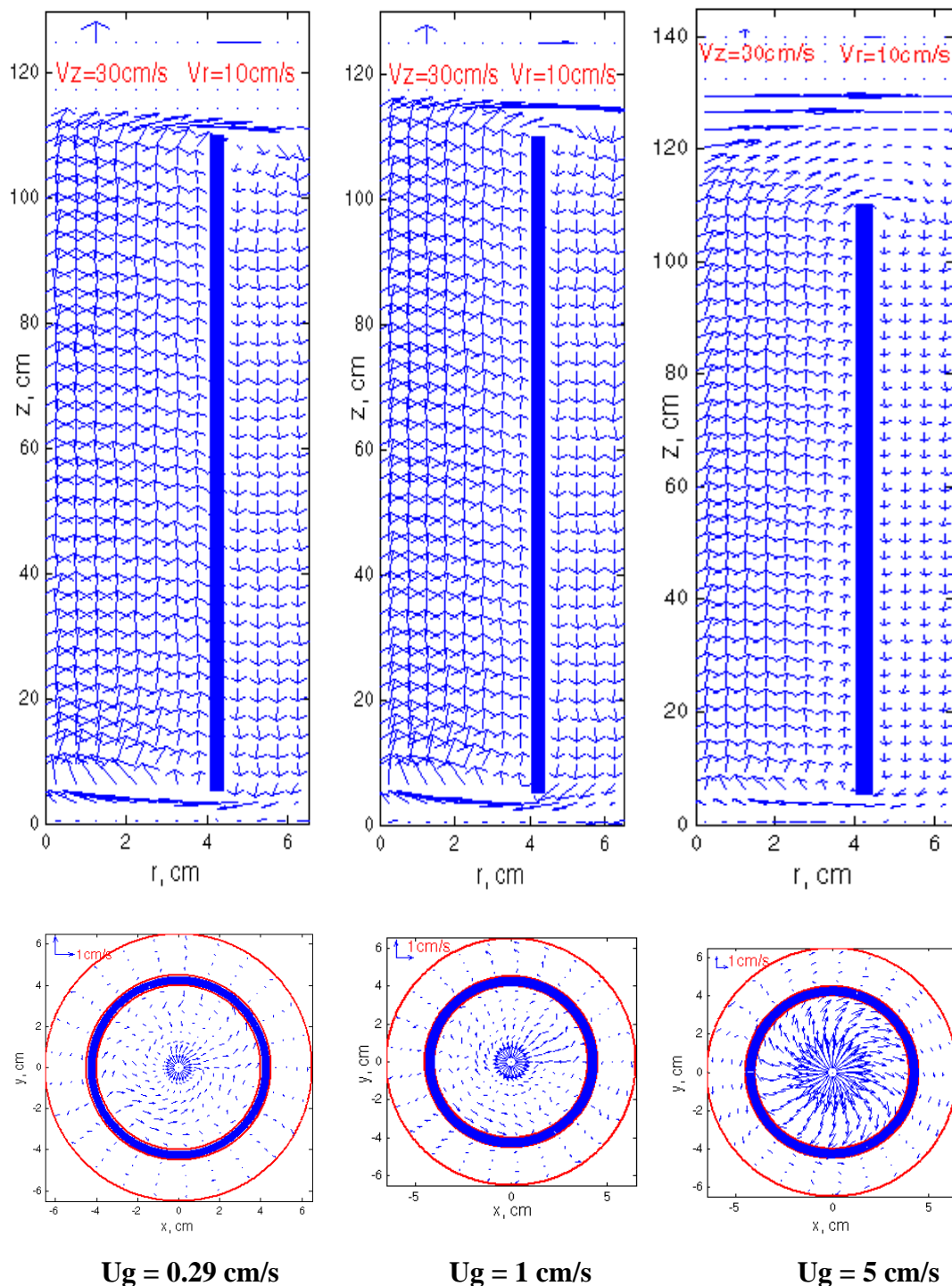


**Figure 5-18.** Visualization of liquid velocity vectors on  $r$ - $z$  and cross-sectional planes (the solid blue area shows the draft tube). Operating conditions:  $U_g = 1$  cm/s, bottom clearance = 5 cm, top clearance = 3 cm. Please note the different scales used to present the velocities in the radial and axial directions for better visualization on the  $r$ - $z$  plane.

**Effects of Superficial Gas Velocity** As shown in Figure 5-19a, further axial averaging (within the fully developed flow zone,  $z = 30\sim 80$  cm) the liquid velocity vectors on the  $r$ - $z$  plane yields the axial liquid velocity profile for different superficial gas velocities. Clearly, the axial liquid velocity profiles in the Downcomer are flatter than they are in the Riser for all superficial gas velocities. Once again this suggests a more uniform flow in the Downcomer. The effects of the superficial gas velocity can also be seen in Figure 5-19a. The velocity profiles for lower superficial gas velocities are flatter and smaller in magnitude. A big gap between  $U_g$  of 1 cm/s and 5 cm/s can also be observed, indicating a possible regime transition between these two operating conditions (this is clearer from a overall gas holdup analysis, as discussed later).

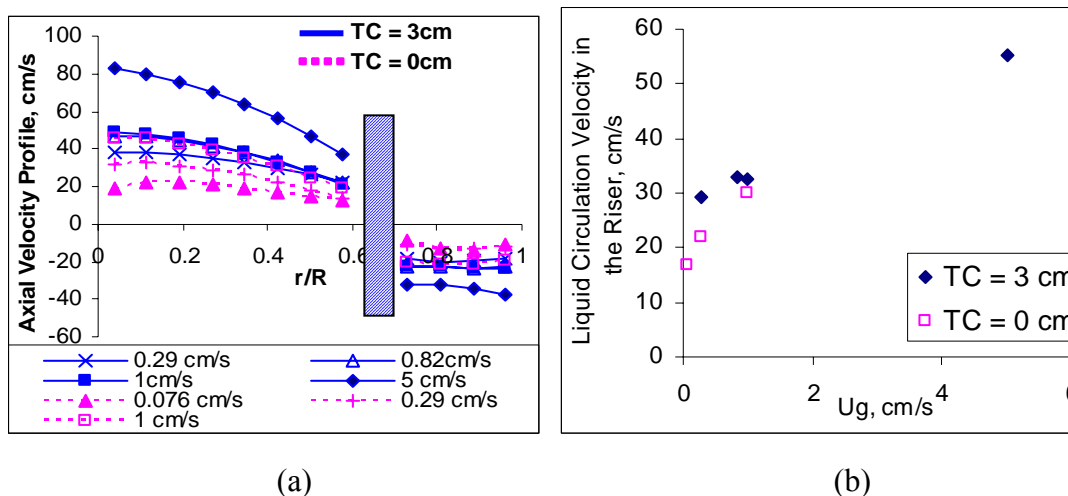


**Figure 5-19.** Effects of superficial gas velocity on the liquid flow velocities: (a) Effects on the axial liquid velocity profiles; (b) Effects on the liquid circulation velocity (normalized by the Riser cross-sectional area).

Moreover, it is also clear that the liquid circulation flux is lower for lower superficial gas velocities. Such circulation flux is usually expressed as the circulation liquid velocity normalized by the cross-sectional area of the Riser:

$$U_L = \frac{\int_0^{R_r} u_l \cdot 2\pi r \cdot dr}{\int_0^{R_r} 2\pi r \cdot dr} \quad (5-4)$$

where  $u_l$  is the time and azimuthally averaged liquid velocity, and  $R_r$  is the radius of the Riser. This liquid circulation velocity is an important global hydrodynamic parameter, conventionally used to indicate the liquid mixing and turbulence intensity. It can be measured directly by tracer techniques, or estimated by many empirical correlations produced in the recent decades (e.g., Chisti and Moo-Young, 1988). Figure 5-19b presents the relationship between the circulation velocity and the superficial gas velocity. As can be seen, a linear relationship prevails under a wide range of superficial gas velocities especially for higher top clearances.

**Effects of top and bottom clearances** The effects of top and bottom clearances on the liquid flows are shown in Figure 5-20, together with the liquid circulation velocities. At the same superficial gas velocity but different top and bottom clearances, all the axial liquid velocity profiles have very similar shapes but noticeably different magnitudes: the liquid circulation velocity increases as the size of the top or the bottom regions increases. These results are consistent with the literature (Chisti, 1998) and also with the RTD analyses discussed above.

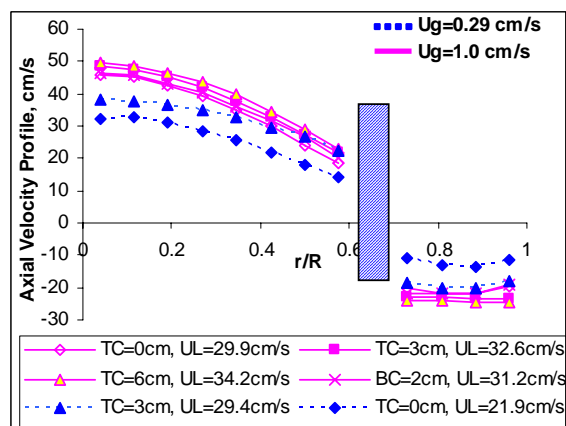


**Figure 5-20.** Effects of Top and Bottom clearances on the axial liquid velocity profiles.

### 5.6.5 Turbulent Kinetic Energy

Due to the direct effects of turbulence on micro-scale mixing and on the mass and heat transfer rates, proper understanding of turbulence in the reactor is always important in reactor modeling and design involving multiphase flows (Jakobson et al., 1996). In gas-liquid flow, the interactions between turbulent eddies in the liquid phase, derived from the bubble-driven flow by buoyancy, is usually characterized by the cross-correlations of the fluctuating velocity components, or the Reynolds stresses\* :

$$\tau / \rho = \begin{bmatrix} \overline{u'_r u'_r} & \overline{u'_r u'_\theta} & \overline{u'_r u'_z} \\ \overline{u'_\theta u'_r} & \overline{u'_\theta u'_\theta} & \overline{u'_\theta u'_z} \\ \overline{u'_z u'_r} & \overline{u'_z u'_\theta} & \overline{u'_z u'_z} \end{bmatrix} \quad (5-5)$$

The turbulent kinetic energy,  $k$ , related only to the normal stresses, is defined as

$$k = \frac{1}{2} \rho \left( \overline{u'^2_r} + \overline{u'^2_\theta} + \overline{u'^2_z} \right) \quad (5-6)$$

Figure 5-21 represents the time- and azimuthally-averaged turbulent kinetic energy distribution on the r-z plane at a superficial gas velocity of 1 cm/s, 3cm top clearance, and 5 cm bottom clearance. Figure 5-21 clearly shows that the turbulent kinetic energies are especially large at the Top and the Bottom regions. Very interestingly, they are not large in the vicinity of the sparger, where bubbles come into being. Such high turbulent kinetic energies in these regions result in significant energy dissipation, which in turn affects the hydraulic resistance and the liquid circulation flux. Hence, the turbulent kinetic energies in the Top and the Bottom regions are important for the liquid circulation flux predictions.

It is noteworthy that artificial effects can also be introduced in the calculations of the turbulent kinetic energy. This is clearly shown in Figure 5-21, where stratified bands in the

---

\* Liquid density is later omitted from this equation in the following sections since it is unity (1 g/cm<sup>3</sup>) for water. Therefore, both the turbulent kinetic energy and the shear stresses are presented in units of cm<sup>2</sup>/s<sup>2</sup>.

axial direction can be observed. It should be pointed out that such bands are a result of reconstruction errors due to the limited number of detectors used in the axial direction. Larger reconstruction errors are usually obtained between two detectors levels. Due to the nature of the turbulent kinetic energy, these reconstruction errors are squared and summed together. The turbulent kinetic energy, thus, is inevitably over-estimated. However, it should be also pointed out that this is not the case in calculating the other variables, such as the time-averaged liquid velocity and the Reynolds shear stress. In calculating these variables, the reconstruction errors usually offset each other with a zero mean.

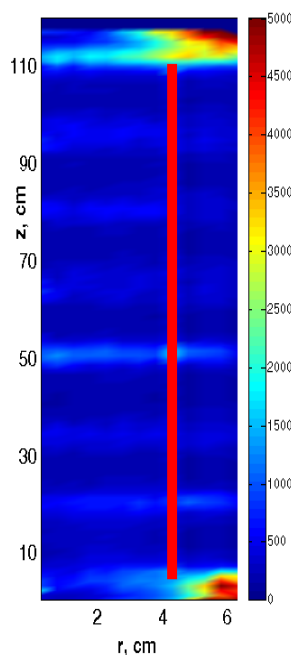


**Figure 5-21.** Visualization of time- and azimuthally-averaged turbulent kinetic energy in r-z plane (unit:  $\text{cm}^2/\text{s}^2$ ) at 1cm/s  $U_g$ , 5 cm bottom clearance, and 3 cm top clearance.

**Effects of the superficial gas velocity** Figure 5-22 exhibits the radial profiles of the turbulent kinetic energy in the fully developed flow zone at different superficial gas velocities. In Figure 5-22, the magnitude of the turbulent kinetic energy increases as superficial gas velocity increases, with a large gap between  $U_g$  of 1cm/s and 5cm/s. The turbulent kinetic energies are much larger in the Riser than they are in the Downcomer for a superficial gas velocity of 5cm/s. However, for superficial gas velocity below or equal to

1 cm/s, the radial profiles of  $k$  are quite flat, and  $k$  in the Riser is just slightly larger than  $k$  in the Downcomer. Such a small difference between the Riser and the Downcomer for turbulence intensity is not consistent with common sense. Generally, the Riser and the vicinity of the sparger, characterized by their intense gas-liquid interaction, should be much more turbulent than the Downcomer and the fully developed flow zones.

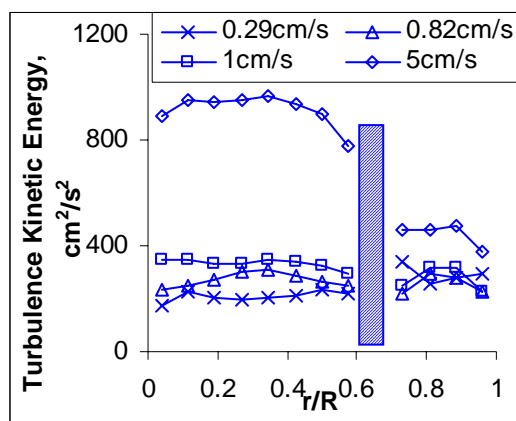
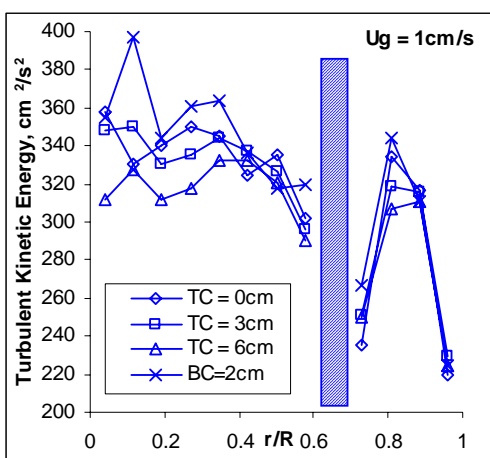


**Figure 5-22.** Radial profile of the time- and azimuthally-averaged turbulence kinetic energy,  $k$ , in the fully developed flow zone ( $H = 30\sim 80$  cm) at different superficial gas velocities with 5 cm bottom clearance and 3 cm top clearance.

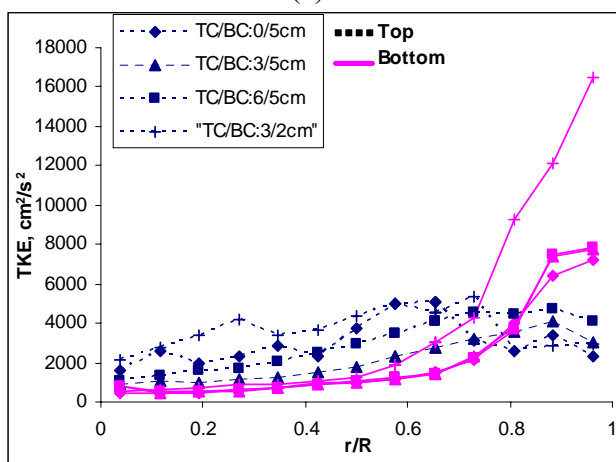
These findings could be a result of the reconstruction error. Since the reconstruction error is slightly larger in the Downcomer than in the Riser as mentioned earlier, the turbulent kinetic energy obtained for the Downcomer region is more erroneous, or more artificially over-estimated. However, these findings might also suggest that the bubble induced turbulence is not as significant as the bulk liquid turbulence in the bubbly flow regime. Indeed, since the cross-sectional areas for the Riser and the Downcomer are comparable ( $A_r/A_d = 0.73$ ), the Reynolds numbers for these two regions are in the same order of magnitude ( $Re_r/Re_d \approx 2$ ). Therefore, if the bubble induced turbulence is not important in the bubbly flow regime, as suggested by some researchers (Jacobsen, 1996; Sokolichin et al., 2004), the turbulence kinetic energies for these two regions should also be comparable. Such bubble induced turbulence is important only in the transitional or churn-turbulent flow regimes, as shown in Figure 5-22 for superficial gas velocity of 5 cm/s (Jacobsen,

1996; Sokolichin et al., 2004). Such information is important to guide the CFD simulations which will be discussed in Chapter 6.

**Effects of the Top and the Bottom clearances** The effects of the Top and the Bottom clearances on the turbulent kinetic energy are shown in Figure 5-23a for the fully developed flow zone and in Figure 5-23b for the top and bottom regions. In the fully



(a)



(b)

**Figure 5-23.** Effects of the top and bottom clearances on the radial profiles of time- and azimuthally-averaged turbulent kinetic energy at superficial gas velocity of 1 cm/s: (a) in the fully developed flow zone; (b) in the Top and the Bottom regions (axially averaged to cover the whole Top or Bottom regions). A schematic diagram of the draft tube column is also shown.

developed flow zone,  $k$  increases to some extent in the Riser but hardly changes in the Downcomer as the top and the bottom clearances decrease. However,  $k$  in the Top and Bottom regions, an order of magnitude larger than  $k$  in the fully developed flow zone, changes significantly as the size of the top and bottom regions changes.

Furthermore, the turbulent kinetic energy at the outward corner (region A as illustrated in Figure 5-23b) in the Bottom increases drastically. This explains the decrease of the liquid circulation velocity when the bottom clearance decreases as discussed earlier. It is also consistent with the results of the RTD analyses that the sizes of the Top and the Bottom clearances significantly affect the energy dissipation in the Top and Bottom regions, and in turn affect the overall liquid flow and macro-mixing in the draft tube column.

### **5.6.6 Shear Stress**

The magnitude of the fluid hydraulic forces, often expressed as shear stress or shear rate, is another important parameter for bioreactor design and operation. High shear stress can break microorganism cells, and must be avoided in all cases. Proper understanding of the hydrodynamic shear stress thus is crucial for successful design of airlift column reactors.

However, little quantitative information exists on the shear stress field in airlift column reactors, largely due to the lack of suitable measurement techniques. As a result, many researchers have resorted to dimensional analyses and tried to purely empirically correlate the shear stress (or shear rate) to operating conditions (e.g., superficial gas velocity) (Chisti, 1998). Although these correlations have been widely used, their capability to capture the correct order of magnitude of the real hydrodynamic shear stress is doubtful (Pertersen and Margaritis, 2001). Moreover, these correlations can provide only a single global value, which is usually deceptively low, considering the fact that microorganism cells can be ruptured in some high shear stress zones. Therefore, a reliable technique which



can estimate and map in 3D the local shear stress distribution is necessary for successful bioreactor design.

Based on CARPT measurements, the Reynolds shear stress can be estimated by Equation (5-4) as the covariance of the fluctuating liquid velocities. Figure 5-24 represents the time- and azimuthally-averaged shear stress,  $\tau_{rz}$ , distribution in the r-z plane, and Figure 5-25 presented the radial profile of shear stress at different superficial gas velocities which have been axially averaged within the fully developed flow zone. The other components of the Reynolds stresses, i.e.,  $\tau_{tt}$ ,  $\tau_{rt}$ , and  $\tau_{tz}$ , are not presented here due to their low magnitudes.

Figure 5-24 clearly shows that the shear stresses are significantly large not only in the top and the bottom regions (as are turbulent kinetic energies), but also in the vicinity of the sprayer. These results imply that the gas-liquid interaction does have significant effects on the Reynolds shear stresses.

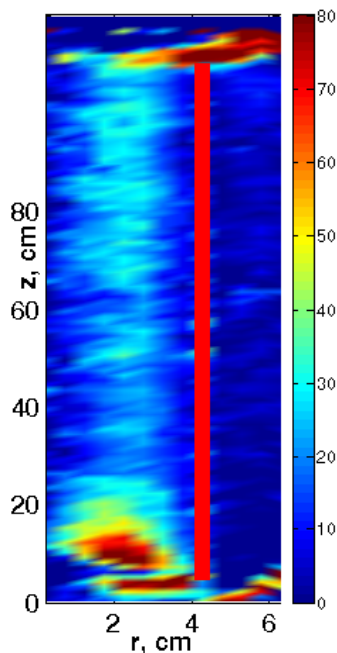


**Figure 5-24.** Visualization of time- and azimuthally-averaged shear stress ( $\tau_{rz}$ ) in r-z plane at 1 cm/s superficial gas velocity, 5 cm bottom clearance, and 3 cm top clearance.

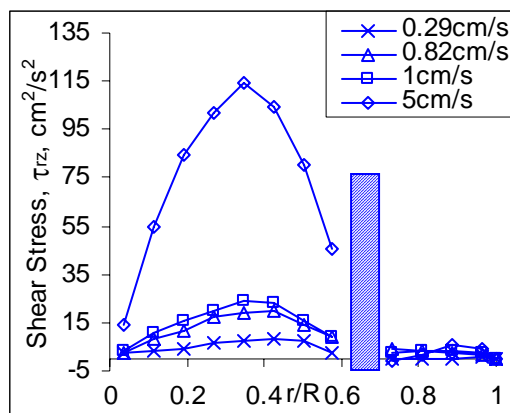
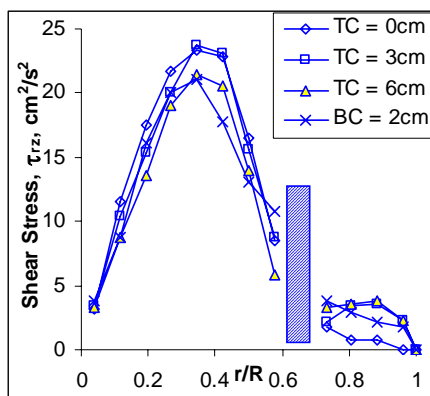


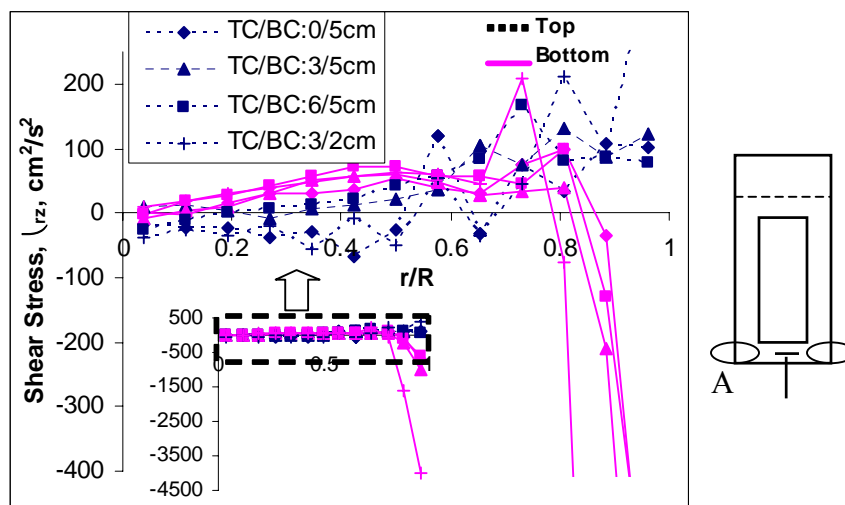
**Figure 5-25.** Radial profile of the time- and azimuthally-averaged shear stress ( $\tau_{rz}$ ) in the fully developed flow zone ( $H = 30\sim 80$  cm) at 5 cm bottom clearance and 3 cm top clearance.

On the other hand, for the fully developed flow zone, the shear stress profiles shown in Figure 5-25 present a peak in the middle of the riser (i.e.,  $r/R = 0.3$ ) but are quite uniform in the downcomer, with considerably smaller magnitudes. They also increase as superficial gas velocity increases. These findings are reasonable since the liquid flow at the middle of the Riser is least confined by the reactor geometry, while the gas holdup is much lower in the Downcomer. Moreover, Figure 5-25 also shows clearly that the magnitudes of the shear stresses,  $\tau_{rz}$ , are much lower than the normal stresses (i.e., the turbulent kinetic energies). This indicates that the cross-correlation (shear stress) between the velocity components is not as strong as the autocorrelations (normal stresses) (Chen et al., 1994).

**Effects of the top and bottom clearances** The effects of the top and bottom clearances on the shear stress distributions are presented in Figure 5-26, where the radial profiles of shear stresses,  $\tau_{rz}$ , are shown in the fully developed flow zones as well as in the top and bottom regions. As shown in Figure 5-26a, the shear stress profiles for different sizes of top and bottom regions have very similar trends with slightly different magnitudes in the fully developed flow zones. However, a huge difference can be observed in Figure 5-26b for the top and bottom regions, especially in the outside corner of the bottom region (circled in the illustration).



(a)



(b)

**Figure 5-26.** Effects of Top and Bottom clearances on the radial profiles of time- and azimuthally-averaged shear stress ( $\tau_{rz}$ ) at superficial gas velocity of 1 cm/s: (a) in the fully developed flow zone; (b) in the Top and the Bottom regions (axially averaged to cover the whole Top or Bottom regions). A schematic diagram of the draft tube column is also shown, with the outer corner circled.

In fact, as the bottom clearance decreases from 5cm to 2cm, the shear stresses at certain spots in the Bottom region are orders of magnitude larger. This could be hazardous for many microorganisms (Molina Grima et al., 1994b). Apparently, the reason is that the liquid flow at the bottom is strictly confined by the column walls, and a large amount of energy is dissipated by liquid solid collisions. In contrast, the gas-liquid free surface on the

top considerably relieves such energy dissipations. These results again confirm that changing the size of the top and bottom will greatly alter the flow structures in these regions, and in turn will affect the bulk liquid flow in the whole reactor. This may result in great loss of reactor performance.

### **5.6.7 Turbulent Eddy Diffusivity**

Turbulent eddy diffusivity is an important parameter to quantify the liquid micro-mixing in a multiphase reactor, which can be related to the dispersion coefficient ( $E_z$ ) in Equation (5-2) (Ong, 2002). In many phenomenological models for reactor design and scale-up, this parameter has to be supplied (Degaleesan, 1997). However, due to the lack of information, many researchers have used empirically assigned turbulent eddy diffusivity instead of experimentally evaluated one, which introduced considerable uncertainty to the prediction capabilities of the phenomenological models. Accurate evaluation of the turbulent eddy diffusivities from experimental measurements thus is important for successful reactor design and scale-up.

The turbulent eddy diffusivities can be evaluated from CARPT measured Lagrangian information as described by Degaleesan (1997) and Ong (2002). Figure 5-27 shows the radial profiles of the axial and the radial eddy diffusivities corresponding to the fully developed flow region. Both the axial and the radial eddy diffusivities increase as the superficial gas velocities increase. Moreover, the axial eddy diffusivities profiles incline upwards in the riser but downwards in the Downcomer as if there is a maximum at the position of the draft tube. This suggests the prominent uncertainty of the axial liquid flow in the draft tube vicinity. As for the radial eddy diffusivity profiles, local maximum values can be found at both the middle of the Riser and the Downcomer. These maximum values occur at the position where the liquid flow is less confined, while low values corresponds to where the liquid flow is more strictly confined, such as the column center region (confined by the axial symmetric geometry) and the flow at the wall regions (confined by the wall).

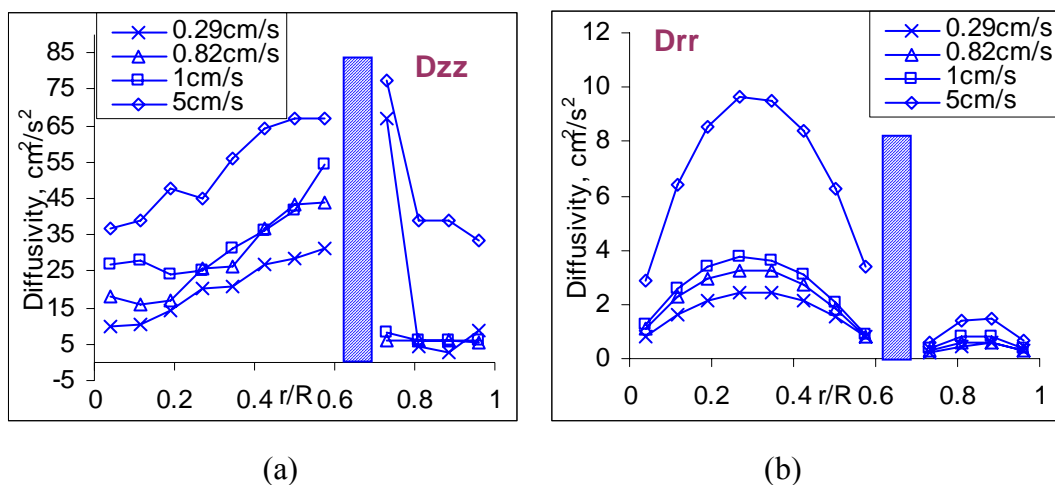


**Figure 5-27.** Radial profiles of the eddy diffusivities at different superficial gas velocities with 5 cm bottom clearance and 3 cm top clearance: (a) axial eddy diffusivity; (b) radial eddy diffusivity.

**Effects of top and bottom clearances** The effects of the top and bottom clearances on the shear stress are exhibited in Figure 5-28, where the radial profiles of the eddy diffusivities at the fully develop flow zone for different size of top and bottom regions are shown. Similar to the results of shear stresses, slight difference can be observed among the profiles for both the axial and the radial eddy diffusivities.

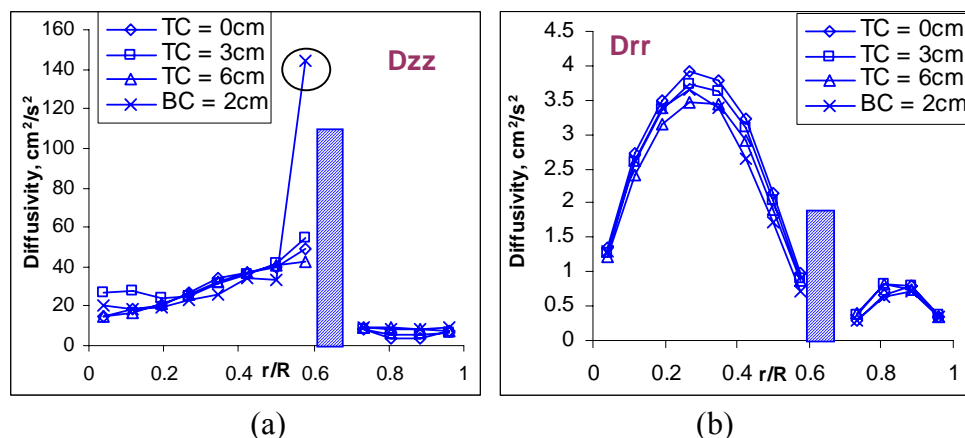


**Figure 5-28.** Effects of top and bottom clearances on the radial profiles at 1 cm/s superficial gas velocities: (a) axial eddy diffusivity (Please note the circled point is viewed as a runaway point, however, the reason is not clear); (b) radial eddy diffusivity.

### 5.6.8 Gas holdup

For gas-liquid contactors such as airlift column reactors, gas holdup directly relates to the gas-liquid interfacial area, and thus, the mass transfer rate. Moreover, since gas expansion and arising are the driving forces to the liquid flow in the airlift reactors, gas holdup, especially the local gas holdup, is essential to understand the flow dynamics and the liquid mixing in the reactors.

Determined by the CT technique, the local gas holdups at 1 cm/s superficial gas velocity, 5 cm bottom clearance, and 3 cm top clearance are shown in Figure 5-29. The time-averaged local gas holdups are visualized at five axial levels of the column as mentioned at section 5.4. It clearly shows a plume of the gas phase rising from the sparger, soon spreading to the whole cross-section of the Riser at the level of  $H=34\text{cm}$ , and then reaching the Top where part of the gas phase separates from the liquid phase and moves downwards to the Downcomer.

In the radial direction, a high concentration of gas bubbles can be observed for all levels in the column center, suggesting the bubble's radial movement to the reactor center in the riser. Although many researchers tried to explain such radial movement of bubbles by theory of lift forces, the physical existence and the mathematic realization of these lift forces are still in debate (Jacobsen, 1997; Sokolichin et al., 2004). Therefore, reliable experimental data of the radial gas holdup distribution is critical to verify these hypotheses, and to guide the CFD simulations which is discussed in Chapter 6.

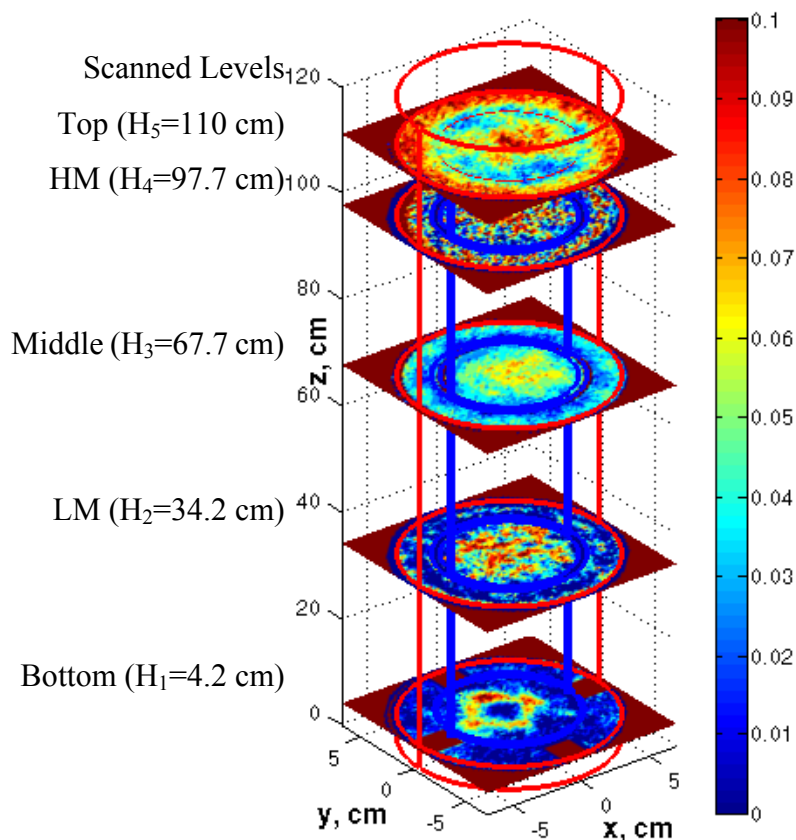


**Figure 5-29.** Visualization of time-averaged local gas holdup in different axial levels of the column at 1 cm/s superficial gas velocities, 5 cm bottom clearance, and 3 cm top clearance. Scanned axial levels are: Top ( $H=110$ cm), HM (higher middle,  $H=97.7$ cm), Middle ( $H=67.7$ cm), LM (lower middle  $H=34.2$ cm), and Bottom ( $H=4.2$  cm)

In the axial direction, although difference of the gas holdups can hardly be observed in the riser, there is a clear trend in the Downcomer, i.e., gas holdup is larger at higher axial levels. Such phenomenon is clearer in Figure 5-30, where the radial profiles of the azimuthally-averaged gas holdups at different axial levels are shown. It is consistent with the reports in the literature (Chisti and Moo-Young, 1988) that only small bubbles can be carried into the downcomer and the depth they can reach depends on their size. Additionally, the gas holdup profiles in the downcomer are not symmetric especially in the

high levels. This is because of the high radial velocity of the liquid phase on the top, which pushes the bubbles outwards to the outer wall.

Such local gas holdup profiles displayed in Figure 5-30 can also relate to the shear stress profiles as mentioned above. Since the drag force between the rising bubbles and the surrounded liquid phase is the driving force of the liquid flow, a flat gas holdup distribution suggests a small gas-liquid shear stress and a large gradient implies a large shear stress. As shown in Figure 5-26, the local gas holdups in the Riser are large in the reactor center with a small variation, and decrease sharply as the radius increases. Correspondingly, the shear stress in the Riser is low at the reactor center, and reaches a peak at  $r/R$  of 0.3, and finally decreases until reach the outer cylinder as displayed in Figure 5-25.

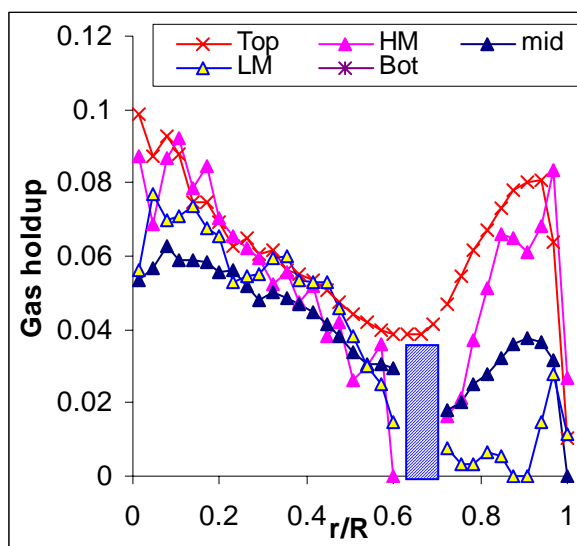


**Figure 5-30.** Axial evolution of the radial profiles of time- and azimuthally-averaged gas holdup at 1cm/s superficial gas velocities, 5 cm bottom clearance, and 3 cm top clearance.

**Effects of superficial gas velocities** The effects of superficial gas velocities on the local gas holdup profiles in the fully developed flow zone (i.e., the scanned middle level) are shown in Figure 5-31, where similar trends but different magnitudes are demonstrated for all superficial gas velocities investigated. Additionally, the effect of superficial gas velocity on the overall gas holdup is demonstrated in Figure 5-32.



Usually, the overall gas holdup can be easily calculated from the bed expansion or the differences between the static and the dynamic liquid levels, which is used to determine the transitional flow regime (Vial et al., 2001). Apparently, from Figure 5-32, the transition from the bubbly flow to the churn-turbulent regime for the studied reactor happens at around superficial gas velocity of 2 cm/s. In both the bubbly and the churn-turbulent flow regimes, the overall gas holdups are linear functions to the superficial gas velocities with different slopes.

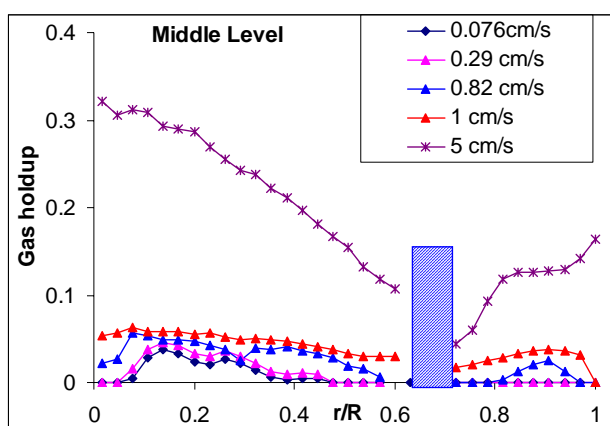


**Figure 5-31.** Effects of superficial gas velocities on the time- and azimuthally-averaged local gas holdup profiles in the middle of the column ( $H = 67.7$  cm) at operating condition of 5 cm bottom and 3 cm top clearances.

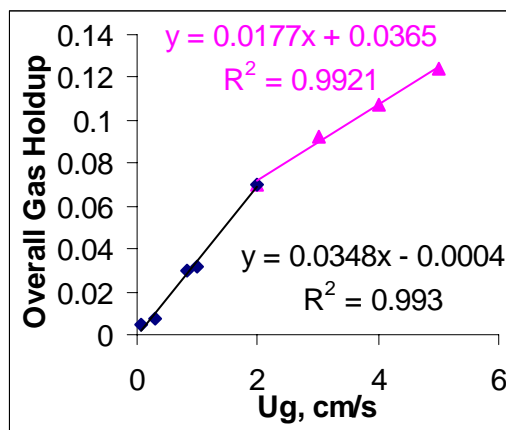


**Figure 5-32.** Effects of superficial gas velocities on the overall gas holdup at operating condition of 5 cm bottom and 3 cm top clearances.

**Effects of top and bottom clearance** The effects of top and bottom clearance on the local gas holdup profiles in the fully developed flow zone are shown in Figure 5-33. When top or bottom clearances change, the gas holdups in the Riser change only slightly while clear difference of the gas holdups in the Downcomer can be observed. In fact, the gas holdup in the Downcomer decreases as the top clearance increases. This indicates that an improved gas-liquid separation in the Top prevents bubbles being entrained into the Downcomer. On the other hand, the gas holdup in the Downcomer decreases considerably as the bottom clearance decreases, apparently due to the lower liquid flow velocity. These phenomena again confirm that the top and bottom clearances have an important effect on the gas-liquid separation in the Top and the energy dissipation on both the Top and the Bottom regions. They are consistent with the reports in the literatures, and also with the results of the Residence Time Distribution analysis.

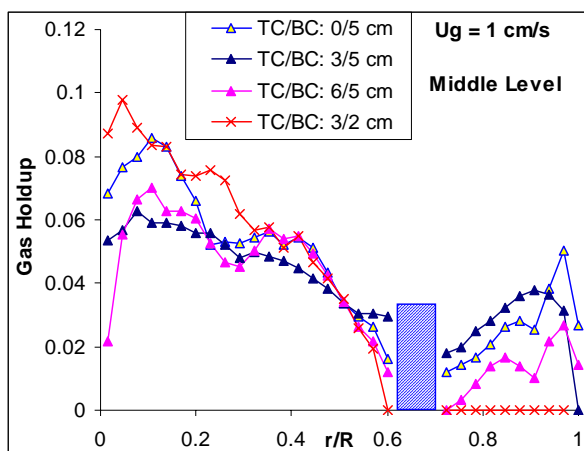


**Figure 5-33.** Effects of top and bottom clearances on the time- and azimuthally-averaged local gas holdup profiles in the middle of the column ( $H = 67.7$  cm) at operating condition of 1 cm/s superficial gas velocity.

## 5.7 Photobioreactor Analysis

The rich information obtained from the CARPT and CT experiments discussed above can be further utilized for photobioreactor analysis and to validate the dynamic growth rate model developed in Chapter 4.

### 5.7.1 Characterization of Flashing Lights

The methodology discussed in Chapter 4 was applied to characterize the light availability and fluctuations that a cell may experience, using CARPT measured particle trajectories obtained in this work. The temporal irradiance patterns were first calculated based on Equation (4-1) using the parameters listed in Table 4-2. Then the over-/under- charged cycles were identified from the irradiance patterns. Finally, the dynamic features of the irradiance pattern were represented by the PDFs of the cycle frequency and the dimensionless relaxation time as discussed below.

In Chapter 4, it was found that the flashing light effects are not prominent at operating conditions of low light intensities and low biomass concentrations (e.g., Case I at cell concentration of  $8 \times 10^6 \text{ cells/ml}$  and external light intensity of  $250 \mu\text{E/m}^2\text{s}$ , the initial operating condition of the experiments performed by Merchuk et al., 2000). Under such conditions, photolimitation effects are dominant and the time averaged light intensity is just slightly different from the volume averaged quantity. Therefore, only the other case discussed in Chapter 4 is considered here, i.e., Case II at a cell concentration of  $80 \times 10^6 \text{ cells/ml}$  (about the highest biomass concentration achieved in the experiments performed by Merchuk et al. 2000) and an external light intensity of  $2000 \mu\text{E/m}^2\text{s}$  (typical sunlight irradiance at noon). This case represents a typical operating condition for photobioreactors with industrial interest.

A typical irradiance pattern calculated for Case II is shown in Figure 5-34, together with the time averaged irradiance and the volume averaged irradiance for reference. It was

calculated by Equation (4-1) using CARPT measured particle trajectories obtained at operating conditions of 1cm/s superficial gas velocity, 5 cm bottom clearance, and 3 cm top clearance. The PDFs of the frequency and the dimensionless relaxation time for the identified over-/under- charged cycles are shown in Figure 5-35.

Figure 5-34 shows that the time-averaged irradiance is around 10% larger than the volume-averaged irradiance delivered to the cells. This is consistent with the results presented in Figure 5-10, where the occurrence density distribution of the particle is quite uniform in the whole reactor. Additionally, the dynamic features of the light fluctuations shown in Figure 5-31 are very similar to the features discussed in Chapter 4. The fluctuations are dominated by the high frequency cycles, and the light periods in the over-/under- charged cycles are very likely to be the same as the dark periods. Considering the isotropic nature of turbulence in the current bubbly flow regime, this is reasonable, as discussed in Chapter 4.

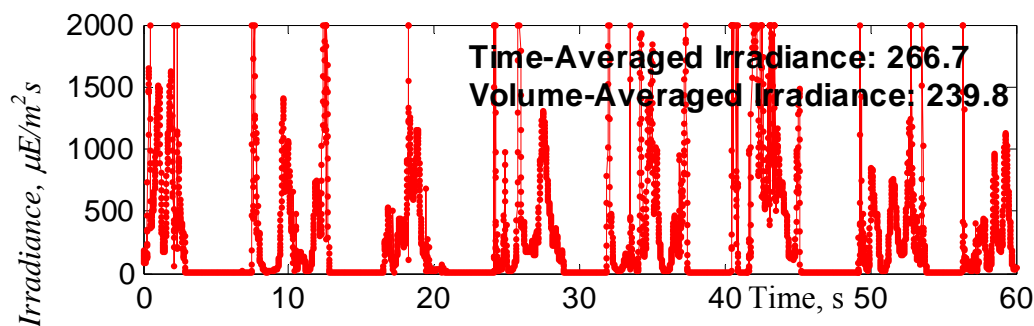


**Figure 5-34.** Temporal irradiance pattern calculated by Equation (4-1) using CARPT measured particle trajectories obtained at operating conditions of 1cm/s superficial gas velocity, 5 cm bottom clearance, and 3 cm top clearance. Calculation conditions: External Irradiance= $2000 \mu E m^{-2} s^{-1}$ ; Cell concentration= $80 \times 10^6$  cells/ml

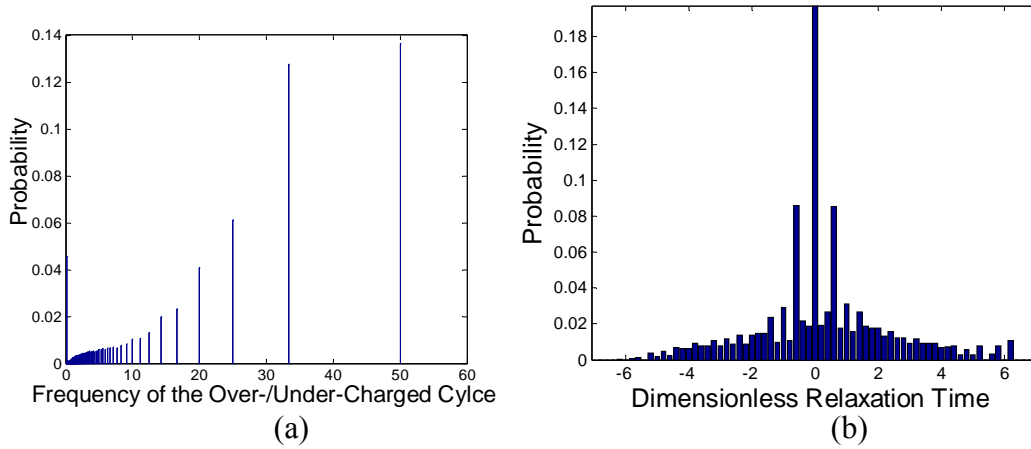


**Figure 5-35.** Characteristics of the light fluctuations delivered to the cells at the operating conditions of 1 cm/s superficial gas velocity, 5 cm bottom clearance, and 3 cm top clearance. (a). PDFs of the frequency for the over-/under- charged cycles; (b). PDFs of the dimensionless relaxation time,  $\varphi$ , for the over-/under- charged cycles.

**Effects of Superficial Gas Velocity** The effects of superficial gas velocities on the light fluctuations are shown in Table 5-2. The time-averaged irradiance and the average frequency of the over-/under- charged cycles are defined as:

$$I_{av}^t = \frac{1}{T} \int_0^T I(t) dt ; \quad f_{av} = \frac{N_c}{\sum_{N_c} 1/f_i} \quad (5-7)$$

where  $T$  is total sampling time,  $I(t)$  is the instant irradiance the cell experiences,  $N_c$  is the total number of over-/under- charged cycles identified, and  $f_i$  is the frequency of the  $i^{th}$  over-/under- charged cycle. The averaged dimensionless relaxation time ( $t_{over}/t_{under}$ ) shown in Table 5-2 is simply an arithmetic average for all cycles identified.

Table 5-2 does not show a clear trend of the time-averaged irradiances with the superficial gas velocity increases. When the superficial gas velocity increases, the time-averaged irradiance first decreases and then increases with a large variance. Moreover, a small change in superficial gas velocities from 0.82 cm/s to 1 cm/s results in a 15% difference in the time-averaged irradiances, which is quite unlikely. These results, quite similar to the trends observed for the macro-mixing status as discussed above, suggest that the

time-averaged irradiance is sensitive to the superficial gas velocity. However, just how superficial gas velocity affects the time-averaged irradiance is not clear.

On the other hand, the trends for the other parameters are very clear. As  $U_g$  increases, the averaged over-/under-charged cycle frequencies increase monotonically, while the dimensionless relaxation times are almost the same. These results indicate that faster light fluctuations can be achieved by increasing the superficial gas velocity, apparently due to the increased turbulence intensity, shown in Figure 5-22.

**Table 5-2.** Characteristics of light availability and fluctuation for the studied draft tube column reactor in an air-water system

$U_g$ , cm/s	Top Clearance, cm	Bottom Clearance, cm	$I_{av}^t$ , $\mu E/m^2 s$	$f_{av}$	$t_{over}/t_{under}$
0.29	3	5	284.7	0.81	0.46
0.82	3	5	227.1	0.94	0.46
1.0	3	5	266.7	1.10	0.47
5	3	5	324.0	1.85	0.48
1	0	5	271.0	0.99	0.47
1	3	5	266.7	1.10	0.47
1	6	5	264.8	1.16	0.47
1	3	2	209.0	0.95	0.46

**Effects of Top and Bottom Clearances** Table 5-2 also shows the effects of top and bottom clearances on the light fluctuations. As the top clearance increases, the time-averaged irradiances decrease noticeably, and the averaged frequency of the over-/under- charged cycles increases slightly. On the other hand, as the bottom clearance decreases, both the time-averaged irradiance and the over-/under- charged cycle frequency decrease to some extent. These trends are consistent with the changes of the liquid circulation velocities reported earlier.

### 5.7.2 Reactor Performance Evaluation

The CARPT data obtained in this study also provide information for the validation of the dynamic growth rate model developed in Chapter 4. Using this model, the performances of the studied draft tube airlift column at different superficial gas velocities were predicted. These predictions used the photosynthetic growth rate parameters estimated by Wu and Merchuk (2001), which are listed in Table 4-2, and the CARPT data obtained at corresponding superficial gas velocities in this study. The results are shown in Figure 5-36, together with the experimental data measured by Merchuk et al. (2000) and the predictions made in Chapter 4, in which the CARPT data obtained from a larger draft tube column reactor (20 cm diameter) were used.

Figure 5-36 clearly shows that the predictions for all superficial gas velocities based on the CARPT data obtained in this study considerably over-estimated the reactor performance compared to the experimental data. The predictions are even worse than the predicted results obtained in Chapter 4. A possible reason for such over-estimation is the air-water system used in this study. Since the physical properties can be very different in a real culturing system (further discussion of this topic is presented in Chapter 7), the measured particle trajectories in an air-water system may not be suitable.

The viscosity in a real culturing system is usually much higher than the viscosity in the air-water system (Eteshola et al., 1996, 1998; Geresh et al., 2002). Increasing the viscosity of the liquid phase enlarges the turbulent sub-layer near the column walls, where the turbulent intensity is low. The cells thus have less chance to access the highly illuminated surface, resulting in a lower time-averaged intensity. Additionally, the light fluctuations in a real culturing system may also be not as prominent as those in a water-system. For these reasons, the predictions based on CARPT data obtained from the air-water system over-estimate the reactor performance.

This over-estimation also contributes to the coincidentally good prediction made in Chapter 4. A larger column has a smaller surface to volume ratio, thus less light is supplied to the cells inside. For example, the time-averaged light intensity calculated from the CARPT data for the larger column (diameter of 20 cm) at superficial gas velocity of 1 cm/s is  $135 \mu E m^{-2} s^{-1}$  (as shown in Table 4-1 for Case I). Under the same conditions, the time-averaged light intensity for the smaller column is  $159 \mu E m^{-2} s^{-1}$ . As a result, these two contradictory effects, i.e., using CARPT data obtained from a larger column and using an air-water system, offset each other, resulting in a fairly good match with the experimental data.

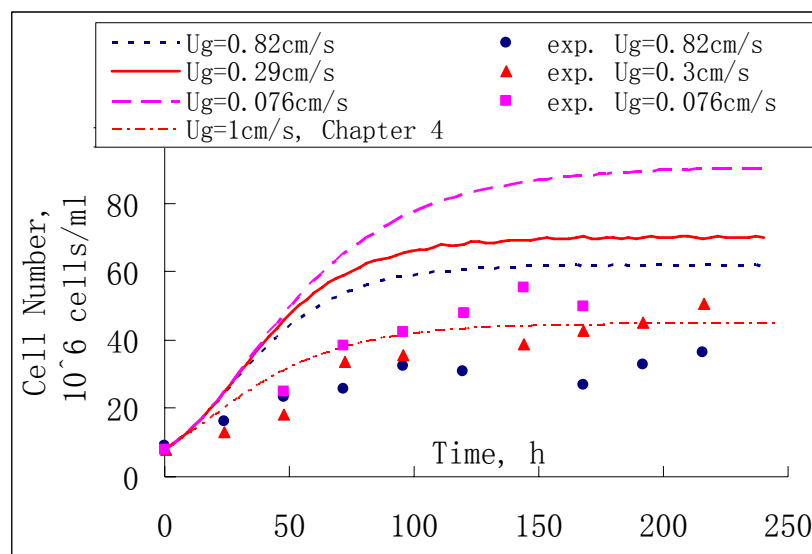


**Figure 5-36.** Photobioreactor performance predictions at different superficial gas velocities compared with the experimental data measured by Merchuk et al. (2000).

It should be pointed out that, although the predictions in this study over-estimated the reactor performance, Figure 5-36 also clearly shows that these predictions captured the trend of the reactor performance with changing superficial gas velocity. Among all conditions presented, the best reactor performance was obtained at a superficial gas velocity of 0.076 cm/s and the worst was obtained Ug of 0.82 cm/s. However, it is not clear



if increasing superficial gas velocity has similar effects on the liquid flow structures for both the air-water system and real microalgae culturing systems. Therefore, these results may be a coincidence again. Apparently, further verification of the dynamic model using CARPT data obtained from real culturing systems is required, which is discussed in Chapter 7.

## 5.8 Summary and Conclusions

In this study, hydrodynamics in a draft tube column reactor similar to the one used by Merchuk et al. (2000) were investigated using two advanced measurement techniques, i.e., CARPT and CT techniques. The local phenomena of the multiphase flow were discussed in detail providing in-depth information for reactor design and scale-up. Moreover, the results presented in this work provide rich information for photobioreactor analyses and for CFD simulation verifications, which is discussed in Chapter 6.

The following conclusions can be reached:

- A true residence time distribution analysis showed that the overall macro-mixing in the draft tube column reactor is close to plug flow, which is also true for the Riser and Downcomer regions. However, there is considerable bypassing and stagnancy in the Top and the Bottom regions, which can hardly be modeled as a CSTR.
- Significantly large turbulent kinetic energy is present in the Top and the Bottom regions, and spots of high shear stress exist there as well as the vicinity of the sparger.
- The transitional regime starts from  $U_g = 2\text{cm/s}$ .
- Increasing the superficial gas velocity considerably increases the gas holdup, the liquid flow velocities, and turbulence in the whole reactor, but does not necessarily improve the macro-mixing in the reactor, especially in the individual regions.
- The Top and Bottom clearances have significant effects on the flow structures (e.g., the turbulent kinetic energy, the shear stresses) in the Top and Bottom regions, and

the gas holdup in the Downcomer. These clearances thus influence the bulk liquid flow at the Riser and Downcomer. Decreasing the top or bottom clearances can radically change the magnitudes of the turbulent kinetic energy and the Reynolds shear stress in these two regions, which may have substantial effects on the photobioreactor performance.

- A light fluctuation analysis revealed that increasing the superficial gas velocity enhances the light fluctuations and affects light availability delivered to the cells. However, how superficial gas velocity affects the light availability is not clear.
- The predictions based on the dynamic growth rate model developed in Chapter 4 and using the CARPT data obtained in an air-water system considerably over-estimated the photobioreactor performance measured by Merchuk et al. (2000). However, the predictions captured the trend of the reactor performance with superficial gas velocity. Further verification of the dynamic model using CARPT data obtained from real culturing systems is required, which is discussed in Chapter 7.

It should be point out that the CARPT and CT techniques are not generally accessible to most researchers. Therefore, CFD modeling, a widely available technique, is a more favorable technique to study the local multiphase flow phenomena in photobioreactors for reactor design, scale-up, operation, and process intensification. The model validation of CFD simulations and its applicability on PBR analysis are discussed in the next chapter.

## **Chapter 6**

# **CFD Simulations for Local Flow Dynamics, Particle Tracking, and PBR Analysis in a Draft Tube Airlift Column Reactor**

### **6.1 Scope**

In-depth information of multiphase flow dynamics obtained by CARPT and CT techniques was primarily relied on to analyze photobioreactors and to integrate with photosynthesis for PBR performance evaluation in the previous chapters. However, it has to point out that, CARPT and CT are not generally accessible to most researchers in this field. A more widely available technique is required to study the local multiphase flow phenomena in photobioreactors for reactor design, scale-up, operation, and process intensification.

CFD technique, a powerful tool in obtaining rich information of flow dynamics, is such a favorable technique. It can provide an alternative method to obtain essential information for the PBR performance evaluation other than CARPT and CT measurements with much

lower cost. Therefore, successful integration of the CFD modeling with a photosynthetic model will form a more general approach for the photobioreactor analysis, which is attempted in this study.

In this Chapter, the feasibility of using CFD simulations to obtain needed hydrodynamic information for photobioreactor analysis is discussed. Using a commercialized CFD code, CFX-5.7 from Ansys Inc., both 2D and 3D simulations based on a two fluid model are used to study the multiphase flow dynamics in the draft tube column reactor investigated in Chapter 5. Different turbulence models and correlations for the interfacial momentum forces are tested against the experimental data obtained in Chapter 5, with the optimum models and correlations identified. A computationally feasible and promising model with the identified closures is further utilized to predict the motions of small neutrally buoyant particles (mimicking microorganism cells) for photobioreactor performance evaluations. Encouraging results were obtained; however, more realistic particle trajectories with better turbulent prediction and occurrence density distribution are required to apply CFD simulation for photobioreactor analysis.

## 6.2 Theory

A two-fluid model (Drew, 1983; Mudde and Van Den Akker, 2001) was used to study the multiphase flow dynamics at bubbly flow regime in the draft tube airlift column reactor investigated in Chapter 5. This approach is based on the Eulerian-Eulerian approach as discussed in Chapter 2. In this study, the commercialized CFD software package CFX5.7 (Ansys Inc.) was used to solve the obtained governing equations.

### 6.2.1 Mathematic Modeling of the Two-Fluid Model

Basic assumptions of the two-fluid model are:

- All phases are treated as interpenetrating continua. The probability of any one phase occurs in the multiphase flow field is given by the instantaneous volume fraction of that phase at that point. The sum total of all volume fractions at a point thus should be unity;
- Both fluids are treated as incompressible with uniform pressure field:

$$p = p_{\alpha} \quad \alpha = 1,2 \quad (6-1)$$

- The gas phase is assumed to be in the form of spherical bubbles;
- Turbulence in either phase is modeled separately;
- Mass exchange between phases is neglected;
- Isothermal condition is assumed in the whole domain; thus heat exchange is not considered.

Based on these assumptions, the conservation equations can be written as follows (CFX5.7 Manual). A more comprehensive derivation of these equations can be found elsewhere (Jacobsen, 1997; Joshi, 2001).

#### Continuity Equations

$$\frac{\partial}{\partial t}(r_{\alpha}\rho_{\alpha}) + \nabla \cdot (r_{\alpha}\rho_{\alpha}\vec{U}_{\alpha}) = 0 \quad (\alpha = 1, 2) \quad (6-2)$$

where  $\rho_\alpha$ ,  $\vec{U}_\alpha$  and  $r_\alpha$  are the density, the velocity vector, and the volume fraction of phase  $\alpha$ , respectively. The constraint for  $r_\alpha$  has to be imposed:

$$\sum_{\alpha=1}^2 r_\alpha = 1 \quad (6-3)$$

### Momentum Equations

$$\underbrace{\frac{\partial}{\partial t} (r_\alpha \rho_\alpha \vec{U}_\alpha)}_{\text{Time variance term}} + \underbrace{\nabla \cdot (r_\alpha (\rho_\alpha \vec{U}_\alpha \vec{U}_\alpha))}_{\text{Convection term}} = \underbrace{-r_\alpha \nabla p}__{\text{Pressure Gradient term}} + \underbrace{r_\alpha \rho_\alpha \vec{g}}_{\text{Body force term}} + \underbrace{\nabla \cdot (r_\alpha \mu_{\alpha, \text{eff}} (\nabla \vec{U}_\alpha + (\nabla \vec{U}_\alpha)^T))}_{\text{Reynolds Stress force term}} + \underbrace{\vec{M}_\alpha}_{\text{Interfacial momentum transfer term}} \quad (\alpha = 1, 2) \quad (6-4)$$

where  $\vec{g}$  is the gravity vector,  $p$  is pressure, and  $\mu_{\alpha, \text{eff}}$  is the effective viscosity of phase  $\alpha$ . The effective viscosity considers the contribution from both the molecular viscosity ( $\mu_\alpha$ ) and the dynamic viscosity ( $\mu_\alpha^T$ ) due to turbulence:

$$\mu_{\alpha, \text{eff}} = \mu_\alpha + \mu_\alpha^T \quad (6-5)$$

For turbulent flow, the dynamic viscosity is usually much larger than the molecular viscosity. It is a flow property and needs to be calculated by correlations or closures.

The fourth term on the right hand side of Equation (6-4),  $\vec{M}_k$ , takes into account of the inter-phase momentum transfer between different phases due to interfacial forces:

$$\vec{M}_\alpha = \sum_{\beta \neq \alpha} \vec{M}_{\alpha\beta} = \sum_{\beta \neq \alpha} \left( \vec{M}_{\alpha\beta}^D (\text{Drag Force}) + \vec{M}_{\alpha\beta}^L (\text{Lift Force}) + \vec{M}_{\alpha\beta}^{VM} (\text{Virtual Mass Force}) + \vec{M}_{\alpha\beta}^{TD} (\text{Turbulence Dispersion Force}) + \dots \right) \quad (6-6)$$

where  $\alpha$  and  $\beta$  stand for different phases (in the following sections,  $\alpha$  stands for the liquid phase and  $\beta$  stands for the gas phase). Closures are needed to model these interfacial forces, which is discussed in the following sections.

## 6.2.2 Multiphase Turbulent equations

The dynamic viscosity shown in equation (6-5) is a flow property. In gas-liquid flows, since the dispersed phase, i.e., the gas phase, has a much smaller density than the continuous phase (i.e., the liquid phase), it is well-known that the flow inside of the bubbles has very limited effect on the liquid flow (Drew, 1983). Therefore, a simple algebraic model is adopted in this work to compute the dynamic viscosity of the dispersed phase, which relates its dynamic viscosity to the continuous phase's viscosity as (Markatos, 1986; CFX5 manual, 2004):

$$\mu_{\beta}^T = \frac{\rho_{\beta}}{\rho_{\alpha}} \frac{\mu_{\alpha}^T}{\sigma} \quad (6-7)$$

where  $\alpha$  stands for the liquid phase and  $\beta$  stands for the gas phase.

The situation is much more complex in computing the continuous phase's dynamic viscosity. In multiphase flow, turbulence could be stemmed from either the shear stresses within the continuous phase or the rising bubbles. The dynamic viscosity thus contains two components, i.e., viscosity due to the shear induced turbulence,  $\mu_{\alpha}^{s,T}$ , and viscosity due to the bubble induced turbulence,  $\mu_{\alpha}^{b,T}$ .

Many approaches have been proposed to compute the shear induced dynamic viscosity (Markatos, 1986), such as the  $k$ - $\varepsilon$  model (after modified for multiphase flow) and the Reynolds shear stress model. For example, the  $k$ - $\varepsilon$  turbulent model, proposed by Launder and Spalding (1974), calculates the shear induced dynamic viscosity by:

$$\mu_{\alpha}^{s,T} = C_{\mu} \rho_{\alpha} \left( \frac{k_{\alpha}^2}{\varepsilon_{\alpha}} \right) \quad (6-8)$$

where  $C_{\mu}$  is a constant,  $k_{\alpha}$  is the turbulent kinetic energy and  $\varepsilon_{\alpha}$  is the turbulent dissipation rate for phase  $\alpha$ . The conservation equations for  $k_{\alpha}$  and  $\varepsilon_{\alpha}$  are:

$$\frac{\partial}{\partial t} (r_{\alpha} \rho_{\alpha} k_{\alpha}) + \nabla \cdot (r_{\alpha} \rho_{\alpha} \bar{U}_{\alpha} k_{\alpha}) = \nabla \cdot (r_{\alpha} (\mu_{\alpha} + \frac{\mu_{\alpha}^{s,T}}{\sigma_k}) \cdot \nabla k_{\alpha}) - r_{\alpha} (P_{\alpha} - \rho_{\alpha} \varepsilon_{\alpha}) \quad (6-9)$$

and

$$\frac{\partial}{\partial t}(r_\alpha \rho_\alpha \varepsilon_\alpha) + \nabla \cdot (r_\alpha \rho_\alpha \vec{U}_\alpha \varepsilon_\alpha) = \nabla \cdot (r_\alpha (\mu_\alpha + \frac{\mu_\alpha^{s,T}}{\sigma_\varepsilon}) \cdot \nabla \varepsilon_\alpha) + r_\alpha \frac{\varepsilon_\alpha}{k_\alpha} (C_{\varepsilon 1} P_\alpha - C_{\varepsilon 2} \rho_\alpha \varepsilon_\alpha) \quad (6-10)$$

where  $C_{\varepsilon 1}$ ,  $C_{\varepsilon 2}$ ,  $\sigma_k$  and  $\sigma_\varepsilon$  are constants; and the production term,  $P_\alpha$ , is defined as:

$$P_\alpha = \mu_\alpha^{s,T} \nabla \vec{U} \bullet (\nabla \vec{U} + \nabla \vec{U}^T) - \frac{\mu_\alpha^{s,T}}{\rho \text{Pr}_t} \vec{g} \bullet \nabla \rho \quad (6-11)$$

As for the bubble induced dynamic viscosity, the model proposed by Sato and Sekaguchi (1975) was used:

$$\mu_\alpha^{b,T} = 0.6 \rho_\alpha r_\beta d_b |\vec{U}_\beta - \vec{U}_\alpha| \quad (6-12)$$

where  $d_b$  is the bubble diameter.

## 6.2.3 Interfacial Momentum Forces

Interfacial momentum forces in the governing momentum Equation (6-4) account for the interactions between the continuous phase and the dispersed phase. For gas-liquid flows, important interfacial forces include drag, lift, turbulent dispersion, and added mass or virtual mass forces. Closures are required to model these forces, which have been extensively discussed in the literature (Jacobsen et al., 1997; Joshi, 2001), and are briefly introduced in this section.

### 6.2.3.1 Drag Force

Drag force arises when bubbles move at a different velocity to the surrounded liquid phase. It is the most important interfacial force, and is a function of the local slip velocity between the continuous and the dispersed phases:

$$n_p \vec{D}_p = \frac{3}{4} \frac{C_D}{d_p} r_\beta \rho_\alpha |\vec{U}_\beta - \vec{U}_\alpha| (\vec{U}_\beta - \vec{U}_\alpha) \quad (6-13)$$



where  $C_D$  is the drag coefficient required to compute the drag force,  $\alpha$  stands for the liquid phase, and  $\beta$  stands for the gas phase. Many different correlations can be found in the literature to compute the drag coefficient,  $C_D$ . In this work, the following drag correlations were tested:

**Constant Drag Coefficient (Jacobsen et al., 1997; Joshi, 2001):**

$$C_D = 0.44 \quad (6-14)$$

**Ishii-Zuber Correlation (1979):**

$$C_D(\text{ellipse}) = 2/3 \times Eo^{1/2}, \quad Eo = \frac{g \cdot (\rho_\alpha - \rho_\beta) \cdot d_b^2}{\sigma} \quad (6-15)$$

Where  $Eo$  is the Eotvos number considering the bubble shape (i.e., the ratio between the gravitational and the surface tension forces) and  $\sigma$  is the surface tension of the gas phase.

**Schiller Naumann Correlation (1935):**

$$C_D = \frac{24}{Re_b} (1 + 0.15 Re_b^{0.678}) \quad (6-16)$$

where the bubble Reynolds number,  $Re_b$ , is defined as:

$$Re_b = \frac{\rho_\alpha |\vec{U}_\beta - \vec{U}_\alpha| d_\beta}{\mu_\alpha} \quad (6-17)$$

**Grace Correlation (Grace et al., 1976):**

$$C_D = \frac{4}{3} \frac{gd}{U_T^2} \frac{\nabla \rho}{\rho} \quad (6-18)$$

where the terminal velocity for the bubble,  $U_T$ , is given by:

$$U_T = \frac{\mu_\beta}{\rho_\alpha \cdot d} M^{-0.149} (J - 0.857) \quad (6-19)$$

$$J = \begin{cases} 0.94H^{0.757} & 2 < H < 59.3 \\ 3.42H^{0.441} & H > 59.3 \end{cases}$$

$$H = \frac{4}{3} Eo \cdot M^{-0.149} \left( \frac{\mu_\alpha}{0.0009} \right)^{-0.14}$$

$$M = \frac{g\mu_\alpha^4(\rho_\alpha - \rho_\beta)}{\rho_\alpha^2 \sigma_\alpha^3}$$

### 6.2.3.2 Lift Force

Lift force is a term referring to interfacial forces acting on the lateral direction, the direction perpendicular to the major flow direction. Lateral forces with different mechanisms have been proposed, such as the Magnus force due to bubbles' rotations, and the Saffman force due to the shear flow or the velocity gradient around the bubbles (Jacobsen et al., 1997). In bubbly flow regime, Saffman (1965, 1968) found that the Saffman force is usually an order of magnitude larger than the Magnus force. Therefore, only the Saffman force was tested in this work (Jacobsen et al., 1997):

$$\vec{F}_\alpha = r_\beta \rho_\alpha C_L (\vec{U}_\beta - \vec{U}_\alpha) \times (\nabla \times \vec{U}_\alpha) \quad (6-20)$$

where  $C_L$  is non-dimensional lift force coefficient,  $\alpha$  stands for the liquid phase, and  $\beta$  stands for the gas phase.

### 6.2.3.3 Turbulent Dispersion Force

Turbulent dispersion force takes into account of the turbulent diffusion of the dispersed phase in the continuous phase. It is derived by Favre-averaging the multiphase Navier-Stokes equation (Lopez de Bertodano, 1998):

$$\vec{M}_\alpha^{TD} = -\vec{M}_\beta^{TD} = -C_{TD} \rho_\alpha k_\alpha \nabla r_\alpha \quad (6-21)$$

where  $C_{TD}$  is a constant, usually in the range of 0.1~0.5.

## 6.2.4 Particle (Cell) Tracking

In a photobioreactor, the algal cells' movement determines the pattern of how they are exposed to the light energy, and thereby their growth rate. Hence, it is very important to track the cells' trajectories for photobioreactor analysis, design, and process intensification. These cells' trajectories should be able to statistically represent the behavior of all cells in the reactor for a meaningful analysis. Thus, the trajectories should cover the whole flow domain with statistically plenty of occurrence numbers at everywhere in the domain. This requires to trace either a single algal cell for a very long time (e.g., 24 hours as in CARPT experiments discussed in Chapter 5), or to trace a large number of cells for a relatively short time. In CFD simulation, the first approach is usually very time-consuming. Therefore, the second approach was used in this work.

The movement of algal cells in the reactor was simulated by introducing particles with same characteristics (i.e., density and size) as algal cells into the fluid domain. In a Lagrangian reference, the motion of the particles was computed by solving the famous Basset-Boussinesq-Oseen motion equation which takes into account of the forces acting on the particle (CFX manual, 2004; Delnoij et al., 1997a)

$$\begin{aligned}
 m_p \frac{d\vec{v}_p}{dt} = & \underbrace{\frac{1}{8} \pi \rho d^2 C_D |\vec{v}_f - \vec{v}_p| (\vec{v}_f - \vec{v}_p)}_{\text{Term I}} + \underbrace{\frac{\pi d^3 \rho_f}{6} \frac{d\vec{v}_f}{dt}}_{\text{Term II}} \\
 & + \underbrace{\frac{\pi d^3 \rho_f}{12} \left( \frac{d\vec{v}_f}{dt} - \frac{d\vec{v}_p}{dt} \right)}_{\text{Term III}} + \underbrace{\frac{\pi d^3}{6} (\rho_p - \rho_f) \vec{g}}_{\text{Term IV}}
 \end{aligned} \tag{6-22}$$

where  $m_p$  is the particle mass,  $d$  is its diameter,  $\rho$  is its density, and  $\vec{v}$  is the velocity vector, with the subscripts  $p$  stands for particle and  $f$  for the fluid (the continuous phase). The terms on the right hand of the equation is explained as follows.

- Term I is the drag force due to the slip velocity between the continuous phase and the particle. The drag coefficient  $C_D$  is calculated by Schiller Naumann's correlation as incorporated in the CFX5.7 code.
- Term II considers the force applied on the particle due to the pressure gradient surrounding the particle caused by the fluid acceleration.
- Term III is the virtual mass force due to the acceleration of the particle. Since the density difference between the particle and the continuous phase is very small, there is no much difference between their velocity accelerations. Therefore, this term is not important and neglected in this study.
- Term IV is the body force due to buoyancy.
- Other forces, such as the Basset force and Saffman force, are not important with relatively smaller magnitude, and thus neglected in this work.

Due to the random nature of turbulent flow, the motion equation (6-22) needs to be solved in a Eulerian-Lagrangian reference in transient simulations. However, tracking a large amount of particles (e.g., more than 4000) in a 3D domain could be computationally extremely expensive. Therefore, in this work, a pseudo Eulerian-Lagrangian approach (Rammahan, 2002) was used, i.e., solving the motion equation (6-22) in a steady state simulation but considering the effects of turbulence on the particle motion (more details of this approach are discussed in Chapter 2). This approach first uses an Euler/Euler approach to generate the liquid flow field by steady state simulations, and then introduces particles into the simulated flow field, by which the particles' motions (i.e., trajectories) within the flow domain are numerically computed by solving equation (6-22).

Since a steady state simulation gives a time independent flow field (e.g.,  $dv_f/dt = 0$ ), the particle velocities,  $v_p$ , computed by equation (6-22) are actually a time-averaged quantity. Under such conditions, the computed particle trajectories are deterministic. In other words, the trajectory of a particle injected at a given location is unique, which is not true due to the chaotic nature of turbulence. Therefore, a fluctuating component has to be added to the mean particle velocity to consider the turbulent dispersion of the tracer particles.

To consider the turbulent dispersion of the tracer particles, following assumptions are made in CFX5.7 code.

- A particle is always within a single turbulent eddy with characteristic fluctuating velocity ( $v_f'$ ), lifetime ( $\tau_e$ ), and length scale ( $l_e$ ).
- A particle immediately acquires the eddy's fluctuating velocity when the particle enters the turbulent eddy.
- Only when the particle-eddy interaction time exceeds the eddy's lifetime,  $\tau_e$ , or the displacement of the particle relative to the eddy is larger than the eddy's length,  $l_e$ , the particle is assumed to be entering a new turbulent eddy and acquires a new fluctuating velocity.

Based on the mean local turbulence properties, the fluctuating velocity, the eddy lifetime and length were calculated as (CFX manual, 2004):

$$\vec{v}_f' = \Gamma \sqrt{2k/3}, \quad \tau_e = \frac{l_e}{\sqrt{2k/3}}, \quad \text{and} \quad l_e = \frac{C_\mu^{3/4} k^{3/2}}{\varepsilon} \quad (6-23)$$

where  $k$  and  $\varepsilon$  are, respectively, the continuous phase's local turbulent kinetic energy and the dissipation rate obtained from the turbulence model,  $C_\mu$  is the turbulent constant in equation (6-8), and variable  $\Gamma$  is a randomly chosen number. This random number has a normal distribution and takes into account of the non-deterministic nature of the turbulent flow.

### 6.2.5 Mathematical Solution

The commercial code CFX5.7 employs a finite control volume approach to discretise the governing Navier-Stokes equations. High resolution scheme was used in this work to compute the advection terms. This scheme, combining the first order upwind difference scheme with a numerical advection correction term, is believed to be both accurate (close to second order scheme) and bounded (CFX5.7 manual, 2004).

The discretised governing equations are a set of linear equations. In CFX5.7, a coupled solver is used to solve these equations, which are solved in a fully implicit mode.

## 6.3 CFD Simulation Types

The flow dynamics in the draft tube column reactor studied in Chapter 5 and shown in Figure 5-1 were simulated by both 2D and 3D CFD simulations.

### 6.3.1 2D Simulations

Due to its simplicity and low computational costs, 2D symmetric steady state simulations have been widely used in the literature. In this work, such simulations were first conducted to test their capability on capturing the mean flow within the bubbly flow regime (i.e., at superficial gas velocity of 1cm/s). Figure 6-1 shows the geometry and the gridings used in the computations. The computational domain is consists of a 30° wedge cut from the column with the draft tube and the sparge regions being further cut out. This computational domain has a height of 1.16 *m*, same to the dynamic liquid level observed in experiments, and a radius of 0.065m, same to the column dimension. An equally spaced mesh in both the radial and the axial directions were used, with the mesh size of 2.5mm in a fine griding case and 5mm in a coarse griding case (to obtain a mesh size free solution). On the tangential direction, only one mesh cell was considered in the 2D simulations as shown for the top face in Figure 6-1.

Neumann boundary conditions with zero gradient (e.g.,  $du/dr=0$ ) were applied to the center axis ( $r = 0$ ) and the front and back planes, where symmetric has to be imposed due to the nature of 2D simulations. On the upper surface of the sparger, the Dirichlet boundary condition was applied with gas upward velocity of 0.38 m/s and volume fraction of 0.5 to give a superficial gas velocity of 1 cm/s (for other superficial gas velocities, these two values need to be specified). On the top surface of the whole column, a degassing boundary condition was applied. Such degassing boundary condition was implemented by adding an extra sink term for both phases on the top domain surface, so that the liquid elements touched this surface are bounded back while the gas phase can be eliminated in a way as if it goes out of the domain. Such degassing boundary condition can considerably reduce the computational cost because only the part of the column below the gas-liquid interface

needs to be modeled. It also has an advantage of enhance solution convergence as observed in the numerical experiments when a pseudo-steady state can be assumed.

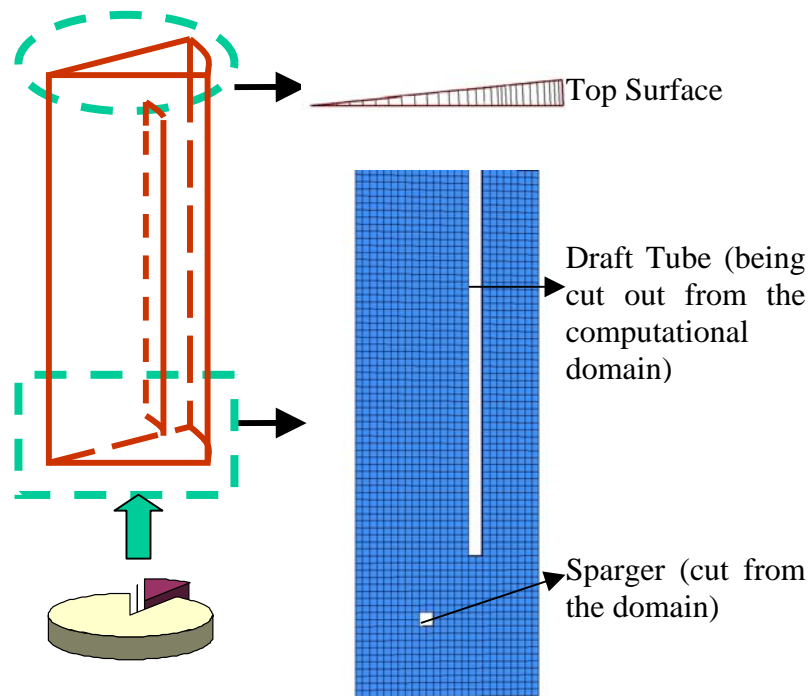


**Figure 6-1.** Geometry and gridding for the 2D steady state simulations

### 6.3.2 3D simulations

Both 3D transient and steady state simulations were carried out in this work to capture the flow dynamics. However, due to the high computational cost of the transient flow simulations, 3D steady state simulations were mainly used to test the turbulent models and the closures. This is justified by the low superficial gas velocity used in this work, thus a pseudo-steady state could be reached.

Figure 6-2 shows the geometry and the gridings used in the 3D simulations. In 3D transient simulations, the whole column was considered (i.e.,  $H=1.5\text{m}$ ), while in 3D steady state simulations, only the part of the column below the gas-liquid interface was modeled (i.e.,

H=1.16m). In all 3D simulations, the draft tube and the sparger were cut out from the computational domain. Moreover, the real circular ring sparger as shown in Figure 5-1 was modeled as a rectangular ring (shown in Figure 5-2b). Such modification of the sparger in the simulation is justified by the fact that the sparger shape has very limited effects on the global flow dynamics in the airlift column reactor with aspect ratio more than 8 (Chisti, 1998). The aspect ratio of the riser for the studied column is 13. This modification has also an advantage of applying structured hex gridding, which is important in reducing the computational error and facilitating the solution convergence.

Figure 6-2c shows the gridding on a cross-sectional plane, where finer gridding at the wall regions was used. This is also true for the gridding on the axial direction as shown in Figure 6-3d. Cases with two different mesh sizes were tested for the 3D simulations. The cases with coarse gridding have totally 48,132 elements with a mesh size of around 5mm, while cases with fine gridding have totally 271,360 elements with a mesh size of around 2.5 mm.

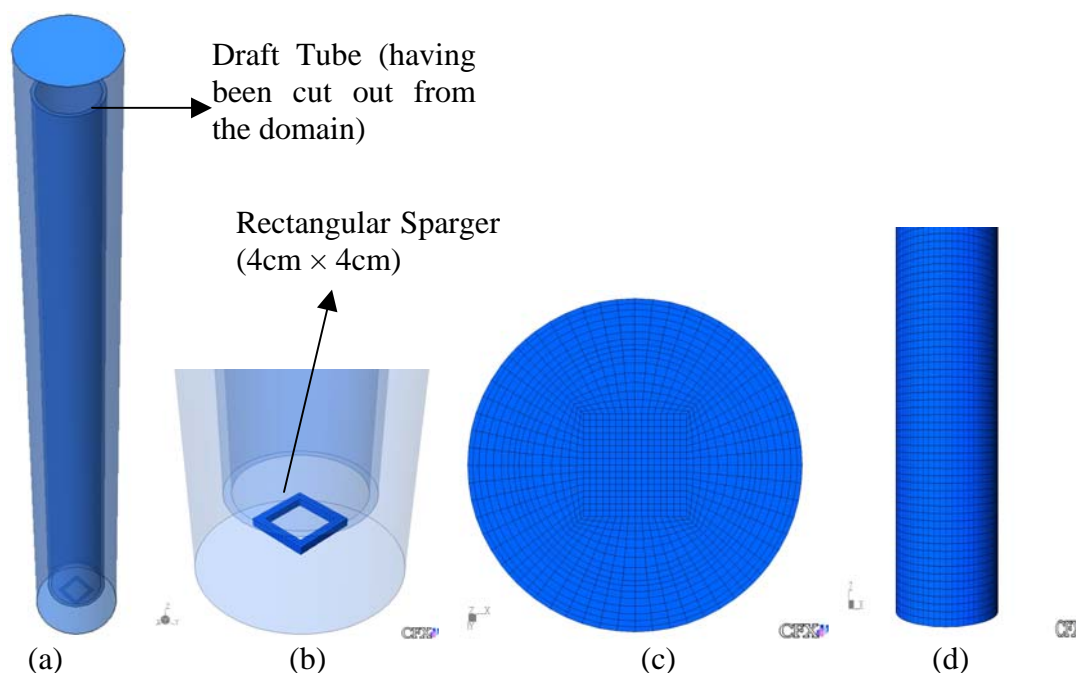


**Figure 6-2.** Configurations of the computational domain in 3D simulations. (a) Overview of the computational geometry for a 3D steady state simulation with height of 1.16m (the whole column with height of 1.5m is modeled in a 3D transient simulation); (b) Sparger configuration; (c) Mesh on the cross-sectional plane for the fine gridding; (d) Mesh in the axial direction for the fine gridding.



Similar to the 2D simulations, a Dirichlet boundary condition was applied to the upper face of the sparger, where the gas inlet velocity and its volume fraction are specified. The product of these two variables gives the desired superficial gas velocity of the simulations. On the top domain surface, a degassing boundary condition was applied for 3D steady state simulations, while a constant pressure boundary condition ( $P=1\text{ atm}$ ) was applied on the top domain surface for 3D transient simulations, in which a pseudo-steady state does not need to be assumed.

As for the initial conditions, a close to the pseudo-steady state condition was assigned to facilitate the convergence of the solution in 3D steady state simulations, while in the 3D transient simulations, the initial conditions were assigned to be the same as the real conditions before experiments start:

$$r_g = \begin{cases} 1 & H > 1.16m \\ 0 & H \leq 1.16m \end{cases}; \quad u_g = u_l = 0m/s \quad (6-24)$$

## 6.4 Closure Evaluations

Numerical CFD simulations were carried out to study the flow dynamics in the draft tube airlift column reactor using commercial code CFX5.7 (Ansys Inc.). The results for operating condition of  $1\text{ cm/s}$  superficial gas velocity are discussed in this section. Under the default options (i.e., the  $k-\varepsilon$  turbulence model, Grace drag law, Lopez de Bertodano's turbulent dispersion force with coefficient of 0.3), different types of simulations (i.e., 2D, 3D, steady state, and transient simulations) with different gridding sizes were first conducted to identify a type of simulation with low computational cost but good accuracy.

Such type of simulation then was relied on to test the turbulent models and various closures for the interfacial momentum forces (i.e., the drag force, the lift force, the turbulent dispersion force). To identify optimum models and closures, the simulation results were compared against the CARPT and CT data obtained in Chapter 5 in terms of the axial

liquid velocity, turbulent kinetic energy, and the local gas holdup. These parameters are the most sensitive ones to the simulation. The simulation accuracy of other flow dynamic parameters, such as the shear stresses, is usually within the range of the simulation accuracy of the above mentioned three parameters. The identified models and closures were further utilized to simulate the flow dynamics at different superficial gas velocity, and more importantly to predict the trajectories of small neutrally buoyant particles (mimicking *Porphyridium sp.* cells) for photobioreactor performance evaluation. The following sections discuss these results.

#### **6.4.1 Effects of Types of Simulations and Griding Size**

Three types of simulations (i.e., 2D steady state, 3D steady state, and 3D transient simulations) were tested to find the balance between the computational cost (in terms of the CPU time, the net time a computer CPU spends on the simulation job) and the simulation accuracy. Figures 6-3 show the comparison of these simulations with the experimental data obtained by CARPT (for axial liquid velocity and turbulent kinetic energy profiles) and CT (for local gas holdup profile at the middle scanned level,  $H=67.7$  cm).

It is clear from these figures that the 2D simulation results noticeably deviate from the experimental data, especially for the gas holdup profiles, although results with finer griding are slightly better as shown in Figure 6-3b. This is consistent with the literature that 2D symmetric steady state simulations can even hard to capture the mean multiphase flows (Bertola et al., 2003). On the other hand, the 3D steady state simulations precisely captured the axial liquid velocity, reasonably agreed with the local gas holdup profiles, but considerably under-estimated the turbulent kinetic energies. Considering the errors from both the experiments and the simulations, the agreements between them are encouraging.

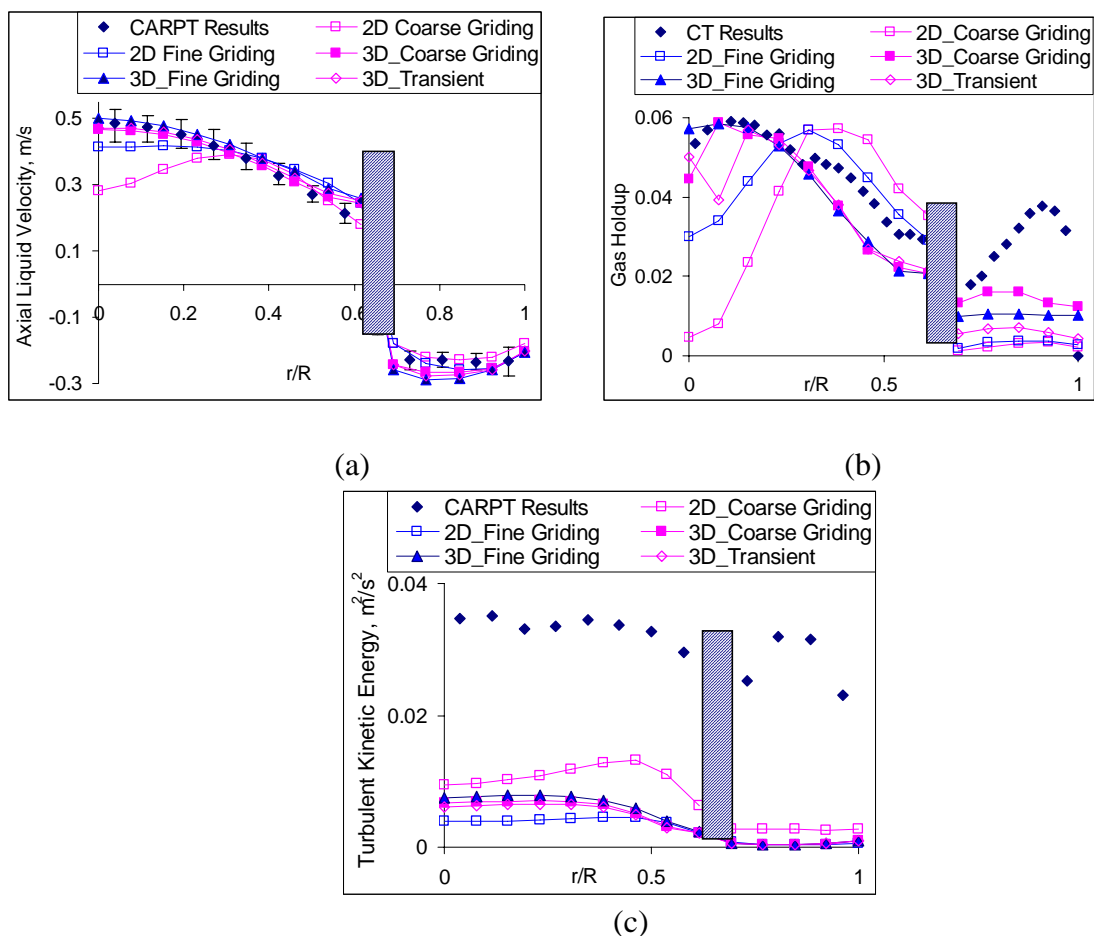


**Figure 6-3.** Effects of gridding on the CFD simulations. (a) Effects on the axial liquid velocity profile; (b) Effects on the gas holdup profile; (c) Effects on the turbulent kinetic energy profile.

Generally, CARPT technique is considered to be an accurate measurement for the time averaged liquid velocities but not for the turbulent kinetic energy as discussed in Chapter 5. The white noises and the  $\gamma$ -ray radioactivity fluctuation nature introduce noises into the CARPT reconstruction errors, and thus in the computations of the fluctuating velocity. Since the errors are squared and summed in the calculation of the turbulent kinetic energy, this technique usually over-estimates the turbulent kinetic energy even after introducing the advanced wavelet filtering method. In addition, since uniform bubble size is used in the

CFD simulations, it is hard for the simulation to capture the gas holdups in the downcomer regions where many tiny bubbles were observed in the experiments.

It is also very obvious from Figure 6-3 that the 3D steady state simulation results based on either the coarse or the fine gridings are very close to each other. This is because of the used  $k-\varepsilon$  turbulent model, which is well-known to over-estimate the eddy viscosity and damp out the small scale turbulences. Therefore, decreasing the griding size after certain value does not affect the simulation results, but considerably increases the computational cost. For example, the convergence CPU time associated with the fine griding in 3D steady state simulations is four times more than the time associated with the coarse griding.

Very similar results were also obtained from the 3D transient simulation using the coarse griding. These results were time-averaged for quantitative comparison. However, such 3D transient simulation usually takes more than one week to get any quantitative meaningful results. Therefore, it is not realistic to use 3D transient simulations for closure tests. Instead, 3D steady state simulations using a coarse griding were used in the following sections to test the turbulent models and closures.

### **6.4.2 Turbulent Models**

Since the  $k-\varepsilon$  model considerably under-estimates the turbulent intensity in the studied airlift reactor, a Reynolds shear stress model incorporated in CFX5.7 was also tested. This Reynolds shear stress model expresses each component of the Reynolds shear stresses with separate transportation equations derived from the Navier-Stokes equations. It is believed that such treatments can better resolve the small scale turbulence. However, due to the introduction of second and third order correlations, further modeling of these high order correlations are inevitable, which impose considerable challenges to apply such turbulent model in multiphase flow simulations.

Figure 6-4 shows the simulation results of the Reynolds shear stress model together with the simulation results of the  $k-\varepsilon$  model and the experimental data obtained by CARPT and CT. Although the turbulent kinetic energies predicted by the Reynolds shear stress model are closer to CARPT data comparing to the results of the  $k-\varepsilon$  model, its predictions on the mean multiphase flow, i.e., the axial liquid and the gas holdup profiles, are even worse. Moreover, due to the complexity of this model, the convergence is not as good as the  $k-\varepsilon$  model (the momentum residuals are almost one order of magnitude larger). Considering these, the  $k-\varepsilon$  model will be used further to test the closures for interfacial momentum transfer.

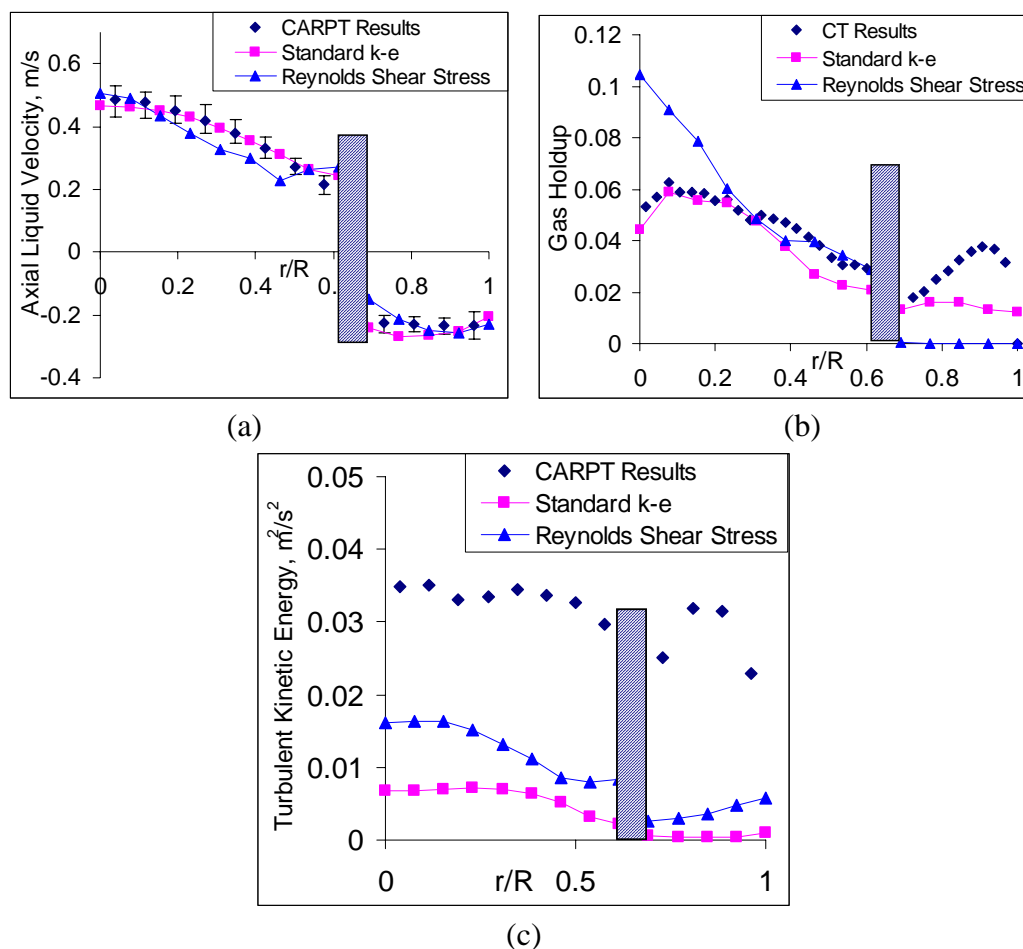


**Figure 6-4.** CFD simulation results by different turbulent models. (a) Results of the axial liquid velocity profile; (b) Results of the gas holdup profile; (c) Results of the turbulent kinetic energy profile.

### 6.4.3 Effects of Turbulent Dispersion Coefficient, $C_\mu$

A simple and widely used method to compensate the  $k-\varepsilon$  model's limitations on the turbulent intensity prediction for two-phase flow is to adjust the turbulent dispersion coefficient,  $C_\mu$  in Equation (6-8) (Sokolinchin et al., 1994). When this coefficient decreases, the dynamic viscosity calculated by Equation (6-8) decreases, resulting in a higher turbulent intensity. This simple method is attempted in this work.

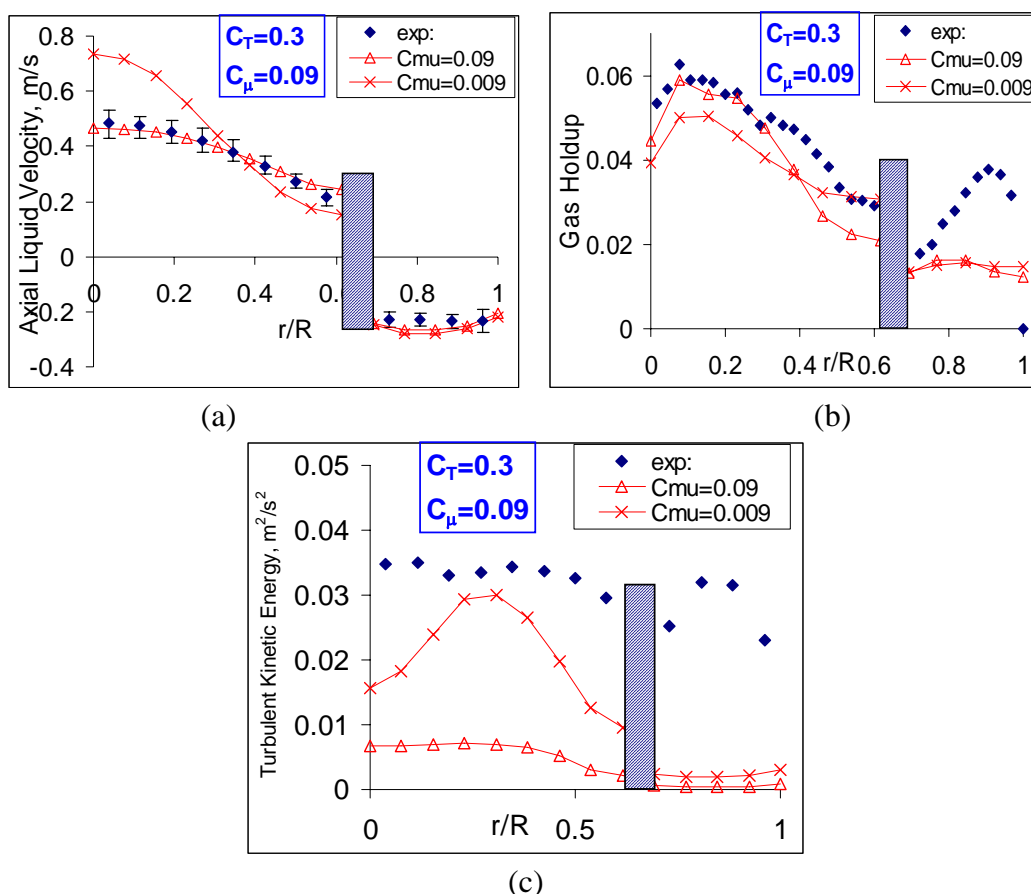


**Figure 6-5.** CFD simulation results using different magnitude of turbulent dispersion coefficient,  $C_\mu$ . (a) Results of the axial liquid velocity profile; (b) Results of the gas holdup profile; (c) Results of the turbulent kinetic energy profile.

Figure 6-5 shows the effects of reducing the turbulent dispersion coefficient in 3D steady state simulations. When  $C_\mu$  decreases for 10 times, almost one order of magnitude larger turbulent kinetic energies were obtained at  $r/R=0.3\sim 0.4$ . The obtained kinetic energies are closer to the CARPT measurement comparing to the simulations using the standard  $C_\mu$  value.

However, the effects of reducing  $C_\mu$  are twofold: as the turbulent intensity increases, the turbulent diffusion of the dispersed phase is also enhanced, resulting in a less steeper gas holdup profile as shown in Figure 6-5b. Due to the enhanced interfacial momentum transfer, the slip velocity between the gas and the liquid phases decreases which in turn results in a steeper axial liquid velocity profile as shown in Figure 6-5a. Therefore, although reducing the turbulent dispersion coefficient results in a larger turbulent intensity predicted by the  $k-\varepsilon$  model, such improvement can be greatly offset by the loss of mean flow prediction capability. Indeed, when using a low  $C_\mu$  in a 3D transient simulation, a highly dynamic multiphase flow was observed in one attempt, which however could be very misleading. Accordingly, the standard  $C_\mu$  value will be used throughout the rest of numerical experiments.

#### 6.4.4 Drag Correlations

Due to the significance of the drag force on multiphase flow simulations, the following drag coefficient correlations were tested: constant coefficient ( $CD=0.44$ ), Schiller Naumann's (1935), Ishii-Zuber's (1979), and Grace's (1976) correlations. These correlations were developed for bubbly flow regime.

Figure 6-6 shows the simulation results together with the experimental data. It's clear from Figure 6-6 that, the predicted axial liquid velocity and turbulent kinetic energy profiles are quite close to each other for all drag laws, while the obtained gas holdup profiles are quite different. Simulations based on a constant drag coefficient and Schiller Nauman's

correlation considerably under-estimate the gas holdups in both the riser and the downcomer region. On the other hand, simulations based on both Grace's and Ishii-Zuber's correlations properly predicted the CARPT measured axial liquid velocities, and reasonably agree with the CT measured gas holdups. Among these simulations, clearly the simulation based on Ishii-Zuber's correlation agrees with the experimental data best.

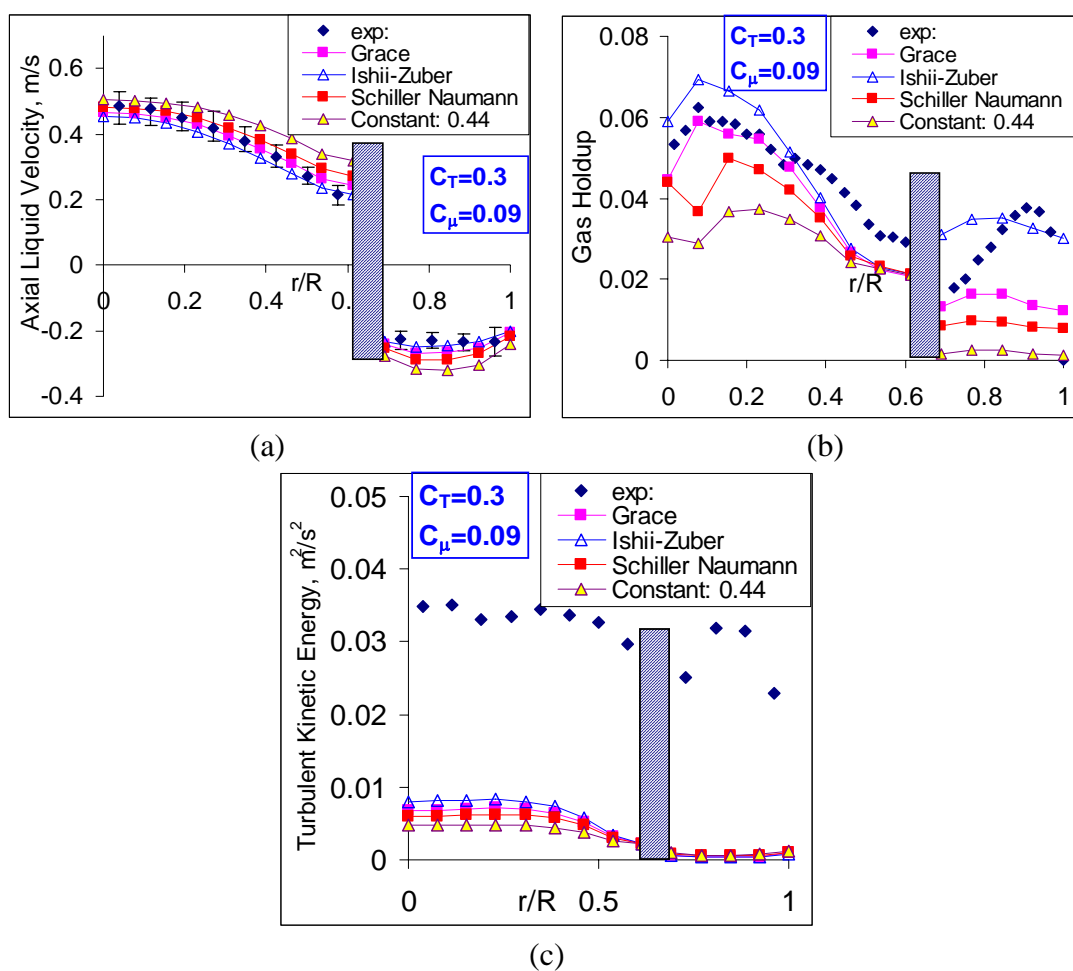


**Figure 6-6.** Effects of drag correlations on the CFD simulations. (a) Effects on the axial liquid velocity profile; (b) Effects on the gas holdup profile; (c) Effects on the turbulent kinetic energy profile.



### 6.4.5 Effects of Turbulent Dispersion Force

Turbulent dispersion force takes into account of the turbulent diffusion of the dispersed phase in the continuous phase. It is therefore can move the dispersed phase on the lateral directions. As shown in Figure 6-7, the dispersed phase spreads more obviously in the radial directions as the coefficient increases due to the higher turbulent diffusion. With a coefficient of 0.3, the predicted gas holdup profile agrees best with the experimental data. However, although the gas holdup profiles change considerably as the coefficient

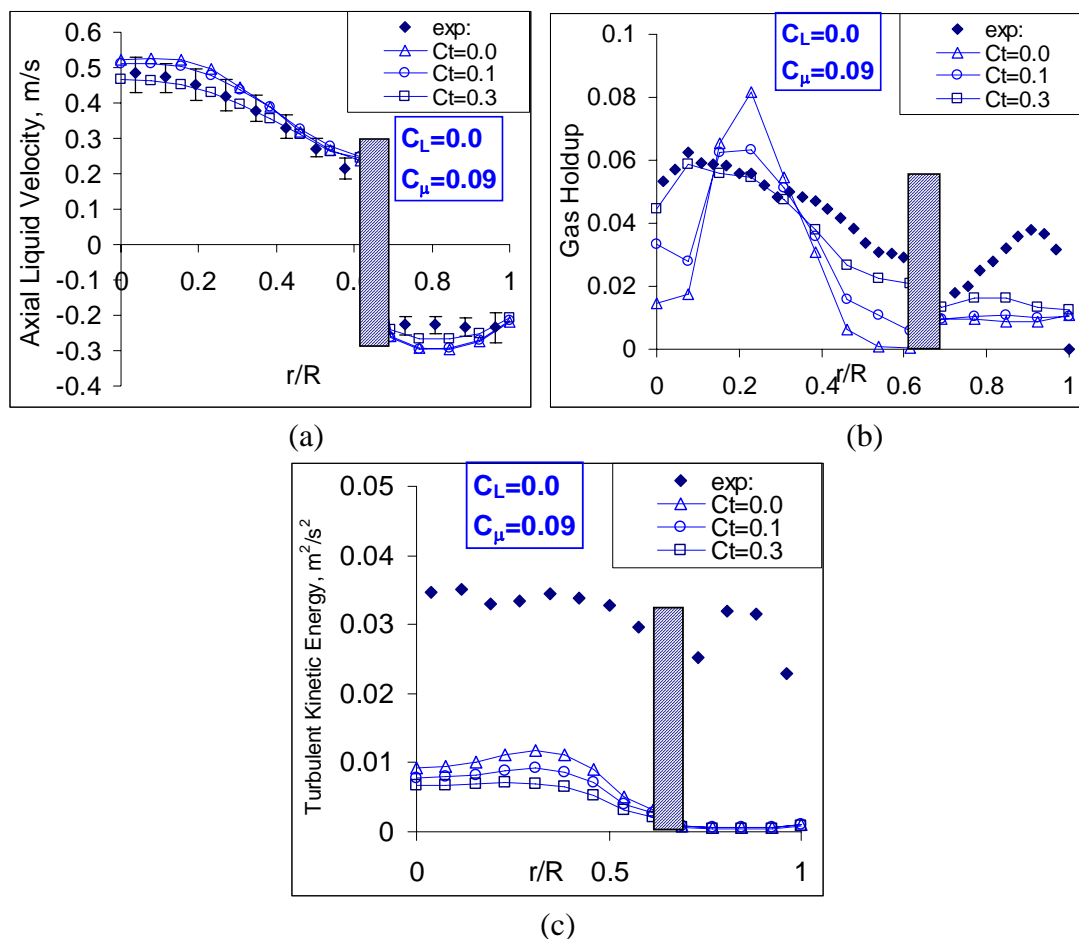


**Figure 6-7.** Effects of the turbulent dispersion force on the CFD simulations. (a) Effects on the axial liquid velocity profile; (b) Effects on the gas holdup profile; (c) Effects on the turbulent kinetic energy profile.

increases, the axial liquid velocity and the turbulent kinetic energy profiles have only minor difference. Moreover, considering the turbulent dispersion force does not computationally introduce convergence problem. These features make the turbulent dispersion force great in fine tuning the CFD simulations.

#### **6.4.6 Effects of Saffman Force**

Saffman force has been extensively discussed in the literature for the lateral movements of the dispersed bubbles in the liquid flows (Jokobsen, 1993; Jokobsen et al, 1997; Sokolichin et al., 2004). However, its physical existence and the mathematical representation are still under debate (Sokolichin et al., 2004), especially considering the fact that bubbles deform in the flow domain (Jakobsen et al., 1997). The direction of the force acted on a deformable bubble has been observed to be opposite to the direction on a spherical bubble. Such arguments imply that the coefficient of the Saffman lift force could be a flow property, thus it is hard to predict.

Different coefficients with opposite signs were tried in 3D steady state simulations. As shown in Figure 6-8, a positive Saffman force coefficient tends to move the bubbles to the walls in both the riser and the downcomer flow regions. This results in flatter profiles for all three profiles shown. In contrast, a negative coefficient has exactly the opposite effects. As for the turbulent kinetic energy, moving the bubbles to the wall region obviously reduces the turbulent due to the wall limitation, while moving the bubbles to the reactor center promote the turbulence. However, it's obvious that the simulation without considering the Saffman lift force best matches the experimentally measured mean flow in the currently studied case, when the turbulent dispersion force was considered. Moreover, it was found that the convergence is much harder to reach when the Saffman force is considered. Therefore, the Saffman lift force was not considered in this work.

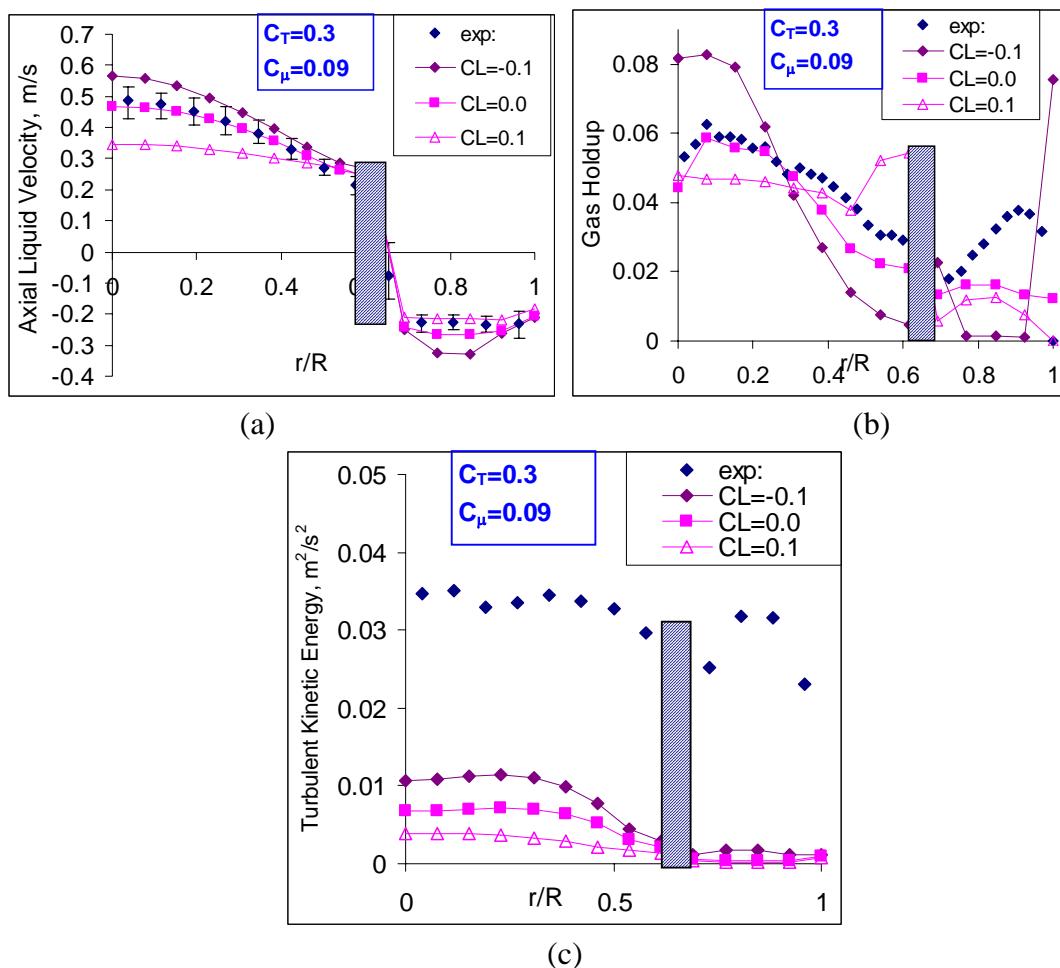


**Figure 6-8.** Effects of the Saffman lift force on the CFD simulations. (a) Effects on the axial liquid velocity profile; (b) Effects on the gas holdup profile; (c) Effects on the turbulent kinetic energy profile.

Based on the above evaluation against CARPT and CT data obtained in Chapter 5, the following closures were identified to study the multiphase flow dynamics in the studied draft tube column reactor:

- 3D steady state simulation using a coarse gridding as described in section 6.3.2
- The  $k-\varepsilon$  model with  $C_\mu$  of 0.09
- Ishii-Zuber correlation (1979) for the drag force
- Lopez de Bertodano correlation (1998) with coefficient of 0.3 for the turbulent dispersion force)

## 6.5 Simulations for Different Superficial Gas Velocities

Based on the selected turbulent models and the correlations, 3D steady state simulations were utilized to simulate the flow dynamics at superficial gas velocities of 0.3 and 5 cm/s to further test the prediction capability of the CFD simulations on different flow regimes. The simulation results are shown in Figure 6-9. The simulation results for superficial gas velocity of 0.3cm/s, still within the bubbly flow regime, agree with the experimental data nicely in terms of the axial liquid velocity and the gas holdup profiles, although the turbulent kinetic energies are still under-estimated. However, the simulation results for superficial gas velocity of 5cm/s, within the churn-turbulent flow regime, fail to capture even the mean flows in the studied airlift column.

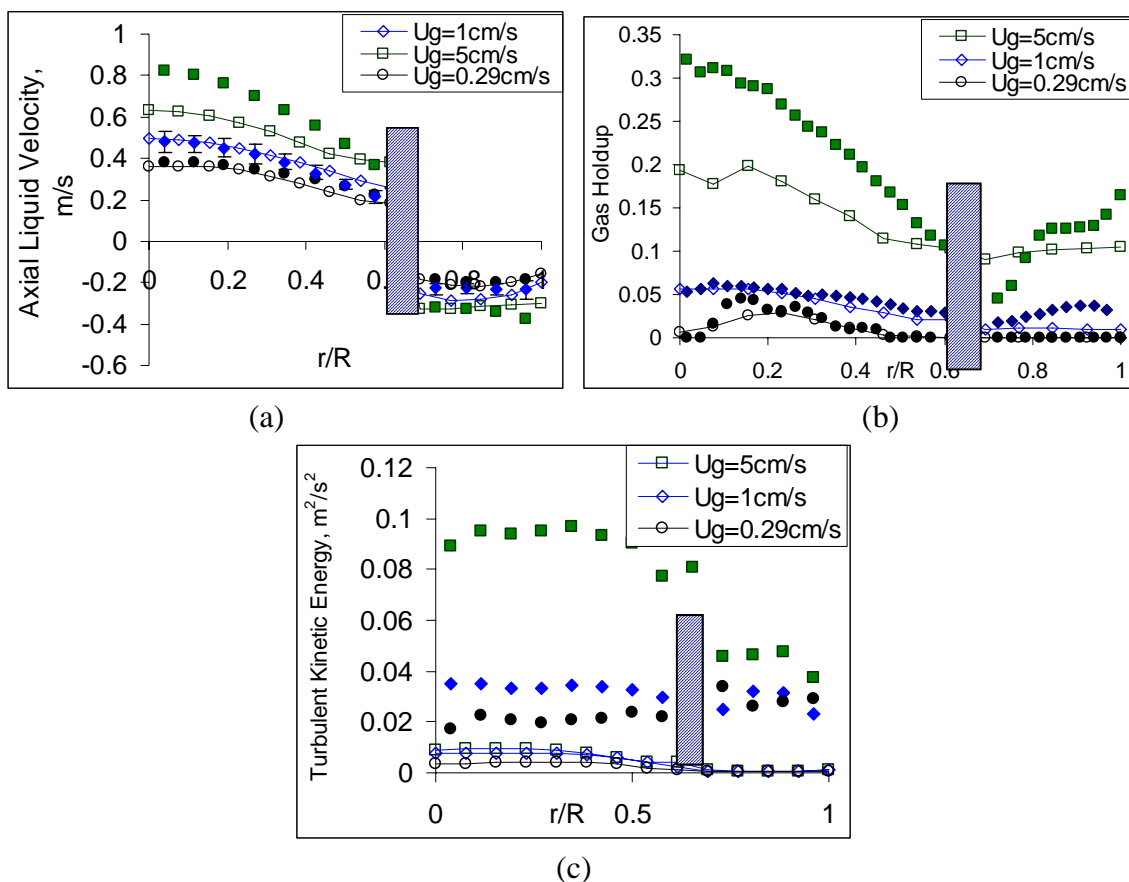


**Figure 6-9.** CFD simulations for different superficial gas velocities. (a) Results of the axial liquid velocity profile; (b) Results of the gas holdup profile; (c) Results of the turbulent kinetic energy profile.

Such results suggest that the correlations and closures identified above can not be applied to the churn-turbulent flow regime but only to the bubbly flow regime. In fact, it is well-known that the bubble break-up and coalescence are very prominent in the churn-turbulent flow regime, resulting in a wide range of bubble size distribution. The drag force correlations used in this work which were developed from homogeneous spherical bubble distribution, thus cannot describe the complex bubble dynamics under such churn-turbulent condition. On the other hand, due to the highly dynamic feature at the churn-turbulent flow regime, it is obvious that a transient simulation is required for CFD simulations under such conditions. Indeed, the convergence of the simulation at superficial gas velocity of 5cm/s was also much worse than the simulations for lower superficial gas velocities.

## **6.6 Particle (Cell) Trajectory Evaluation**

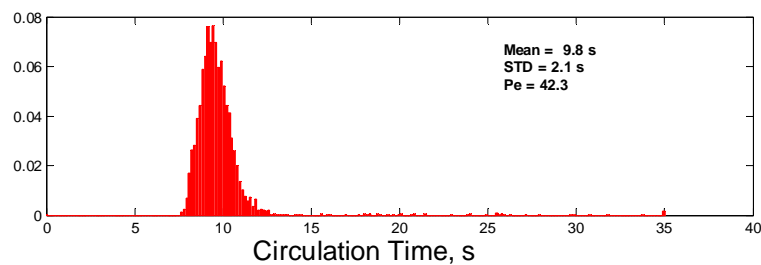
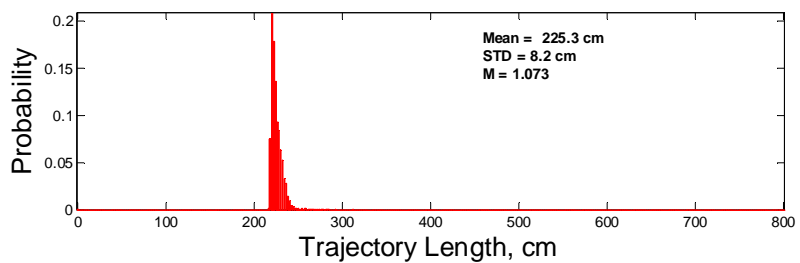
Since the information of the microorganism cells' movement in a photobioreactor is important for the reactor performance evaluation, the two-fluid model with the above identified closures was further adopted to simulate the cells' movements in the studied draft tube airlift column. This is justified by the fact that photobioreactors are usually operated under bubbly flow regime.

To mimic the movement of microorganism cells, 4000 small (i.e., with sizes evenly distributed between 5 and 10  $\mu\text{m}$ ) and neutrally buoyant particles (i.e., density of 1000  $\text{g}/\text{cm}^3$ ) were introduced from the bottom of the airlift column and traced for up to 40 seconds for each particle in a 3D steady state simulation. By this approach, the simulation results provided particle trajectories with total effective tracing time of around 11 hours, and total effective particle positions of more than 2.5 million in the studied airlift column. With such a large amount of particle trajectories, it was found that further increasing the tracer particle numbers does not affect the statistical results of the particle trajectories.

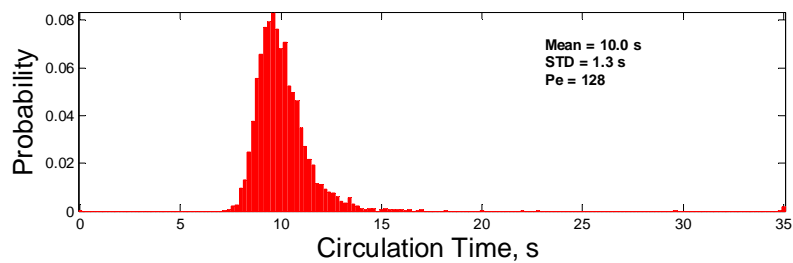
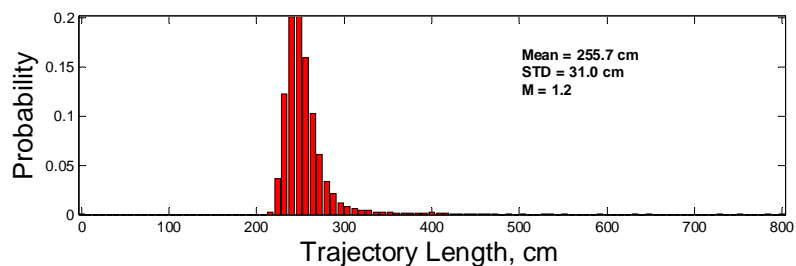
Due to the non-deterministic nature of the particle trajectories in a turbulent multiphase flow, it is impossible to directly compare the CFD simulated particle trajectories against the CARPT measured ones. Therefore, statistical method was used in this study. Following the single trajectory analysis discussed in Chapter 3 and 5, the circulation time and the single trajectory length distributions were plotted as probability density functions.

Figure 6-10 shows the PDFs for the CFD simulated single trajectories together with the PDFs for the CARPT measured trajectories at superficial gas velocity of 0.82 cm/s. The relative difference between the predicted and the CARPT measured mean trajectory is 11.9%, and the relative difference is 2% for the mean circulation time. The PDFs of the CFD simulated trajectories are similar to but narrower than the distributions of the CARPT measured data, especially for the trajectory length distribution. Apparently, this is due to the lower turbulent intensity predicted in the CFD simulations. With less turbulence, the particles are more likely to follow the mean liquid flow which orderly circulates around the draft tube in the column, resulting in a flow close to plug flows.

The capability of the CFD simulations on simulating a particles movement can be further revealed from Figure 6-11. In Figure 6-11, the radial profile of the occurrence density (A detailed discussion of this parameter is presented in Chapter 5) was shown as a radial profile together with the results obtained from CARPT measured particle trajectories. As can be seen, instead of a quite uniform distribution as CARPT measured trajectories demonstrated, the CFD simulated trajectories are more likely concentrated on the wall regions. This implies that the momentum transfer forces considered in Equation (6-22) may not have fully represented the reality. A more realistic modeling is thus required for better capture the intrinsic particle movements, which is out of the scope of this work.



(a)



(b)

**Figure 6-10.** PDFs of the trajectory length and the circulation time distributions based on single trajectory analysis. (a). CFD simulation results; (b) CARPT results. Operating conditions:  $U_g$  of 0.82cm/s, top clearance of 3cm, and bottom clearance of 5cm.

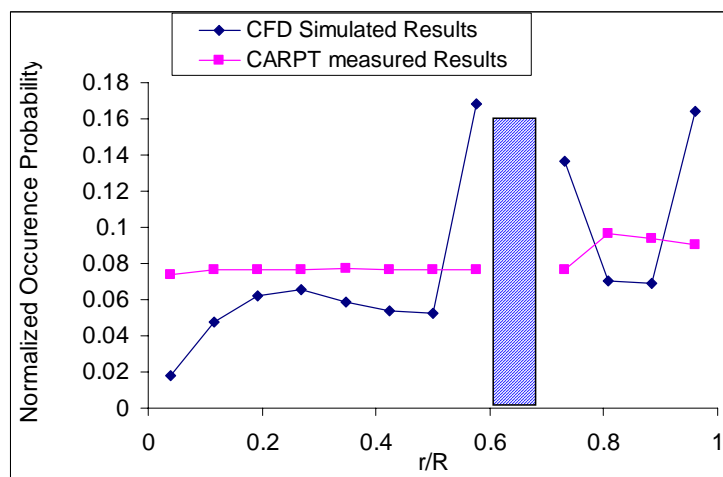


**Figure 6-11.** Radial profile of the normalized occurrence probability for the tracer particle in the airlift column reactor (normalized by the total number of occurrences) at superficial gas velocity of 0.82 cm/s.

## 6.7 Photobioreactor Performance Prediction Using CFD Results

CFD is a widely accessible technique with many codes has been successfully commercialized, such as CFX, Fluent, AVL, CFDLIB. A general approach can be formed for photobioreactor performance evaluation by integrating CFD simulations with the dynamic growth rate model developed in Chapter 4. This general approach is attempted in this section. The particle trajectories simulated in the previous section were further integrated with photosynthetic kinetics based on the dynamic growth rate model. Same model parameters listed in Table 4-2 (the parameters estimated by Merchuk et al., 2000) were used. The predicted photobioreactor performance is shown in Figure 6-12, together with the experimental data measured by Merchuk et al. (2000) and the predictions based on CARPT measured particle trajectories obtained in Chapter 5 at superficial gas velocity of 0.82 cm/s.



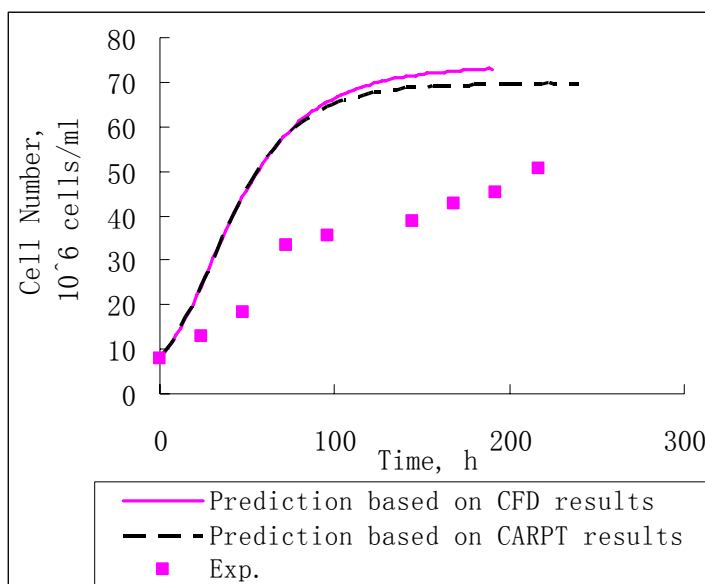


**Figure 6-12.** Predicted photobioreactor performance using CFD simulated trajectories together with the experimental data measured by Merchuk et al. (2000) and prediction using CARPT data. Simulation conditions: External irradiance:  $250 \mu E m^{-2} s^{-1}$ , Superficial gas velocity: 0.82 cm/s.

Apparently, the prediction based on CFD simulated particle trajectories considerably over-estimated the experimental reactor performance, but close to the prediction based on the CARPT data obtained in Chapter 5. This is because both particle trajectories give close time averaged light intensities. Calculated based on Equation (4-1), the intensity for the CFD simulated trajectory is  $159.4 \mu E/m^2$  and the intensity for the CARPT measured trajectory is  $155.3 \mu E/m^2$  (calculated under Case I as discussed in Chapter 4 with conditions of: External Irradiance:  $250 \mu E m^{-2} s^{-1}$ ; Cell concentration:  $8 \times 10^6$  cells/ml).

As discussed earlier, as the external light intensity equal to the optimum light intensity for *Porphyridium* sp. ( $250 \mu E/m^2$ ), the growth of the cells inside the reactor at such condition are dominated by the photolimitation effects without prominent photoinhibition. Thus the level of the time-averaged light intensity largely determines the predictions. As the prediction based on CFD simulated particle trajectories over-estimated the reactor performance, it can be concluded that the time averaged light intensity is also

over-estimated. This is consistent with the results shown in Figure 6-11. The CFD simulated trajectories are likely concentrated on the wall regions, where light energy abundant.

Based on these results, it is fair to say that, more realistic particle trajectories with better turbulent prediction and occurrence density distribution are required to use CFD simulation for photobioreactor analysis. Such particle trajectories are possible to be obtained by fine tuning the interfacial momentum forces acted in the particles described in Equation (6-22). Moreover, under real microalgal culturing conditions, the physical properties of the liquid phase could be very different (a more detailed discussion is presented in Chapter 7), and some closures identified in this work for the air-water system might not work. Therefore, a further systematic research on utilizing CFD simulation for the PBR analysis is required, which calls for a flow dynamic study using a real microalgal culturing system as discussed in the next chapter.

## **6.7 Summary**

CFD simulations based on a two-fluid Eulerian-Eulerian model were attempted in this work to provide needed flow dynamic information for multiphase photobioreactor performance analysis. Using commercial CFD code CFX5.7 (Ansys Inc.), different types of simulations, turbulent models, and correlations for various interfacial momentum forces were tested and evaluated against the experimental data obtained from CARPT and CT techniques in Chapter 5. The bases of the evaluations include the mean multiphase flow fields (i.e., the time averaged axial liquid velocities and the local gas holdups), the turbulent intensities, and the particle trajectories. The obtained information was also directly integrated with photosynthetic kinetics for photobioreactor analysis. Following conclusions can be reached.

- A computationally promising CFD simulation model was identified to study the multiphase flow dynamics in a draft tube airlift column reactor under the bubbly flow regime. This model uses 3D steady state simulations, the standard  $k-\varepsilon$  turbulent model with  $C_\mu$  of 0.09, and closures such as Ishii-Zuber's drag force correlation and Lopez de Bertodano's turbulent dispersion force with coefficient of 0.3.
- The identified CFD model and closures properly captured the mean multiphase flow field, but considerably under-estimated the turbulent kinetic energy in the studied airlift column.
- A pseudo Eulerian-Lagrangian approach was utilized to simulate the movements of small neutrally buoyant particles in the airlift column. The computed particle trajectories reasonably matched the experimental data based on the single trajectory analysis but are biased to the wall region from the occurrence distribution analysis.
- The photobioreactor analysis using the CFD simulated particle trajectories obtained in this study considerably over-estimated the overall growth rate. Careful consideration of the interfacial momentum forces acted in the particles as described in Equation (6-22) is required to obtain more realistic particle trajectories for photobioreactor analysis.

## **Chapter 7**

# **Culturing *Porphyridium sp.* in Airlift Column Photobioreactors**

### **7.1 Scope**

The dynamic growth rate model developed in Chapter 4 provides a direct and comprehensive tool for photobioreactor analysis. Verifications of this model against the experimental results obtained by Merchuk et al. (2000) were attempted in both Chapter 4 and 5, using CARPT measured flow dynamic information obtained in air-water systems. In these attempts, the reactor performance was over-predicted by the model. Moreover, since the external light intensities used in Merchuk et al. (2000) are quite low, the effects of flashing light and photoinhibition on the reactor performance are not prominent in their experiments and thus were not properly evaluated. Therefore, further verifications of the model using hydrodynamic data obtained from real culturing systems and high incident light intensity are required.

This Chapter focuses on further verification of the dynamic growth rate model for photobioreactor analysis developed in Chapter 4. *Porphyridium sp.*, the same red marine alga used by Merchuk et al. (2000), was grown in three types of airlift column photobioreactors in two light intensity regimes (i.e., moderate and high Photosynthetic Photon Flux Densities (PPFD)) and two superficial gas velocities (i.e., mild and moderate gas agitations). The physical properties (e.g., the viscosity) of the culture medium and the reactor performance were monitored by various analytical methods (e.g., optical density, dry biomass concentration, chlorophyll concentration, etc.). Moreover, the multiphase flow dynamics in the draft tube column reactor were also investigated by both CARPT and CT techniques. Using these flow dynamic data, the dynamic growth rate model nicely predicted the reactor performances measured by the Merchuk et al. (2000). The model also nicely predicted the experimental data obtained in this study when justified photosynthetic kinetic parameters were used. These encouraging results indicate the applicability of the developed dynamic growth rate model on operating conditions with industrial interests.

## 7.2 Introduction

As mentioned before, autotrophic cell cultures are complex systems coupling many elements, with multiple time and length scales involved. To accurately predict the reactor performance, any mathematical model for photobioreactors requires three major types of information as inputs. They are flow dynamics (e.g., how the microorganism cells move in the reactor and the stress they face), irradiance distribution inside the reactor (i.e., how light energy is delivered to the cells), and the photosynthetic reaction kinetics (i.e., how the microorganism responds to the light history). The accuracy of these inputs determines the reliability of the mathematical model's predictions.

In Chapter 4, a dynamic growth rate model was developed which integrates the information of flow dynamics, light intensity distribution, and photosynthetic kinetics based on the first principles. To verify the developed model, CARPT measured particle trajectories obtained from a draft tube column of 20cm diameter in an air-water system were used to predict the performance of a draft tube column photobioreactor of 13cm diameter for *Porphyridium sp.* cultures (Merchuk et al., 2000). The photosynthetic kinetic parameters estimated by Wu and Merchuk (2001) were used. Although the prediction reasonably matches the experimental data, it was later found to be a coincidence as discussed in Chapter 5. Indeed, the apparent difference between the reactor configurations and the operating conditions of these two systems makes the comparison very debatable.

To further verify this dynamic model, multiphase flow dynamics were studied in detail by both CARPT and CT techniques in Chapter 5. A draft tube column reactor similar to that used by Merchuk et al. (2000) was operated at same operating conditions they studied, but in an air-water system. Using these hydrodynamic data, the model predictions successfully captured the trend of the reactor performance with increasing superficial gas velocities. However, the reactor performances were over-predicted by the model. It was suspected

that the over-estimation is due to the hydrodynamic data used, which was obtained from an air-water system. The physical properties of an air-water system could be very different from those of a real culturing system, resulting in different local flow dynamics.

Apparently, a successful verification of the dynamic growth rate model requires accurate inputs from all three aspects of the photobioreactor performance mentioned above. This requires a flow dynamic study in a real culturing system under the same operating conditions as the reactor performance experiments. A reliable light intensity distribution model and accurate photosynthetic kinetic parameters are also essential. Moreover, it is also important to test the applicability of the dynamic growth rate model at conditions of high light intensity and high biomass concentration. These conditions, with significant flashing light and photoinhibition effects, are essential for mass production of microalgae/cyanobacteria.

This Chapter focuses on further verification of the developed dynamic model in terms of all three of the above mentioned aspects for photobioreactor analysis. The following sections first describe the materials and methods used in the experiments, and then carefully discuss the observations and results obtained from these experiments. They are followed by the dynamic growth rate model predictions, and finally conclusions are drawn.

## **7.3 Experiments**

### **7.3.1 Algae Culture Preparation**

A red marine alga, *Porphyridium sp.* (UTEX 637), obtained from the culture collections of the University of Texas, was grown in an artificial seawater medium prepared according to Jones et al. (1963). The alga was first grown in 500ml Erlenmeyer flasks on a shaker with culture temperature of 31°C and pH of 7.6. Light was supplied from the side by a cool

white fluorescent lamp at a photon flux density (PFD) of  $30\mu E/m^2 s$ . To avoid contamination, no extra  $CO_2$  was supplied to the small-scale cultures. After the cultures reached the stationary growth stage, they were moved to the large-scale airlift column photobioreactors.

## **7.3.2 Airlift Column Photobioreactors**

### **7.3.2.1 Reactor Configurations**

Three types of airlift column photobioreactors were used in this study, as shown in Figure 7-1. They are actually the draft tube column studied in Chapter 5 modified for different configurations, such as without internals (bubble column), with a draft tube (draft tube column), or with a splitting plate (split column). This column, made from acrylic, has an outer cylinder with a diameter of 0.13 m and a height of 1.5 m. When it was running as a draft tube column, a draft tube with a diameter of 0.09 m and a height of 1.05 m was mounted coaxially with the outer cylinder. On the other hand, when the column was running as a split column, a plastic plate was inserted down the reactor's center dividing the column into two zones with equal cross-sectional areas. The liquid volumes for these reactors are 15 L.

The top clearances (i.e., the distance from the top of the internal to the static liquid level, as shown in Figure 5-2) for the draft tube and the split columns were 3 cm, while the bottom clearances for these two configurations were 5cm, in order to avoid high shear stress spots in the bottom regions. At the bottom of the column, the same ring sparger used in Chapter 5 was installed at the reactor center and used to distribute the gas phase (the sparger was moved to one side when running as a split column, so that it was still in the center of the Riser).



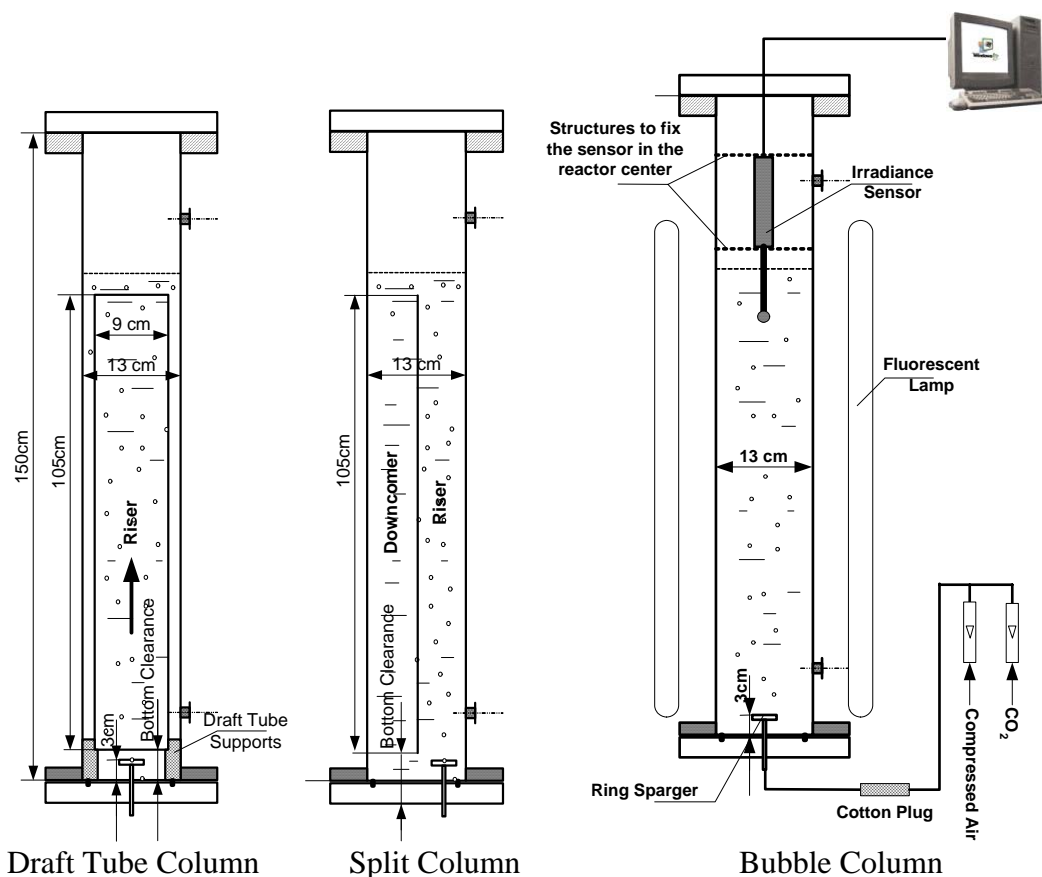


**Figure 7-1.** Configuration of three types of airlift column photobioreactors (same procedure has been applied to these reactors)

### 7.3.2.2 Experimental Procedure and Operating Conditions

Before each experiment, the whole column was carefully washed with soap water and thoroughly rinsed with deionized water. To avoid contamination, all culture media were sterilized in an autoclave under pressure of 15 lb for 20 minutes. A cotton plug filtered the compressed air before it entered the column through the ring sparger, and the column was loosely covered by a lid. No significant contamination was observed under a microscope in any of the experiments.

The compressed air, enriched with 3%  $\text{CO}_2$  (Merchuk et al., 2000), was introduced into the reactor through the ring sparger, providing both a carbon source and agitation to the

photobioreactors. Light energy was supplied continuously by a bank of cool white Sylvania fluorescent lamps (four 40Watt lamps with an intensity of 3000Lumen and eight 60W high output lamps with an intensity of 3281 Lumen) evenly distributed around the airlift column. Such a configuration of the lamp bank, as shown in Figure 7-2, generated a fairly uniform light intensity distribution around the illuminated column surface. Continuous illumination was applied throughout the experiments without applying day and night cycles (i.e., these cycles are usually used to mimic conditions of real outdoor cultures).

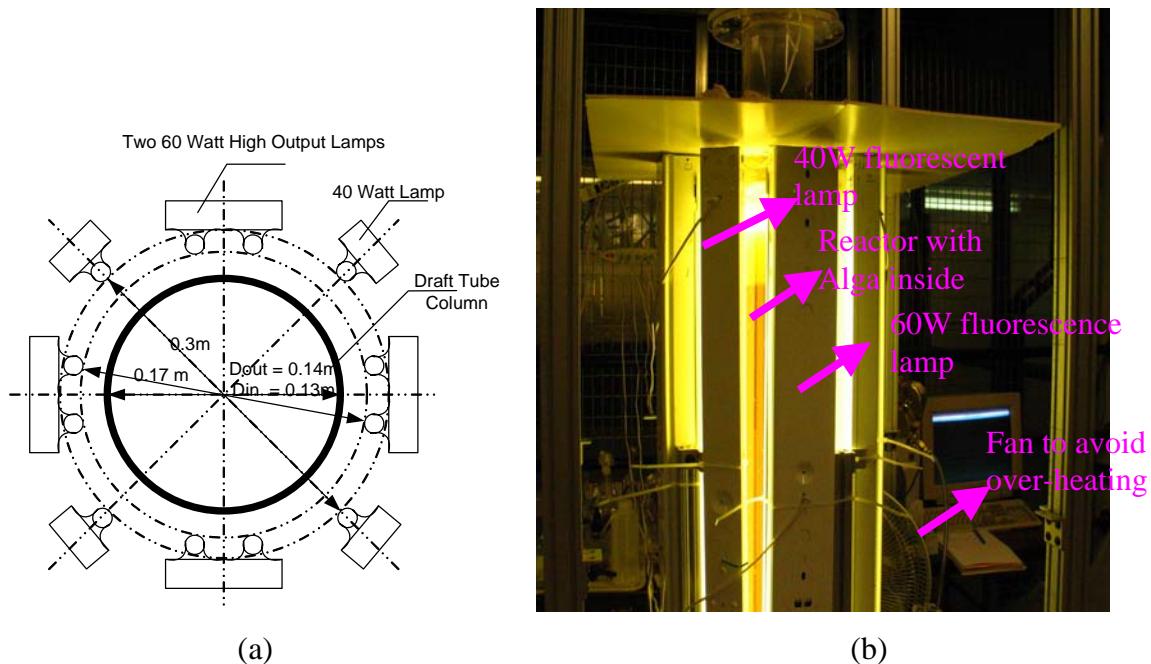


**Figure 7-2.** Configuration of the lamps to illuminate the reactor. (a) Schematic diagram of the configuration; (b) photo taken during the real experiments.

After the airlift column photobioreactor was inoculated with *Porphyridum sp.*, the optical density of the culture was initially very low (i.e., less than 0.01). To avoid photoinhibition and to shorten the lag time the cells need to adjust to the new environment, the reactor was first run for 12 hours at low light intensity and at low superficial gas velocity (i.e.,

illuminated only by the room lamps without switching on any bank lamps, Photon Flux Densities (PFD) was around  $26 \mu E/m^2 s$  and the superficial gas velocity was 0.3 cm/s). Then, four 40W lamps were switched on while keeping the same superficial gas velocity, giving a PFD around  $275 \mu E/m^2 s$  on the illuminated surface. Such a PFD is close to the optimum irradiance for *Porphyridium sp.*'s growth ( $250 \mu E/m^2 s$ , Wu and Merchuk, 2001). After the optical density of the culture reached 1.0 (thick enough to avoid detrimental photoinhibition at very high PFD), all lamps were switched on, giving a high irradiance (i.e., around  $1850 \mu E/m^2 s$ ). Finally, to test the effects of mixing intensity on the airlift column photobioreactor performance, the superficial gas velocity was increased to 1 cm/s while keep all lamps on.

### **7.3.3 Liquid Phase Physical Properties**

The viscosities and the surface tension of algae samples in the different growth stages were measured at room temperature. The viscosities were measured by a viscometer (model AR2000, TA instruments, Inc.) using an aluminum cone geometry (cone diameter of 60mm and angle of 59'49"). And the surface tension was measured by a tensiometer (Sigma 701, KSV instruments Inc.).

### **7.3.4 Hydrodynamic Characterization under Real Culture Conditions**

Both CARPT and CT experiments were carried out to characterize the local flow structures in the airlift column photobioreactors under real microalgae culture conditions. These measurements used the same experimental setup and procedures described in detail in Chapter 5 for an air-water system. The CARPT and CT experiments were carried out separately, as the instruments reside in different labs.

In the CARPT experiments, light was supplied from six lamps, mounted vertically on the aluminum supports shown in Figure 5-3. The external irradiance was around  $220 \mu E/m^2 s$ . The CARPT experiments started after the microalgae culture reached the active growth stage, with optical density around 0.2. Experiments at a superficial gas velocity of 0.076 cm/s were done first, immediately followed by the experiments for a Ug of 0.3 cm/s. The optical density eventually reached about 0.5 after these experiments, which took three days.

A similar procedure was applied to the CT experiments. However, due to the limited space, light was supplied from only four lamps, which were mounted horizontally around the column base. The light intensity supplied thus was not uniform in the whole reactor and gave a lower value. The optical density was around 0.2~0.4 throughout the CT experiments. The middle scans (H = 67cm) were performed first for both superficial gas velocities, followed by the top scans (H = 110 cm). The bottom scans (H = 4.2 cm) were carried out at last.

### **7.3.5 Light intensity measurements**

Photon Flux Density (PFD) in the reactor was measured by a quantum scalar irradiance sensor (QSL-2100, Biospherical Instruments, Inc.) with a spherical collector of 1.9cm diameter. This accurate sensor measures photosynthetic active radiations (PAR) arriving from all directions in both aquatic and dry environments. This sensor was also placed in the reactor center during the experiments to monitor the cells' growth, as shown in Figure 7-3. Such information can be used to estimate the extinction coefficient of irradiance due to cellular absorption.

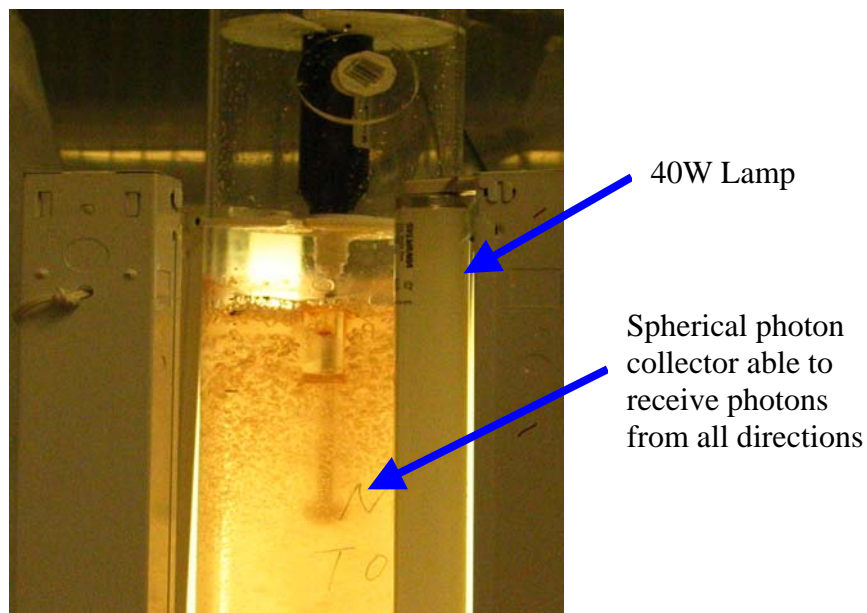


**Figure 7-3.** Quantum scalar irradiance sensor (placed in the reactor center to monitor the biomass concentration)

### 7.3.6 Biomass Concentration measurements

To monitor the biomass concentration and thus the bioreactor performance, a 100ml sample was taken from the top of the airlift column (around 5~10cm below the liquid level) at least twice a day. To keep the dynamic liquid level, the same amount of fresh medium was added each time after a sample was taken. This sample was divided into several parts for different biomass concentration measurements, such as optical density, dry biomass weight, direct cell number counting, and chlorophyll concentration. The following sections describe the details of these methods.

#### 7.3.6.1 Optical Density

Optical densities of the algae samples were measured at least twice a day (usually at 10 o'clock in both the morning and the evening, and sometimes once more in the afternoon). A spectrophotometer (Spectronic Genesys 8, Thermo Spectronic Instruments, Inc.) and

cuvettes with path length of 1cm are used for the measurements at wavelength of 663nm (Merchuk et al., 2000). For each optical density measurement, an average of three samples was taken as the real optical density, although the standard deviation was usually quite low. When the biomass concentration was very high, the samples were diluted with de-ionized water to give a reading between 0.5~1.0. The real optical density was expressed as the product of the reading times the number of dilutions. The calibration curve shown in Figure 7-4 demonstrates that this method gives a linear relationship between the measured optical density and the dry biomass weight:

$$\text{optical density (dimensionless)} = 0.4777 \times \text{Dry Biomass (g/L)} \quad (7-1)$$

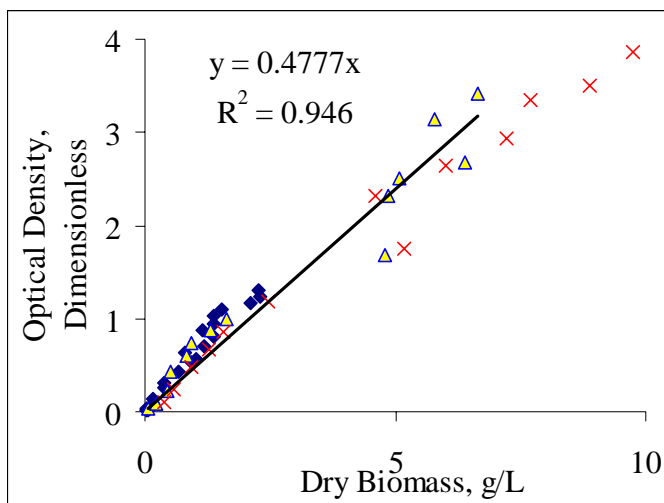


**Figure 7-4.** Calibration curve of optical density versus dry biomass concentration

### 7.3.6.2 Dry Biomass Weight

The dry biomass weight was measured twice a day (around 10 o'clock in the morning and the evening) with two samples each time. Initially, 20ml of each sample was filtered through a 0.8 $\mu$ m filter paper (GC/G, Fisher Healthcare Co.) and washed with a few milliliters de-ionized water. When the cell concentration was high and required a very long

filtration time, the volume of samples to be filtered was reduced, but the absolute dry biomass weight was kept high. The filter paper with algae was then oven dried ( $105^{\circ}\text{C}$ ) for 24 hours and weighed. An average of the two samples was taken as the dry biomass weight.

### 7.3.6.3 Cell Number Counting

Cell numbers were counted using a counting chamber (Bright-line counting chamber, Fisher Healthcare) under a microscope (Olympus 324, Olympus Inc.) with  $400\times$  zoom. A calibration curve was determined as shown in Figure 7-5, which gives a linear relationship between the cell numbers and the optical densities:

$$\text{Optical Density (dimensionless)} = 0.0435 \times \text{Cell Number (} 10^6 \text{ cells/ml)} \quad (7-2)$$

In addition, the morphology of the algae was also routinely observed under the same microscope.

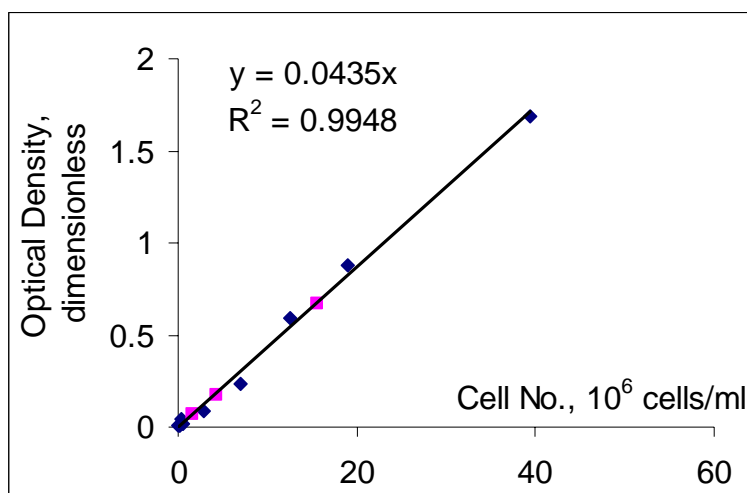


**Figure 7-5.** Calibration curve of cell numbers versus the optical density.

### 7.3.6.4 Concentration of Chlorophyll (a)

Chlorophyll (a) concentration was measured once a day (10 o'clock in the morning) with two samples each time. To measure the concentration of chlorophyll (a), two samples of 20ml alga (or 5 ml when the concentration was high) were first filtered through a 0.8 $\mu$ m filter paper (GC/F, Fisher Healthcare) under dim light as soon as the samples were collected (the samples were always covered with aluminum foil to prevent pigment changes during transportation). The filter papers with alga were then placed in vials and frozen in a refrigerator. When enough samples (usually 8) were collected, these samples were analyzed all at the same time, following the method described in Clesceri et al. (1998). The chlorophyll on the filter paper was extracted overnight by 10ml 90% aqueous acetone solution containing trace magnesium carbonate in the dark at 4°C. The extraction solution was then clarified by a 0.4 $\mu$ m syringe filter with its volume also measured.

The optical densities of the extract under different wavelengths (i.e., OD750, OD664, OD647, and OD630) were determined in a spectrophotometer (Spectronic Genesys 8, Thermo Spectronic Instruments Inc.). The concentration of chlorophyll (a) was then calculated by (Clesceri et al., 1998):

$$Ca = 11.85(OD664) - 1.54(OD647) - 0.08(OD630) \quad (7-3)$$

$$\text{Chlorophyll (a), mg/L} = \frac{Ca \times \text{extracted volume, L}}{\text{volume of sample, L}} \quad (7-4)$$

where  $Ca$  is the concentrations of chlorophyll (a), and  $OD664$ ,  $OD647$ , and  $OD630$  are optical densities at respective wavelengths corrected by  $OD750$  (e.g.,  $OD664$  is the optical density at 664nm less the optical density at 750nm).



## 7.4 Results and Discussions

### 7.4.1 Physical Properties of the Culture Medium

The physical properties of the culture medium, mainly the viscosity and the surface tension, have important effects on the fluid dynamics in the reactor, and in turn affect the overall reactor performance. Microalgal *Porphyridium* sp. is encapsulated within sulphated cell-wall polysaccharides and is a well-known polysaccharide producer (Eteshola et al., 1996; Gu and Liu, 2001). These polysaccharides, accumulating in the culture medium especially at the stationary growth stage, can significantly affect the culture medium's rheological properties (Eteshola et al., 1996, 1998; Geresh et al., 2002).

Figure 7-6 shows the measured viscosities for the culture medium at different biomass concentrations. Initially when the biomass concentration is very low, the medium's viscosity should be very close to water. However, the medium soon became Non-Newtonian when the biomass concentration increases, with a typical shear-thinning character. Apparent viscosity decreases exponentially as shear stress increases. As the biomass concentration increases, the apparent viscosities increase significantly in the low shear stress range, but keep almost constant in the high shear stress range.

These results, consistent with the literature (Eteshola et al., 1996, 1998), confirm that the polysaccharides produced can significantly affect the viscosity of the culture medium. However, the surface tension of the culture medium was found to be very close to that of pure water. The measured surface tension for the same medium used for viscosity measurements at an optical density of 4.0 is  $72.184 \times 10^{-3} \text{ N/m}$  (the surface tension of pure water is  $71.94 \text{ mN/m}$  at  $25^\circ\text{C}$ ). The reason for the small change in surface tension is not very clear, and surface tension measurements have rarely been reported in the literature.

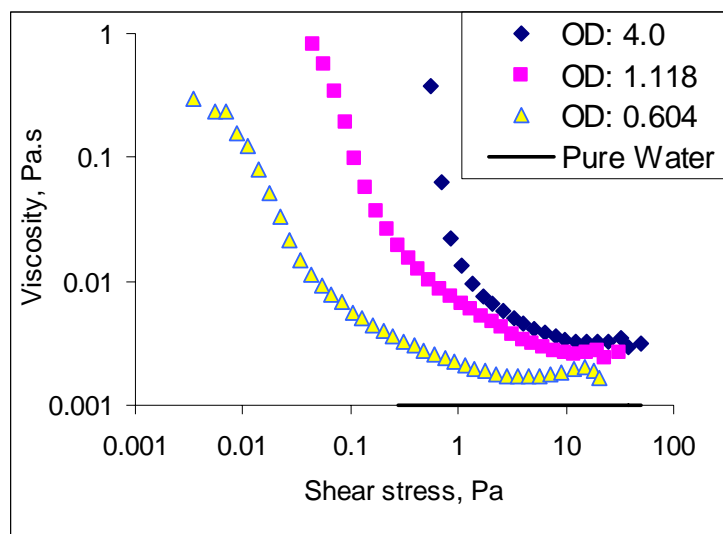


**Figure 7-6.** Profiles of apparent viscosity versus shear stress at different biomass concentrations.

#### 7.4.2 Fluid Dynamics of the Draft Tube Photobioreactor

Gas, liquid, and cell phases are present in the real microorganism culturing systems. Due to the size (in  $\mu\text{m}$ ) and density (very close to water) of most microorganisms, it is reasonable to assume that the liquid and the cells form a so-called pseudo-homogenous phase. However, it is noteworthy that the rheological properties of this pseudo-homogenous phase can be different from those of both the liquid and the cell phases. These properties can be affected by the cell concentration, the composition of the aqueous salt solution (e.g., the electrolyte solution is well-known to hinder bubble coalescence (Chisti, 1998)), whether or not cells aggregate and form larger particles. Moreover, many microorganisms excrete viscous secondary metabolic products that could easily turn the Newtonian fluid into non-Newtonian fluid as shown in Figure 7-6. These factors usually have different effects on the multiphase flow, and thus considerably complicate the already complex flow dynamic characteristics in airlift column reactors.

As a result, studies on local hydrodynamic characteristics using a real microorganism system are rare (Chisti, 1998; Pertersen and Margaritis, 2001). Instead, there are many studies using different media to mimic the real microorganism culturing systems, such as an aqueous salt solution (Posarac and Petrovic, 1991), a non-Newtonian carboxymethyl cellulose solution (Li et al., 1995), and a three-phase system using glass beads as the solid phase (Koide et al., 1992). In these studies, the effects of physical properties and operating conditions on the multiphase flow are investigated separately (Yuan et al. 1994; Hill, 1993).

Moreover, inconsistent findings have been reported in the literature. For example, in a draft tube column reactor, Yuan et al. (1994) observed that the overall gas holdup and liquid circulation rates in an air-water system are very similar to an air-aqueous ethanol solution system, but much larger than they are in an air-yeast broth system. However, Fraser and Hill (1993) obtained almost identical overall gas holdups in an external-loop airlift reactor using three different media (water, aqueous salt solution, and an alga culture system). Therefore, it is necessary to compare the local hydrodynamics in a real culturing system with those in the air-water system to better understand the multiphase flow dynamics of algae culturing systems.

In this study, to characterize the local flow dynamics in a *Porphyridium sp.* culturing system, both CARPT and CT experiments were implemented in the draft tube photobioreactor during the active growth stage, when the optical density increases from 0.2 to 0.6. The same procedure used for the air-water system discussed in Chapter 5 was applied. Figure 7-7 displays these results for the fully developed flow zones, together with the results obtained from the air-water system for a comparison. These results are the radial profiles of the normalized occurrence density, the axial liquid velocity, the turbulent kinetic energy, the Reynolds shear stress ( $\tau_{rz}$ ), and the local gas holdup at the middle section ( $H = 67\text{cm}$ ). A detailed discussion of these parameters was presented in Chapter 5. Please note that, since the cultures were run at the active growth stage in a batch mode, the optical density of the culture was not a constant, and neither were the other physical

properties of the medium. Therefore, exact matches of conditions found in the CARPT and CT experiments were not possible, although those experiments were run at the same superficial gas velocities. This situation hindered a more thorough analysis of the obtained multiphase fluid dynamics.

Figure 7-7 (a) clearly shows that the tracer particle or cells in a real culturing system have less chance to visit the outer wall regions than those in the air-water system. This is due to the increase of the viscosity in the real culturing system as shown in Figure 7-6. Increasing the liquid viscosity enlarges the turbulent sub-layer, where the particle or the cells have difficulty accessing. Since the outer cylinder wall is the illuminated reactor surface, this phenomenon reduces the light availability delivered to the interior cells, and thus can affect the reactor performance.

It is also clear from Figure 7-7 that the presence of microalgal just slightly changes the axial liquid velocities and the shear stress, but noticeably enhances the gas holdup and the turbulent kinetic energy. These results suggest that the multiphase flow structures could be different in a real culture system from the structures in an air-water system.

As reported in the literature, increasing viscosity reduces the terminal velocity of bubbles in the liquid phase, and thus tends to increase the gas holdup in the reactor. Moreover, the bubble size distribution can also be very different. The electrolyte solution usually inhibits bubbles' coalescence (Chisti, 1998), and the polysaccharide produced by *Porphyridium* sp. cells can also significantly promote or inhibit bubbles' coalescence (a small amount of foaming was observed on the top of the culture at the early active growth stage, which became significant as biomass concentration increases). Such a change in bubble size distribution has significant effects on the multiphase flow dynamics, since the rising bubbles in the airlift reactors are the driving force of the bulk liquid circulation. However, how the bubble size distribution changes is not clear, which requires further study of the bubble dynamics under real culturing conditions and is out of the scope of this study.

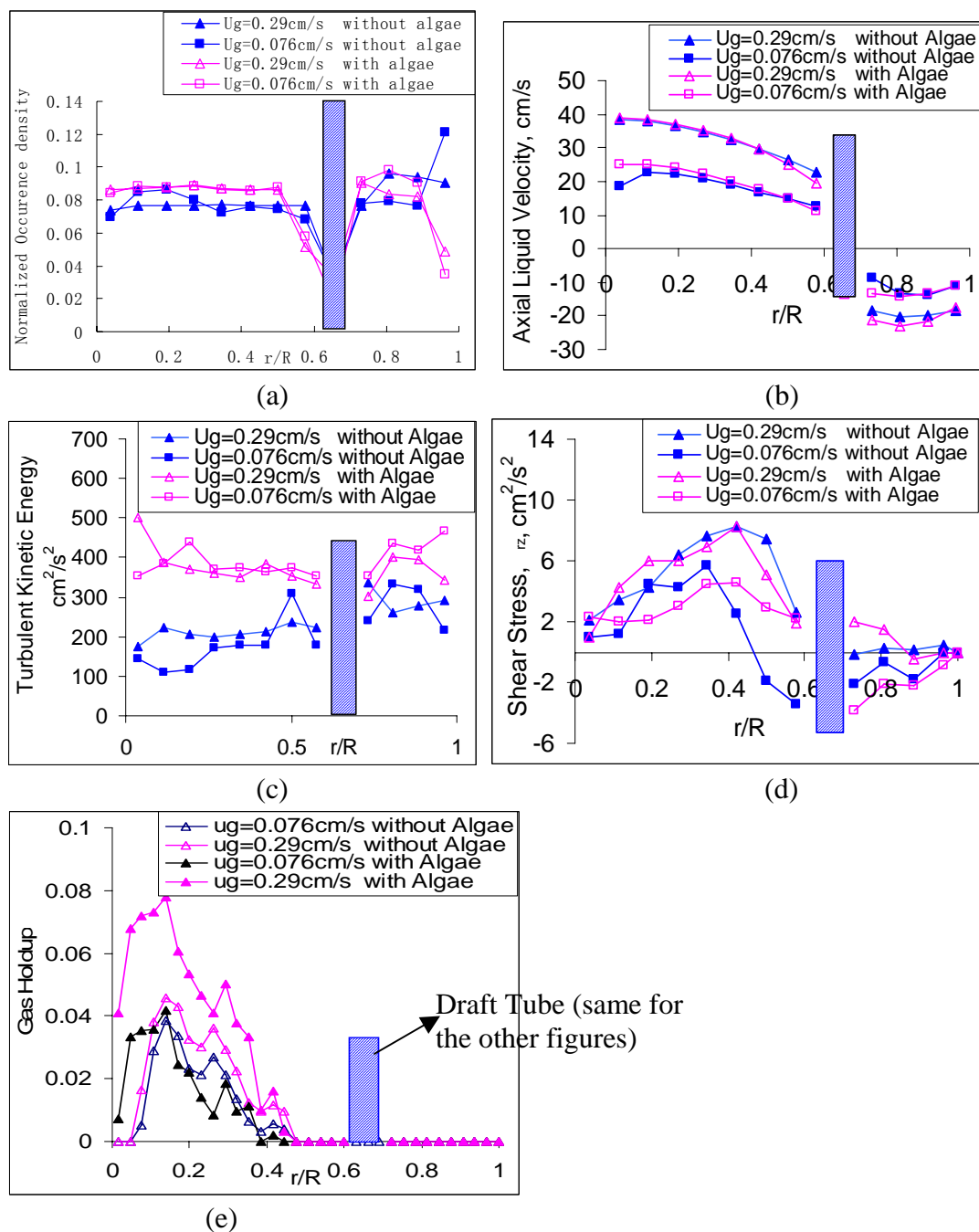


**Figure 7-7.** Comparison of the local hydrodynamic characteristics in the draft tube column between the real alga culture system obtained in this Chapter and the air-water system obtained in Chapter 5. (a) Radial profile of the occurrence density normalized by the total number of occurrences; (b) axial liquid velocity profiles; (c) turbulent kinetic energy profiles; (d) profiles of the Reynolds shear stress,  $\tau_{rz}$ ; (e) gas holdup profiles at the middle level ( $H = 67$  cm). Operating conditions: bottom clearance = 5 cm and top clearance = 3 cm (for  $U_g = 0.076$  cm/s in the air-water system, the top clearance is 0 cm).

It should be pointed out that the flow dynamics study presented above was conducted at fairly low biomass concentrations. When the cell culture reaches the stationary stage with higher biomass concentration, the apparent viscosity can be much larger, as shown in Figure 7-6. Under such conditions, the multiphase flow dynamics, especially the local structures, could be much more complex. Indeed, both tiny and very large bubbles (in centimeters by visual observations) were observed at the end of the cultures, resulting in a wide range of bubble size distribution. Moreover, the small scale turbulence with low shear rates could also be greatly damped out due to the high apparent viscosity. These phenomena could certainly reduce the light fluctuations the microorganism cells experienced in the photobioreactor and enhance photoinhibition. These analyses, based on fluid dynamic principles, provide a knowledge base to understand the photobioreactor's performance.

### **7.4.3 Irradiance Distribution inside the Reactors**

Governed by the radiative transfer theory (Vincenti and Kruger, 1965; Cassano et al., 1995), the irradiance distribution inside a PBR is a complex function of incident irradiance, biomass concentration and composition, flow dynamics, and reactor geometry (Molina Grima et al., 1996a) (a detailed discussion of the irradiance distribution inside PBRs is presented in Appendix D). Figure 7-8a shows the irradiance measured immediately after the inoculation (optical density is 0.006) at different locations in the reactor but at the same axial level (around 10cm below the free liquid surface).

The irradiance in either the Riser or the Downcomer were quite uniform, with averages of 324 and 267  $\mu E/m^2s$ , respectively, except at one point at the left side of the Downcomer. The uniformity of the measured irradiance implies that the lamp bank provided a rather uniform illumination on the reactor surface. It is noteworthy here that the irradiance inside the draft tube were interestingly larger than the irradiance in the Downcomer. This is due to the curved surface of the liquid filled column and the low biomass concentration presented

in the reactor. Since the light attenuation at low biomass concentration is not prominent, the incident photons can penetrate deeply to the reactor center. Moreover, due to the curved reactor surface, more photons travel through the reactor center. As the irradiance sensor can detect photons from all directions, the measured irradiance is higher in the reactor center.

Such an effect is not significant when the medium's optical density is high, as the photon transportation is dominated by cellular absorption. In Figure 7-8b, both irradiance inside and outside of the reactor were measured at the same axial level as in Figure 7-8a, but under a higher biomass concentration (optical density of 0.990) and higher irradiance (all lights were switched on).

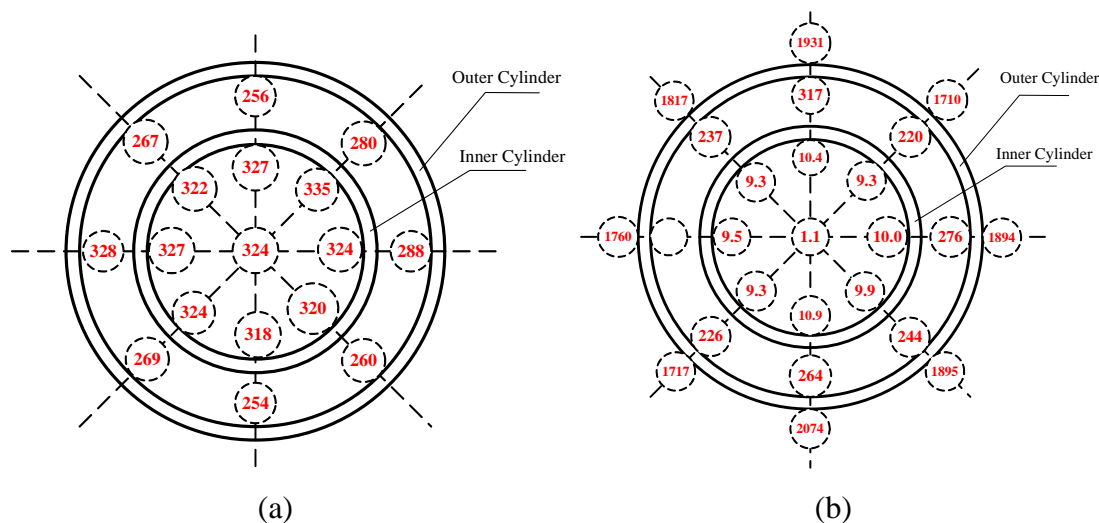


**Figure 7-8.** Irradiance measurements in the draft tube column reactor. (a) Under low PFD and biomass concentration (optical density of 0.006 with four lamps on). (b) Under high PFD and biomass concentration (optical density of 0.99 with all lamps on).

It is obvious that the irradiance decrease sharply as the light penetration depth increases at high biomass concentration. Plotting the measured irradiance (after azimuthally averaged) versus the distance from the sensor center to the wall on a logarithm coordinate gives roughly a straight line, as shown in Figure 7-9. This confirms the widely used assumption

that the irradiance distribution inside the airlift column reactor at high biomass concentration is likely to follow the Lambert-Beer law (a detailed discussion of irradiance distribution inside the reactor is presented in Appendix D):

$$\frac{I}{I_w} = \exp(-k_x \cdot x \cdot d) \quad (7-5)$$

where  $I_w$  is the irradiance on the illuminated wall,  $k_x$  is the extinction coefficient due to cellular absorption,  $x$  is the biomass concentration, and  $d$  is the distance from the sensor center to the wall.

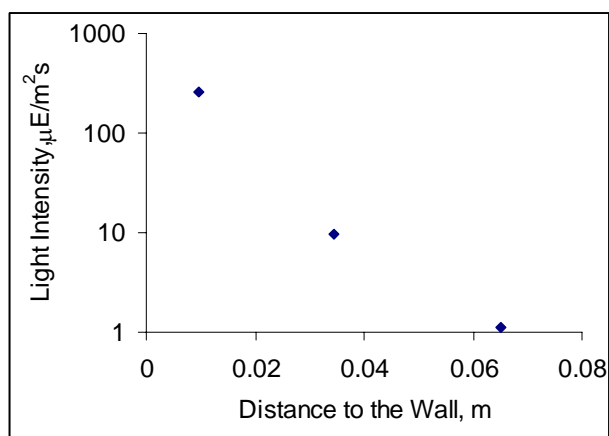


**Figure 7-9.** Azimuthally averaged irradiance versus distance from the sensor to the outer illuminated wall.

To estimate the extinction coefficient due to cellular absorption, the irradiance in the center of the bubble column photobioreactor was monitored during the *Porphyridium sp.* cultures (refer to the biomass evolution section for details). The results for the bubble column reactor were used since it does not have any internals. Following the method proposed by Ación Fernández et al. (1997) and Reboloso Fuentes et al. (1999), the measured irradiance in the center of the bubble column reactor were normalized by the initial irradiance and plotted versus the medium's optical density, as shown in Figure 7-10. The slope of the obtained straight line thus is the product of the extinction coefficient with the distance of



the irradiance sensor center to the illuminated wall. In a bubble column reactor, this distance should be the averaged distance of any points on the spherical sensor to the wall. That is:

$$\bar{d} = \frac{1}{r} \int_0^r (R - \sqrt{r^2 - x^2}) dx = R - \frac{\pi}{4} r = 0.0575m \quad (7-6)$$

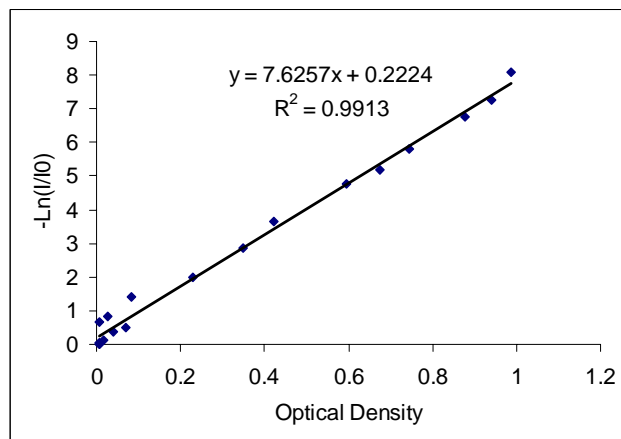


**Figure 7-10.** Relationship between the optical density and the light intensity in the bubble column photobioreactor center.

Therefore, the extinction coefficient due to the cellular absorption is:

$$k_x = 7.6257 / 0.0575 = 132.5 \text{ m}^{-1} \quad (7-7)$$

This value is larger than the value reported by Reboloso Fuentes (1999) ( $82\text{m}^{-1}$ ), who used a similar approach to evaluate this parameter. It is also slightly above the range of  $k_x$  ( $68.7\sim 126\text{m}^{-1}$ ) reported by Oswald (1977). Wu and Merchuk (2001) arbitrary selected the lowest value (i.e.,  $k_x = 68.7$ ) from this range.

On the other hand, the light transmittance of acrylic is reported to be 82% over 3mm thickness (<http://www.sdplastics.com/ac350.html>). This transmittance corresponds to an attenuation coefficient of  $-\ln(0.82)$ . For a 5mm thick wall, the attenuation coefficient thus is:

$$k_w = -\ln(0.82)/3*5 = 0.33 \quad (7-8)$$

The light intensity inside the reactor thus can be expressed as:

$$\frac{I}{I_w} = \begin{cases} \exp[-k_x \cdot x \cdot d] & (\text{Outside or without the draft tube}) \\ \exp[-(k_x \cdot x \cdot (d - 0.005) + k_w)] & (\text{within the draft tube}) \end{cases} \quad (7-9)$$

where  $k_x$  and  $k_w$  are  $132.5 \text{ m}^{-1}$  and  $0.33$ , respectively.

#### 7.4.4 Photobioreactor Performance of the Draft Tube Column

The performance of the draft tube airlift column on *Porphyridium sp.* culturing is demonstrated in Figure 7-11, where the evolution of the culture medium's optical density, the dry biomass concentration, the chlorophyll (a) concentration, and the measure irradiance in the reactor center are shown. A lag time as long as 70 hours was observed, suggesting large difference between the culture environments in the small and in large scale cultures. This is reasonable considering the large irradiance difference between these two cultures and the large dilution rate during the inoculums.

After the cells have adapted to the new environment, the culture enters an active growth stage. The optical density, the dry biomass concentration, and the chlorophyll (a) concentration increase almost linearly with time. Correspondingly, the light intensity in the reactor center also decreases linearly, indicating that photolimitation effects start to dominate the cellular growth as the low light intensity zone grows. Under such conditions, the flashing light effects are not prominent due to the low light intensity used, and the overall growth rate of the reactor is fairly proportional to the total light energy supplied. In this stage, most of the *Porphyridium sp.* cells are quite small as observed under a microscope (comparing to the later growth stages).

To investigate the photoinhibition and the flashing light effects on the draft tube airlift column photobioreactor, eight high output fluorescence lamps were switched on when the culture's optical density reached one. This gave a total photon flux density on the illuminated surface as high as  $1850 \mu\text{E}/\text{m}^2\text{s}$ , as mentioned above. As shown in Figure 7-11, the overall growth rate and the dry biomass concentration were considerably enhanced due

to enhanced light availability. However, the chlorophyll (a) concentration dropped radically, and recovered somewhat after some time. Since the chlorophyll contents reflect the strategies the microorganisms adopted to handle the light intensity stress (Falkowski and Raven, 1997), such behavior demonstrates the existence of photoinhibition in the reactor under high PFD.

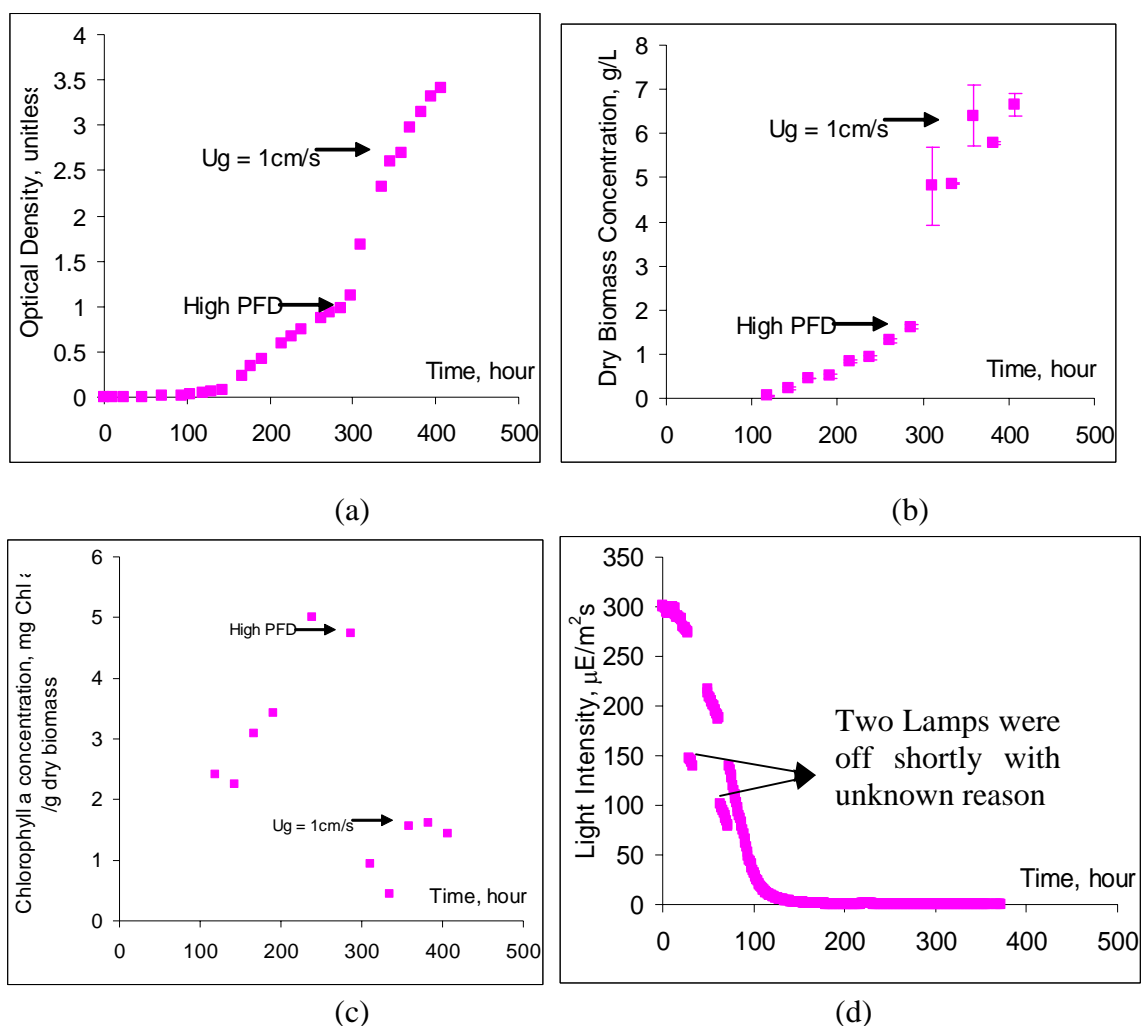


**Figure 7-11.** Biomass concentration evolutions in the draft tube airlift column photobioreactors for *Porphyridium sp.* culturing. (a) Evolution of the culture medium's optical density; (b) Evolution of the dry biomass concentration; (c) Evolution of the normalized chlorophyll (a) concentration by the dry biomass concentration; (d) Evolution of irradiance in the reactor center.

To further investigate the effects of the mixing intensity on the reactor performance, the superficial gas velocity was increased to  $1\text{ cm/s}$ , when the medium's optical density reached about 2.5. As shown in Figure 7-11a, a small jump of the optical density can be observed after the superficial gas velocity was increased. However, such enhancement did not last long, and it is not clear from the dry biomass weight profiles shown in Figure 7-11b. The measurements of the dry biomass weight usually have large variance. Nevertheless, these results imply that increasing the superficial gas velocity at a high biomass concentration has only minor effects on the reactor performance.

Indeed, under conditions of high biomass concentration, the light energy is concentrated in the highly illuminated wall region. This region lies in the turbulent sub-layer and is low in turbulent intensity. Moreover, the liquid phase becomes non-Newtonian with a high apparent viscosity at low shear rate as mentioned above, which could further damp out the turbulent intensity in the wall region. Therefore, although increasing the superficial gas velocity enhances the turbulent intensity in the wall region and thus improves the overall growth rates, such effects can not last long, as the medium's apparent viscosity also increases fast due to the growth. Moreover, as observed in the experiments, increasing superficial gas velocity at the late growth stage generated a large amount of foaming, which carried liquid phase out of the column. When the liquid dynamic level of the liquid phase decreased, the experiment eventually failed and the biomass concentration in culture dropped suddenly (not shown in the figure).

Figure 7-12 compares the reactor performance measured in this work with the experimental data obtained by Merchuk et al. (2000). Both experiments were carried out in a draft tube column with similar configurations and superficial gas velocities ( $U_g$  of  $0.3\text{ cm/s}$ ). But the experiments done by Merchuk et al. (2000) started with a high initial biomass concentration and had a little bit lower incident light intensity ( $250\mu\text{E}/\text{m}^2\text{s}$  compares to  $267\mu\text{E}/\text{m}^2\text{s}$  in this work).

To better compare these experimental data, Merchuk et al.'s data (2000) were shifted rightwards, since the lag times for these two set of data are very different. Moreover, since the experimental results of Merchuk et al. (2000) were originally presented by cell number concentration, the optical density data measured in this study were converted into cell number concentration using Equation (7-2). The optical density measurements are more accurate and consistent than other biomass measurements performed in this work.

Figure 7-12 clearly shows the difference between these experimental results. Without a discernible lag period, the biomass concentration profile measured by Merchuk et al. (2000) initially has a slope close to the profiles obtained in this study, but shows a jump at time around 170<sup>th</sup> hour, and eventually reaches a higher biomass concentration than the experiments performed in this study. Although it's not clear what intrigued such a jump and why the biomass concentration profile did not reach a plateau in their results as our and other reported results in the literature (Hu et al., 1998; Muller-Feuga et al., 2003), these results clearly indicate a better reactor performance achieved in the experiments performed by Merchuk et al. (2000).

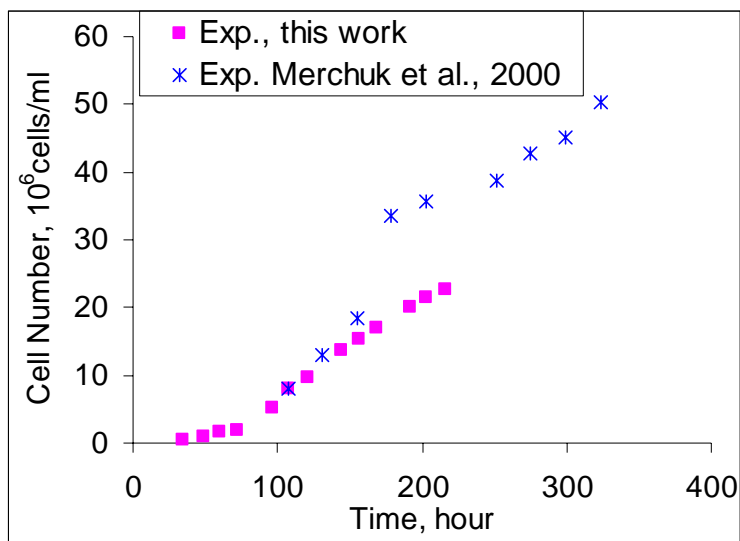


**Figure 7-12.** Comparison of the reactor performance data measured in this study and the ones measured by Merchuk et al. (2000) at superficial gas velocity: 0.3 cm/s. Please see the text for the details of the operating conditions. Only data obtained at the low PFD stage in this work are shown for better comparison.

These results suggest that the photosynthetic efficiency and thus the kinetic parameters of *Porphyridium* sp. could be quite different even the PBRs were operated at very similar operating conditions. This is reasonable considering the complexity of the microalgal culturing system and the difficulty in handling *Porphyridium* sp., which is a rather hard to handle species as pointed out by Dr. Fernandez Sevilla during personal communications. Many factors could affect the experimental results such as nutrient composition, pH value, trace chemical presented in the media, and temperature. In fact, the culture temperature, not controlled in this study, was slightly lower than the experiments performed by Merchuk et al. (2000). The experimental setup in this study was located immediately below the air-conditioning outlet of the whole room, so the temperature was slightly below the overall room temperature (about 21~22°C compared to 24~25°C of Merchuk et al., 2000).

#### **7.4.5 Effects of Reactor Geometry on Performance**

Figure 7-13 demonstrates the effects of reactor geometry on the photobioreactor performance in terms of the optical density, the dry biomass concentration, and the chlorophyll (a) concentration normalized by the dry biomass concentration. Please note that, due to the different lag times present for the cultures and to better compare the reactor performances at different growth stage, the biomass evolution curves were shifted to match the same point where the high PFD stage starts (i.e., the time when all lamps were switched on).

As shown in Figures 7-13(a), the measured optical densities for the studied PBRs increase almost linearly at the active growth stage, when the optical density was in the range of 0.1 to 1.0. The optical density profile of the split column has a higher slope than the other columns as further demonstrated in Figure 7-14, indicating a faster growth at this active growth stage in this type of PBR. When all lamps were switched on, the optical densities for the draft tube and the bubble columns increase exponentially, while the optical density

for the split column increases still almost linearly. However, the optical densities for all three columns eventually reach a level very close to each other at about the 320<sup>th</sup> hour. When superficial gas velocity increased to 1 cm/s, the biomass concentration in the bubble column soon reaches a plateau while the concentrations in the draft tube column and the split column keep increasing to a higher level. These trends are not clear from Figure 7-13(b) due to the higher variance for the dry biomass concentration measurements.

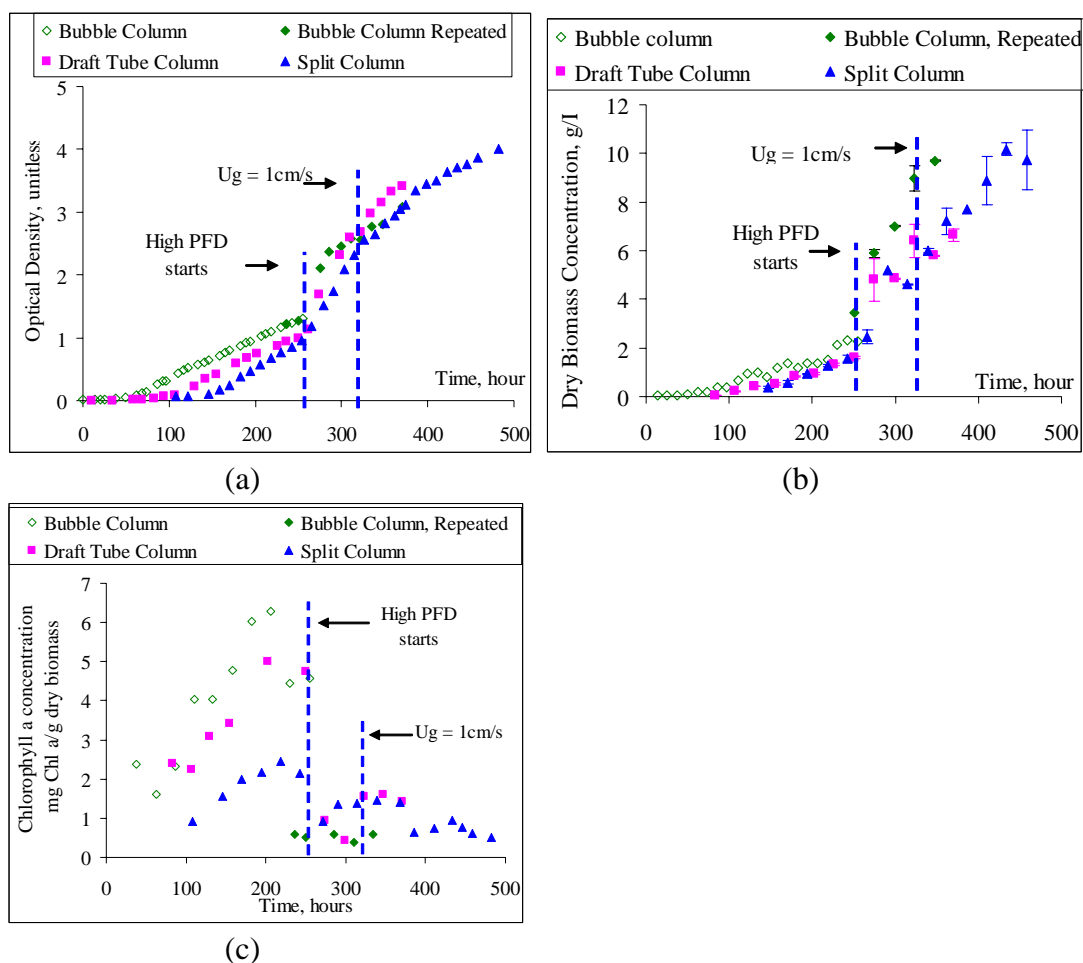


**Figure 7-13.** Biomass concentration evolutions in three airlift column photobioreactors for *Porphyridium sp.* culturing. (a) Evolution of the culture media's optical density; (b) Evolution of the dry biomass concentration; (c) Evolution of chlorophyll (a) concentration normalized by the dry biomass concentration. Please note that the culture in the bubble column failed due to overheating after the high light intensity lamps were switched on (halogen lamps was used in the first trial). The experiment with high PFD in the bubble column therefore was repeated using fluorescent lamps as described in the experimental section.

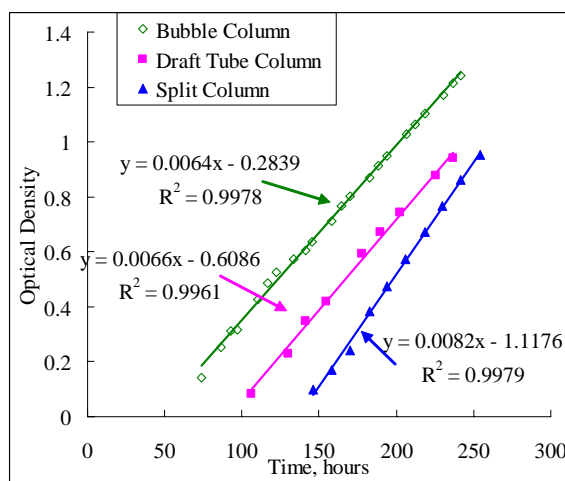


**Figure 7-14.** Evolution of the optical density in the studied PBRs for *Porphyridium* sp. culturing at the active growth stage.

The observed faster growth rate in the split column at low PFD stage can be further proofed by the normalized chlorophyll (a) concentration profile as shown in Figure 7-13(c). The normalized chlorophyll (a) concentration of the split column is considerably lower than that of the other columns. Based on photosynthetic principles (Falkowski and Raven, 1997), such lower pigment contents suggest that the cells in the split column face higher light stress. This implies that these cells have more chance to visit the wall regions, therefore resulting in a better performance. These results are consistent with the discussions presented in Chapter 3 and Chapter 4. In the split column, the cells' spiral movements found in Chapter 3 enhance the cells' accessibility to the outer wall region where light is abundant, promote the light fluctuations experienced by the cells, and thus improve the reactor performance.

When all lamps were switched on, a sudden drop of the chlorophyll (a) concentration was observed for all the studied columns, indicating that photoinhibition effects became prominent. Moreover, the chlorophyll (a) concentrations of the split and the draft tube columns eventually settled down at a similar level, which is higher than that of the bubble column. Unfortunately, because the experiment for the bubble column failed initially and was repeated, it is not clear the lower pigment concentration presented in the bubble



column is a result of the experimental error or due to more prominent photoinhibition effects.

These results suggest that the reactor geometry can affect the reactor performance. However, it should be pointed out that due to the limited experimental results presented in this study, it is not clear if the observed reactor performance behaviors are reproducible. Apparently, to better understand the effects of the reactor geometry, and thus the local flow dynamics, on the PBR performance, more comprehensive studies are required.

## **7.5 Simulations of the Dynamic Growth Rate Model**

To verify the dynamic model previously developed in Chapter 4, two cases were considered. The CARPT data obtained from the *Porphyridium sp.* culturing system in the draft tube column reactor were first utilized to predict the reactor performance measured by Merchuk et al. (2000), and then to predict the reactor performance measured in this study.

### **7.5.1 Simulation for the Reactor Performance of Merchuk et al. (2000)**

To simulate the reactor performance measured by Merchuk et al. (2000), the parameters listed in Table 4-1 were used. The results are presented in Figure 7-15, together with the experimental data and the predictions made in Chapter 5, which are based on CARPT data obtained in an air-water system. The figure clearly shows that the predictions based on CARPT data obtained in a real culturing system reasonably fit the experimental data, and significantly excel the predictions made in Chapter 5. Those predictions were made based on CARPT data obtained from air-water system. Apparently, the physical property changes have a significant role in this situation, as discussed earlier. These changes affected the occurrence density distribution of the cells in the reactor as shown in Figure 7-7(a), and in turn the light availability, as shown in Figure 7-15.

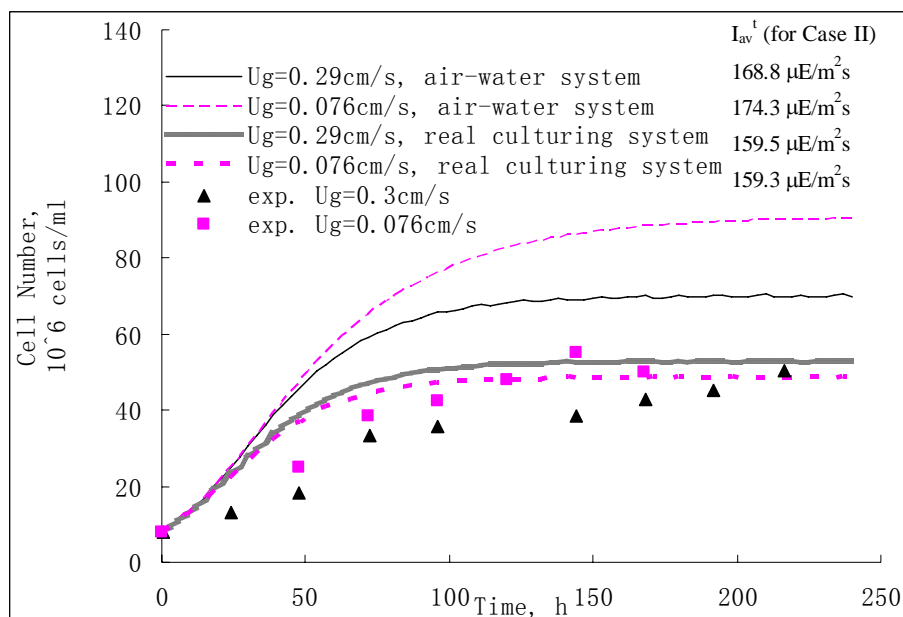


**Figure 7-15.** Dynamic simulation of the reactor performance measured by Merchuk et al. (2000) using CARPT data obtained from *Porphyridium sp.* culturing system. The prediction made in Chapter 5 based on CARPT data obtained from an air-water system is also shown. The time-averaged light intensities were calculated by Equation (4-1) for Case I (i.e., External Irradiance= $250\mu E m^{-2} s^{-1}$ ; Cell concentration= $8 \times 10^6$  cells/ml). Model parameters listed in Table 4-2 were used for all simulations.

### 7.5.2 Simulation for the Reactor Performance of this Work

The reactor performance measured in this study was also simulated. This simulation used the CARPT data obtained from this study and Equation (7-9) for the light intensity distribution inside the reactor. Moreover, since the growth rates present in this study are about half of the rates measured by Merchuk et al. (2000), two parameters in the photosynthetic kinetic model listed in Table 4-2, i.e., the yield of the photosynthesis reaction ( $k$ ) and the maintenance parameter ( $Me$ ), were reduced by half. That is equivalent to assuming that the efficiency of the dark reactor is reduced by half:

$$\frac{1}{x} \frac{dx}{dt} = \mu = k \cdot \gamma \cdot x_2 - Me \quad (2-11)$$

The other photosynthetic parameters listed in Table 4-2 were used unchanged.

Figure 7-16 shows the simulation results and the experimental data. It is obvious that the dynamic model remarkably matched the reactor performance measured in this work, in both the low and high PFD regions. These results strongly suggest that the dynamic growth rate model developed in Chapter 4 can be used to predict the performance of photobioreactors under conditions of high biomass concentration and high PFD. However, recalling the unsuccessful predictions made in Chapter 4, 5 and 6, it has to be pointed out that reliable information about flow dynamics, light intensity distributions, and photosynthesis are essential for the prediction capability of the dynamic model. Therefore, in-depth knowledge of the flow dynamics, the irradiance distribution, and the kinetics for the photosynthesis are critical for photobioreactor design, scale-up, operation, and process intensification.

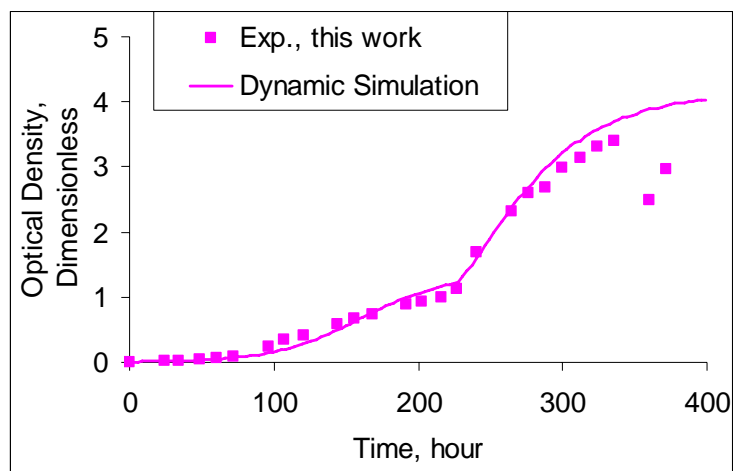


**Figure 7-16.** Dynamic simulation of the reactor performance measured in this study using the CARPT data obtained in *Porphyridium sp.* culturing system. Model parameters: equation (7-9) was used for the light intensity distribution and parameters listed in Table 4-2 were used for photosynthetic growth rates with justified  $k$  and  $Me$ .

## 7.6 Summary

In this Chapter, a red alga, *Porphyridium sp.*, was cultured in three types of airlift column reactors. The physical properties of the liquid phase, local flow dynamic characteristics,

light intensity distribution inside the column, and the growth of the cells were studied, which presented rich information for photobioreactor analysis. Moreover, the reactor performances were simulated using the experimentally measured data. The following conclusions can be drawn from this work:

1. *Porphyridium sp.* excretes polysaccharides, which significantly changed the physical properties of the culture medium. As a result, the medium showed a typical shear-thinning property.
2. The present of microalgae in the liquid phase considerably affected the local multiphase flow dynamics in the draft tube column reactor: the particle's occurrence number at the wall regions considerably decreased; the liquid phase turbulent kinetic energy and the local gas holdups in the fully developed flow zone increased appreciably; and the overall liquid circulation velocity and the shear stress changed slightly.
3. At high biomass concentration, the light intensity distribution inside the draft tube column photobioreactor is likely to follow the Lambert-Beer law. The attenuation coefficient due to cellular absorption was also estimated.
4. The effects of reactor geometry, external light intensity, and superficial gas velocity on the reactor performance of the *Porphyridium sp.* cultures were investigated by monitoring the biomass concentration evolution, i.e., the optical density of the medium, dry biomass weight, chlorophyll (a) concentration, as well as the cell morphology. The results demonstrate that, at the earlier active growth stage, the split column reactor works slightly better than the bubble and the draft tube column reactors and had the lowest photoinhibition effects. At high PFD, photoinhibition is significant and increasing the superficial gas velocity had limited effects on the reactor performance.
5. The dynamic growth rate model developed in Chapter 4 successfully predicted the reactor performances measured in this study and the performance measured by Merchuk et al. (2000). These results demonstrated the robustness of the developed dynamic growth rate model and indicated potential applications in conditions of high PFD and biomass concentration. However, it is noteworthy that the reliability

of this model is largely determined by the accuracy of the inputs from knowledge of flow dynamics, light intensity distribution, and the photosynthetic kinetics. Better understanding of such knowledge thus is crucial to photobioreactor design, scale-up, and operation.

## **Chapter 8**

# **Conclusions and Recommendations**

### **8.1 Summary and Conclusions**

The overall objective of this research is to advance the understanding of the role of hydrodynamics in the photobioreactor performance, and to develop a fundamentally based modeling approach for cell growth predictions that integrates the hydrodynamics, photosynthesis, and irradiance distribution. To accomplish the objective, this research used two advanced hydrodynamic measurement technique, i.e., CARPT and CT, and a computational technique, i.e., CFD simulation, to study the local multiphase flow dynamics in airlift column reactors.

#### **8.1.1 Using the CARPT Technique for PBR Analysis**

The first part of this thesis, Chapters 3 and 4, began with testing the feasibility of using the CARPT technique for PBR analysis. Based on the findings from the CARPT measurement, we further proposed a mechanism for the interactions between the flow dynamics and photosynthesis. Methodologies to characterize the light availability and fluctuations delivered to the microorganism cells were also suggested. A novel fundamentally based modeling approach was developed which directly integrates the

principles of flow dynamics, photosynthesis, and irradiance distribution inside the reactor for photobioreactor performance evaluation.

The following major conclusions can be drawn from the results presented in the first part of this thesis:

- The CARPT technique is very promising for photobioreactor analysis. It provides fundamental information needed to advance cell growth rate predictions for PBR modeling, design, scale-up, and operations.
- Different types of airlift columns, e.g., draft tube, split, and bubble columns, were studied. These reactors involve three types of liquid phase mixing mechanisms, which induce flashing lights experienced by the cells. The time scales of the mixing or the light fluctuations are not only in seconds, but also in 10 ms. This range of time scales overlaps the range associated with the photosynthesis. As a result, when the cell moves between the highly illuminated surface and the dark center, the reaction centers of the photosynthetic apparatus of a cell can relax promptly and avoid over-reduction. Therefore, it is possible to keep the quantum yield and the light utilization efficiency high. Moreover, the photoinhibition effect can also be greatly reduced as the prompt “relaxation” prevents some proteins from over-oxidization. These proteins are responsible for photoinhibition.
- The temporal irradiance patterns can be calculated from the CARPT measured particle trajectories using an appropriate irradiance distribution model. These patterns contain a cascade of light fluctuations with different frequencies due to the chaotic nature of flow dynamics. Based on the principles of how flow dynamics interact with photosynthesis, a concept of over-/under- charged cycle was proposed. This concept was also applied to quantitatively characterize the light availability and fluctuations delivered to the cells by three parameters: the time averaged irradiance, the frequency of the over-/under- charged cycles, and the dimensionless relaxation time.
- A novel dynamic modeling approach was developed for PBR performance evaluation. This general approach integrates first principles of photosynthesis,

hydrodynamics, and irradiance distribution within the reactor. It can be extended to include other physiologically based photosynthesis rate models and irradiance distribution models. Hence, this approach provides a direct and comprehensive tool for photobioreactor analysis, which should be essential for proper and efficient reactor design and scale-up for large-scale biomass production.

### **8.1.2 Using CARPT, CT, and CFD to Obtain Flow Dynamic Information**

The second part of this thesis, Chapters 5 and 6, focused on advancing the knowledge of local flow phenomena in airlift photobioreactors, and on developing accessible techniques to obtain needed hydrodynamic information for PBR analysis. A comprehensive study was carried out using both the CARPT and CT techniques to study the local hydrodynamic characteristics in a draft tube airlift column reactor in an air-water system. The acquired rich information was further used to guide the development of a computationally feasible and promising CFD model targeting needed flow dynamic information for PBR analysis.

From this part of the thesis, the following major conclusions were reached:

- A residence time distribution analysis showed that the overall macro-mixing in the draft tube column reactor is close to plug flow, which is true for both the Riser and Downcomer regions. However, considerable bypassing and stagnancy occur in the Top and the Bottom regions, which can not be modeled as a CSTR.
- Increasing the superficial gas velocity considerably increases the liquid flow velocities, turbulent intensities, and the gas holdups in the whole reactor, but does not necessarily improve the macro-mixing in the reactor.
- The Top and Bottom clearances have significant effects on the flow structures (e.g., the turbulent kinetic energy, the shear stresses) at the Top and Bottom regions and the gas holdup in the Downcomer. These clearances thus influence the bulk liquid flow in the Riser and Downcomer. In particular, decreasing the top or bottom clearances can radically change the magnitudes of the turbulent kinetic energy and



the Reynolds shear stress in these two regions, which may have substantial effects on photobioreactor performance.

- A light fluctuation analysis revealed that increasing the superficial gas velocity enhances the light fluctuations and affects light availability delivered to the cells. However, how superficial gas velocity affects the light availability is not clear.
- The predictions based on the dynamic growth rate model developed in Chapter 4 and the particle trajectories measured in an air-water system considerably over-estimated the photobioreactor performance as measured by Merchuk et al. (2000). However, the predictions captured the trend of the reactor's performance with superficial gas velocity.
- A computationally promising CFD simulation model has been identified to study the multiphase flow dynamics in an internal loop airlift column reactor under the bubbly flow regime. This model is based on 3D steady state simulations and uses the  $k-\varepsilon$  turbulent model, Ishii-Zuber's drag force correlation, and Lopez de Bertodano's turbulent dispersion force with a coefficient of 0.3.
- The identified CFD model and closures satisfactorily captured the mean multiphase flow field, but considerably under-estimated the turbulent intensity in the studied airlift column.
- A pseudo Eulerian-Lagrangian approach was utilized to simulate the movements of small neutrally buoyant particles in the airlift column. The computed particle trajectories reasonably matched the experimental data based on the single trajectory analysis. However, the computed trajectories were biased to the wall regions.
- The photobioreactor analysis using the CFD simulated particle trajectories obtained in this study considerably over-estimated the overall growth rate.

### 8.1.3 Verifying the Dynamic Growth Rate Model

The third part of this thesis, Chapter 7, presented an extensive verification of the dynamic growth rate model developed in Chapter 4. A red marine alga, *Porphyridium sp.*, was

cultured in three types of airlift column reactors, i.e., draft tube, split, and bubble columns. The physical properties, multiphase flow dynamics, irradiance distribution inside the reactor, evolution of the biomass concentration, and photoinhibition effects were examined. The following conclusions can be drawn from this study:

- *Porphyridium sp.* excretes polysaccharides, which significantly changed the physical properties of the culture medium. The medium shows a typical shear-thinning property.
- The present of microalgae in the liquid phase considerably affects the local multiphase flow dynamics in the draft tube column reactor: the algal occurrence density at the wall regions considerably decreased, the liquid phase turbulent kinetic energy and the local gas holdups in the fully developed flow zone appreciably increased, and the overall liquid circulation velocity and the shear stress varied slightly.
- The light intensity distribution inside the draft tube column photobioreactor at high biomass concentration is likely to follow the Lambert-Beer law. The attenuation coefficient due to cellular absorption was also estimated.
- Effects of reactor geometry, illuminating irradiance, and superficial gas velocity on the reactor performance of the *Porphyridium sp.* cultures were investigated by monitoring the evolution of the biomass concentration. The biomass concentration was measured in terms of the optical density of the medium, dry biomass weight, chlorophyll (a) concentration. The limited experimental data presented in this study demonstrated that, at the earlier active growth stage, the split column reactor works slightly better than the bubble and the draft tube column reactors and has the lowest photoinhibition effects. At high PFD, photoinhibition is significant. However, increasing the superficial gas velocity has limited effects on the reactor performance.
- The dynamic growth rate model developed in Chapter 4 successfully predicted the reactor performances measured in this study and the performance measured by Merchuk et al. (2000). In these predictions, the CARPT data obtained from the *Porphyridium sp.* cultures were used and other needed parameters were selected

corresponding to the different cases. These results demonstrated the robustness of the developed dynamic growth rate model and indicated its potential applicability in industrial interested conditions (i.e., high incident light intensity and biomass concentration).

## 8.2 Recommendations

Recommendations for future work on PBR analysis and modeling work are as follows:

1. **The photosynthetic rate model:** The only available model in the literature, the three-state photosynthetic rate model proposed by Eilers and Peeters (1988), was employed in this research to represent the photosynthetic kinetics. It is a simple and easy to handle model based on physiology. However, some important physiological processes are not included in this model, such as photo-acclimation, photo-adaptation, photo-respiration, and so on. Including these processes in the model could considerably enhance the reliability of the predictions based on this model. However, this effort requires an excellent understanding of complex photosynthesis and is out of the scope of this research. On the other hand, it should be pointed out that the estimated model parameters were relied on experiments conducted under low flashing light frequencies (Wu and Merchuk, 2001). Better designed experiments could certainly help to estimate more realistic model parameters and to improve the model's capability to capture the high frequency flashing light effects.
2. **Light fluctuations:** Three parameters were recommended to quantitatively characterize the light availability and fluctuations delivered to the cells. These parameters can be used to advance our understanding of the flashing light effects and to analyze photobioreactors. However, these parameters have not been directly related to the reactor performance due to the limited experimental data. It could be very helpful if these parameters could be directly related to the reactor performance, using empirical or semi-empirical correlations. A bridge between the reactor performance and the

reactor geometry and operating parameters thus could be established. It could greatly facilitate photobioreactor design, scale-up, and process intensification, especially considering the fact that the CARPT technique is not widely accessible.

3. **Reactor performance studies under real culturing conditions:** As shown in Chapter 7, the physical properties and the multiphase flow dynamics in a real autotrophic cell culture system are very different from the air-water system studied here. A comprehensive study in a more realistic culturing system thus is needed for better verification of the developed novel approach for PBR analysis. For example, instead of running in the batch mode for the liquid phase, the photobioreactor should be operated at constant biomass concentrations and be maintained at more controlled operating conditions, such as temperature, pH, and nutrient concentrations. Thus the effects of the operating conditions, e.g., the superficial gas velocity and reactor geometry parameters, can be better understood. Moreover, other types of photobioreactors, such as tubular reactors, could also be tested, with the ultimate goal of developing cost effective and efficient photobioreactors for mass autotrophic cell production.
4. **Improvement of CARPT technique:** In this research, we relied on the CARPT technique to provide in-depth and fundamental knowledge of the local flow phenomena inside the reactors. Although this technique has been developed in our laboratory for many years and has achieved high reliability, it still has some room for improvement, especially for its application in PBR analysis. A smaller particle is needed to capture the local flow phenomena in the reactor. Considering the difference between the tracer particle size used in this study and the size of a microorganism cell, some small scale turbulence has been ignored. Also, a radioactive particle with stronger strength may help reduce the white noise magnitude.
5. **The irradiance distribution model:** A more realistic and fundamentally based irradiance distribution model and photosynthetic rate model should be adopted for

photobioreactor analysis. The Lambert-Beer law used in this research to present the irradiance distribution inside the reactor is straightforward, but too simple to capture the real irradiance the cells may have experienced. It is well-known that visible light with different wavelengths has different attenuation coefficients in the culture medium, and thus different penetration depth. Moreover, it has different quantum yields for the light reactions in the photosynthetic apparatus, depending on the type of pigments an autotrophic cell possesses. Considering the fact that light is the limiting factor for PBR performance, the accuracy of the irradiance distribution model could considerably affect the reliability of the developed approach for PBR performance evaluation.

6. **CFD simulations:** As a very powerful and fast advancing tool in the study of multiphase flow dynamics, CFD simulation can provide in-depth knowledge of hydrodynamic information for photobioreactor analysis. Successful integration of CFD and the dynamic growth rate model developed in this work can form a more general and favorable modeling approach for PBR design, scale-up, and process intensification. Experimental work in studying the physical properties and flow dynamics may be very helpful in guiding the CFD simulation.

## **Appendix A**

### **Automatic Calibration Device for CARPT Experiments**

An automated calibration device was specifically developed in this study to facilitate the experimental work. This automated device is needed although a manual and another automated calibration device are available in our laboratory. CARPT experiments using the manual calibration device is generally very time-consuming, unsafe to the experimentalists, and has low accuracy. On the other hand, although the available automated calibration can be used for high pressure system, it can only be applied to six inch diameter columns. It is able to move radioactive particles only in axial and angular directions. Therefore, CARPT experiments using this calibration device are generally also time consuming and labor intensive.

This novel calibration device allows full automation in moving the radioactive particle in radial, axial, and angular directions. It can also be applied to different size of columns (up to 18 inch) at atmospheric pressure. Moreover, it is more reliable and accurate than the currently available manual calibration device. And it is fast (needs around 5 hours to complete more than 1000 calibration positions). Therefore, this calibration device can not only be applied to this study but also be applied to many other studies requiring CARPT experiments in our laboratory.

The design and operation of the new calibration device developed in this study are described as follows.

## A.1 Structure of the calibration device

A schematic diagram of the calibration device is shown in Figure A-1 while a picture is shown in Figure A-2. The device consists of four major parts: a base plate, a rotation system, two unislides, and several rods. The rotation system is mounted on the base plate for angular motions, while the unislides are mounted on the rotational plate to move the radioactive particle in radial and axial directions. With the radioactive particle attached on the tip of the calibration rods, which are mounted on the unislides, the whole system thus can move the radioactive particle in radial, axial, and angular directions to the desired positions. To guarantee the precision and the smoothness of the particle's movements, the designs have been carefully made as discussed below.

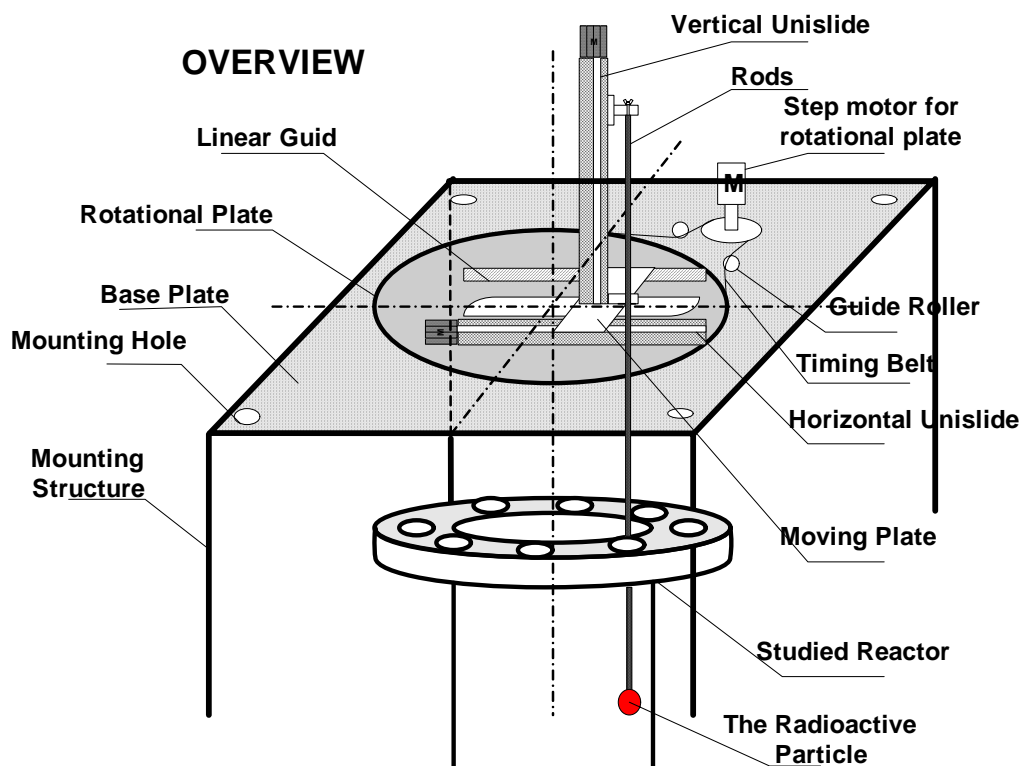


**Figure A-1.** Schematic diagram of the calibration device (Please note the drawing is not in scale)

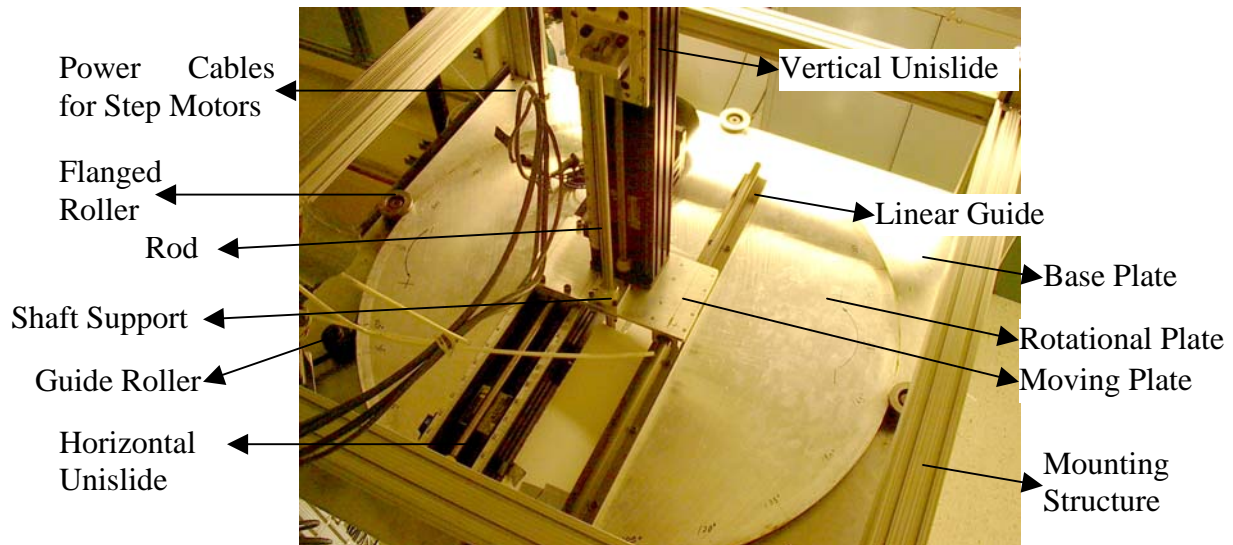


**Figure A-2.** Picture of the automatic calibration device

1. The base plate is a square aluminum alloy plate of 33 inch wide and  $\frac{3}{4}$  inch thick as shown in Figure A-3. An 18 inch diameter hole is cut out from the base plate in the center so that the calibration rods can go through. Therefore, this calibration device can be applied to CARPT experiments for reactors up to 18 inch in diameter.
2. The rotation system, mounted on the base plate, moves the radioactive particle in angular directions. It has a rotational plate, four flanged rollers, a step motor, a timing belt, and two guiding rollers as shown in Figures A-4. The rotational plate, a round aluminum alloy with 29 inch diameter and  $\frac{3}{4}$  inch thickness, is edged by four flanged rollers. These rollers have top and bottom flanges with a distance between them that is marginally larger than the thickness of the rotational plate. Therefore, the rotational plate can not move horizontally but rotate. Such rotation is driven by a step motor with a timing belt. To avoid slip between the belt and the rotational plate, a V-shape belt with larger contact surface is used which is installed in the middle of the rotational plate (in vertical direction). The tension of the belt can also be adjusted by moving the step motor forward or backward. Moreover, two guiding rollers are used to increase the contact surface between the timing belt and the



motor. By these designs, the precision of the rotational plate's movement is ensured.

3. Two unislides, made by Velmex Inc., move the radioactive particle in radial and axial ( $r, z$ ) directions. These unislides have step motors installed and are well-known linear motion equipment with high precisions. The first unislide, with a stroke length of 15 inch, is horizontally mounted on the rotational plate for radial movement of the radioactive particle. The second unislide, with a stroke length of 20 inch, is vertically mounted on a moving plate for axial movement of the particle. This moving plate is actually a bridge with one end mounted on the rotational plate and the other end mounted on a linear guide. Parallel to the horizontal unislide, the linear guide is necessary to balance the weight of and the load on the vertical unislide. Hence, the smoothness of the moving plate's movements and the verticalness of the second unislide are guaranteed.
4. Four rods, with  $\frac{1}{2}$  inch diameters, are available which can be connected one by one to form a long rod with length of 72 inch (i.e.,  $4 \times 18$ inch). These rods are installed vertically with one end fixed on the vertical unislide. To guarantee the verticalness of these rods and to protect them from shaking, a shaft support is mounted on the moving plate. Moreover, a rod wiper is installed on the bottom of the shaft support to clean the rod from dirties.

Therefore, by controlling the step motors, we can move the rods and thus the radioactive particle in radial, axial, and angular directions.

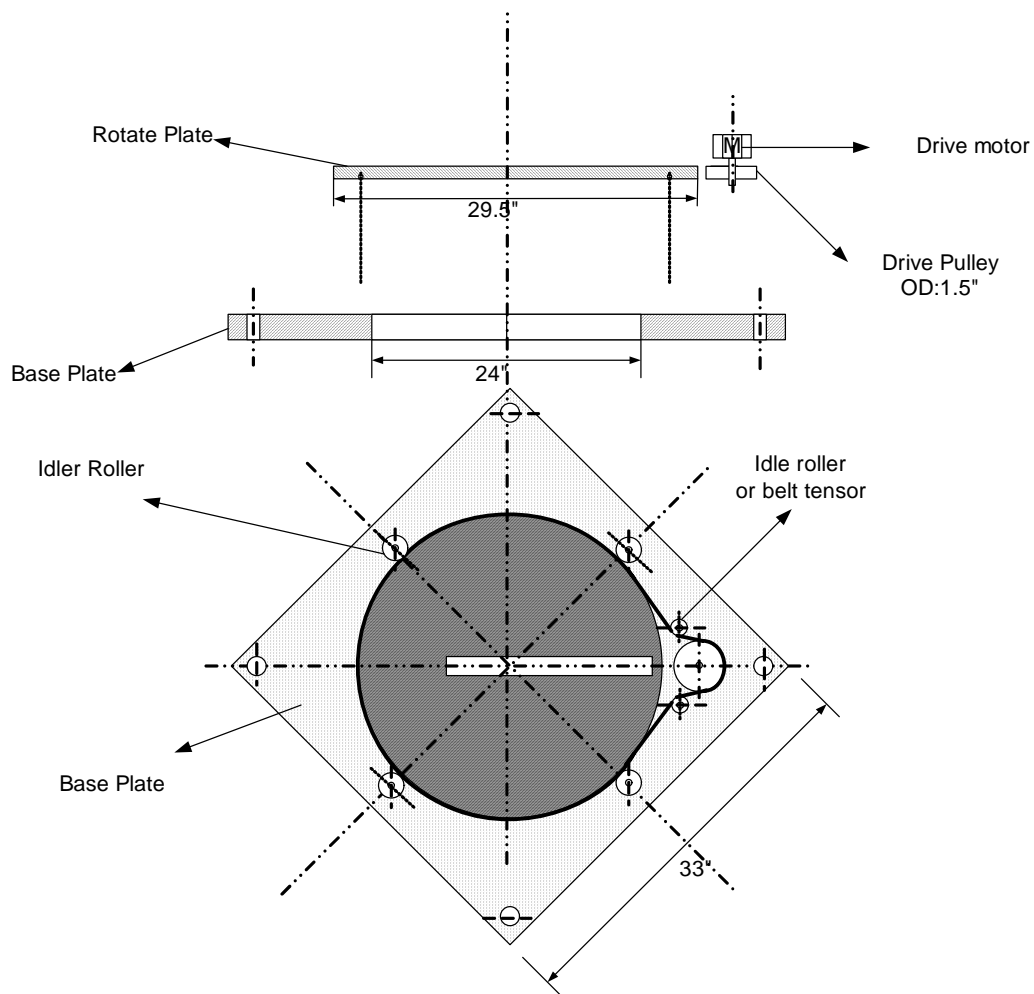


**Figure A-3.** Major dimensions of the base and the rotate plates for the calibration Device



## **A.2 Operation of the Calibration Device**

To operate the calibration device, a motor controller made by Velmex Inc. is used to control the step motors for axial, radial, and tangential movements. Basically, the motor controller receives signals sent by the user from the computer and converts the signals to electrical pulses. These pulses then will be sent to the desired step motors designated by the user. Two methods can be used to generate such signals: the software developed by Velmex Inc. can be used to test the device, while the developed C/C++ programs can be used for continuous calibration in CARPT experiments. In these C/C++ programs, all motor parameters have been set and do not need to be modified. Users just need to follow the instructions on the screen and specify how they want to move the radioactive particle.

## **A.3 Summary**

Recently, this calibration device has been extensively tested and good calibration results have been obtained. We found that this calibration device can considerably speed up CARPT experiments with higher accuracy and much less efforts than the manual methods. Although the calibration device is mounted on a structure with the reactor installed below it, it can also be mounted on any other nicely leveled place. Therefore, it is noteworthy that this calibration device can be widely applied to other applications where the reactor is open to the atmosphere. Such condition has to be imposed since the calibration rods have to be inserted into the reactor from the top.

## Appendix B

### Measurement Errors of the CARPT Experiments

Two major sources may introduce errors to the reconstructed tracer particle position in CARPT experiments as discussed by Romahhan et al. (2001) and Roy et al., (2002). The first type of error is introduced due to the imperfect of the reconstruction algorithm and the errors in the calibration data. It happens when using the calibration data, the time-averaged  $\gamma$ -ray intensity registered by a detector (thus free of white noises), to determine the distance from the tracer particle to that detector. In this step, uncertainties or error could be introduced by the reconstruction algorithm, the detectors' solid angle effects, the calibration, and the dynamic gas holdups (Roy et al., 2002). The second major source of reconstruction error stems from the quantized nature of the  $\gamma$ -ray. The emitted radiation intensity of the radioactive particle exhibits continuous fluctuations in time following a Poisson distribution. Therefore, the signals recorded by the detectors are contaminated by white noises.

To determine the first type of reconstruction errors, the calibration data were input back to the reconstruction algorithm to determine the calibration positions. Figure B-1 shows the typical comparisons between the real calibration positions and the reconstructed calibration positions on both the cross-sectional plane and the x-z plane. To further quantify these error, extra calibration positions were performed, which have not been used to form the calibration curve in the reconstruction algorithm. The reconstruction error of the first type and its projection on the radial direction can be calculated from:

$$e_d = \frac{\sum \sqrt{(x_{real} - x_{rec})^2 + (y_{real} - y_{rec})^2 + (z_{real} - z_{rec})^2}}{N}$$

$$e_r = \frac{\sum \sqrt{(x_{real} - x_{rec})^2 + (y_{real} - y_{rec})^2}}{N}$$
(B-1)

where  $e_d$  and  $e_r$  are, respectively, the reconstruction error in a 3D domain and its radial component; subscription of *real* indicates the real particle positions while *rec* indicates the reconstructed ones.

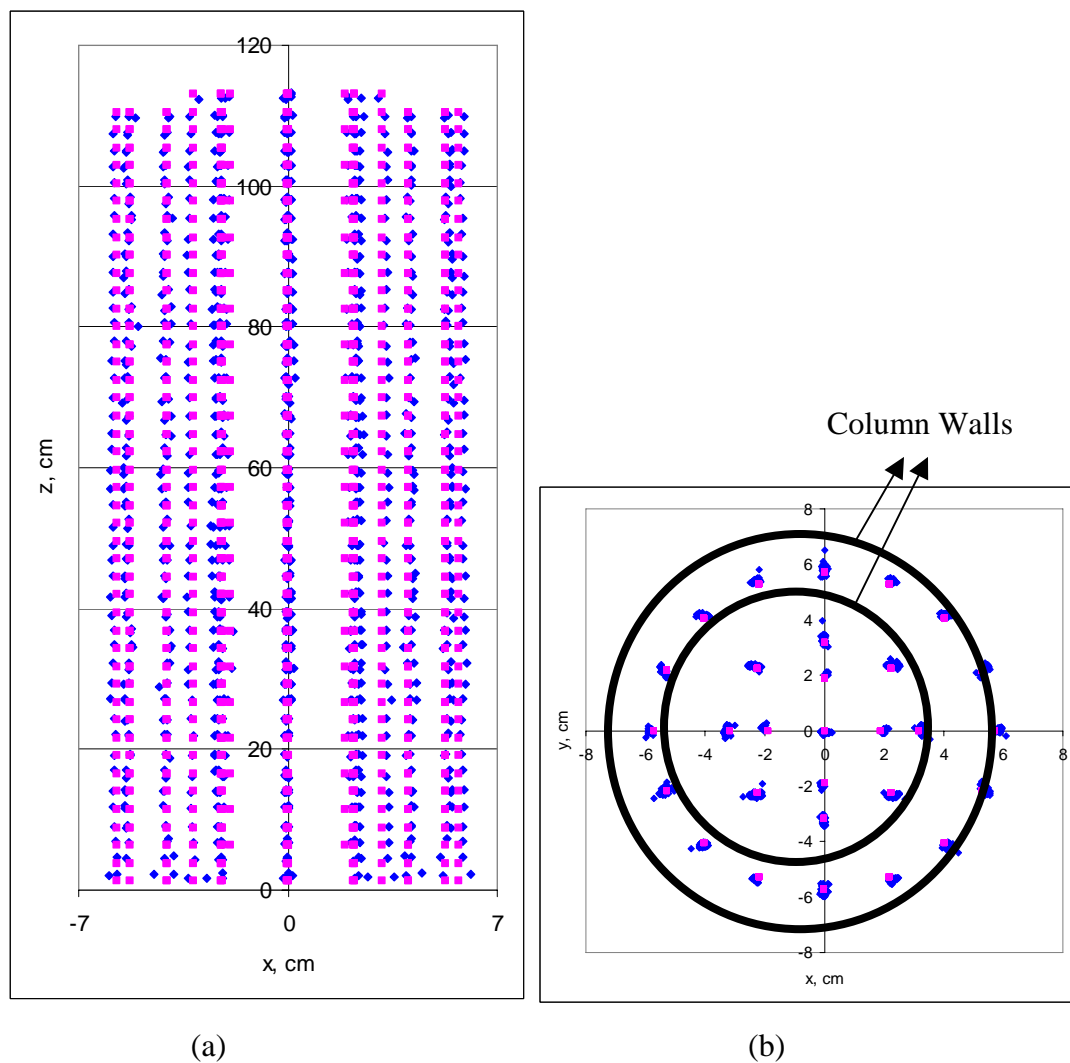


**Figure B-1.** Comparisons of the real particle positions and the reconstructed positions in a calibration. (a) Particle positions on the x-z plane; (b) Particle positions on the cross-sectional plane. Please note the dots with light color are the real particle positions while the dots with dark color are the reconstructed ones.

In this study, more than 80 such extra known particle positions are used to estimate the errors. Errors in the Riser and Downcomer obtained for a typical operating condition are

listed in Table B-1. As can be seen, the errors are around 3~5 mm for  $e_d$  and around 1~2mm for  $e_r$ , indicating that the errors on the axial direction are larger than the errors on the radial direction. This is because of the limited number of detectors used on the axial directions and of the detectors' solid angle effects.

**Table B-1.** Estimated reconstruction error for a typical measurement

	$e_r$ (cm)	$e_d$ (cm)
Riser	0.163	0.304
Downcomer	0.164	0.417

Moreover, it can also be observed that the absolute errors in the Downcomer are larger than those in the Riser. The reason is illustrated by Figure 5-6, which is also shown below. When the radioactive particle is in the Downcomer, the emitted  $\gamma$ -rays need to pass through the plastic outer cylinder once to reach the nearest detector (i.e., one wall thickness). But the  $\gamma$ -rays have to pass through three column walls to reach the detectors on the other side of the column. Such inequity doesn't happen when the particle is in the Riser, where the  $\gamma$ -rays always have to pass through two column walls to reach the detectors. Since the radiation attenuation coefficient for the plastic wall is different from that of water and is hard to be considered in the reconstruction algorithm (i.e., Mont-Carol method has been attempted in our laboratory to consider this effect but it is computationally very expensive). Thus the reconstructed particle positions are usually more erroneous when the particle is in the Downcomer region than it is in the Riser region.

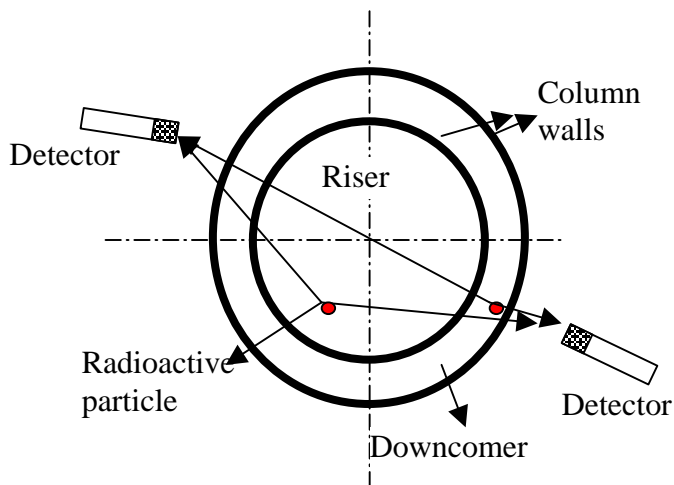


**Figure 5-6.** Illustration of the different reconstruction errors when the radioactive particle is in different reactor regions.

The second major source of reconstruction error stems from the quantized nature of the  $\gamma$ -ray as the radiation intensity of the radioactive particle exhibits continuous fluctuations in time following a Poisson distribution. Moreover, the noises introduced by the electronic transfer processes can also affect the radiation intensities recorded by the detectors. Therefore, the instantaneous particle locations reconstructed from these radiation intensity data can be very erroneous. To get rid of the white noises from the raw data, a wavelet filtering method proposed by Degaleesan et al. (2002) is used in this work.

The effects of the wavelet filtering and the errors introduced by the white noises can be revealed from Figure B-2a and 2b. These figures show the reconstructed instantaneous positions of a radioactive particle, which has been fixed on the reactor wall for some time. Ideally, the reconstructed particle positions should be identical for that period time. However, this is not the case due to the white noises as shown in Figure B-2a and 2b, each consists of 6000 points (or 1 minute). As can be seen, the reconstructed particle positions before the wavelet filtering (shown in Figure B-2a) are much more scattered with a larger variance than the reconstructed positions after the filtering (shown in Figure 5b). Clearly, without changing the mean coordinate of the reconstructed position, the wavelet filtering



considerably reduces the reconstruction errors. These errors are in the order of 1 mm (variance) with, once again, a larger error on the axial direction than on the radial direction.

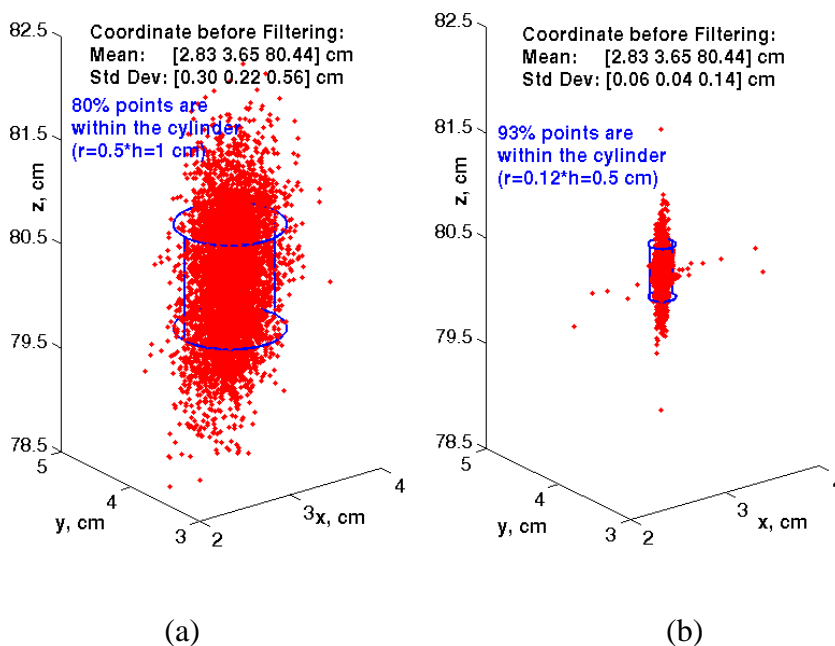


**Figure B-2.** Reconstruction errors for a fixed radioactive particle on the reactor wall. (a) before the wavelet filtering; (b) after the wavelet filtering. Please note that, since the tracer particle was fixed on the wall at position of ( $x=2.83\text{cm}$ ,  $y=3.65\text{cm}$ , and  $z=80.44\text{cm}$ ), all reconstructed position of the tracer ideally should be identical. However, due to the white noise, the reconstructed tracer positions were actually scattered around the mean. Wavelet filtering technique significantly reduced the scattering as shown above.

## Appendix C

### Flowchart of the Algorithm for the Dynamic Growth Rate Model

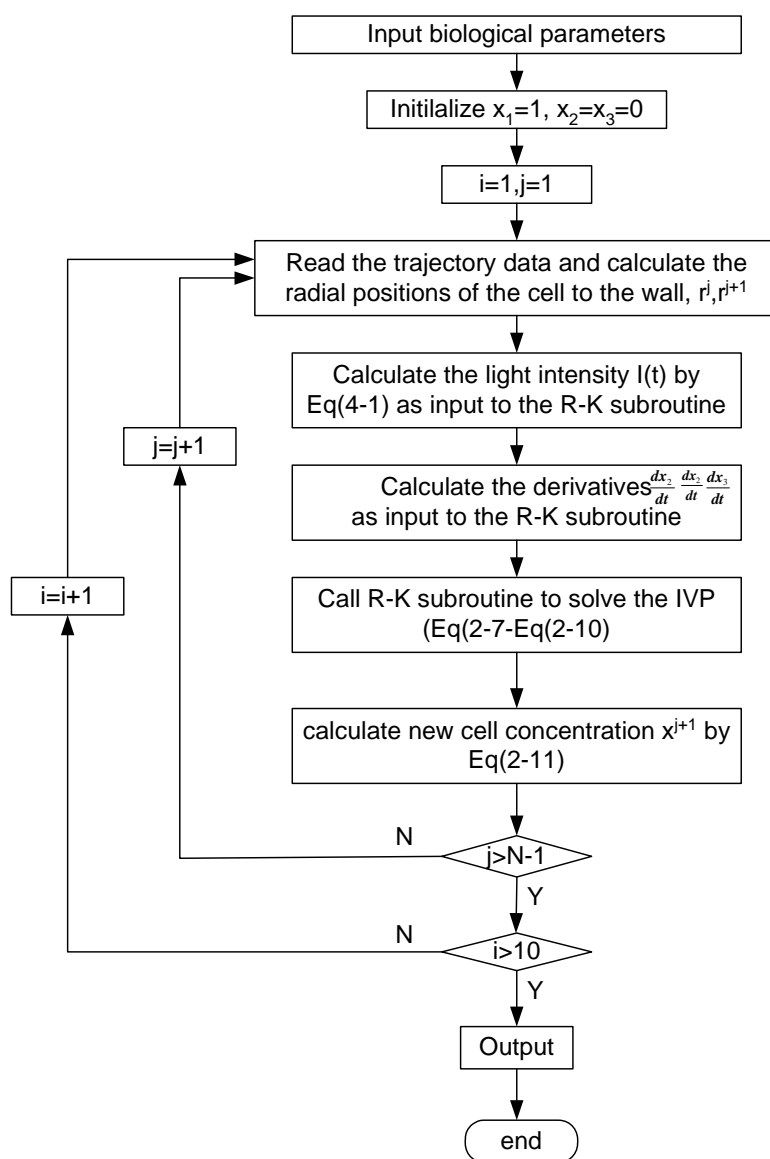


**Figure C-1.** Flowchart of the numerical simulation algorithm for the overall growth rate based on CARPT measured trajectories.

## Appendix D

### Irradiance Distribution inside Photobioreactors

Sunlight is the ultimate energy source for microalgae and cyanobacteria. Although solar radiation has a wide range of wavelength, only radiation with wavelength between 400nm and 700nm can be utilized by the microalgae and cyanobacteria. Such radiation is called Photosynthetic Active Radiation (PAR), and is considered throughout this thesis. Generally, the term of irradiance or light intensity is defined as the level of illumination obtained on certain area, i.e., the amount of light actually striking the surface of objects. This quantity depends upon the intensity and distance of the light source, and has a unit of energy per unit time and unit area, such as  $\text{W}/\text{m}^2$  (Cassano et al., 1995). In the field of photosynthesis, to consider the wavelength range most important to plants, the level of PAR actually hit on photosynthetic apparatuses in microorganism cells is called photosynthetic photon flux density (PPFD). This quantity is usually expressed as the number of photons which would fall on (or pass through) a unit area of the photosynthetic apparatus at a unit time, i.e.,  $\text{mol}/\text{m}^2\cdot\text{s}$ . Most often, the unit of  $\mu\text{E}/\text{m}^2\cdot\text{s}$  is adopted (an Einstein of photon, E, is defined as a mole of photon).

Governed by radiative transfer theory (Vincenti and Kruger, 1965; Cassano et al., 1995), the irradiance distribution inside PBRs is a complex function of incident irradiance, biomass concentration and composition, flow dynamics, and reactor geometry. The real PPFD reached a cell is the total photons come from all directions (i.e., different solid angles) with different wavelengths. A rigorously derived photon transport equation was established by Cassano et al. (1995), which ended with a very complex equation. Solving

this equation requires very expensive computation costs and many model parameters are also required to determine.

Therefore, it is a common practice to simplify the photon transport equation, such the famous Lambert-Beer law. Although the Lambert-Beer law is only valid for one-dimensional light propagation from a single source, it was found to be sufficiently accurate for irradiance distribution estimation (Ever, 1990; Acien Fernandez, et al., 1997). Assuming that the reactor surface is homogenously illuminated, and thus each point on the surface can be viewed as a light source, Ever (1990) developed a model to estimate the irradiance distribution inside the reactor using the Lambert-Beer law:

$$I(s, W) = \frac{I_{in}}{\pi} \int_0^{\pi} \exp\{-\alpha W[(r - s) \cos \theta + (r^2 - (r - s)^2 \sin^2 \theta)^{0.5}]\} d\theta \quad (D-1)$$

where  $I_{in}$  is the incident irradiance on the homogenously illuminated reactor surface,  $\alpha$  is the extinction coefficient, and  $W$  is the biomass concentration. The schematic diagram of this model is shown in Figure D-1 (Ever, 1990).

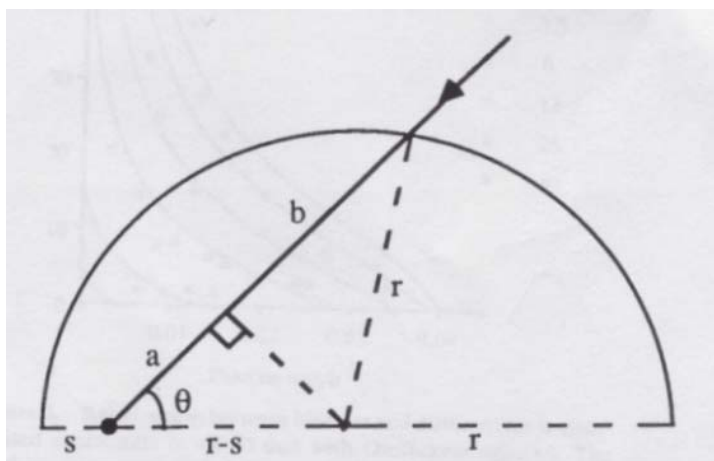


**Figure D-1.** Schematic Diagram of one-half of a cross-section through a cylinder PBR.  $ab$  is light path,  $r$  is cylinder radius,  $s$  is distance to the reactor surface, and  $\theta$  is angle between light path and the straight line through the column center (Ever, 1990).

Based on Ever's model, Wu (2001) further assumed that the photon transfer is dominated by the cellular absorption in a photobioreactor. The reactor thus can be viewed as a cylinder with infinite large cylinder, with the irradiance purely determined by the distance from the illuminated surface. Under such condition, the irradiance distribution inside the reactor can be expressed as:

$$I = I_E \cdot \exp[-(k_x \cdot x + k_w) \cdot d] \quad (4-1)$$

Wu (2001) compared these two models with his experimental data, and found both models reasonably matched the experimental data with slight difference. Apparently, this model is only valid for high biomass concentration conditions. However, due to its simplicity, Equation (4-1) was evaluated in Chapter 7 and used in this thesis to discuss the effects of hydrodynamics on photosynthesis.

## Reference

Acien Fernández G., García-Camacho F., Sánchez J.A., Fernández J.M., and Grima Molina E. (1997). A model for light distribution and average solar irradiance inside outdoor tubular photobioreactors for the microalgal mass culture, *Biotechnol. Bioeng.*, 55, 701-714.

Aiba S. (1982). Growth kinetics of photosynthetic microorganisms. *Adv. Biochem. Eng.* 23, 85-156.

Anderson T.B. and Jackson R. (1967). A fluid dynamical description of fluidized beds. *Industrial Engineering and Chemistry Fundamentals*, 6, 527-534

Bannister TT. (1979). Quantitative description of steady state, nutrient-saturated algal growth, including adaptation. *Limnol. Oceanogr.*, 24(1), 76-96

Barber J. and Andersson B. (1992). Too much of a good thing: light can be bad for photosynthesis. *Trends Biochem. Sci.*, 17, 61-66

Baten J.M., Ellenberger J., and Krishna R. (2003). Using CFD to describe the hydrodynamics of internal air-lift reactors. *Can. J. Chem. Eng.*, 81, 660-668

Becker E.W. (1994). Microalgae: Biotechnology and microbiology. In: J. Baddiley NH, Carey I.J., Higgins, Potter WG. *Cambridge Studies in Biotechnology*, Series 10. Cambridge: CUP

Becker S., Sokolichin A., and Eigenberger G. (1994). Gas-liquid flow in bubble columns and loop reactors: Part II. Comparison of detailed experiments and flow simulations. *Chem. Engng Sci.*, 49, 5747-5762

Bello R.A., Robinson C.W., and Moo-Young M. (1984). Liquid circulation and mixing characteristics of airlift contactors, *Can. J. Chem. Eng.*, 62, 573-577

- Bello R.A., Robinson C.W., and Moo-Young M. (1985). Gas hold-up and overall volumetric oxygen transfer in airlift contactors, *Biotech. Bioeng.*, 27, 369-381
- Benemann J.R. (1992). Microalgae aquaculture feeds. *J. Appl. Phycol.* 1, 239– 245.
- Bertola F., Vanni M., and Baldi G. (2003). Application of computational fluid dynamics to multiphase flow in bubble columns, *International Journal of Chemical Reactor Engineering*, v1, Article A3
- Borchers O., Busch C., Sokolichin A., Eigenberger G. (1999). Applicability of the standard k- $\epsilon$  turbulence model to the dynamic simulation of bubble columns. Part II: Comparison of detailed experiments and flow simulations. *Chem. Eng. Sci.*, 54, 5927-5935
- Borowitzka M.A. (1992) Algal biotechnology products and process: matching science and economics. *J Appl Phycol*, 4, 267 - 279
- Borowitzka M.A. (1996). Commercial production of microalgae: ponds, tanks, tubes and fermenters. *J. Biotechnol.*, 70, 313-321
- Bosca C., Dauta A., and Marvalin O. (1991). Intensive outdoor algal cultures: how mixing enhances the photosynthetic production rate. *Bioresource Technology*, 38, 185-188
- Camacho Rubio F., García Camacho F., Fernández Sevilla J.M., Chisti Y., and Molina Grima E. (2003). A mechanistic model of photosynthesis in microalgae. *Biotech. Bioengi.*, 81(4), 459-473
- Cassano A.E., Martin C.A., Brandi R.J., and Alfano O.M. (1995). Photoreactor analysis and design: fundamentals and applications. *Ind. Eng. Chem. Res.*, 34, 2155-2201
- CFX5.7 manual, Solver Theory, Ansys Inc. 2004
- Chaumont D., Thepenier C., Gudin C. (1988). Scaling up tubular photobioreactors. In: Stadler T et al. (editors) *Algal Biotechnology*. Elsevier, London, p199
- Chen J.J., Jamialahmadi M., and Li S.M. (1989). Effect of liquid depth on circulation in bubble columns: a visual study, *Chem. Eng. Res. Des.*, 67, 203
- Chen N.Y., Kondis E.F., and Srinivasan S. (1987). Low-pressure airlift fermenter for single cell protein production I. Design and oxygen transfer studies. *Biotech. Bioeng.* 29, 414-420

- Chen R.C., Reese J., and Fan L-S., (1994). Flow structure in a three-dimensional bubble column and three-phase fluidized bed, *AIChE J*, 40,1093
- Chini Zettelli G., Pastorelli R., and Tredici MR. (2000). A modular flat panel photobioreactor (MFPP) for indoor mass cultivation of *Nannochloropsis sp.* under artificial illumination, *J. Appl. Phycol.*, 12, 521-526
- Chini Zettelli G., Rodolfi L., and Tedici M.R. (2003). Mass cultivation of *Nannochloropsis sp.* in annular reactors. *J. Appl. Phycol.*, 15, 107-114
- Chisti Y. (1998). Pneumatically agitated bioreactors in industrial and environmental bioprocessing: Hydrodynamics, hydraulics, and transport phenomena. *Appl. Mech. Rev.*, 51(1), 33-112
- Chisti Y. and Moo-Young M. (1986). Disruption of microbial cells for intracellular products, *Enzyme Microb. Technol.*, 8, 194-204
- Chisti Y. and Moo-Young M. (1988). Liquid circulation in ALR. *Chem. Eng. Sci.*, 43,451-457
- Clesceri L.S., Greenberg A.E., and Eaton A.D. (1998). *Standard methods for the examination of water and wastewater*, 20th edition, American Public Health Association, Baltimore, Maryland. P10-18~10-27
- Clift R., Grace J.R., and Weber M.E. (1978). Bubbles, Drops, and Particles. New York, USA: Academic, 400pp.
- Contreras A., García F., Molina Grima E., and Merchuk J.C. (1999). Influence of sparger on energy dissipation, shear rate, and mass transfer to sea water in a concentric-tube airlift bioreactor, *Enzyme and Microbial Technology*, 25, 820-830
- Cornet J.F. and Albiol J. (2000). Modeling photoheterotrophic growth kinetics of *Rhodospirillum rubrum* in rectangular photobioreactors. *Biotechnol. Prog.*, 16, 199-207
- Cornet J.F., Dussap C.G., and Gros J.B. (1998). Kinetics and energetics of photosynthetic microorganisms in photobioreactors, *Adv. in Biochemical Engineering/Biotechnology*, 59, 153-224
- Crill P.A. (1977). The photosynthesis-light curve: a simple analog model. *J.Theor. Biol.* 64, 503-516



- Degaleesan S. (1997). Fluid dynamic measurements and modeling of liquid mixing in bubble columns. Doctoral thesis, Washington University in Saint Louis, Missouri, USA
- Degaleesan S., Dudukovic M., and Pan Y. (2001). Experimental study of gas-induced liquid-flow structures in bubble columns, *Fluid Mechanics and Transport Phenomena*, 47(9), 1913-1931
- Degaleesan S., Dudukovic M.P., and Pan Y. (2002). Application of wavelet filtering to the radioactive particle tracking technique. *Flow Measurement and Instrumentation*, 13(1-2), 31-43
- Delnoij E., Kuipers J.A.M., and Van Swaaij W.P.M. (1997b). Dynamic simulation of dispersed gas-liquid two-phase flow: effect of column aspect ratio on the flow structure, *Chem. Engg. Sci.*, 52(21/22), 3759-3772
- Delnoij E., Lammers F.A., Kuipers J.A.M., and Van Swaaij W.P.M. (1997a). Dynamic simulation of dispersed gas-liquid two-phase flow using a discrete bubble model, *Chem. Engg. Sci.*, 52(9), 1429-1458.
- Delnoij E.A., Kuipers J.A.M., and Van Swaaij W.P.M. (1997c). Computational fluid dynamics applied to gas-liquid contactors, *Chem. Engg. Sci.*, 52(21/22), 3623-3638..
- Devanathan N., Dudukovic M.P., Lapin A., and Lubbert, A. (1995). Chaotic flow in bubble column reactors, *Chem. Engg. Sci.*, 50, 2661.
- Devanathan N., Moslemian D., and Dudukovic M.P. (1990). Flow mapping in bubble columns using CARPT. *Chemical Engineering Science*, 45(8), 2285-91
- Drew D.A. (1983). Mathematical modeling of two-phase flow, *Ann.Rev.Fluid Mech.*, 15, 261-291
- Eilers P.H.C. and Peeters J.C.H. (1988). A model for the relationship between light intensity and the rate of photosynthesis in phytoplankton. *Ecological Modeling*. 42, 199-215.
- Eilers P.H.C. and Peeters J.C.H. (1993). Dynamic behavior of a model for photosynthesis and photoinhibition. *Ecological Modeling*. 69, 113-133
- El-Hassan, Molina Grima E., and Chisti Y. (2000). A process for high yield and scaleable recovery of high purity eicosapentaenoic acid esters from microalgae and fish oil, *Process Biochemistry*, 35(9), 951-969

- Eteshola E., Gottlieb M., and Malis Arad S. (1996). Dilute solution viscosity of Red microalga exopolysaccharides, *Chemical Engineering Science*, 52(9), 1487-1494
- Eteshola E., Karpasas M., Malis Arad S., and Gottlieb M. (1998). Red microalga exopolysaccharides: 2. Study of the rheology, morphology and thermal gelation of aqueous preparations, *Acta. Polym.*, 49, 549-556
- Evers E.G. (1991). A model for light limited continuous cultures. *Biotechnol. Bioeng.* 38, 254-259
- Falkowski P.G and Raven J.A. (1997). *Aquatic photosynthesis*. London, U.K.: Blackwell Science.
- Fernandez F.G.A., Camacho F.G., Perez J.A.S., Sevilla J.M.F., Molina Grima E. (1998). Modeling of biomass productivity in tubular photobioreactors for microalgal cultures: Effects of dilution rate, tube diameter, and solar irradiance. *Biotech. Bioeng.* 58, 605-616
- Ferziger J. and Peric M. (1997). *Computational methods for fluid dynamics*, Springer: Berlin
- Fraser R.D. and Hill G.A. (1993). Hydrodynamic characteristics of a spinning sparger, external loop airlift bioreactor, *Can. J. Chem. Eng.*, 71, 419-425.
- Garcia Camacho F., Contreras Gomez, Acien Fernandez, Fernandez Sevilla, Molina Grima. (1999). Use of concentric-tube airlift photobioreactors for microalgal outdoor mass cultures. *Enzyme and Microbial Technology*, 24, 164-172
- Geresh S., Manontov A., and Weinstein J. (2002). Sulfation of extracellular polysaccharides of red microalgae: preparation, characterization and properties, *J. Biochem. Biophys. Methods*, 50, 179-187
- Grace J.R., Wairegi T., and Nguyen T.H. (1976). Shapes and Velocities of Single Drops and Bubbles Moving Freely Through Immiscible Liquids, *Trans. Instn. Chem. Engrs.*, 54, 67
- Grobbelaar J.U. (1994). Turbulence in mass algal cultures and the role of light-dark fluctuations. *J. Appl. Phycol.* 6(3), 331-335
- Gu N.Y. and Liu Y.F. (2001). Bioactive substances of Porphyridium and their applications. *ZhongGuo HaiYang YaoWu*, 84(6), 43-48

Hagberg C.G. and Krupa F.X. (1976). A mathematical model for bubble column reactors and applications of it to improve a cumene oxidation process. *Proceedings of Fourth International Symposium on Chemical Reactor Engineering*, Heidelberg, Germany

Han B.-P. (2001). Photosynthesis-Irradiance response at physiological level: a mechanistic model. *J. theor. Biol.* 213, 121-127

Han B.-P. (2002). A mechanistic model of algal photoinhibition induced by photodamage to photosystem-II. *J. theor. Biol.* 214, 519-527

Han B.-P., Virtanen M., Koponen J., and Straskraba M. (2000). Effect of photoinhibition on algal photosynthesis: a dynamic model. *J. Plankton Res.* 22, 865-885

Harel M., Koven W., Lein I., Bar Y., Behrens P., Stubblefield J., Zohar, Y., and Place A.R. (2002). Advanced DHA, EPA and ArA enrichment materials for marine aquaculture using single cell heterotrophs, *Aquaculture*, 213(1-4), 347-362.

Heijnen J.J., Mulder A., Weltevrode R., Hols J., and van Leeuwen H.L.J.M. (1990). Large scale anaerobic/aerobic treatment of complex industrial wastewater using immobilized biomass fluidized bed gaslift suspension bioreactors. *Chem. Eng. Technol.*, 13, 145-220

Hsu Y.C. and Dudukovic M.P. (1980). Gas holdup and liquid circulation in gaslift reactors, *Chem. Eng. Sci.*, 35, 135-141

Hu Q. and Richmond A. (1996). Productivity and photosynthetic efficiency of *Spirulina platensis* as affected by light intensity and rate of mixing in a flat plate photobioreactor. *J Appl Phycol*, 8, 139-145

Hu Q., Zarmi Y., and Richmond A. (1998). Combined effects of light intensity, light-path and culture density on output rate of *Spitulina platensis* (Cyanobacteria). *Eur. J. Phycol.*, 33, 165-171

Huntley M.E., Niiler P.P., and Redalje D. (1996). Method of control of microorganism growth process. US Patent No. 5541056.

Ishii M. and Zuber N. (1979). Drag Coefficient and Relative Velocity in Bubbly, Droplet or Particulate Flows, *AIChE J.*, 25, 843-855

Iwakuma T. and Yasuno M. (1983). A comparison of several mathematical equations describing photosynthesis-light curve for natural phytoplankton populations, *Arch. Hydrobiol.* 97, 208-226.

Jakobsen H.A. (1993). On the modeling and simulation of bubble column reactors using two-fluid model, Dr. Ing. Thesis 97, NTH, Trondheim

Jakobsen H.A., Sannaes B.H., Grevskott S., and Svendsen F. (1996) "Modeling of bubbly flows", Engineering Foundation Conference in Computational Fluid Dynamics in Chemical Reaction Engineering, San Diego, October 13-18

Jakobsen H.A., Sannæs B.H., Grevskott S., and Svendsen, H.F. (1997). Modeling of vertical bubble-driven flows. *Ind. Eng. Chem. Res.*, 36, 4052-4074

Janssen M. (2002). Cultivation of microalgae: effect of light/dark cycles on biomass yield, D.Sc thesis, Wageningen University, Wageningen, The Netherlands

Janssen M., Kuijpers T.C., Veldhoen B., Brik Ternbach M., Tramper J., Mer L.R., and Wijffels R.H. (1999). Specific growth rate of *Chlamydomonas reinhardtii* and *Chlorella sorokiniana* under medium duration light/dark cycles: 13-87 s. *Journal of Biotechnology*, 70, 323-333

Jassby A.D. and Platt T. (1976). Mathematical formulation of the relationship between photosynthesis and light for phytoplankton. *Limnol. Oceanogr.* 21, 540-547

Jassen M., Baijens B., Tramper J., Mur L.R., Snel J.F.H., and Wijffels R.H. (2000). Scale-up aspects of photobioreactors: effects of mixing-induced light/dark cycles, *Journal of applied phycology*, 12, 225-237

Jassen M., Slenders P., Tramper J., Mur L.R., Snel J.F.H., Wijffels R.H. (2001). Photosynthetic efficiency of *Dunaliella tertiolecta* under short light/dark cycles, *Enzyme Microb. Tech.*, 29, 298-305

Javanmardian M. and Palsson B.O. (1991). High-density photoautotrophic algal cultures: design, construction, and operation of a novel photobioreactor system, *Biotech Bioeng.* 38, 1182-1189

Jones R.F., Speer H.L., and Kury W. (1963). Studies on the growth of the red alga *Porphyridium cruentum*, *Physiologia Plantarum*, 16, 636-643

Joshi J.B. and Sharma M.M. (1979). A circulation cell model for bubble columns. *Trans. Inst. Chem. Eng.* 57, 244-251

- Joshi J.B., Ranade V.V., Gharat S.D., and Lele S.S. (1990). Sparged loop reactors, *Can. J. Chem. Eng.*, 68(10), 705-741
- Joshi, J.B. (2001). Computational flow modeling and design of bubble column reactors. *Chem. Eng. Sci.*, 56, 5893
- Junge W. (1977). Photosynthetic electron transfer and photophosphorylation, In Trebst M. (Editor), *Photosynthesis I.*, Springer Verlag, Berlin, 73.
- Katinger H.W.D., Scheirer W., and Kromer E. (1979). Bubble column reactor for mass propagation of animal cells in suspension culture. *German Chemical Engineering*, 2, 31.
- Kawase Y. and Kumagai T. (1991). Heat transfer in bubble column and airlift bioreactors: Newtonian and non-Newtonian fermentation broths. *Journal Of Chemical Technology And Biotechnology*. 51,323-34.
- Klein J., Vicente A.A., and Teixeira J. (2003). Hydrodynamics of a three-phase airlift reactor with an enlarged separator—application to high cell density systems. *Can. J. Chem. Eng.*, 81, 433-443
- Kolbel H. and Ralek M. (1980). The Fischer-Tropsch synthesis in the liquid phase. *Catalysis in Review-Science Engineering*, 27(2), 225
- Krishna R., Urseanu M.I., Van Baten J.M., and Ellenberger J. (1999). Influence of scale on the hydrodynamics of bubble columns operating in the churn-turbulent regime: Experiment vs. Eulerian simulations, *Chem. Engg. Sci.*, 54, 4903-4911.
- Krishna R., Van Baten J.M., and Urseanu M.I. (2000). Three-phase Eulerian simulations of bubble column reactors operating in churn-turbulent regime: a scale up strategy. *Chem. Eng. Sci.*, 55(16), 3275-3286
- Kulick M.M. (1995). The potential for using cyanobacteria (blue-green algae) and algae in the biological control of plant pathogenic bacteria and fungi, *Eur. J. Plant Path.*, 101, 585-599.
- Kumar S., Vanderheyden W.B., Devenathan N., Padiyal N.T., Dudukovic, M.P., and Kashiwa B.A. (1995). Numerical simulation and experimental verification of gas-liquid flow in bubble columns, in international mixing fundamentals with applications, *AIChE Symposium Series* No. 305, Vo. 91, 11-19

Kumar S.B. (1994). *Computed tomographic measurements of void fraction and modeling of the flow in bubble columns*, Ph.D. Thesis, Florida Atlantic University: Boca Raton, FL, USA.

Kumar S.B. and Dudukovic M.P. (1997). Computer assisted gamma and X-ray tomography: Application to multiphase flow. In Chaouki, J., Larachi, F. and Dudukovic, M.P. (Eds.), *Non-invasive monitoring of multiphase flows*, Amsterdam, The Netherlands: Elsevier.

Lain S., Broder D., and Sommerfeld M. (1999). Experimental and numerical studies of the hydrodynamics in a bubble column, *Chem. Eng. Sci.*, 54, 4913-4920.

Lapin A. and Lubbert A. (1994). Numerical simulations of the dynamics of two-phase gas-liquid flows in bubble columns, *Chem. Engr. Sci.*, 49, 3661.

Lauder B.E. and Spalding D.B. (1974). The numerical computation of turbulent flows, *Comp Meth Appl Mech Eng*, 3:269-289

Laws E.A., Terry K.L., Wichman J., and Chalup M.S. (1983). A simple algal production system designed to utilize the flashing light effect. *Biotech. Bioengi.* 25, 2319-2335

Lee Y. and Pirt S.J. (1981). Energetics and photosynthetic algal growth. Influence of intermittent illumination in short (40s) cycles. *J.Gen. Microbiol.* 124, 43-52

Lee Y.K. (1986). Enclosed bioreactors for the mass cultivation of photosynthetic microorganisms: the future trend, *Trend Biotechnology.* 4, 186-189

Levenspiel O. (1972). *Chemical Reaction Engineering*. John Wiley, New York

Lin T.J., Bass G.B., Tsuchiya K., and Fan L.S. (1999). Distributor effects on hydrodynamics of high pressure bubble columns. *Chem. Engng. Sci.*,

Lo C.S. and Hwang S.J. (2003). Local hydrodynamic properties of gas phase in an internal-loop airlift reactor. *Chem. Eng. J.*, 91, 3-32

Lopez de Bertodano M. (1998). Two Fluid Model for Two-Phase Turbulent Jet, *Nucl. Eng. Des.*, 179, 65-74

Lu W.-J., Hwang S.-J., and Chang C.-M. (1994). Liquid mixing in internal loop airlift reactors, *Ind. Eng. Chem. Res.*, 33, 2180-2186

Luo H.-P. and Al-Dahhan M.H. (2004). Analyzing and modeling of photobioreactors by combining first principles of physiology and hydrodynamics. *Biotech. Bioeng.*, 85(4), 382-393

Luo H.-P., Kemoun A., Al-Dahhan M.H., Fernández Sevilla J.M., García Sánchez J.L., García Camacho F., Molina Grima E. (2003). Analysis of photobioreactors for culturing high value microalgae and cyanobacteria via an advanced diagnostic technique: CARPT. *Chem. Eng. Sci.* 58(12), 2519-2527

MacIntyre H.L., Kana T.M., Anning T., Geider R. (2002). Photoacclimation of photosynthesis irradiance response curves and photosynthetic pigments in microalgae and cyanobacteria, *J. Phycol.*, 38, 17-38

Magard R.O., Tonkyn D.W., and Sehft W.H. (1984). Kinetics of oxygenic photosynthesis in planktonic algae. *Journal of Plankton Research.* 6(2), 325-337

Markatos N.C. (1986). The mathematical modeling of turbulent flows, *Applied Mathematical Modeling*, 10, 190-220

Markl H. (1980). Modeling of algal production systems. Amsterdam: Elsevier. p361-383.

Mei R. (1992). An approximate expression for the shear lift force on a spherical particle at finite Reynolds number. *International J. of Multiphase Flows*, 18, 145-147

Merchuk J. and Berzin I. (1995). Distribution of energy dissipation in airlift reactors, *Chem. Eng. Sci.*, 50(14), 2225-33

Merchuk J.C. and Stein Y. (1981). Local hold-up and liquid velocity in airlift reactors. *AIChE J.*, 27, 377-388

Merchuk J.C., Contreras A., Garcia F., and Molina Grima E. (1998b) Studies of mixing in a concentric tube airlift bioreactor with different spargers, *Chem. Eng. Sci.*, 53(4), 709-719

Merchuk J.C., Gluz M. and Mukmenev I. (2000). Comparison of photobioreactors for cultivation of the microalga *Porphyridium sp.* *J. Chem. Technol. Biotechnol.* 75(12), 1119-1126

Merchuk J.C., Ladwa N., Cameron A., Bulmer M., Pickett A. (1994). Concentric-tube airlift reactors: effects of geometrical design on performance. *AIChE J.* 40, 1105-17

- Merchuk J.C., Ronen M., Giris S., Arad S. (1998). Light/Dark cycles in the growth of the red microalga *Porphyridium Sp.* *Biotech. Bioengi.* 59(6), 705-713.
- Molina Grima E., Camacho F.G., Peres J.A.S., Fernandez F.G.A., and Sevilla J.M.F. (1997). Evaluation of photosynthetic efficiency in microalgal cultures using averaged irradiance, *Enzyme and Microbial Technology*. 21, 375-381
- Molina Grima E., Fernandez F.G.A., Camacho F.G., and Chisti Y. (1999). Photo-bioreactors: light regime, mass transfer, and scaleup. *J. Biotech.* 70: 231-247.
- Molina Grima E., Fernandez Sevilla J.M., Sanchez Perez J.A., and Garcia Cmacho F. (1996a). A study on simultaneous photolimitation and photoinhibition in dense microalgal cultures taking into account incident and averaged irradiances. *J. of biotech.*, 45, 59-69
- Molina Grima E., Garcia Camacho F., Sanchez Perez J.A., Fernandez Sevilla J., Acien Fernandez F.G., and Contreras Gomez A. (1994). A mathematical model of microalgal growth in light limited chmostat cultures. *J.Chem.Technol.Biotechnol.* 61, 167-173
- Molina Grima E., Robles Medina A., Gimenez Gimenez A., and Ibanez Gonzalez M.J. (1996b). Gram-scale purification of eicosapentaenoic acid (EPA, 20: 5n3) from wet *Phaeodactylum tricornutum*, *J. Appl. Phycol.*, 8, 359-367
- Morsi S.A. and Alexander A.J. (1972). An investigation of particle trajectories in two-phase flow systems. *Journal of Fluid Mechanics*, 55(2), 193-208
- Mudde R.F. and Van Den Akker H.E.A. (2001). Two-fluid model simulations of an internal airlift loop reactor, *PVP*, 424(1), 101-108
- Nakao K., Azakami F., Furumoto K., Yoshimoto M., and Fukunaga K. (2003). Measurement and correlation of critical gas and liquid velocities for complete circulation of solid particles in external loop airlift bubble columns, *Can. J. Chem. Eng.*, 81, 444-450
- Nedbal L., Tichy V., Xiong F., and Grobbelaar J.U. (1996). Microscopic green algae and cyanobacteria in high-frequency intermittent light. *Journal of Applied Phycology*, 8, 325-333
- Oels U., Lucke J., Buchholz R., and Schugerl K. (1978). Influence of Gas distributor type and composition of liquid on the behavior of a bubble column bioreactor. *Ger. Chem. Eng.*, 1, 115



- Okauchi M. (1991). The status of phytoplankton production in Japan. In: Fulks W. and Main K.L. (Eds), *Rotifer and Microalgae culture systems*. Proceedings of a U.S.-Asia workshop. The Oceanic Institute, Honolulu, Hawaii, USA, pp. 247-256
- Olaizola M. (2000). Commercial production of astaxanthin from *Haematococcus pluvialis* using 25,000-liter outdoor photobioreactors. *J. Appl. Phyco.*, 12, 499-506
- Onozaki M., Namiki Y., Sakai N., Kobayashi M.Y., Nakayama Y., Yamada T., and Morooka S. (1999). Dynamic simulation of gas-liquid dispersion behavior in coal liquefaction reactors, submitted to *Chem. Eng. Sci.*, (1999).
- Oswald W.J. (1977). The engineering aspect of microalgae. In: Laskin A. and Lechevalier H.A. (Ed). *CRC handbook of microbiology*, CRC Press, Cleveland. P519-552
- Padial N.T., VanderHeyden W.B., Rauenzahn R.M., and Yarbrow S.L. (2000). Three-dimensional simulation of a three-phase draft-tube bubble column. *Chem. Eng. Sci.*, 55, 3261-3273
- Pahl-Wostl C. and Imboden D.M. (1990). DYPHORA-a dynamic model for the rate of photosynthesis of algae. *Journal of Plankton Research*. 12(6), 1207-1221
- Pan Y., Dudukovic M.P., and Chang M. (1999). Dynamic simulation of bubbly flow in bubble columns. *Chem. Eng. Sci.*, 54(13-14), 2481-2489.
- Pan Y., Dudukovic M.P., and Cheng M. (2000). Numerical investigation of gas-driven flow in 2-D bubble columns, *AIChE J.*, 46, 434-449.
- Petersen E. and Margaritis A. (2001). Hydrodynamic and mass transfer characteristics of three-phase gaslift bioreactor systems, *Crit. Rev. Biotechnol.*, 21(4), 233-294
- Pfleger D., Gomes S., Gilbert N., and Wagner H.-G. (1999). Hydrodynamic simulations of laboratory scale bubble columns fundamental studies of the Eulerian-Eulerian modeling approach. *Chem. Eng. Sci.*, 54, 5091-5099.
- Phillips J.N. and Myers J. (1954). Growth rate of *Chlorella* in flashing light. *Plant Physiol.* 29, 152
- Pirt S.J. (1986). The thermodynamic efficiency (quantum demand) and dynamics of photosynthetic growth, *New Phytol.*, 102, 3-37
- Pollard D.J., Ison A.P., Shamlou P.A., and Saez A.E. (1998). Reactor heterogeneity with *Saccharopolyspora erythraea* airlift fermentations. *Biotech. Bioeng.*, 58, 453-463

- Pruvost J., Legrand J., and Legentilhomme P. (2002). Simulation of microalgae growth in limiting light conditions: flow effect. *AIChE J.*, 48(5), 1109-1120
- Pulz O. and Scheibnbogen K. (1998). Photobioreactors: Design and performance with respect to light energy input. *Adv. Biochem. Engi./Biotech.*, 59, 123-151
- Rafique M., Al-Dahhan M.H., and Dudukovic M.P. (2002). Influence Of Different Closures On The Hydrodynamics Of Bubble Column Flows, *17th International Symposium on Chemical Reaction Engineering (ISCRE17)*, Hong Kong, Aug. 25-28
- Rammohan A., Kemoun A., Al-Dahhan M.H., Dudukovic M.P., and Larachi F. (2001). CARPT dynamic bias studies: evaluation of accuracy of position and velocity measurements. *Recents Progres en Genie des Procedes*, 15, 59-67
- Rammohan A.R. (2002). Characterization of single and multiphase flows in stirred tank reactors. D.Sc. Thesis, Washington University, St. Louis, Missouri.
- Ranade V.V. (1992). Numerical simulation of dispersed gas-liquid flows, *Sadhana*, 17, 237-273.
- Ranade V.V. (1995). Computational fluid dynamics for reactor engineering, *Reviews in Chemical Engineering*, 11, 229-289.
- Ranade V.V. (1997). Modeling of turbulent flow in a bubble column reactor, *Transactions of the Institution of Chemical Engineers*, 75A, 14-23.
- Reboloso Fuentes M.M., García Sánchez J.L., Fernández Sevilla J.M., Acien Fernández F.G., Sánchez Pérez J.A., and Molina Grima E. (1999). Outdoor continuous culture of *Porphyridium cruentum* in a tubular photobioreactor: quantitative analysis of the daily cyclic variation of culture parameters, *Journal of Biotechnology*, 70, 271-288
- Reboloso Fuentes M.M., García Sánchez J.L., Fernández Sevilla J.M., Acien Fernández F.G., Sánchez Pérez J.A., Molina Grima E. (1999). Outdoor continuous culture of *Porphyridium cruentum* in a tubular photobioreactor: quantitative analysis of the daily cyclic variation of culture parameters, *Journal of Biotechnology*, 70, 271-288
- Rhie C.M. and Chow W.L. (1983). Numerical study of the turbulent flow past an airfoil with trailing edge separation, *AIAA J.*, 21, 1525-1532
- Rivas O., Bresolin G.A., Estevez L.A., Santamaria X., and Cavicchioli I. (1987). Effect of gas distribution on the fluid dynamics of three-phase bubble columns. *Rev. Tec. Intevp.*, 7,2, 97-102

- Rizk M.A. and Elgobashi S.E. (1989). A two-equation model for dispersed dilute confined two-phase flows, *Int. J. Multiphase Flow*, 15, 119-133.
- Robinson P.K., Mak A.L., and Trevan M.D. (1986). Immobilized algae: a review, *Process Biochem.* 21, 122-127
- Rorrer G.L. and Mullikin R.K. (1999). Modeling and simulation of a tubular recycle photobioreactor for macroalgal cell suspension cultures. *Chem. Eng. Sci.* 54(15-16), 3153-3162
- Rosenzweig M. and Ushio S. (1974). Protein from methanol. *Chemical Engineering*, 62.
- Roy S., Larachi F., Al-Dahhan M.H., and Dudukovic M.P. (2002). Optimal design of radioactive particle tracking experiments for flow mapping in opaque multiphase reactors. *Applied Radiation and Isotopes*, 56, 485-503
- Rubinow S.I. and Keller J.B. (1961). The transverse force on a spinning sphere moving in a viscous fluid. *J.Fluid Mech.*, 11, 447-459
- Saffman P.G. (1965). The lift on a small sphere in a slow shear flow, *J. Fluid Mech.*, 22, 385
- Saffman P.G. (1968). Corrigendum to 'The lift on a small sphere in a slow shear flow'. *J.Fluid Mech.*, 31, 624
- Sanchez Miron A., Contreras Gomez A., Garcia Camacho F., Molina Grima E., and Chisti Y. (1999). Comparative evaluation of compact photobioreactors for large-scale monoculture of microalgae. *Journal of Biotechnology*, 70, 249-270
- Sankaranarayanan K., Shan X., Kevrekidis I.G., and Sundaresan S. (2000) Analysis of drag and virtual mass forces in bubbly suspensions using an implicit formulation of the Lattice Boltzmann method, July 20, 2000, *Engineering Foundation Conference on CFD*, Quebec.
- Sanyal J., Vasquez S., Roy S., and Dudukovic M.P. (1999). Numerical simulation of gas-liquid dynamics in cylindrical bubble column reactors, *Chem. Engng. Sci.*, 54, 5071-5083
- Sato Y. and Sekoguchi K. (1975). Liquid velocity distribution in two-phase bubble flow, *Int. J. Multiphase Flow*, 2, 79

- Schiller L. and Naumann A. (1935). A Drag Coefficient Correlation, *Z. Ver. Deutsch. Ing.*, 77:318
- Schwarz M.P. and Turner W.J. (1988). Applicability of the standard k- $\epsilon$  model to gas stirred baths, *App. Math. Modeling*, 12, 273-279.
- Shioya S., Dang N.D.P., and Dunn I.J. (1978). Bubble column fermenter modeling: A comparison for pressure effects. *Chem. Eng. Sci.*, 33, 1025-30.
- Sittig M. (1967). *Organic Chemical process encyclopaedia*. USA: Noyes Dev. Corp.
- Smidt J., Hafner W., Jira R., Seiber R., Sedimeier J., and Sabel A. (1962). Olefunoxydation mit Palladiumchlorid-Kataclysatoren. *Angew. Chemie*, 74, 93
- Soderberg D.J. (1980). Circulating bubble columns, D.Sc Thesis, University of Cambridge, Cambridge, UK
- Sokolichin A. and Eigenberger G. (1994). Gas-liquid flow in bubble columns and loop reactors: Part I: Detailed modeling and numerical simulation, *Chem. Engg. Sci.*, 52, 5735.
- Sokolichin A. and Eigenberger G. (1999). Applicability of the standard k- $\epsilon$  turbulence model to the dynamic simulation of bubble columns. Part I. Detailed numerical simulations. *Chem. Eng. Sci.*, 54, 2273-2284
- Sokolichin A., Eigenberger G., and Lapin A. (2004). Simulation of buoyancy driven bubbly flow: Established simplifications and open questions. *AIChE Journal*, 50(1), 24-45.
- Sokolichin A., Eigenberger G., Lapin A., and Luebbert A. (1997). Dynamic numerical simulation of gas-liquid two-phase flows. Euler/Euler versus Euler/Lagrange. *Chem. Eng. Sci.*, 52, 611-626
- Steele J.H. (1977). In: Lapidus L. and Amundson N.R. (Eds), *Microbial kinetics and dynamics in chemical reactor theory*. Prentice-Hall, Englewood Cliffs, NJ, pp. 405-483
- Stewart and Wendroff. (1984). *Journal of Computational Physics*, 56, 363-409
- Sukenik A. (1999). Production of Eicosapentaenoic acid by the marine eustigmatophyte *Nannochloropsis*. In: Cohen Z. (Ed.), *Chemicals from Microalgae*. Taylor & Francis, London, pp. 41-56

- Svendsen H.f., Jakobsen H.A., and Torvik R. (1992). Local flow structure in internal loop and bubble column reactors, *Chem. Engg. Sci.*, 47(13/14), 3297-3304.
- Tamiya H., Hase E., Shibata K., Mituya A., Iwamura T., Nihei T., and Sasa T. (1953). Kinetics of growth of *Chlorella*, with special reference to its dependence on quantity of available light and on temperature. In: Burlew J.S. (Ed.), *Algal culture from laboratory to pilot plant*. Carnegie Institution of Washington, Washington DC, pp. 204-232
- Terry K.L. (1986). Photosynthesis in modulated light: quantitative dependence of photosynthetic enhancement on flashing rate. *Biotech. Bioeng.*, 28, 988-995
- Thakre S. S. and Joshi J.B. (1999). CFD simulation of bubble column reactors: importance of drag force formulation, *Chem. Engng. Sci.*, 54, 5055-5060
- Theofanus T.G. and Sullivan J.P. (1982). *J. Fluid Mechanics*, 116, 343
- Torvik R. and Svendsen H.F. (1990). Modeling of slurry reactors: A fundamental approach, *Chem. Engr. Sci.*, 45, 2325.
- Tredici M.R. (2004). Mass production of microalgae: photobioreactors. In: Richmond A. (Ed.), *Handbook of microalgal culture: Biotechnology and applied phycology*, Blackwell Publishing, Iowa, USA, pp. 178-214
- Tredici M.R. and Zittelli G.C. (1998). Efficiency of sunlight utilization: Tubular versus flat photobioreactors. *Biotechnol Bioeng.* 57, 187-197
- Tsuchiya K. and Nakanishi O., (1992). Gas holdup behavior in a tall bubble column with perforated plate distributors, *Chem. Engng. Sci.*, 47, 13/14
- Van Baten J.M. and Krishna R. (2001). Eulerian simulations for determination of the axial dispersion of liquid and gas phases in bubble columns operating in the churn-turbulent regime. *Chem. Eng. Sci.*, 56, 503-512
- Van Oorschot J.L.P., (1955). Conversion of light energy in algal cultures. *Med Van Lund. Wang.* 55, 225-277
- Verlaan P., Van Eijs A.M., Tramper J., Van't Riet K., and Luyben K. (1989). Estimation of axial dispersion in individual sections of an airlift-loop reactor, *Chemical Engineering Science*, 44, 1139-1146

- Vial C., Poncin S., Wild G., and Midoux N. (2001). A simple method for regime identification and flow characterisation in bubble columns and airlift reactors. *Chemical Engineering and Processing*, 40(2), 135-151.
- Vial C., Poncin S., Wild G., and Midoux N. (2002). Experimental and theoretical analysis of the hydrodynamics in the riser of an external loop airlift reactor, *Chem. Eng. Sci.*, 57, 4745-4762
- Villiermaux J. (1996). Trajectory Length Distribution (TLD), a novel concept to characterize the mixing in flow system. *Chem. Eng. Sci.*, 51, 1939-1946
- Vincenti W.G. and Kruger C.H. (1965). Introduction to physical gas dynamics, Wiley, New York
- Vonshak A. (1992). Microalgal biotechnology: is it an economic success? In: Da Silva E.J., Ratledge C., and Sasson A. *Biotechnology: economic and social aspects, Issue for developing countries*, Cambridge: CUP
- Weiland P. and Onken U. (1981). Fluid dynamics and mass transfer in an airlift fermentor with external loop. *Ger. Chem. Eng.*, 4, 40-42
- Weller S. and Franck J. (1941). Photosynthesis in flashing light. *J. Phys Chem.* 45, 1359-1373
- Winokur M. (1948). Growth relationship of *Chlorella* species. *Am. J. Bot.* 35, 118-129
- Wu X. and Merchuk J.C. (2001). A model integrating fluid dynamics in photosynthesis and photoinhibition processes. *Chem. Eng. Sci.* 56, 3527-3538
- Wu X. and Merchuk J.C. (2002). Simulation of algae growth in a bench-scale bubble column reactor. *Biotech. Bioeng.* 80(2), 156-168
- Wu X. and Merchuk J.C. (2003). Measurement of fluid flow in the downcomer of an internal loop airlift reactor using an optical trajectory-tracking system. *Chem. Eng. Sci.*, 58(8), 1599-1614.
- Young M.A., Carbonell R.G., and Ollis D.F. (1991). Airlift bioreactors: analysis of two-phase hydrodynamics, *AIChE J.*, 37(3), 403-428

Yuan N., Gu X., Li I., Zhu D., and Ding F. (1994). Study on an airlift loop reactor with membranous gas distributor and its application in fermentations of baker's yeast, in *Better Living Through Biochemical Engineering*, Teo W.K., Yap M.G.S., and Oh S.K.W. (eds), Univ. of Singapore, Singapore, 426-428.

Zhang X., Zhou B., Zhang Y., Cai Z., Cong W., and Ou Yang F. (2002). A simple and low-cost airlift photobioreactor for microalgal mass culture, *Biotechnol. Letters*, 24, 1767-1771

Zonneveld C. (1998). Photoinhibition as affected by photoacclimation in phytoplankton: a model approach. *J. theor. Biol.* 193, 115-123

Zou N., Zhang C.W., Cohen Z., and Richmond A. (2000). Production of cell mass and eicosapentaenoic acid (EPA) in ultrahigh cell density cultures of *Nannochloropsis sp.* (Eustigmatophyceae). *Eur. J. Phycol.*, 35, 127-133

## Vita

<b>Name</b>	Hu-Ping Luo
<b>Date of Birth</b>	April 2, 1974
<b>Place of Birth</b>	Jiangxi, China.
<b>Degrees</b>	B.E. in Chemical Engineering, July 1994 Dalian University of Technology, Dalian, China MS in Chemical Engineering, July 1999 East China University of Science and Technology, Shanghai, China D.Sc. Chemical Engineering, August 2005 Washington University, Saint Louis, MO, USA.
<b>Industrial Experience</b>	Process Engineer, August 1994-August 1996 Juhua Group Corporation, Quzhou, China
<b>Professional Societies</b>	American Institute of Chemical Engineers

### Publications

- Analyzing and Modeling of Photobioreactors by Combining First Principles of Physiology and Hydrodynamics, Luo, H.-P., and Al-Dahhan, M.H. (2004). *Biotech. and Bioeng.* 85(4), 382-393



- Analysis of photobioreactor for culturing high value microalgae and cyanobacteria via an advanced diagnostic technique: CARPT. Luo, H.-P., Kemoun, A., Al-Dahhan, M.H., Fernandez, J.M., and Molina G.E. (2003). *Chem. Eng. Sci.*, 58(12), 2519-2527.
- A reactive distillation process for a cascade and azeotropic reaction system: carbonylation of ethanol with dimethyl carbonate. Luo, H.-P.; Xiao, W.-D. (2001). *Chem. Eng. Sci.*, 56(2), 403-410.
- Isobaric Vapor-Liquid Equilibria of Binary Mixtures Containing Dimethyl Carbonate under Atmospheric Pressure. Luo, H.-P.; Zhou, J.-H.; Xiao, W.-D.; Zhu, K.-H. (2001). *J. of Chem. & Eng. Data*, 46(4), 842-845.
- Process for preparing diethyl carbonate. Fang, Yunjin; Luo, Huping; Xiao, Wende. (2001). *Faming Zhuanli Shenqing Gongkai Shuomingshu*. 7 pp. Patent No.: CN1314338. Date: 20010926
- Continuous manufacture of diethyl carbonate. Fang, Yunjin; Luo, Huping; Xiao, Wende. (2001). *Faming Zhuanli Shenqing Gongkai Shuomingshu*. 10 pp. Patent No.: CN1320594. Date: 20011107
- Isobaric vapor-liquid equilibria of alkyl carbonates with alcohols. Luo, H.-P.; Xiao, W.-D.; Zhu, K.-H. (2000). *Fluid Phase Equilibria*, 175(1-2), 91-105.
- A fractionating reactor for manufacturing of dimethyl carbonate, Luo H.-P., Xiao W.D., Zhu K.H. (1999). *Proceedings of Asia-Pacific Chemical Reaction Engineering (APCRE) Symposium*, Hong Kong, June 13-17

### **Presentations and Posters**

- An Example of Flow Pattern and Mixing in Bioreactors using Laboratory Tools, Hu-Ping Luo and Muthanna H. Al-Dahhan (2004). *Process Development Symposium: Working Right on the Right*, Chicago, June 20-23

- A Novel Modeling Approach for Predictions of the Dynamic Growth of Microalgae in Multiphase Photobioreactors, Al-Dahhan, M.H. and Luo, H.-P. (2004). *Invited lecture in Biophex Conference*, San Francisco, Sep. 28-30
- Local Characteristics of Flows in Airlift Photo-Bioreactors via CARPT experiments and CFD simulation, Al-Dahhan, M.H., Luo, H.-P., (2003). *Computational Fluid Dynamics in Chemical Reaction Engineering III*, Davos, Switzerland, May 25-30
- Analyzing and Modeling of Photobioreactors by Combining First Principles of Physiology and Hydrodynamics, Hu-Ping Luo and Muthanna H. Al-Dahhan (2003). *1<sup>th</sup> International Congress on Bioreactor Technology in Cell-, Tissue Culture and Biomedical Applications*, Tampere, FINLAND JULY 14 - 18
- Analysis Of Photobioreactor For Culturing High Value Products: Microalgae And Cyanobacteria Via Advanced Diagnostic Techniques. Al-Dahhan M.H., Luo H.-P., Kemoun A., Fernandez J.M., Grima E.M. (2002). *17th International Symposium on Chemical Reaction Engineering (ISCRE17)*, Hong Kong, Aug. 25-28
- Photobioreactors for Culturing High Value Microalgae and Cyanobacteria: Experimentation and Modeling. Luo, H.-P., Al-Dahhan, M.H. (2002). *AICHE annual meeting*, Indianapolis, Iowa, Nov. 4-6.
- A reactive distillation process for a cascade and azeotropic reaction system: Carbonylation of ethanol with dimethyl carbonate, Luo H.P., Xiao W.D. (2000). *ISCRE 16*, Poland, August.

**Short Title: Analyze Airlift Photobioreactors**

**Luo, D.Sc. 2005**